

Universidade do Minho
Escola de Engenharia

Leonardo Filipe Guilherme Rodrigues Robustness of multi-story timber buildings in seismic regions

Leonardo Filipe Guilherme Rodrigues

Robustness of multi-story timber buildings in seismic regions

FCT Fundação para a Ciência e a Tecnologia

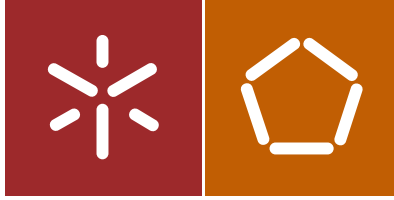
MINISTÉRIO DA CIÊNCIA, TECNOLOGIA E ENSINO SUPERIOR



UMinho | 2019

fevereiro de 2019





Universidade do Minho
Escola de Engenharia

Leonardo Filipe Guilherme Rodrigues

Robustness of multi-story timber buildings in
seismic regions

Tese de Doutoramento
Engenharia Civil

Trabalho efetuado sob a orientação de
Professor Doutor Jorge M. Branco
Professor Doutor Luís A. C. Neves

DECLARAÇÃO

Nome Leonardo Filipe Guilherme Rodrigues

Endereço electrónico: leonardofgrodrigues@gmail.com

Telefone: 961125266

Número do Bilhete de Identidade: 13038868

Título da tese:

Robustness of multi-story timber buildings in seismic regions

Orientador(es):

Professor Doutor Jorge M. Branco, Universidade do Minho

Professor Doutor Luís A. C. Neves, Universidade de Nottingham

Ano de conclusão: 2018

Designação do Doutoramento: Doutoramento em Engenharia Civil

É AUTORIZADA A REPRODUÇÃO INTEGRAL DESTA TESE/TRABALHO APENAS PARA EFEITOS DE INVESTIGAÇÃO, MEDIANTE DECLARAÇÃO ESCRITA DO INTERESSADO, QUE A TAL SE COMPROMETE;

Universidade do Minho,

Assinatura:

STATEMENT OF INTEGRITY

I hereby declare having conducted my thesis with integrity. I confirm that I have not used plagiarism or any form of falsification of results in the process of the thesis elaboration.

I further declare that I have fully acknowledged the Code of Ethical Conduct of the University of Minho.

University of Minho,

Full name:

Signature:

Acknowledgements

I would not have been able to reach this step without the people who have been helping me to make it here. Thus, I would like to express my gratitude to:

- My supervisors: Prof. Jorge Branco and Prof. Luís Neves for the knowledge and technical expertise imparted and for listening to me during discouragement times. Thank you for the support given.
- Prof. André Barbosa, for always taking the time to teach me and make me grow as a researcher. More than the technical knowledge shared, I am grateful for the long conversations about the important aspects of life. Thank you for hosting me in your research group.
- Fellow colleagues: There are a lot of people that made this accomplishment possible, and contributed in a direct or indirect way. I would like to thank to researchers from FCT/UNL, IST, FEUP, LNEC, University of Minho, University of Trento, IVALSA, and Oregon State University.
- Professors from previous public institutions of education I attended: I would like to acknowledge the professors that taught me in Chelas (Vale Fundão), Marvila (n.193), Reboleira (n.3), Roque Gameiro, ESA (Escola Secundária da Amadora), and FCT/UNL.

There are no words to express my gratitude to my family and friends, which have been encouraging me throughout these 32 years of a life well-lived. I would like to thank you all for the moments we shared and the lessons that you taught me. This thesis is dedicated to all of you.

Uncertainties are present in our lives every single day, aleatory events come up and can cause unpredictable consequences. I am glad that I met someone that has been changing my life in such a good way. Thank you Susana Moreira.

This work had financial support of the Portuguese Science Foundation (FCT), through Ph.D. grant PD/BD/113679/2015 included in InfraRisk-Ph.D. program.

Abstract

In the past few years, the construction of multi-storey timber buildings has increased significantly in locations where high intensity ground motions are likely to occur. On the other hand, the fast development of wood engineered products, as glued-laminated timber (GLT) and cross-laminated timber (CLT), has been challenging researchers to provide adequate guidelines for design and assessment of structures built in seismic regions. Some guidelines and analysis methods considered in seismic design can improve robustness, which is commonly described as the ability of structures to sustain limited damage without disproportionate effects. This thesis main objective is the development of numerical modeling approaches for seismic and robustness assessment of multi-storey timber buildings. The work is divided in three distinct parts that complement each other. First, given the importance of diaphragms to transfer inertial loads to the lateral resisting systems, a phenomenological computational model approach for CLT diaphragms was proposed and validated by comparing numerical results to experimental data obtained from a two-story full-scale building tested on a shake-table.

A second part of the thesis focused on the seismic performance of a three-story building through a probabilistic approach, which accounts for uncertainties in mechanical properties of members and connections. Nonlinear static analyses and multi-record incremental dynamic analyses were performed to characterize the q -factor and develop fragility curves for different damage levels. The results indicate that the detailing requirements of Eurocode 5 and Eurocode 8 are sufficient to achieve the required performance, even though they also indicate that these requirements can be optimized to achieve more cost-effective connections and members.

Finally, the progressive collapse potential of seismic resistant heavy-timber structures was studied through an alternate load path analysis (ALPA). This robustness assessment involved nonlinear static analyses (pushdown analyses) that include uncertainties related to material properties and applied loads. Fragility functions were developed for different column loss scenarios and for two distinct diaphragm solutions. The first one makes use of cross-laminated timber (CLT) panels connected with half-lap joints, while the second solution consists of a low weight solution with 18 mm oriented strand boards fastened to the GLT joists. The results indicate that the structural capacity for developing alternative load paths is highly dependent on the rotational capacity of connections.

Resumo

Nos últimos anos, a construção de edifícios de madeira de vários andares, em regiões sísmicas, tem aumentado significativamente. Por outro lado, o rápido desenvolvimento na produção de produtos derivados de madeira, como lamelados colados (GLT) e lamelados colados cruzados (CLT), tem desafiado investigadores de todo o mundo a propor critérios adequados para o dimensionamento e avaliação de estruturas construídas em regiões sísmicas, que por sua vez podem também aumentar a robustez, comumente descrita como a capacidade da estrutura para resistir a uma falha local, sem atingir níveis de dano desproporcionados. Esta tese tem como objetivo o desenvolvimento de metodologias de modelação numérica para avaliação sísmica e de robustez de edifícios de madeira de vários andares. Este trabalho divide-se em três partes distintas, mas que se complementam. Primeiro, dada a importância dos diafragmas na transferência de forças de inércia para os sistemas de resistência lateral, uma abordagem fenomenológica para modelação numérica dos diafragmas da CLT foi proposta e validada, comparando os resultados numéricos com os dados experimentais obtidos num ensaio de mesa sísmica de um edifício de dois andares.

A segunda parte da tese focou-se no desempenho sísmico de um edifício de três andares através de uma análise probabilística, que contabiliza as incertezas nas propriedades mecânicas dos elementos e das ligações. Análises estáticas não lineares e incrementais dinâmicas, com múltiplos registos sísmicos foram utilizadas para caracterizar o coeficiente de comportamento e desenvolver curvas de fragilidade para diferentes níveis de dano. Os resultados indicam que os requisitos de pormenorização dos Eurocódigos são suficientes para alcançar o desempenho exigido, embora contraponham que esses requisitos podem ser otimizados de forma a obter ligações e elementos com uma menor razão custo-benefício.

Finalmente, o potencial para o colapso progressivo de estruturas em madeira, resistentes a sismos, foi estudado através de uma análise de caminhos alternativos de carga (ALPA). Esta avaliação de robustez envolveu análises estáticas não lineares (análise pushdown), que incluíram incertezas relacionadas com as propriedades do material e com as cargas aplicadas. As funções de fragilidade foram desenvolvidas para diferentes cenários de perda de elementos e para duas tipologias de diafragma. O primeiro tipo consiste em painéis de CLT ligados através de ligações mecânicas, enquanto o segundo tipo consiste numa solução de baixo peso com placas de 18 mm de OSB fixas a vigas de GLT. Os resultados indicam que a capacidade estrutural para desenvolver caminhos alternativos de carga é substancialmente dependente da capacidade de rotação das ligações.

Se não foi pa legendary, foi pa quê?

Antes de apontar gun, aponta no caderno o teu porquê.

Se não der pa acabar com a fam' em Saint-Tropez

Quem sabe aos domingos atacarmos o buffet.

João Batista Coelho a.k.a. Slow J

Contents

Acknowledgements	i
Abstract	iii
Resumo	v
List of Tables	xi
List of Figures	xv
List of Symbols	xxi
List of Acronyms	xxv
1 Introduction	1
1.1 Motivation	1
1.2 Relevant multi-story heavy-timber buildings	4
1.3 Objectives	10
1.4 Thesis outline	11
2 Shake-table test and modeling of CLT diaphragms	13
2.1 Introduction	13

2.2	Experimental setup and instrumentation	18
2.2.1	Test structure design	22
2.2.2	Instrumentation for the diaphragms	23
2.3	Shaking Table Test Results	24
2.3.1	Floor horizontal accelerations along the building height	24
2.3.2	Peak Accelerations within diaphragms	28
2.3.3	Relative displacements within diaphragm CLT panels	30
2.4	Numerical modeling approach for CLT diaphragm	35
2.4.1	Key aspects of the modelling approach	35
2.4.2	In-plane stiffness of CLT panels	37
2.4.3	Numerical model of diaphragm connections	38
2.5	Nonlinear static analyses (pushover)	40
2.5.1	Numerical Results	41
2.5.2	Influence of in-plane stiffness values on surface splines	46
2.5.3	Chord splices results	49
2.6	Final Remarks	50
2.7	Conclusions	51
3	Seismic assessment of a heavy-timber frame structure	55
3.1	Introduction	55
3.1.1	Numerical modeling of cyclic behavior of timber connections	57
3.1.2	Fragility curves for timber structures	59
3.1.3	Objectives	60

3.2	Methodology	61
3.3	Case study: A three-story heavy-timber frame building	64
3.3.1	Description of the structure	64
3.3.2	Finite element modeling and analysis	66
3.3.3	Basic random variables and assumed statistical correlations	70
3.3.4	Ground motion selection	77
3.4	Performance assessment	79
3.4.1	Pushover analysis	79
3.4.2	Incremental Dynamic Analysis	82
3.5	Fragility Analysis	85
3.6	Conclusions	88
4	Robustness Assessment of a heavy-timber frame structure	91
4.1	Introduction	91
4.1.1	Review of progressive collapses cases	93
4.1.2	International projects on structural robustness and timber buildings	99
4.1.3	Robustness analyses	104
4.1.4	Design procedures, codes and regulations for robustness	107
4.2	Objectives	113
4.3	Methodology	113
4.4	Case study: a three-story heavy-timber frame building	116
4.4.1	Lateral resisting systems	116
4.4.2	CLT floor diaphragm	119

4.4.3	Light-weight diaphragm	121
4.5	Finite element modeling and analysis	122
4.5.1	Numerical modeling of members and connections	123
4.5.2	Basic random variables and assumed statistical correlations	145
4.5.3	Other variables assumed	147
4.5.4	Removal procedures in Opensees	148
4.6	Alternative path method implementation	151
4.6.1	Pushdown analysis results	151
4.6.2	Fragility analysis	155
4.7	Conclusions	159
5	Conclusions and Future work	161
5.1	Summary of the research work	161
5.2	Summary of major findings	163
5.3	Limitations of the research work	166
5.4	Applications	167
5.5	Future Work	167
	Bibliography	169
	References	169

List of Tables

2.1	Maximum accelerations measured at different heights of the building	26
2.2	Constitutive law parameters for multi-linear plastic models (SAP 2000)	40
2.3	Longitudinal stresses of steel plates of a chord splice at 1st floor	50
3.1	Points used to define the backbone curve	67
3.2	Parameters used to model the degradation	70
3.3	Random variables for timber material properties	70
3.4	Intra-element correlation coefficient matrix (PMC)	71
3.5	Inter-element correlation coefficient matrix	71
3.6	Lognormal parameters for moment-resisting joints properties	74
3.7	Post-yielding rotations variability	76
3.8	Set of ground motion records selected	78
3.9	Lognormal parameters for q -factor estimates	80
3.10	Lognormal parameters for limit state interstory drift ratios	82
3.11	Fragility curves parameters for IO, LS and CP	86
3.12	Lognormal parameters for peak interstory drift ratio and spectral acceleration at GC	87

3.13	LS and CP fragility curves parameters for different levels of q - factors	87
4.1	Strength and stiffness comparison between monotonic tests (Dorn, de Borst, & Eberhardsteiner, 2013) and EC5 calculations for steel-to-timber connections with a single dowel	127
4.2	Envelope curve parameters to define the response of multiple bolted connections	128
4.3	Parameters used to define <i>Pinching4</i> model to represent steel-to-timber joints .	131
4.4	Parameters used to define <i>Pinching4</i> model to half-lap joints experimental tests (Closen, 2017)	131
4.5	Parameters used to compute withdrawal capacity per fastener of half-lap joints tested in Closen (2017)	134
4.6	Parameters used to compute withdrawal capacity per fastener of half-lap joints used in the structure	135
4.7	Parameters used to define <i>Pinching4</i> model to represent overlap connections between CLT and glulam beams	135
4.8	Parameters used to compute withdrawal capacity per fastener of overlap connections between CLT and glulam beams used in the structure	138
4.9	Parameters used to define <i>Pinching4</i> model to represent overlap connections between CLT and glulam beams	139
4.10	Strength and stiffness properties for rotational response of overlap connections between CLT and glulam beams per screw	139
4.11	Parameters used to define <i>Pinching4</i> model to represent half-lap joints	141
4.12	Ratios between <i>Pinching4</i> parameters for cyclic and monotonic tests	142
4.13	Envelope curve parameters for monotonic and cyclic tests	143
4.14	<i>Pinching4</i> parameters for concealed joints with screws at 45 degrees	144
4.15	Parameters used to define <i>Pinching4</i> model to represent OSB-to-joists	146

4.16	Mean properties used to model OSB orthotropic material	148
4.17	Mean properties used to model CLT orthotropic material	148
4.18	Lognormal parameters used to represent the variability of maximum vertical displacements measured at the control node	154
4.19	Lognormal parameters for maximum relative rotations between floor elements (Glulam joists and CLT) and main glulam beams	154
4.20	Fragility curves parameters for overload factors related to distinct damage scenarios	156
4.21	Probability of failure and respective reliability indexes for overload factor of 2.0	158

List of Figures

1.1	Albina Yard Building in Portland, Oregon, U.S.	4
1.2	John W. Olver Building at University of Massachusetts Amherst, U.S.	5
1.3	Arbora complex in Montreal, Canada	7
1.4	Origine (13 stories) in Quebec, Canada	7
1.5	International House in Sydney, Australia	8
1.6	Treet building, in Bergen, Norway	9
1.7	Stadthaus building, in London, United Kingdom	10
1.8	Outline of the thesis	11
2.1	Two-story structure tested during the summer 2017 at the UC San Diego outdoor shake-table	15
2.2	Structural layouts: (a) First floor level; (b) Second floor level; (c) N-S Elevation; (d) E-W Elevation	20
2.3	Distinct connections used at diaphragm levels	21
2.4	Diaphragm details: (a) Chord splices at the second floor; (b) Single surface spline; (c) Panel connection at first floor boundaries; (d) Composite solution . . .	23
2.5	Average of the peak Accelerations measured at different diaphragm levels: (a) Phase 1; (b) Phase 2 (c) Phase 3	28

2.6	Diaphragm peak accelerations measured during Phase 1	31
2.7	Diaphragm peak accelerations measured during Phase 2	32
2.8	Diaphragm peak accelerations measured during Phase 3	33
2.9	Relative displacements: (a) between CLT panels at 1st Floor; (b) between CLT and GLT beams at both Floors; (c) between CLT panels at 2nd Floor; (d) LP used at 1st Floor; (e) LP used for sliding between CLT and GLT at 1st Floor; (f) LP used at 2nd Floor	36
2.10	Two dimensional finite element model: (a) Mesh-refinement; (b) Beam-to-beam connection; (c) Chord splices; (d) Wall connection	38
2.11	Numerical model features: (a) CLT-to-Beam friction scheme; (b) Envelope Curve for screws	41
2.12	Deformation diagram at the first level diaphragm	42
2.13	Numerical results for MCE hazard level earthquakes at surface spline SS1: (a) Separation - Test 13; (b) Sliding - Test 13; (c) Forces - Test 13; (d) Separation - Test 14; (e) Sliding - Test 14; (f) Forces - Test 14	44
2.14	Numerical results for MCE hazard level earthquakes at surface spline SS2: (a) Sliding - Test 13; (b) Separation - Test 13; (c) Forces - Test 13; (d) Sliding - Test 14; (e) Separation - Test 14; (f) Forces - Test 14	45
2.15	Numerical results for DBE hazard level earthquakes: (a) Separation at SS1 - Test 6; (b) Sliding at SS1 - Test 6; (c) Sliding at SS2 - Test 6; (d) Separation at SS2 - Test 6; (e) Separation at SS1 - Test 19; (f) Sliding at SS1 - Test 19; (g) Sliding at SS2 - Test 19; (h) Separation at SS2 - Test 19	46
2.16	Impact of elastic modulus variability and shear modulus variability on numerical results of surface splines: (a) Sliding at SS1; (b) Separation at SS1; (c) Forces at SS1; (d) Sliding at SS2; (e) Separation at SS2; (f) Forces at SS2	48

3.1	Moment-resisting frame structure:(a) elevation; (b) ring doveled joint - elevation; (c) ring doveled joint - cross section; (d) floor plan; (e) floor components; (f) joist connection	65
3.2	Numerical model of moment-resisting joints (a) OpenSees model for moment-resisting joint; (b) <i>Pinching4</i> parameters; (c) Experimental test and numerical results; (d) Energy dissipated: test vs numerical results	69
3.3	Backbone curve used for ring-doweled response	76
3.4	Response spectra used to perform multi-record IDA: (a) Type 1; (b) Type 2	77
3.5	Nonlinear static analysis: (a) Capacity curves; (b) Equivalent bilinear inelastic model	79
3.6	q -factor levels and fitted PDF	81
3.7	Lognormal probability plots for different limit state interstory drift ratio	82
3.8	Single-record IDA Curves: (a) Design structure; (b) Median structure	83
3.9	Multi-record IDA results: (a) mean and median IDA curves; (b) coefficient of variation of $S_a(T_1)$	84
3.10	Multi-record IDA curves for different q -factor levels: (a) median fractile curves; (b) coefficient of variation of $S_a(T_1)$	84
3.11	Fragility curves for different θ_{\max} levels: (a) Immediate Occupancy; (b) Life Safety	86
3.12	Global collapse fragility curves: (a) for different q -factor levels ; (b) median structure and structural set	87
3.13	Fragility curves for different q -factor levels: (a) Life Safety; (b) Collapse Prevention	88
4.1	Ronan Point progressive collapse	94
4.2	Murrah building: (a) intact structure; (b) partial collapse	95
4.3	Siemens Arena Roof: (a) fish shape truss; (b) failure of two main beams (Munch-Andersen & Dietsch, 2009)	96

4.4	Failure of corner connections: (a) due to tension forces (b) due to increased rotation (Munch-Andersen & Dietsch, 2009)	97
4.5	Bad Reichenhall Ice-Arena (Munch-Andersen & Dietsch, 2009)	98
4.6	Collapse of the Bad-Reichenhall Ice-Arena (Munch-Andersen & Dietsch, 2009)	98
4.7	Sports hall in Samobor (Čizmar, Kirkegaard, Sørensen, & Rajčić, 2011)	100
4.8	2D Frame test setup (Lyu et al., 2018)	101
4.9	Beam to Column: (a) Aluminum alloy T-section perforated bracket (b) Double beam connected with bolts (Lyu et al., 2018)	102
4.10	Distinct failures of connections in a 2D frame test (Lyu et al., 2018)	102
4.11	Disproportionate collapse test (Mettem, Bainbridge, Pitts, & Enjily, 1998)	103
4.12	Decision tree for risk analysis (Baker, Schubert, & Faber, 2008)	104
4.13	Removal of a load-bearing column (ARUP, 2011)	105
4.14	Load distribution mechanisms, from ARUP (2011); Huber, Ekevad, Girhammar, and Berg (2018)	107
4.15	Recommended limit of admissible damage: (a) Plan View; (b) Elevation;	112
4.16	Lateral resisting systems	117
4.17	Moment-Resisting Frame: (a) ring doweled joint-elevation; (b) ring doweled joint-section; (c) shoe for columns-elevation; (d) shoe for MRF columns - elevation	117
4.18	Column shoe from braced frame system	118
4.19	Braced timber frame: (a) connections between diagonals and other frames; (b) diagonal cross-section; (c) connections between diagonals and other frames	118
4.20	Connections between moment-resisting frames and braced frame system	119
4.21	CLT diaphragm - plan view	119

4.22	Construction details for overlap connections between CLT and glulam beams . . .	120
4.23	CLT diaphragm - chord splices	120
4.24	OSB diaphragm - plan view	121
4.25	Connections between OSB diaphragm and the lateral resisting systems	122
4.26	Finite element model	122
4.27	Envelope Curve for <i>Pinching₄</i> model	124
4.28	Steel-to-timber joints with center plate (Dorn et al., 2013): (a) typical single-dowel response; (b) connection scheme	125
4.29	Experimental results for steel-to-timber joints with center plate (Dorn et al., 2013)	125
4.30	Multiple bolts connection at braced frame system: (a) OpenSees model for joint; (b) <i>Pinching₄</i> envelope curves for single bolts with center plate	128
4.31	<i>Pinching₄</i> envelope curves for multiple bolted connection: (a) Force-displacement; (b) Moment-rotation	129
4.32	Steel-to-timber joints with side plates: (a) experimental tests and numerical results; (b) energy dissipated: test versus numerical results	130
4.33	Numerical modeling of connections within the braced framed system	130
4.34	Cyclic test layout half-lap joints with screws at 90 degrees	132
4.35	Overlap connections between CLT and glulam beams: (a) experimental tests and numerical results; (b) energy dissipated: test versus numerical results	132
4.36	Numerical modeling of half-lap connections	136
4.37	Numerical modeling of interrupted overlap connections between CLT and glulam beams	137
4.38	Numerical modeling for continuous overlap connections between CLT and glulam beams	138
4.39	Connections with screws installed at 45 degrees	139

4.40	Cyclic test layout half-lap joints with screws at 45 degrees	140
4.41	Half-lap joints with screws at 45°: (a) experimental tests and numerical results; (b) energy dissipated: test versus numerical results	141
4.42	Monotonic test and cyclic response of concealed connection	142
4.43	Joist-to-beam connections: (a) negative moment; (b) positive moment;(c) plan view; (d) numerical model	143
4.44	OSB-to-joists model in Opensees	145
4.45	OSB-to-joists: (a) experimental tests and numerical results; (b) energy dissi- pated: test versus numerical results	145
4.46	Probability density function of the gravity loads applied	147
4.47	Pushdown procedure for progressive collapse assessment	150
4.48	Loss of elements at external bay	152
4.49	Loss of elements at internal bay	152
4.50	Probability density functions for maximum vertical displacements of the model structure for distinct elements loss scenarios	153
4.51	Probability density functions for joist ends rotations and CLT panels connections of the model structure for distinct elements loss scenarios	154
4.52	Pushdown curves for distinct damage scenarios	155
4.53	Fragility curves for distinct column loss scenarios for model structures with light frame diaphragms	156
4.54	Fragility curves for distinct column loss scenarios for model structures with CLT diaphragms	157
4.55	Conditional reliability indexes for overload factors between 1.0 and 2.0	158

List of Symbols

A	Constant to account for the response of isolated dowels
d	Diameter of the fastener
d_h	Head diameter of the fastener
d_s	Smooth shank diameter
D	Local damage
E_m	Bending modulus of elasticity of a glulam member
E_s	Elastic modulus of steel
E_x, E_y, E_z	Elastic moduli in mutually perpendicular directions of engineered wood panels
$E[X]$	Expected value
f_{ax}	Axial withdrawal strength of the threaded part of a screw
$f_{h,\alpha,i}$	Embedment strength of timber in the direction of the load applied on a fastener
f_{head}	Head pull-through capacity
f_{mk}	Characteristic bending strength
f_{tens}	Tensile capacity of the screw
f_u	Ultimate yield capacity of steel in tension
$F_I, F_{II}, F_{III}, F_{IV}$	Parameters defining forces for envelope curves
$F_{ax,R}$	Withdrawal capacity of the fastener
F_c	Compression Force
F_{cl}	Clamping force
F_R	Fragility curve
$F_{R,i}$	Yielding force of the fastener i
F_t	Tension Force

$F_{v,r}$	Dowel resistance force per shear plane
F_{μ}	Friction force
g	Acceleration of gravity
G_n	Nominal gravity loads
G_R	Gravity loads associated to structural failure
G_v	Shear modulus of a glulam member
G_{xy}, G_{yz}, G_{zx}	Shear moduli in mutually perpendicular planes of engineered wood panels
k_{ser}	Slip modulus per shear plane
k_{mod}	Modification factor
k_{90}	Embedment strength factor
$K_{ax,ser}$	Axial slip modulus for threaded screws
K_{el}	Elastic rotational stiffness
K_{ser}	Slip modulus of a connection
l_{ef}	Penetration length of the threaded part of the fastener
M_y	Yielding moment of a connection
$M_{y,dowel}$	Yielding moment of a dowel
$M_I, M_{II}, M_{III}, M_{IV}$	Parameters used to define moments for envelope curves
$\{M\}$	Lumped mass matrix
n_{ef}	Effective number of fasteners
n_{sp}	Number of shear planes
N_{Ele}	Number of element loss scenarios considered
N_{GMR}	Number of ground motion records
N_{IDA}	Number of incremental dynamic analysis
N_{Sim}	Number of models in the structural set
N_{Set}	Number of structural sets
p_f	Probability of failure
$\{p_i\}$	Vector of lateral loads
q	Behavior factor
r_i	Distance of each fastener from the center
r_{max}	Distance between the center and the farthest dowel
R	Response modification factor

$R_{c,0}$	Compression strength of a glulam member parallel to grain
R_m	Bending strength of a glulam member
$R_{t,0}$	Tension strength of a glulam member parallel to grain
R_v	Shear strength of a glulam member
R_μ	Ductility factor
R_Ω	Overstrength factor
$S_a(T_1)$	Spectral acceleration at the fundamental period
S_{DS}	Design spectral acceleration
t	Time
t_i	Thickness of the members
T	Fundamental period
T_1	First natural period
T_2	Second natural period
W	Tributary weight
X_{II}, X_{III}, X_{IV}	Random variables used to define post-yielding deformations for envelope curves
α	Angle of load applied relative to the grain
β	Reliability index
β_{NM}	Newmark integration beta parameter
β_h	Ratio between the embedment strength of two adjacent members
γ_{NM}	Newmark integration gamma parameter
$\delta_I, \delta_{II}, \delta_{III}, \delta_{IV}$	Parameters to define displacements for envelope curves
δ_{d_i}	<i>Pinching4</i> damage index associated to maximum displacement
δ_{f_i}	<i>Pinching4</i> damage index associated to maximum strength
δ_{k_i}	<i>Pinching4</i> damage index associated to stiffness
θ	Rotation of a connection
θ_y	Yielding rotation of a connection
$\theta_I, \theta_{II}, \theta_{III}, \theta_{IV}$	Parameters used to define rotations for envelope curves

θ_{\max}	Peak interstory ratio
$\lambda_{K_{el}}$	Bias coefficient for the elastic rotational stiffness
λ_{M_y}	Bias coefficient for yielding moment of ring-doweled connections
λ_K	correction factor to adjust stiffness
λ_F	correction factor to adjust strength
μ	Ratio between ultimate and yielding displacements
μ_{ln}	Lognormal mean value
$\nu_{xy}, \nu_{yz}, \nu_{zx}$	Poisson's ratios in mutually perpendicular planes of engineered wood panels
ξ	Damping ratio
ξ_{ln}	Lognormal standard deviation
ρ_{con}	Geometric mean of the density of adjacent members
ρ_{den}	Density of a glulam member
σ	Normal stress
$\{\phi_i\}$	Normalized first mode nodal displacements
φ	Story occupancy parameter
ψ_{E_i}	Combination coefficient
ψ_{2_i}	Quasi-permanent coefficient for variable loads
Φ^{-1}	Inverse cumulative distribution function of the standard normal distribution
Ω	Dynamic amplification factor

List of Acronyms

ALPA	Alternate Load Path Analysis
ASCE	American Society of Civil Engineers
APA	American Plywood Association
ASTM	American Society for Testing and Materials
AWC	American Wood Council
CC	Consequence Class
CDF	Cumulative Distribution Function
CJP	Complete Joint Penetration
CLT	Cross-laminated Timber
CoV	Coefficient of Variation
CP	Collapse Prevention
DA	Design Approach
DC	Disproportionate collapse
DBE	Design Based Earthquake
DCL	Ductility Class "Low"
DCM	Ductility Class "Medium"
DCH	Ductility Class "High"
DL	Dead Load
DLF	Dynamic Load Factor
DMP	Engineering Demand Parameter
DoD	Department of Defense
DOF	Degree-of-Freedom
EC5	Eurocode 5
EC8	Eurocode 8

ELR	Enhanced Local Resistance
EX	Exposure
FEMA	Federal Emergency Management Agency
FF	First Failure
FFT	Fast Fourier Transform
GC	Global Collapse
GLT	Glued-laminated Timber
GM	Ground Motion
IBC	International Building Code
IDA	Incremental Dynamic Analysis
IM	Intensity Measure
IO	Immediate Occupancy
KS	Kolmogorov-Smirnov
LHS	Latin Hypercube Sampling
LP	Linear Potentiometer
LRFD	Load and Resistance Factor Design
LL	Live Load
LS	Life Safety
MC	Moisture Content
MCE	Maximum Considered Earthquake
MEP	Mechanical, Electrical, and Plumbing projects
NDS	National Design Specification
OF	Overload Factor
OSB	Oriented Strand Boards
RC	Risk Categories
RMS	Root-Mean-Square
SC	Structural Capacity
SDOF	Single-Degree-of-Freedom
SF	Scale Factor
SLR	Specific Local Resistance
SLE	Service Level Earthquake
SPF	Spruce-pine-fir

TF	Tie-force Method
TFA	Timber Frame Association
TRADA	Timber Research and Development Association
PDF	Probability Density Function
PEER	Pacific Earthquake Engineering Research
PGA	Peak-ground Acceleration
PMC	Probabilistic Model Code
PVC	Polymerizing Vinyl Chloride
UCSD	University of California San Diego
UFC	Unified Facilities Criteria
WN	White Noise
WTC	World Trade Center
VBIED	Vehicle-born Improvised Explosive Device

Chapter 1

Introduction

1.1 Motivation

In the past few years, the construction of multi-story timber buildings has increased significantly. This fact can be associated with the use of wood engineered products such as glued-laminated timber (GLT) and cross-laminated timber (CLT) that enable construction efficiency and reduce the environmental impacts (Harte, 2017). This thesis focuses on multi-story heavy-timber buildings in seismic zones, which are characterized by members with greater cross-sections than the ones used in light-timber frames, produced mainly with GLT and CLT, enabling larger spans and greater fire safety (Pei et al., 2014; American Wood Council, 2003). For the implementation of these buildings in high seismicity regions as Portugal, Italy, Greece, Turkey, the west coast of the United States or Japan, research has to provide adequate guidelines for seismic and robustness analysis. Hence, the importance of providing practitioners with reliable tools that can be used for the analysis and design of this type of buildings (Pei et al., 2014).

Timber is a material with a low weight-to-strength ratio, which is suitable for locations where high intensity ground motions are likely to occur. On the other hand, the performance of timber structures under intense earthquake ground shaking depends strongly on the type of failure modes, and in particular, their ductility (H. Blaß et al., 1994). The failure of timber elements is usually brittle, whereas the failure of connections between timber elements can be ductile. Being constructed in seismic areas, the requirements promoted by the design codes

are objectively more strict regarding connections and the sizes of timber members. Such recommendations influence positively the ductility of the structures. Design recommendations for timber structures focus on the formation of inelastic deformations on connections by increasing the slenderness of connectors, guaranteeing that failure occurs after yielding of the connectors, and thus enhancing the capacity of joints to withstand large inelastic deformations without rupture. Moreover, seismic resistant multi-story buildings must have adequate bi-directional resistance and stiffness, which is associated with symmetry and uniformity. Such characteristics are also important to prevent torsional effects. Diaphragms are another key component of the seismic resisting system since these allow the inertial forces to be transferred to the different vertical structural components. Consequently, adequate strength and deformation capacity must be provided to the connections, between floors and the lateral resisting systems, ensuring the continuity of the load transfer mechanisms.

Robustness is another concept equally important when studying multi-story timber buildings, which is described as the ability of structures to avoid progressive collapse due to a local damage resulting from an unpredictable event (Branco & Neves, 2011). Some of the aspects sought in seismic resistant structures are also part of the recommendations provided by design codes against progressive collapse due to unpredictable events like explosions and impacts. For multi-story timber buildings, robustness is strongly dependent on the structures capacity to redistribute loads to undamaged parts, and thus, on its redundancy and ductility. After the loss of a load bearing element, alternate load paths can be triggered through the capacity of connections to rotate accompanying the development of tension stresses in beams and floors. Moreover, in structures where long continuous beams are used, this process can be substituted by an increment of bending forces, while the connections between these elements and the floor components withstand large deformations without experiencing brittle failure modes such as splitting, tension perpendicular to the grain and shear block. Another mechanism likely to occur is the membrane action of CLT floors, which is also dependent on the inter-panel connections.

The formation of alternative load-paths is crucial to withstand local failures, but only if the intact members have adequate over-strength. Otherwise, the damage can be extended to adjacent bays and a progressive collapse can occur that can be considered disproportionate to the original cause. Considering this, it is paramount to investigate if structures designed against earthquakes are able to avoid progressive collapse or, on the contrary, if their given capacity to

redistribute loads, will initiate or worsen a situation of disproportionate collapse.

The accuracy of seismic and robustness analyses requires reliable representation of connections' behavior and timber mechanical properties. The uncertainties concerning connections regard not only the values of strength and stiffness properties, but also the shape of the post-yielding branch of the force-deformation curves. This has contributed to the standardization of analyses methods, for the design of multi-story timber buildings in seismic regions, that do not explicitly consider the inelastic behavior of joints. Uncertainties in joints are related to the connectors used, its geometry (e.g. group effect) and the mechanical properties of timber such as density and embedment strength. Timber, as a natural material, presents a high variability in its mechanical properties (Faber et al., 2011), which contributes directly to an increase in the uncertainties associated with the expected strength and peak drift capacities of timber structures. In literature, there is an absence of studies where material uncertainties are considered to compute the ductility properties of timber structures, being therefore crucial the development of studies that account for material uncertainties, as well as, the uncertainties associated with the seismic loading (Foliente, 1997). Together with the quantification of uncertainties inherent to the structure, there is also the necessity to account for uncertainties related to the seismic demand through record-to-record variability.

The failure of several timber long-span roof in Europe under expected snow loads has shown that design and/or construction errors, unexpected deterioration, or even unexpected loading can lead to consequences far greater than the initial event. Robustness methods have been applied to evaluate the susceptibility of these type of structures to these events in order to find better design and construction regulations. Nevertheless, few studies (Lyu et al., 2018; Bitá & Tannert, 2017; Huber et al., 2018) have been carried out regarding numerical models development for progressive collapse assessment of multi-story timber buildings. Such models require advanced three-dimensional finite element models that are able to capture material and geometric nonlinearities, as well as, elements removal due to brittle failures.

All these factors support the necessity of providing numerical modeling strategies for seismic and robustness assessment and design. Particularly in assessment, one must take into consideration the uncertainties related to hazard and inherent variability of timber mechanical properties and connections.

1.2 Relevant multi-story heavy-timber buildings

There are already several examples of constructed multi-story heavy-timber buildings that can attest their structural potential, low carbon footprint, and fast construction. Considering the type of buildings analyzed in this thesis, the examples provided focus on glulam (GLT) post-and-beam structures with floors made of CLT panels, which provide high in-plane stiffness.

The Albina Yard, presented in Figure 1.1, is a 4-story (total height of 15.39 m) office building designed against earthquakes, given its location in Portland, Oregon. The gravity frame is composed by a glulam post-and-beam structure (Figure 1.1b), with connections executed through concealed steel connectors, and Douglas-fir CLT floor/roof panels (Mugabo et al., 2018). Covering the concealed steel connectors with wood, increases the connections fire-resistance, and therefore improves the overall fire safety. The success in design and execution of the concealed connections relies on a close collaboration between the design team and the fabricators. Since it was the first building to include CLT elements in the primary structural system and using CLT solely produced in the U.S., the multidisciplinary group had to deal with particular challenges such as complying with structural and seismic requirements, and dealing with the logistics of fabrication and shipping of CLT elements ready for installation.



(a) Street view



(b) Glulam post-and-beam structure

Figure 1.1: Albina Yard Building in Portland, Oregon, U.S.

Initially, the seismic design of the building was based on the 2015 International Building Code (IBC) (ICC, 2015), which includes CLT as a material, but does not provide much guidance on designing CLT shear walls and diaphragms. Already during the design phase, the introduction of the Statewide Alternate Method, No. 15-01 Cross-Laminated Timber Provisions, by the

State of Oregon Building Codes Divisions, enabled the use of CLT alone diaphragms, but due to a overly conservative Response Modification Factor, R , of 2 for CLT, the design team kept the plywood-sheathed shear walls rather than using CLT shear walls. Outside the State of Oregon, the application of performance-based design as recommended in the Alternate Material and Method provisions in the IBC enables the use of CLT in lateral-resisting systems. The CLT spline connections, and the CLT-to-drag connections were designed to remain essentially elastic. Since a great amount of elements were prefabricated and then brought to site, this required careful planning and coordination between all the teams involved in the project, and the inclusion of acceptable tolerances in components of different materials. The success of the entire project showed that further research is needed to provide adequate design recommendations for CLT members, and that mass-timber buildings enable faster construction with few environmental costs (Patsy, 2017).

The John W. Olver Design Building is an impressive mass-timber building that is part of the campus of the University of Massachusetts Amherst, in the U.S. The building was completed in 2017 and it has three stories on its east side, while on the west side has four stories (Figure 1.2). The building was initially designed as a steel structure, but halfway into the process it was changed to mass-timber. Since this was a possibility from the start, the architectural and structural teams came up with a building layout that could accommodate this change, and according to them no radical alterations or particular solutions are needed for mass-timber. In fact, it was possible to reduce the number of beams by half and distribute them in a way that had less incompatibilities with the Mechanical, Electrical, and Plumbing (MEP) projects. To obtain code approval for several uses of CLT in the design, it was necessary to provide to the authorities state-of-the-art research and test results that would support the design team claims.



(a) Street view



(b) Braced timber frames



Figure 1.2: John W. Olver Building at University of Massachusetts Amherst, U.S.

The gravity framing system is composed of a glulam post-and-beam structure, supporting the CLT-concrete composite floors and CLT roof decking. The CLT shaft walls are also load-bearing. Additionally, the structure of the inside courtyard is composed by a systems of timber and steel composite zipper trusses. In the panel-to-beam, and beam-to-column connections were used self-tapping screws with concealed beam hangers, while the CLT panel-to-panel connections are surface splines with plywood. The glulam beams have a cross-section of approximately 360 mm x 380 mm or 420 mm, while the columns are approximately 360 mm x 570 mm or 650 mm. Most of the glulam members are made out of black spruce, with an maladjusted bending strength of approximately 16.50 MPa. In this particular case, the CLT-concrete composite floor is formed by three layers connected by steel mesh connectors. On top of the 5-ply CLT panels (174.6 m), there is a layer of 25.4 mm rigid insulation (for acoustics), and then a 101.6 mm reinforced concrete, performing a total thickness of approximately 300 mm. This type of solution enables high strength and stiffness at reduced self-weight of the slab, comparing to a full concrete slab. The lateral resisting system was design to sustain seismic and wind loads, being the former more demanding, and it resulted in a combination of CLT shear walls with glulam bracing (Figure 1.2b). According to the capacity design performed, the ductility of the structure will come from the hold down brackets in CLT shear walls and the end connection steel pins and plates in glulam diagonals, which were designed to yield for the design earthquake demand. With regard to construction, the speed of assembly stands out as a great advantage of this kind of structure, also being described as more quiet than regular construction sites and with less waste. It was reported that one of the buildings shear wall cores, which comprises four CLT panels of approximately 18 m, was assembled and anchored to the foundation in one weekend. The efficiency of construction relies on collaborative work, during all stages of the process, particularly between the timber suppliers, and the structural design team (WoodWorks, 2017).

The Arbora complex is a compound of three buildings (two 8-story and one 9-story), which is still under construction, as presented in Figure 1.3, in a residential area of Montreal, in Canada. The gravity system of all three buildings is formed by glulam post-and-beam supporting the CLT floor panels. The lateral resisting system is composed by CLT shear wall panels in perpendicular directions. The 8-story buildings sit on a concrete foundation and first floor concrete podium, while the 9-story building just has a concrete foundation. The construction of the timber structure of the first three floors was reported to take approximately ten weeks. As al-

ready reported in the Albina Yard building, faster construction resulted from more demanding and time-consuming design and planning phases (Oberholzer, 2016).



Figure 1.3: Arbora complex in Montreal, Canada

The Origine project is a 13-story residential building, of which twelve stories are in mass-timber. The building has a total height of 40.9 m and it was concluded in 2017, in Quebec, Canada. The 12 stories are built on a concrete foundation and first floor platform. The principal structural system is a glulam post-and-beam structure with balloon-framed CLT bearing walls supporting the CLT floor panels, as presented in Figure 1.4. The structure was designed against earthquakes, since Quebec is in a seismic area and the soil was considered very poor, being the seismic forces computed with response spectrum analysis. Wind demand was also accounted for, being determined with static and dynamic wind analyses. As result of both analysis, a set of CLT shear walls was distributed symmetrically considering the shortest length of the building (Oberholzer, 2016). The first three floors were reportedly erected in four weeks by six workers (Nordic Structures, 2017).



Figure 1.4: Origine (13 stories) in Quebec, Canada

International House Sydney is the first commercial office building in engineered timber built in



(a) Construction phase



(b) Glulam frames

Figure 1.5: International House in Sydney, Australia

Sydney, Australia, in 2016. The 7-story building comprises a first floor in reinforced concrete, with a colonnade of recycled iron-bark timber from disused rail bridges in Queensland, which provides an elevated platform for the remaining 6 stories completely in mass-timber. Gravity loads transmission is assured by a glulam post-and-beam structure, see Figure 1.5, with CLT panels for floors and walls. The lateral resisting system was built using glulam diagonals bracing on bays of the four façades. The timber-to-timber connections are achieved with concealed steel plates. The building is a certified green building, with solar panels, LED lighting and blackwater treatment, but is the use of a mass-timber structure that reduces carbon emission and enables less finishing materials. Although, initiating construction with no specialized workers, it was reported a fast grow in installation rates, from 8 elements a day to 33 at the peak. Towards the end of construction, the team was taking a week to build one floor structure (Butler, 2016).

The Treet building, in Bergen, Norway, is one of the examples of mass-timber framed structures in Europe. The 14-story building, presented in Figure 1.6 was concluded in 2015, but its design started in 2011 and took two years. Particularly this building, that has most of its components prefabricated, a detailed design phase is essential to have a smooth assembly process. The load-bearing system is elaborate and it can be compartmentalized from floors 1 to 4, floor 5, from floor 6 to 9, floor 10, and from floors 11 to 14. Floors 1 to 4 are supported by the reinforced concrete garage structure and are not connected to the surrounding glulam trusses. These trusses are connected to the glulam trusses strengthening level 5 and support the prefabricated residential modules of that level. On top of this level, there is a reinforced concrete slab that carries the weight of floors 6 to 9, which behave as floors from 1 to 4. Then floor 10 has the same structural system as floor 5, and the concrete slab on the former supports floors from 11 to 14. The roof is also a reinforced concrete slab. Hence there is a repetition of the structural

system along the height of the building and the use of the concrete slabs to increase the mass of the building. The CLT panels used in the balconies, interior walls, and elevator shaft are not part of the load-bearing system (Abrahamsen & Malo, 2014).



Figure 1.6: Treet building, in Bergen, Norway

All glulam connections were built with concealed steel plates and dowels, using hot dip galvanized 12 mm thick steel plates, class S355. The dowels were 12 mm and A4-80 type. The typical glulam column cross-sections are $405 \times 650 \text{ mm}^2$, and $495 \times 495 \text{ mm}^2$, while the diagonal cross-section dimensions are $405 \times 405 \text{ mm}^2$. The glulam strength classes used were the GL30c and GL30h. Most glulam elements were made out of untreated Norway Spruce (*Picea abies*), with exception of the ones exposed to the environment, which were made out of copper-treated lamellas from Nordic Pine (*Pinus sylvestris*). CLT was specified to have properties similar to a C24 structural timber with a bending strength, f_{mk} , of 24 MPa. CLT and timber elements from the modules were made out of Norway spruce. Construction followed the order of modules first, CLT panels and glulam trusses second, and in last the concrete slab (Abrahamsen & Malo, 2014).

Since wind loads were more demanding than seismic loads, there was no design against earthquakes. However, in the design of the Treet building, robustness concepts were also included.

The glulam truss elements or bearing elements of the corridor were designed in a way that they can handle load transferred from neighboring elements, in case of member loss, ensuring that the structure will not experience progressive collapse (Abrahamsen & Malo, 2014). To account for the additional loads, the concrete slabs were designed as continuous and connections reinforced with more screws (Bita & Tannert, 2017).

It is worth noting that robustness design methods were also applied during the design of an eight story building in London (Stadthaus), presented in Figure 1.7. A notional removal of load bearing walls was performed and the progressive collapse propensity was evaluated (Yates et al., 2008) resulting on change to the final CLT floor panels layout. This building structural system is composed by CLT panels for load-bearing walls and floors.



Figure 1.7: Stadthaus building, in London, United Kingdom

1.3 Objectives

The main objective of this thesis is to propose analyses approaches to assist in the design and assessment of heavy-timber structures, due to seismic loads and progressive collapse. These analyses account for uncertainties associated with connections behavior and timber mechanical properties, as well as, the variability in failure modes of the different structural elements and

connections. The following specific objectives contribute to the previously mentioned main objective of the thesis:

- Propose a numerical modeling strategy capable of reproducing the seismic response of CLT diaphragms, suitable for performance assessment and design;
- Evaluate the seismic fragilities of heavy-timber structures with ring-doweled moment resisting joints, through nonlinear static and incremental dynamic analyses;
- Assess the robustness against progressive collapse of a heavy-timber structure designed with ring-doweled moment resisting beam-column connections and braced timber frames.

1.4 Thesis outline

This thesis is organized in five chapters, as presented in Figure 1.8. Chapters 2, 3 and 4 have similar organizations that comprise their own introductions (state-of-the-art), development, discussion, and conclusions.

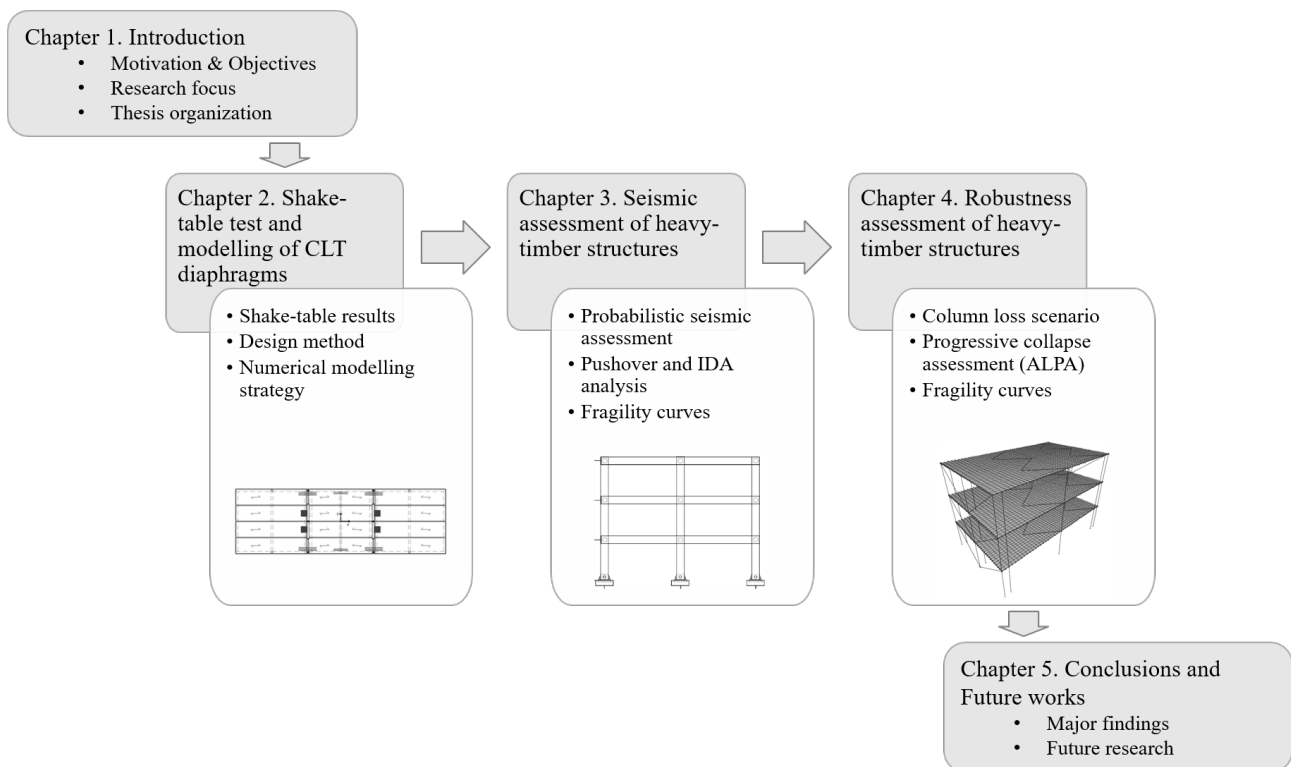


Figure 1.8: Outline of the thesis

The chapters are described as follows:

- Chapter 1. Introduction - presents the motivation and the main objectives associated with the research developed, as well as, a brief description of the background, research focus, and outline of the thesis;
- Chapter 2. Shake-table test and modeling of CLT diaphragms - presents the main results of a full-scale shake-table test performed on a heavy-timber building, as well as, a numerical model developed to represent the diaphragms response and suitable to be used during a design phase;
- Chapter 3. Seismic assessment of a heavy-timber frame structure - presents a probabilistic approach for seismic assessment, which accounts for uncertainties in mechanical properties of members and connections. From the results obtained through nonlinear static and incremental dynamic analyses, it was possible to develop several fragility functions for distinct limit states including immediate occupancy, life-safety, collapse prevention, and global collapse;
- Chapter 4. Robustness assessment of a heavy-timber frame structure - presents the progressive collapse assessment of a heavy-timber structure designed to fulfill the requirements of seismic provisions in terms of member sizing and connections ductility. Given the importance of diaphragms to trigger alternative loads paths, fragility functions are presented for two distinct floor solutions: CLT panels connected with plywood surface-splines, and a low weight solution with OSB panels and glulam joists;
- Chapter 5. Conclusions and future works - presents the main conclusions taken from the research developed in the previous chapters and suggests topics that need further development.

Chapter 2

Shake-table test and modeling of CLT diaphragms

2.1 Introduction

The use of cross-laminated timber (CLT) panels for building construction has increased over the last decades due to their construction efficiency, low environmental impacts, and aesthetics (Pei et al., 2016; Harte, 2017). Recent research efforts have focused on the development of design rules for CLT buildings in Europe (Harris et al., 2013; Thiel & Brandner, 2016; Kohler et al., 2016). In addition, in Canada and the United States of America (USA), a CLT Handbook was published (*CLT Handbook: Cross-Laminated Timber. Canadian Edition*, n.d.; Karacabeyli & Douglas, 2013) containing common design rules. In terms of structural performance assessment and design, the research efforts over the past 20 years in both Europe and North America have focused on the performance and design of lateral resisting systems (Ceccotti et al., 2006; Dujic et al., 2010; Popovski et al., 2010; van de Lindt et al., 2010; Ceccotti et al., 2013; Iqbal et al., 2015; van de Lindt et al., 2016; Sustersic et al., 2016; Ganey et al., 2017).

CLT diaphragms are a key component of the lateral resisting system since these allow the forces to be transferred to the different lateral resisting structural elements. The behavior of CLT diaphragms is usually influenced by strength, ductility, and the flexibility of connections between the CLT panels and the other components (Breneman et al., 2016). The CLT panels making up the floor or the roof diaphragms are known to rotate as essentially rigid bodies

under in-plane loading (e.g. shear). Therefore, the focus is often placed on the performance assessment and design of the panel connectors. Recent works such as Brandner et al. (2017) has focused on presenting the in-plane shear properties derived for CLT diaphragms that can also be applied in the design of CLT diaphragms and beams when subjected to in-plane shear stresses. However, Brandner et al. (2017) and other works failed to provide concepts and methods for the design of the connectors between adjacent CLT panels that compose a CLT floor diaphragm. Kode (2018) performed a single major test on diaphragm as part of a major FEMA P-695 effort currently underway. The diaphragm tested was set up as a cantilever beam according to ASTM E455 – 16 (ASTM, 2016) specification and CLT panels and their connectors were design to exhibit ductile failures with failure in shear. Results indicate that the failure of the diaphragm did not occur as expected and recognized that the chord design of cantilever diaphragms must be given careful consideration to ensure that the failure of the chords do not control the force and deformation capacity of CLT diaphragms. The tests such as the ones in Kode (2018) for other types of connections will allow researchers to gather more data and to compare connection capacities and their influence on the global behavior of the diaphragm and, consequently, these data can be used to improve the CLT building diaphragm design. Current European and North American codes and guidelines fail to provide key parameters for the assessment and design of CLT diaphragms, in particular under seismic actions. In this regard, Spickler et al. (2015) developed a white paper with a proposal for the design of CLT diaphragms for use in Canada and USA.

In terms of computer modeling of CLT diaphragms subjected to lateral loads, and despite CLT panels being composed of kiln-dried boards glued in orthogonal successive layers (Brandner et al., 2016), it is common to model the in-plane behavior through four-node shell elements with homogeneous orthotropic linear elastic behavior (Ashtari et al., 2014). Gsell et al. (2007), for example, showed that the global mechanical behavior of CLT plates can be described using an orthotropic, homogenized, linear elastic material behavior by comparing experimental and numerical modal analysis results. The elastic modulus, in both directions, of CLT panels can be determined according to the method of the composition coefficients proposed in H. Blaß and Fellmoser (2004). Different approaches have also been proposed in the literature to compute the in-plane shear modulus of CLT panels. Analytical solutions for the calculation of shear stresses and shear deformations in CLT-beams loaded in-plane are presented in Flaig and Blaß (2013), where the authors considered the shear strains within the lamellae but also the ones resultant

from rotational and translation displacements at the crossing areas. Besides considering the lamellae shear modulus, the formula used to compute the in-plane shear stiffness accounts for the effective shear modulus of the gross cross-section, which depends on the number of boards, their width, and the slip modulus of the interface between layers. The latter method presents itself as an accurate one, but only when the slip modulus of the interface between layers is obtained experimentally, which is a parameter that introduces considerable uncertainty, hindering the use of this method. Bogensperger et al. (2010) presented simplified equations for in-plane shear modulus that are based on a representative volume sub-element. The method accounts for the shear and torsional moments at the gluing interfaces of boards. In addition, correction coefficients were developed for 3-ply and 5-ply CLT panels, which were extended to 7-ply CLT panels in Dröscher (2014). A shear test configuration for in-plane shear properties of CLT was evaluated in Brandner et al. (2017), where the main influencing parameters were identified through a comprehensive parametric study. Gap execution and layer thickness were confirmed to be the main parameters influencing in-plane shear properties. Characteristic shear properties were then proposed for Nordic Spruce CLT panels manufactured with and without edge bonding.



Figure 2.1: Two-story structure tested during the summer 2017 at the UC San Diego outdoor shake-table

Despite the efforts already developed to characterize the in-plane behavior of CLT panels, it is common to use homogeneous models specially when the main objective is to capture the overall

structural behavior, and it is reasonable to model panels as essentially rigid and concentrate the modeling effort on the modeling of the panel-to-panel connections. In these cases, the influence of panel-to-panel connections behavior is averaged over the model of the diaphragm (Breneman et al., 2016). For example, this strategy was followed in Dujic et al. (2010), where a finite element model was generated to capture the seismic response of a 7-story massive CLT building. The model made use of simplified link elements, with linear and nonlinear behavior representing hold-downs and shear anchors used on the walls. Another example is available in Sustersic et al. (2016), where a 3D model was developed to capture the response of a 4-story case study building. In both cases, the diaphragms were assumed to be essentially rigid.

In fact, if deemed necessary to assess performance or aid in the design of connectors by predicting the demands on the connections, an accurate reproduction of in-plane deformations of diaphragms, during earthquake loading, requires a finite element model that includes a reliable representation of panel-to-panel connection behavior. The models with a high level of fidelity may include link elements to represent the panel-to-panel connections, the connections between panels and load bearing elements (such as beams and walls), and between supporting frames (e.g. beam-to-beam connections). In these cases, the construction of such finite element models may constitute a burdensome task that hinders their application in regular design applications. Nonetheless, a modeling approach, comprising lumped springs for shear transfer between panels, was applied in Breneman et al. (2016) and compared to hand calculation results presented on a horizontal diaphragm design example available in Spickler et al. (2015). From an engineering perspective, the results were favorable and might validate the modeling approach in terms of diaphragm deformation estimates. Nevertheless, it is also important to develop more insight regarding the forces developed in different components of the diaphragm (e.g. shear transfer connections and chord splices). In regard to shear transfer, the common panel-to-panel connections used in CLT diaphragms are plywood surface-splines, half-lap joints, and butt-joints (Hossain et al., 2015). Consequently, the limited experimental campaigns as the ones carried out recently (Sadeghi & Smith, 2014; Closen, 2017; Sullivan, 2017; Kode, 2018) are of great importance to develop calibrated finite element models. However, there is an absence of full-scale experimental tests that focus on CLT diaphragm force distribution.

Friction among different timber elements and between these and other structural materials can play an important role in the mechanical behavior of constructions. However, for design

purposes, the contribution of friction is usually disregarded (Hirai et al., 2008). Due to the vertical component of the earthquake ground motion, uplift phenomena can occur, disabling the friction effect in the connections. Nonetheless, in cases where design and construction are controlled, there is an improved confidence on the effective occurrence of friction forces. For example, the consideration of friction allowed the reduction of the number of shear anchors and hold-downs without compromising the response of a 7-story massive CLT building that was studied on a shaking table test (Dujic et al., 2010). An average friction coefficient of 0.4 was considered for both timber-steel and timber-timber sliding contacts. The friction forces between walls and floor slabs were also considered in Sustersic et al. (2016). Despite the beneficial effects of friction on the seismic resistance of CLT buildings, the authors concluded that the influence of friction must be conservatively neglected considering the actual state of knowledge on the topic. To overcome such gap in the actual knowledge, research has been carried out to study the friction phenomenon between different engineered wood products. The friction forces between Oriented Strand Board (OSB) and Glued Laminated Timber (GLT), for example, were investigated in Steiger et al. (2018). The results obtained through experimental cyclic tests indicated that the friction coefficients decrease with increasing cumulative sliding displacements, given the reduction of asperities on the contact surfaces. However, the friction coefficients were marginally influenced by the compression load magnitude. In Outes et al. (2011), the friction between transverse surfaces (sliding perpendicular to the grain) of GLT specimens was studied. The measured mean value for the static friction coefficient was 0.47, while the mean kinetic coefficient of friction obtained was 0.31. It is worth noting that the specimens were produced with Nordic Spruce species (European Spruce) with a moisture content (MC) of 12%. On the other hand, the design values of the static friction coefficients presented in the European standard EN 1995-2 (CEN, 2004b) for planed timber vary from 0.2 (12% of MC) to 0.4 (16% of MC). There is a lack of research regarding the influence of friction in the response of plywood-CLT, CLT-CLT, and GLT to CLT members. Nonetheless, it has been identified that friction forces are often observed. Thus, in this work, the impact of friction on the modeling of the CLT diaphragms is investigated.

The main objectives of this work are to improve the understanding of the behavior of CLT diaphragms and to develop a computational modeling approach that provides validated results using experimental data collected during the shake-table testing of a two-story mass-timber prototype building shown in Figure 2.1. The mass-timber structure was constructed on the

University of California San Diego shake-table to primarily evaluate the seismic performance of innovative lateral resisting design solutions for tall wood buildings (Pei et al., 2018b). To maximize the data collected during the testing, the building was constructed allowing for swappable lateral resisting systems. Three different lateral resisting system were tested in three phases. In phase 1, a post-tensioned self-centring rocking wall design was tested (Pei et al., 2018a); in phase 2, a non post-tensioned rocking wall system was developed and tested (Blomgren et al., 2018); and lastly, in phase 3, stacked CLT wall lateral resisting systems with standard shear connectors and rod hold-downs were tested (van de Lindt et al., 2018) as part of the FEMA P-695 project developed to propose R -factors for the design of platform type CLT construction (Amini et al., 2018). In each of these phases, the structure was subjected to three levels of earthquake shaking: (i) Service Level Earthquake (SLE) (ii) Design Basis Earthquake (DBE) (iii) Maximum Considered Earthquake (MCE). While floors, beams, and columns were designed to sustain only the gravitational loads, the walls were designed to carry all the seismic loads that were transferred from the diaphragms. The diaphragms were designed to sustain the demands of the three different testing phases with little to no damage. Special attention was paid to the behavior of the resisting walls and diaphragms during the testing program. This chapter describes the fundamental engineering concepts and principles of mechanics used to design the diaphragms of the two-story mass-timber building, the experimental setup and instrumentation of the diaphragms, and a summary of the test results. In addition, a modeling strategy is developed for performance assessment and design of CLT diaphragms connected to CLT Rocking Walls, which is validated with test data.

2.2 Experimental setup and instrumentation

The building is 6700 mm high with a total area equal to 107.9 m². The dimension in plan are 6096 mm in the East-West (E-W) direction and 17700 mm in the North-South (N-S) direction. Figure 2.2 presents the diaphragm plan view for the first level and the second level (roof) diaphragms, with panel dimensions indicated, as well as, arrows indicating the major strength direction for each panel. The diaphragm at the first level was constructed with sixteen 3-ply CLT panels (nominally 104.8 mm thick) with the major strength direction oriented along the N-S direction, while the second level diaphragm was constructed as a CLT-concrete composite floor system with twelve 5-ply CLT panels (174.63 mm thick) and a 57.2 mm thick

reinforced concrete topping slab. At the second level, the CLT panels span along the E-W direction and were connected to the concrete topping with 7 x 200 SDWH Simpson Strong - Tie (SDWH27800G) screws inclined at 45 degrees along the span direction. The CLT diaphragm panels used consisted of V1 grade panels (APA, 2018) per ANSI/APA PRG 320 (APA, 2017).

The gravity system consisted of glued laminated timber (GLT) grade L2 columns and beams from grades 24F-V4 and 24F-V8. The columns located at grid lines [3] and [5] were built with a larger cross-section (190.5 mm x 273.1 mm) than the remaining columns (190.5 mm x 222.3 mm) that are positioned at grid lines [2] and [6]. Moreover, the columns aligned with the walls were continuous, i.e. spanning two floors, while the remaining columns are interrupted at each floor level. Regarding the GLT beams placed at the first floor level, two beam cross-sections were used: the grade 24F-V4 beams spanning the minor dimension of the diaphragm had a 171.45 mm by 495.3 mm cross-section, whereas the remaining 24F-V8 grade beams had a cross section size of 222.3 mm by 495.3 mm. For the second level diaphragm, the beams between grid lines [1] and [3a] and [4a] and [7] had a cross-section of 222.3 mm by 457.2 mm, whereas the ones located between grid lines C and E had a dimension of 222.3 mm by 381 mm. The 5.6 x 200 SDWS Simpson Strong - Tie (SDWS22800 LOG) screws connect CLT panels with GLT beams at the first floor level, while 5.6 x 279.4 SDWS Simpson Strong - Tie (SDWS221100 LOG) were used at the second level diaphragm with the same purpose.

For phases 1 and 2, when CLT rocking wall panels were used, the connection between the wall elements and the CLT diaphragms were executed through the innovative system shown in Figure 2.3a, which make use of steel shear dowels. These steel shear dowels were restrained laterally to the walls in order to transfer the diaphragm in-plane loads to the walls. However, they were free to move vertically in steel slots created on the CLT wall panels. As higher levels of inertial forces were expected at the second level diaphragm, the shear dowels dimensions used were 44.5 mm x 76.2 mm, whereas the ones placed at the first level diaphragm had a cross-section of only 22.23 mm x 76.2 mm. In Figure 2.3a one can see how the 19 mm thick steel transfer plates were fixed to the steel shear dowels. ASTM A490 bolts were used to transmit the loads. Note that as shown in Figure 2.2, the shear transfer plates were only placed on one of the sides of the walls, that is to the left of grid line [3] and to the right of grid line [5], respectively. The steel plates were fastened to the diaphragms using 10 x 140 ASSY VG Plus Myticon screws installed at 45 degrees. Moreover, complete joint penetration (CJP) welds

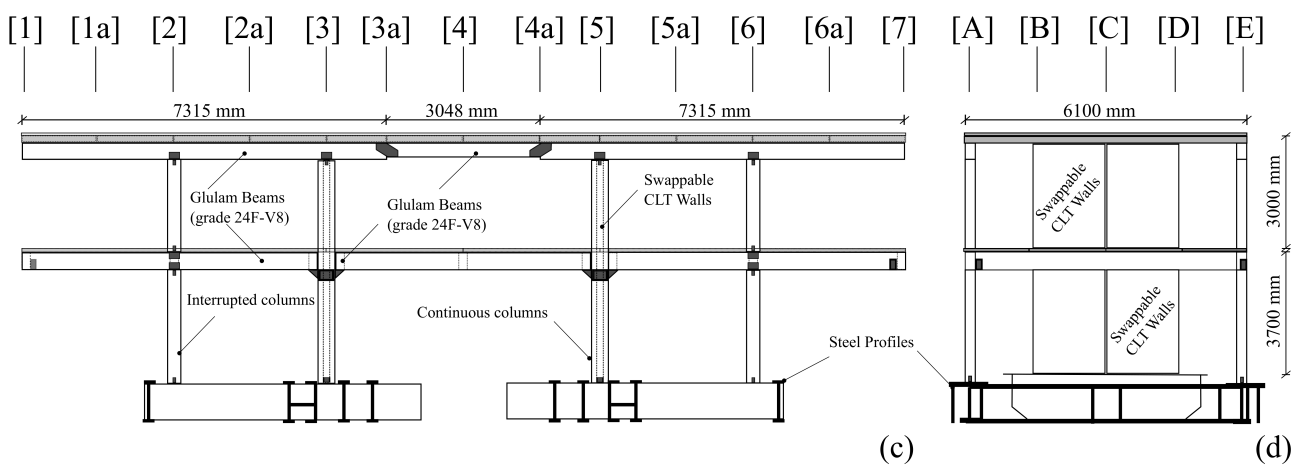
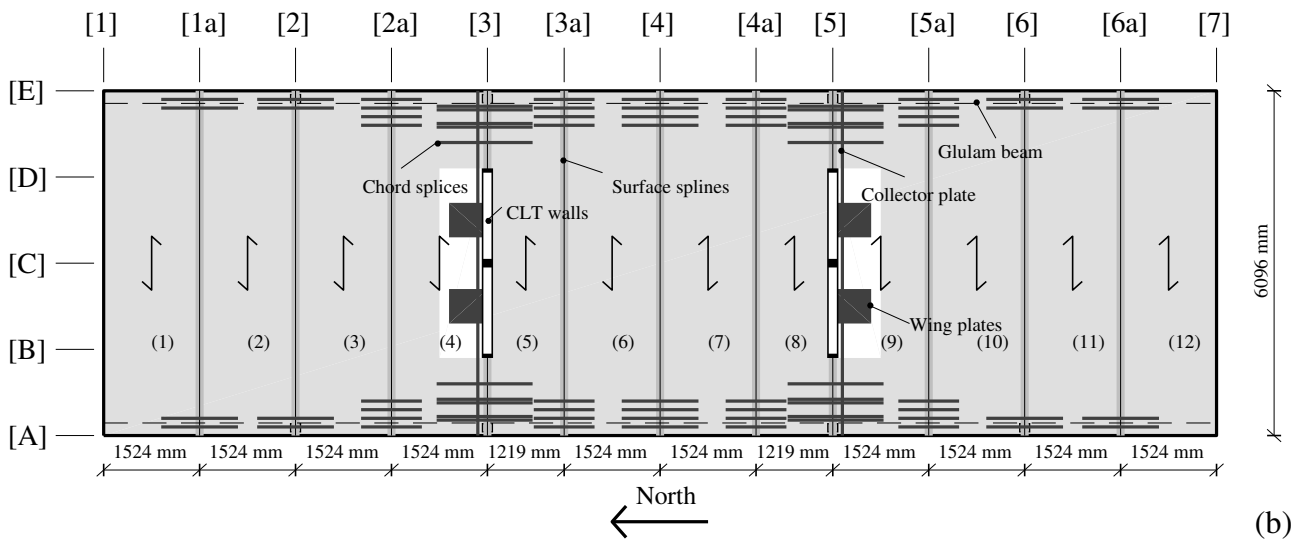
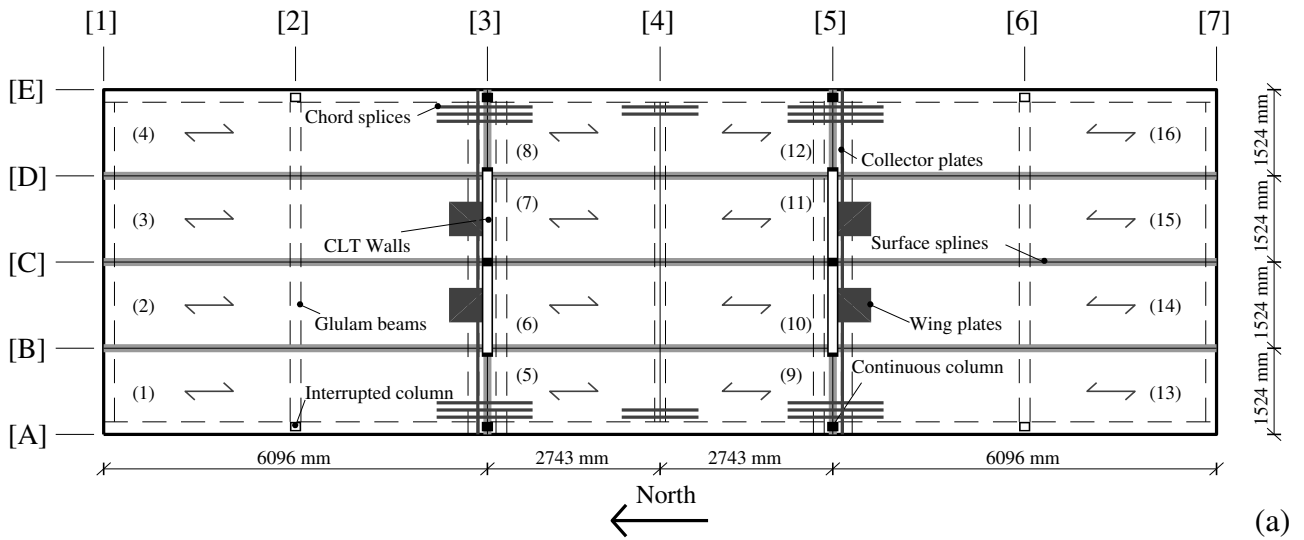


Figure 2.2: Structural layouts: (a) First floor level; (b) Second floor level; (c) N-S Elevation; (d) E-W Elevation

were executed in-situ to transmit the diaphragm forces from the collector plates to the shear transfer plates. Besides the steel shear plates shown in Figure 2.3a, the steel chords, presented in Figure 2.3b, were also designed and constructed on both floor levels which remained attached to the CLT diaphragms through out all testing phases, including phase 3. Moreover, after each shake-table test performed, a visual inspection took place to assess eventual damage at surface splines (e.g. Figure 2.3c) and beam-to-column connections, which were executed as shown in Figure 2.3d.



(a) Diaphragm to wall



(b) Chord splices



(c) Plywood surface spline



(d) Beam-to-column joint

Figure 2.3: Distinct connections used at diaphragm levels

In phase 3, the CLT wall panels were interrupted at each story level. Their position was moved 609.6 mm outwards reducing the cantilevers' length. The test program of phase 3 included three sub-phases with different wall configurations, reflecting different wall panel aspect ratios and the existence of transverse CLT walls. Further details can be found in van de Lindt et al. (2018). Of interest to this work, the connections between wall panels and diaphragms were

executed using 76 mm x 57 mm x 3 mm L-shaped angle brackets with a 121 mm length. These brackets were fastened to the diaphragms using 19 mm fully threaded A36 bolts according to the expected shear demands.

2.2.1 Test structure design

The design of the gravity system and lateral resisting systems tested in the three phases are summarized in three publications (Pei et al., 2018a; Blomgren et al., 2018; van de Lindt et al., 2018). In this section, focus is placed on details on the design of the diaphragms.

Both diaphragms were designed in accordance with principles of mechanics, using values for fastener properties and member strength extracted from the most recent test results (Closen, 2017; Pryor, 2017), National Design Specification (NDS) (AWC, 2015), and CLT manufacturer's specifications (APA, 2018). The white paper by Spickler et al. (2015) was also used as a reference. Moreover, the alternative diaphragm seismic design force level method described in Ghosh (2016) was used to compute the floor horizontal accelerations along the building height. The maximum design forces were obtained for the lateral resisting system of the third phase that was designed for a site located in Berkeley, California. Thus, the first floor was designed for an earthquake-induced horizontal acceleration equal to 1.01 g, while the second level diaphragm was designed for 1.36 g.

The first level diaphragm was considered as a deep beam that responds to the in-plane loading with a fully composite behavior. Consequently, the quantity of screws and their spacing, at each surface spline, were determined according to the shear flow caused by the inertial forces. These forces were calculated with the seismic mass and the design values for the floor horizontal accelerations. The chord forces were obtained by equilibrium in order to resist the diaphragm moments. These forces were divided by the number of steel plates (6.35 mm x 50.8 mm) assumed for each chord. It is worth noting that the fasteners used in surface splines and panel-to-beam connections, presented in Figure 2.4a and Figure 2.4b, were not used to meet the requirements for continuity of diaphragm tension chords.

The composite solution applied at the second floor was studied in Higgins et al. (2017). The inclined screws were designed comparing their strength (Pryor, 2017) with the inertial forces computed using the floor horizontal accelerations and the concrete tributary mass. At the

second floor, each surface spline was designed to guarantee the transmission of the inertial forces to the walls without considering the contribution of concrete. In turn, the chord splices were designed with the same method used for the first level diaphragm, neglecting surface splines and concrete topping contributions. The cross section of the second level diaphragm can be consulted in Figure 2.4d.

It is worth noting that the CLT panels applied on both diaphragms verified the criteria given in AWC (2015) for tension, compression, and bending.

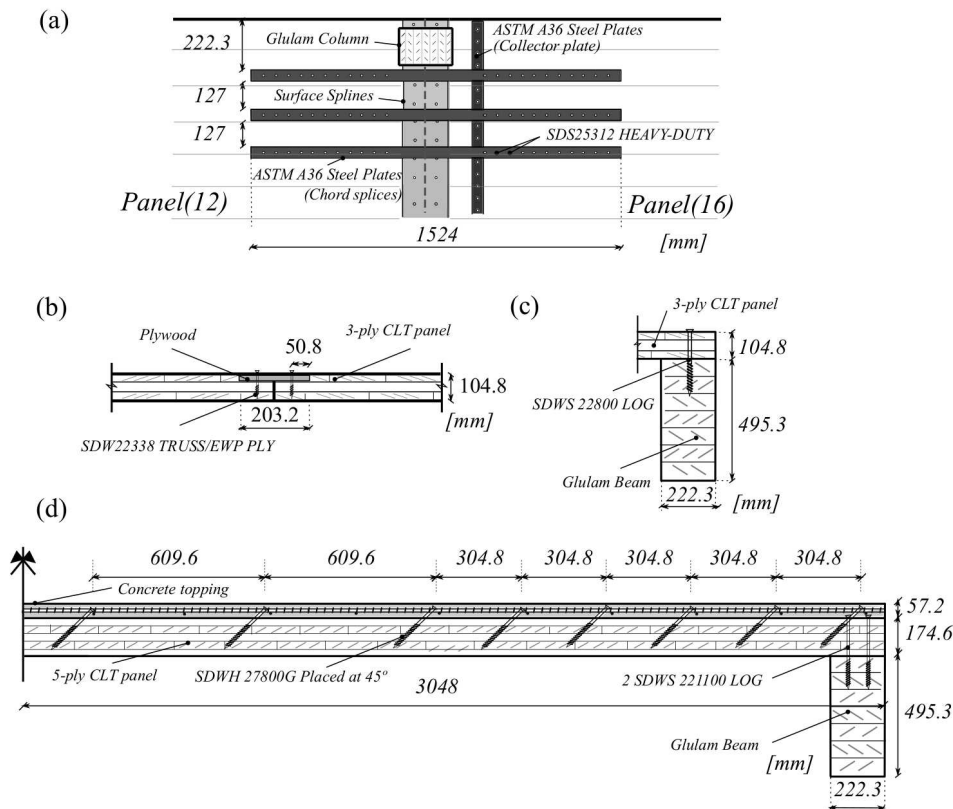


Figure 2.4: Diaphragm details: (a) Chord splices at the second floor; (b) Single surface spline; (c) Panel connection at first floor boundaries; (d) Composite solution

2.2.2 Instrumentation for the diaphragms

In this section, focus is placed on the devices used to evaluate the response of the diaphragms. Nevertheless, it is worth noting that the instrumentation used for the lateral resisting systems can be consulted in Pei et al. (2018a); Blomgren et al. (2018); van de Lindt et al. (2018).

In order to capture the response of the CLT diaphragms different types of sensors were installed

in both diaphragm levels. Linear potentiometers (LP) were used to measure relative displacements to measure the response of different types of connections. For instance, LP sensors were used to measure sliding and separation between adjacent CLT panels, as well as, the sliding of boundary panels on the supporting beams. At the second floor, LP were also used to measure relative displacements between CLT panels and the concrete topping. A total number of 25 LP were installed on the first level diaphragm, while 38 were placed at the second level diaphragm. The deformations of the diaphragms were also assessed through string potentiometers (SP) that measured absolute displacements, vertical and in-plane, at distinct locations within the floors. Both diaphragms were instrumented with 22 string potentiometers (11 at each floor).

Several accelerometers (6 biaxial and 8 triaxial) were used to describe modal modes and the distribution of inertial forces. These sensors covered different positions of the diaphragms allowing to evaluate and compare their flexibility. Both floors had one accelerometer located at each corner as well as at quarter points along the centerline of the diaphragm. The behavior of chord splices was monitored through 40 strain gauges. The strains of concrete topping rebars were also evaluated by the measurements of 2 strain gauges.

2.3 Shaking Table Test Results

A set of 5 natural uni-directional ground motions were scaled to fulfill the characteristics of the three hazard levels (SLE, DBE, MCE). The earthquake records used were: Northridge, 1994 (NR); Superstition Hill, 1987 (SH); Imperial Valley, 1979 (IV); and Loma Prieta, 1989 (LP). The site locations considered to scale the time-history records were San Francisco (Phase 1), Seattle (Phase 2) and Berkeley (Phase 3). In Phase 3, there is no variation on the ground motion record between consecutive tests, being Loma Prieta the one used.

2.3.1 Floor horizontal accelerations along the building height

The design of CLT diaphragms is primarily dependent on the estimation of the earthquake-induced floor horizontal accelerations. They are necessary to obtain in-plane forces (inertial forces) for the design of diaphragms elements and their connections to the lateral force resisting system. In this work, the diaphragm design forces were obtained with the alternative diaphragm

seismic design force level (Ghosh, 2016), which is based on the research developed by Rodriguez, Restrepo, and Carr (2002). This method is applicable for buildings where the vertical elements of the lateral resisting system dominate the overall structure behavior (Ghosh, 2016). The contribution of higher modes is done by using a modal combination technique assuming that ductility (on the lateral resisting system) only effects the accelerations associated to the first mode of the response (Rodriguez et al., 2002).

In this section, the earthquake-induced floor horizontal accelerations measured during the 34 tests are evaluated in order to assess the applicability of the alternative diaphragm seismic design force level to mass-timber structures built with CLT rocking wall systems and stacked CLT wall lateral resisting systems. The sequence of ground motions for all phases of testing is presented by their identification number (ID) in Table 2.1. Moreover, the peak ground accelerations are also available, as well as, the hazard levels considered to scale each ground motion record. It is worth noting that the floor accelerations presented in Table 2.1 are the peak of the mean accelerations, over all accelerometers, measured in the E-W direction.

In Figure 2.5, the induced floor horizontal accelerations can be evaluated in elevation and compared with the ones used during the design phase (Ghosh, 2016) for each phase. For the SLE hazard level, the floor accelerations at the floor levels increased in height for almost all testing phases, which was expected given the lack of non-linear responses. Nevertheless, the magnification of floor accelerations, observed during phase 1, ranged from 1.9 to 2.7, which may indicate that the initial stiffness conferred by the post-tensioning can be adverse for the design of non-structural elements and equipment supported on the floors. Such level of magnification are on the same range of the ones recorded in instrumented concrete wall buildings and braced frames buildings, up to 20 stories, during the Northridge (1994) earthquake (Hall et al., 1996; Rodriguez et al., 2002). Similar responses were observed in phase 2, but with a lower magnification that ranged between 1.0 and 2.0. The floor acceleration magnification tended to diminish as the intensity of the earthquake increased, in phase 1 and phase 2. This occurrence can be associated to the fact that some components of the lateral resisting system have reached the inelastic range and also to rocking at CLT panels' base. Another important finding regards the higher induced accelerations to the first floor when compared to the ones measured at the second level. This was observed during earthquake records scaled to DBE and MCE hazard level, presented in Figure 2.5a and Figure 2.5b. This feature contrasts with the

Table 2.1: Maximum accelerations measured at different heights of the building

(ID) Ground Motion	Phase 1			Phase 2			Phase 3				
	Accel. Table	Accel. 1st Floor	Accel. 2nd Floor	(ID) Ground Motion	Accel. Table	Accel. 1st Floor	Accel. 2nd Floor	(ID) Ground Motion	Accel. Table	Accel. 1st Floor	Accel. 2nd Floor
(1) Loma Prieta ^a	0.159	0.316	0.354	(15) Superstition Hill ^a	0.135	0.198	0.221	(28) Loma Prieta ^{a,c(*)}	0.250	0.391	0.520
(2) Loma Prieta ^a	0.177	0.262	0.344	(16) Imperial Valley ^a	0.198	0.253	0.289	(29) Loma Prieta ^{c(*)}	0.630	1.214	1.490
(3) Northridge ^a	0.188	0.339	0.427	(17) Northridge ^a	0.107	0.179	0.211	(30) Loma Prieta ^{b,c(*)}	0.420	0.718	1.129
(4) Superstition Hill ^a	0.132	0.301	0.337	(18) Loma Prieta ^a	0.140	0.173	0.191	(31) Loma Prieta ^{a,c(**)}	0.240	0.380	0.493
(5) Northridge ^b	0.534	0.805	0.616	(19) Superstition Hill ^b	0.533	0.620	0.472	(32) Loma Prieta ^{c,c(**)}	0.660	1.612	1.595
(6) (×2) Northridge ^b (1.25)	0.550	0.683	0.542	(20) Imperial Valley ^b	0.465	0.421	0.440	(33) Loma Prieta ^{a,c(***)}	0.261	0.372	0.372
(7) Imperial Valley ^a	0.100	0.202	0.273	(21) Northridge ^a	0.125	0.102	0.119	(34) Loma Prieta ^{c,c(***)}	0.680	1.240	1.575
(8) (×2) Northridge ^a (1.25)	0.562	0.507	0.303	(22) Imperial Valley ^b	0.497	0.472	0.430				
(9) Loma Prieta ^b	0.533	0.493	0.443	(23) Northridge ^b	0.447	0.485	0.414				
(10) Superstition Hill ^b	0.664	0.695	0.558	(24) Northridge ^c	0.714	0.616	0.480				
(11) Loma Prieta ^c	0.666	0.551	0.498	(25) Loma Prieta ^a	0.178	0.152	0.170				
(12) Northridge ^c	0.767	0.783	0.670	(26) Imperial Valley ^c (1.2)	0.886	0.782	0.603				
(13) Superstition Hill ^c	0.670	0.901	0.746	(27) Northridge ^c (1.2)	0.831	0.844	0.562				
(14) Northridge ^c (1.2)	0.882	0.840	0.739								

(×2)	Ground motion was run back to back with no time gap in between	(*)	Subphase 3.1 - Stacked CLT Panels
(1.25)	Ground Motion Scaled for 1.25 times the respective Hazard Level	(**)	Subphase 3.2 - Stacked CLT Panels
(1.20)	Ground Motion Scaled for 1.20 times the respective Hazard Level	(***)	Subphase 3.3 - Stacked CLT Panels with transverse walls

^a Service Level Earthquake (SLE)
^b Design Basis Earthquake (DBE)
^c Maximum Considered Earthquake (MCE)

linear relationship established for two stories buildings by the alternative diaphragm seismic design force level (Ghosh, 2016). From the results obtained, it is possible to state that the method proposed in ASCE 7-16 (Ghosh, 2016) fails to predict the earthquake-induced floor horizontal accelerations for structures built with rocking walls. In fact, when CLT wall panels start to rock, the modal properties of the structure change and a period elongation occurs. Consequently, different floor magnification factors must be provided for distinct hazard levels.

Regarding phase 3, the alternative method proposed in ASCE 7-16 (Ghosh, 2016) provides good estimates for the floor horizontal accelerations since they increase with the building height. Their distribution in height can be consulted in Figure 2.5c for all the ground motions of phase 3. In fact, the uplifts (rocking motion) occurred at the base of the walls (van de Lindt et al., 2018) were lower than the ones observed during phase 1 and phase 2. Consequently, the first natural mode governed the response of the building. The magnifications verified floor horizontal accelerations, during DBE and MCE hazard levels, were greater than the ones observed during SLE level tests, which can be justified by the small number of stories. The response presented for test (32) of sub-phase 3.2 are not consistent with the other responses in terms of peak floor accelerations. In this test, the peak floor acceleration was higher at the first floor level since the north cantilever experienced larger accelerations immediately after the failure of nails in shear, which occurred in angle brackets positioned at the base of the north wall (van de Lindt et al., 2018).

It is important to refer that the fundamental period (T), used to calculate the design spectral acceleration (S_{DS}), for all phases, was estimated from equation 12.8-7 available in ASCE (2016) and resulted in period $T=0.20$ s. Before and after each ground motion record, the structure was subjected to a root-mean-square (RMS) white noise (WN) with an amplitude of $0.03 g$, in order to identify the building fundamental periods through Fast Fourier Transform (FFT). In phase 1, the fundamental periods, measured before the tests, ranged between 0.7 s and 0.9 s, while ranging from 0.85 s to 1.1 s for phase 2. These values allow to conclude that the estimation given by ASCE (2016) produces lower values of fundamental period for CLT rocking wall systems. For these particular site locations, San Francisco and Seattle, the design spectral acceleration shifts from the constant acceleration range to the constant velocity range of the response spectrum. Regarding the system tested in phase 3, the equation 12.8-7 available in ASCE (2016) provides better results, since the fundamental periods, measured before each sub-phase, ranged from

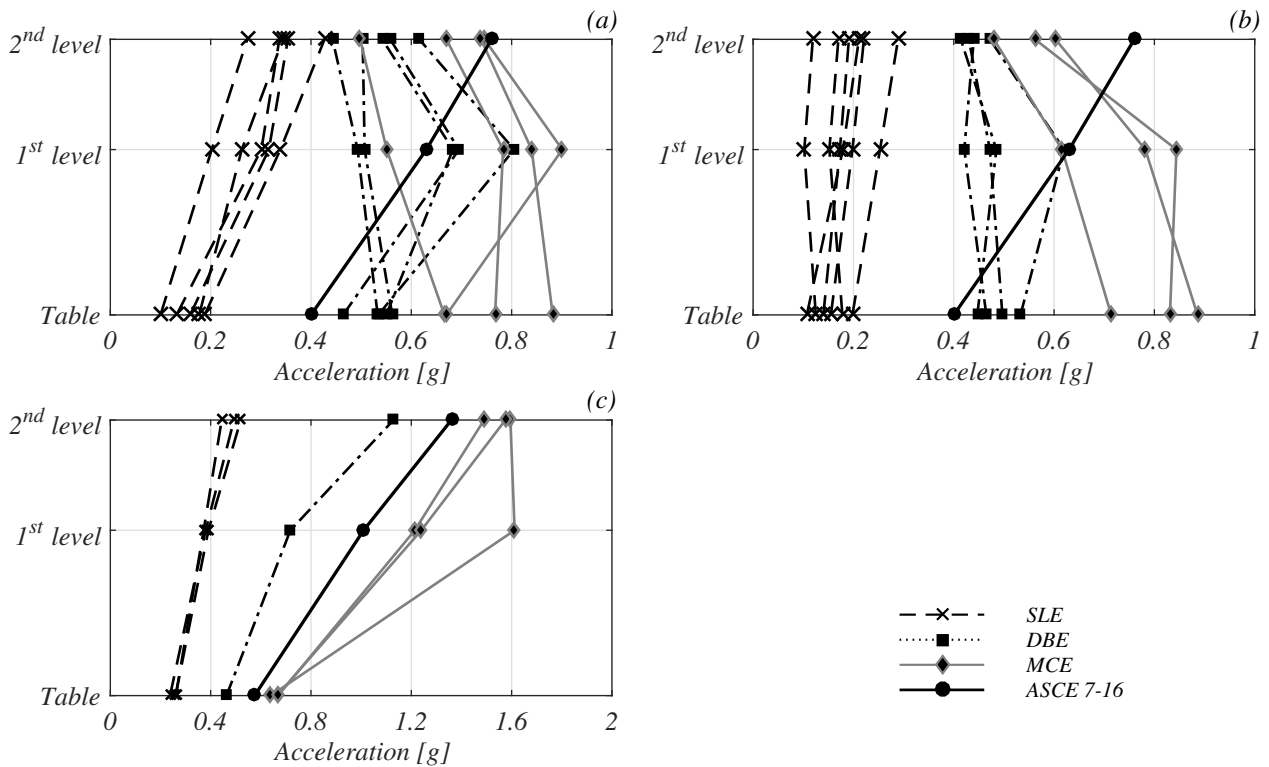


Figure 2.5: Average of the peak Accelerations measured at different diaphragm levels: (a) Phase 1; (b) Phase 2 (c) Phase 3

0.35s to 0.45s. For the last phase (for a Berkeley site location) of tests the design spectral acceleration remains at the constant acceleration range of the response spectrum.

2.3.2 Peak Accelerations within diaphragms

In order to better evaluate the flexibility of both diaphragm solutions, it is important to evaluate the accelerations at different locations within the diaphragms. Thus, from Figure 2.6 to Figure 2.8, the maximum response of each diaphragm is plotted for every earthquake test performed. Rather than provide peak accelerations measured at different diaphragm points, the results represent the highest average acceleration measured during each test. In other words, attention was paid to evaluate if the peaks observed at different accelerations occurred at the same time. This type of assessment allowed to distinguish torsional responses. It is worth noting that the values presented at the diaphragm extremes (North and South) are the average of the peak accelerations measured at their respective corners.

At the first floor level, the majority of the responses (61.8%) are characterized by lower values

at the points located between grid lines [2] and [6] and higher values at both cantilevers' extremes. These tests revealed minimal torsional behavior relative to the response of the first floor diaphragm. The accelerations measured along grid line [C] presented a low variability. If one considers only the three sensors along grid line [C], the coefficient of variation (CoV) of the accelerations remained lower than 15 %, in 82.3 % of the ground motion tests performed. These type of response are easier to identify in DBE and MCE tests presented in Figure 2.6 and Figure 2.7. On the other hand, if one considers the five positions along the diaphragm, the CoV of the peak accelerations increases. In this case, only 35.3 % of the tests present coefficients of variation that are lower than 15 %. This fact can be associated to the change on the lateral stiffness given by the existence of the GLT frames (columns and beam) aligned with grid lines 2 and 6. The latter were initially designed to sustain only gravity loads, but it is evident that they also provide additional in-plane stiffness.

Phase 3 was characterized by having ground motions with higher intensities and a conventional transmission of forces from the diaphragms to the walls. The first level diaphragm presented higher peak accelerations at the northern cantilever than the southern cantilever, which is related to torsion. Similar responses were observed in MCE tests 29 and 32, from sub-phase 3.1 and sub-phase 3.2, respectively. Nevertheless, the differences between the north cantilever and the south cantilever responses are more evident in test 32 since, as mentioned above, the north wall was damaged at the base and experienced large sliding (van de Lindt et al., 2018).

After test 32, the lateral resisting system was changed for a solution similar to the one built in sub-phase 3.1 with an inclusion of transverse walls (N-S), fixed to the main CLT wall panels (E-W). According to the results available in Figure 2.8a, one can conclude that the response of the first floor diaphragm was considerably improved with the inclusion of transverse walls. Furthermore, in tests (33) and (34) the peak accelerations measured at the first floor were practically uniform within the diaphragm.

During phase 1 and phase 2, the cantilevers of the second level diaphragm had slightly higher accelerations than the center of the diaphragm. Nevertheless, these difference is considerably lower than the ones observed at the first floor. If one considers only the three sensors along grid line [C], the CoV of the accelerations remained lower than 15 %, in 82.4 % of the ground motion tests performed. However, when all the positions are considered, 73.5 % of the tests present coefficients of variation that are lower than 15 %. This finding can be confirmed by comparing

diaphragm responses at different floor levels. For example, comparing the responses obtained through DBE tests, presented in Figure 2.6b and Figure 2.6e. The change in in-plane stiffness observed at the first floor (grid lines [2] and [6]) was reduced at the second. Partially, it is caused by the absence a beam, in the E-W direction, connecting the exterior columns. On the other hand, the concrete layer contributed to increase the in-plane stiffness. According to the results, the composite diaphragm presented a quasi-uniform distribution of accelerations throughout all the sub-phases. In addition, the results of phase 3 allow to conclude that different height to width aspect ratios of wall panels, as well as, the inclusion of transverse walls did not affect the response of the composite diaphragm.

Comparing the diaphragm responses of phase 1 and phase 2, one can also conclude that the swap of the rocking walls, executed between these phases, did not influence the behavior of the diaphragm, which is in accordance with what was expected, since the connections between the walls and the diaphragms were kept.

2.3.3 Relative displacements within diaphragm CLT panels

The response of diaphragms can also be evaluated through the response of their connections. From the inspections performed after each shaking-table test, it was possible to confirm that the floor level diaphragm experience very little damage throughout all the phases of testing. An essentially elastic response was obtained as defined during the design. At the second floor, there was no observation of damage on the timber panels. Nevertheless, some small cracks appeared in concrete next to places where PVC pipes were placed to guarantee the installation of bolts for the third phase of testing. The cracks resultant from the curing process did not propagate throughout the testing program. Some cracks occurred next to inclined screws that were fastened without giving enough clearance to concrete.

Despite the little damage observed and the very small displacements measured, some considerations can be drawn by evaluating the response of connections. Figure 2.9 presents the results for DBE and MCE, as well as, the position of the linear potentiometers used to measure separation and sliding motions. Globally, the connections presented larger deformations during phase 3 due to the higher intensities of its ground motions.

At the first floor diaphragm, the surface splines oriented N-S presented larger values of separa-

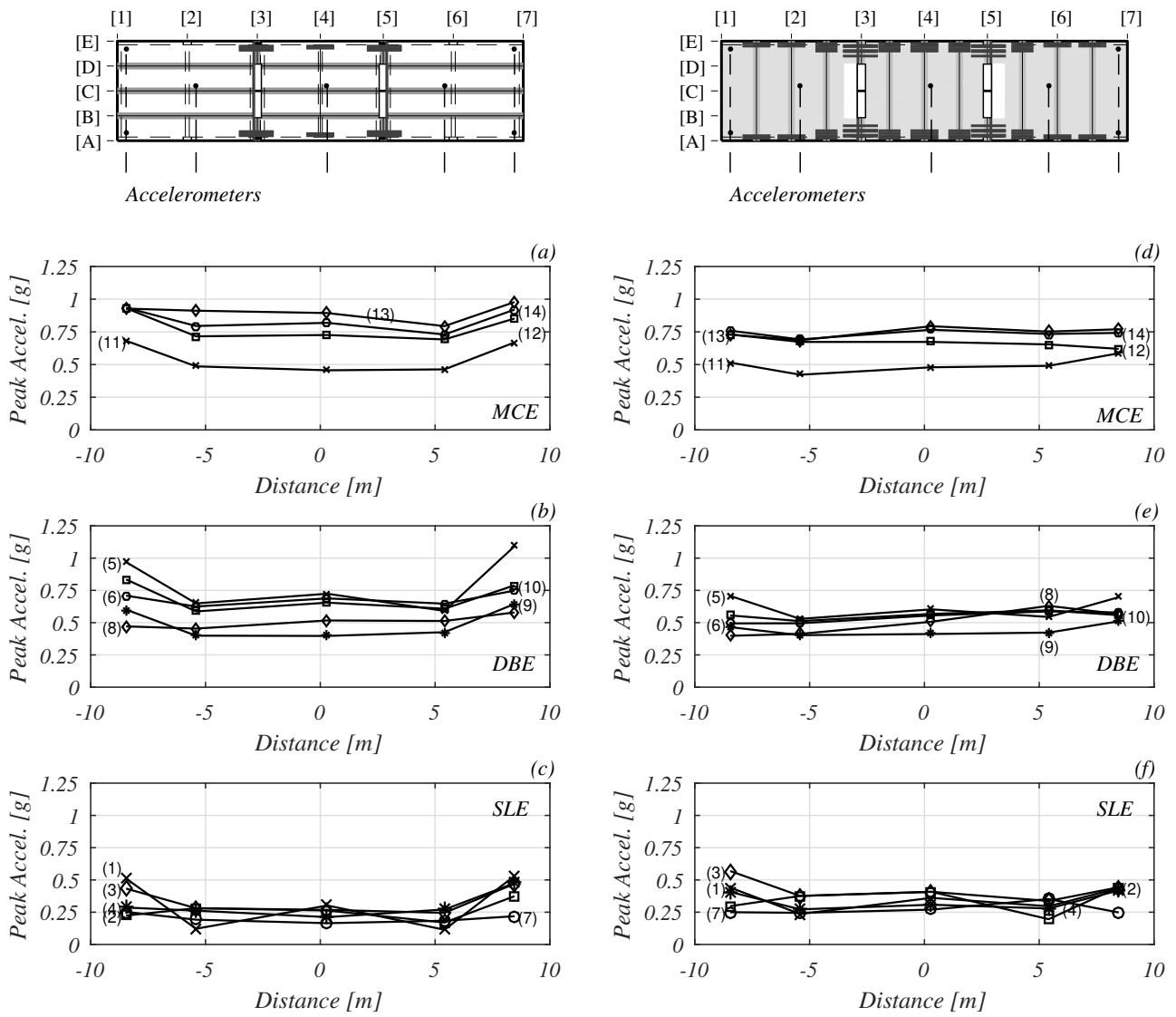


Figure 2.6: Diaphragm peak accelerations measured during Phase 1

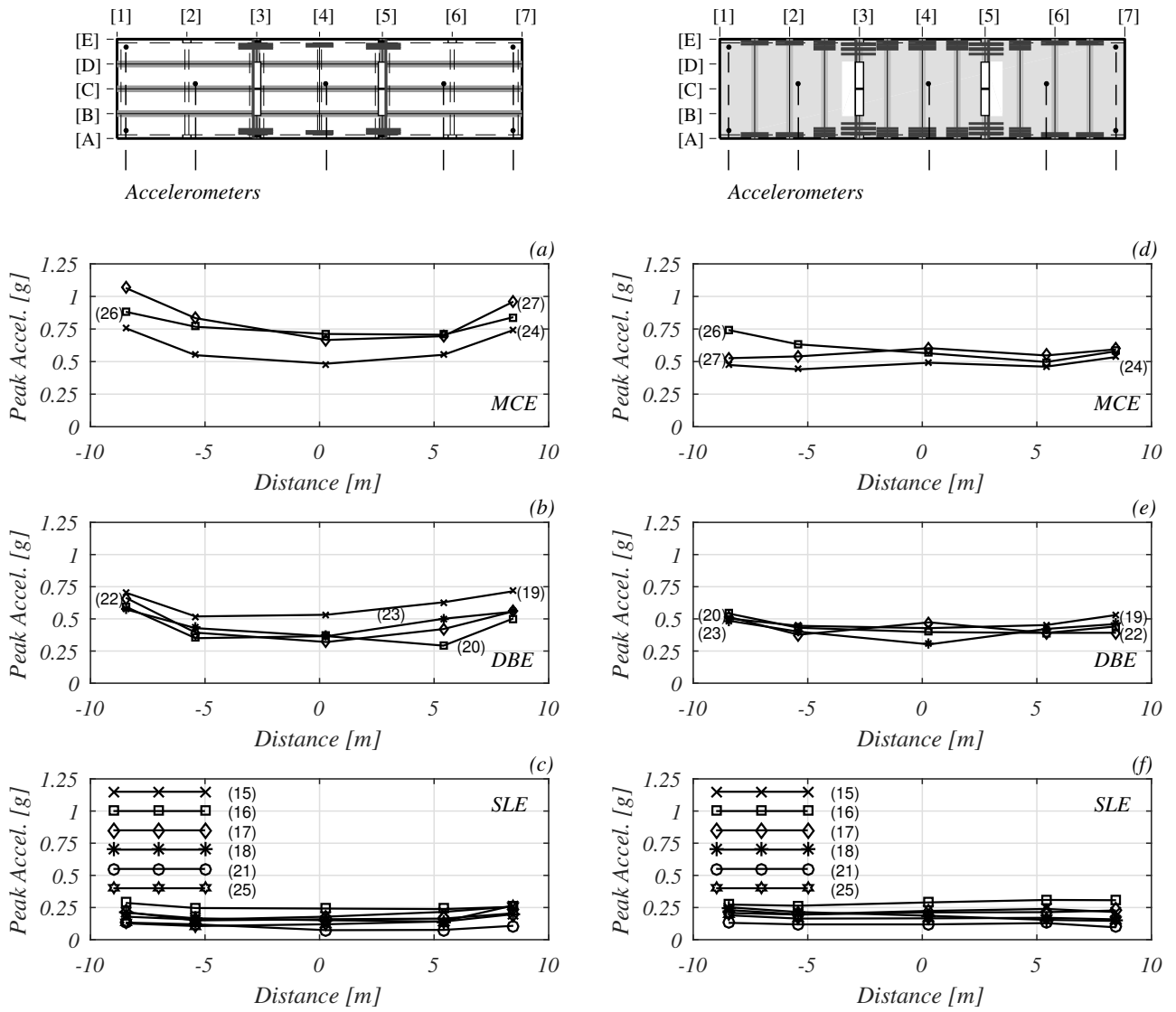


Figure 2.7: Diaphragm peak accelerations measured during Phase 2

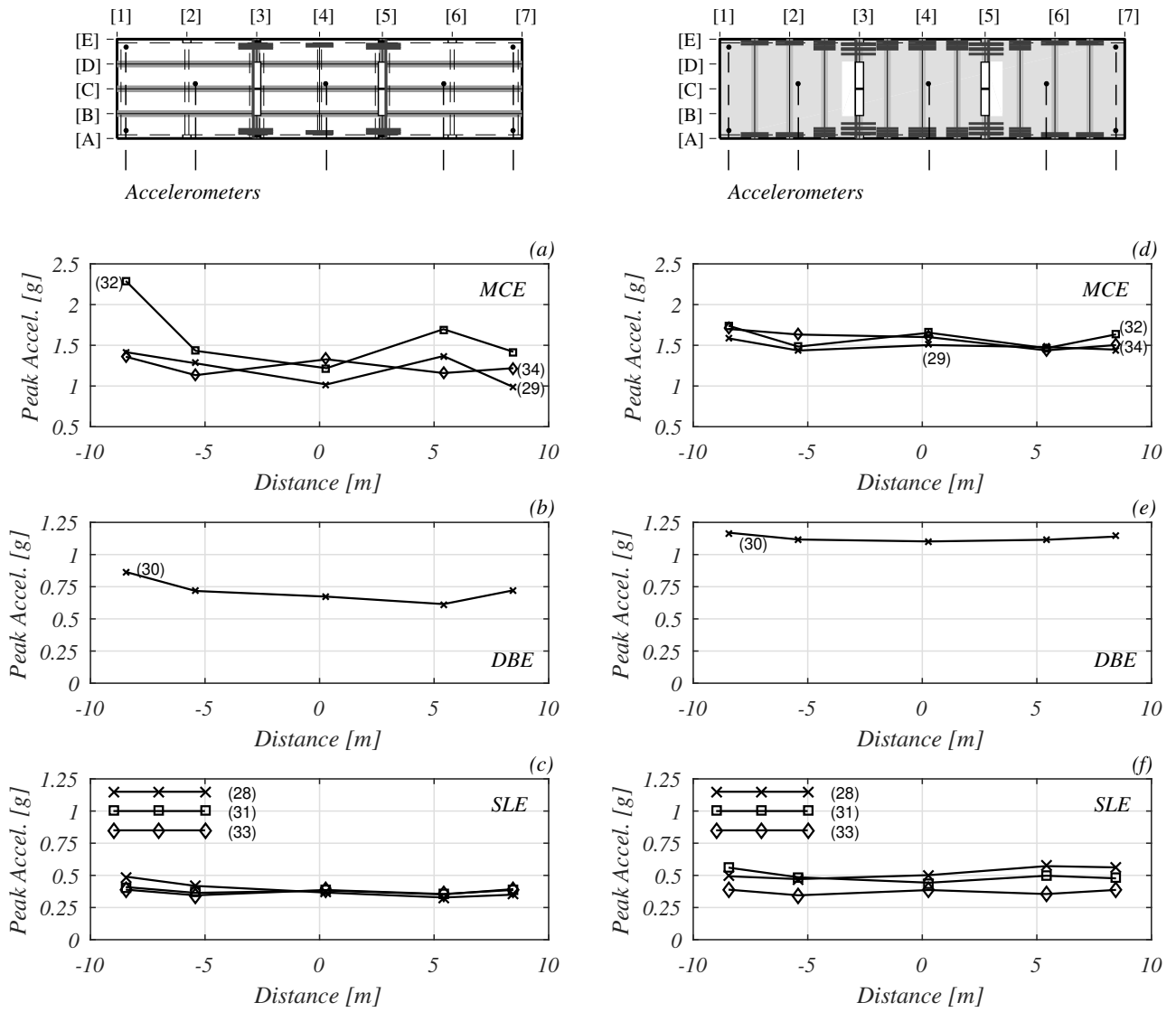


Figure 2.8: Diaphragm peak accelerations measured during Phase 3

tion (Figure 2.9a) than sliding (Figure 2.9b). Despite the small relative displacements measured, it is worth noting that the assumptions made in the design phase did not consider the effect of separation between panels, since a composite behavior was admitted. During phases 1 and 2, the relative displacements measured by LP1E205 and LP1N102 were the highest values in terms of sliding motions. Those splines were responsible to transmit the inertial loads from the center of the diaphragm to the wing plates, where the shear dowel is fastened aiming to connect the diaphragm and the walls. Due to their position, the instrumented surface splines aligned with the grid line [D] present separation between panels, but only on the surroundings of the hole left on the diaphragm in order to swap the CLT walls. During the design phase of the first floor diaphragm the most solicited surface spline was the one aligned with grid line [C]. Precisely the spline located between grid lines [1] and [3], at the north cantilever, and the spline located between grid lines [5] and [7], at the south cantilever (see Figure 2.2a). Nevertheless, the results taken from the south cantilever showed that between grid lines [5] and [6] the relative displacements (separation and sliding) between panels 14 and 15 were practically null. In Figure 2.9a, one can observe that the separation between panels (14) and (15) increased in grid lines [6] and [7]. This sudden difference can also be associated to the change on the lateral stiffness given by the GLT frames (columns and beam).

At the first floor level, the sliding over GLT beams oriented E-W was on the same magnitude of the relative displacements of the surface splines during DBE and MCE, as shown in Figure 2.9b. This is justified by the lower number of screws fastened per beam length when compared to the number of screws used on surface splines. On the other hand, the number of fasteners used to connect CLT panels to GLT beams was higher at the second floor to ensure a good performance for gravity loads. These fact can justify the low values of sliding over beams presented in Figure 2.9d.

Regarding the surface splines of the second level diaphragm, one can state that they had lower deformations when compared with the surface splines located at the first floor. For instance, this can be evaluated by comparing the measurements presented for phase 3. Even with higher floor horizontal accelerations, the deformations presented in Figures 2.9e and 2.9f are lower or on the same range as the ones showed in Figures 2.9a and 2.9b. The composite action due to the concrete topping may be the main contributing factor to justify the responses obtained. However, it is important to note that the orientation of the panels also changed, being the

surface splines aligned with the seismic load direction. Throughout phases 1 and 2, the spline located along grid line [5a] experienced the highest values of panels separation (0.7 mm), as showed in Figure 2.9e. On the other hand, the spline located along grid line [5] had the highest values of sliding. In phase 3, the response changed and the response of the surface splines along grid lines [4a] and [6] increased in terms of separation between panels. Nevertheless, the surface splines along grids [5] and [5a] continued to be the ones with higher values of sliding.

2.4 Numerical modeling approach for CLT diaphragm

The modeling approach proposed in this chapter aims at capturing the peak deformations of the first floor by representing its in-plane behavior through a two-dimensional model. In parallel, the models should reproduce reliably the force distributions in order to be applied on regular design procedures. The software package SAP2000 (CSI, 2017) was used due to its practical and intuitive object-based modeling environment. The tests used to evaluate the modeling approach refer to phase 1 and phase 2, where the connection between walls and diaphragm is executed with a shear dowel fastened to 19 mm steel wing plates. Instead of having a distributed transmission of seismic loads, from diaphragm to walls, this solution implies a concentrated transmission from the wing plates to the walls. The effectiveness of the approach is assessed by comparing the numerical results with the peak deformations observed during different ground motions scaled to DBE and MCE hazard levels.

2.4.1 Key aspects of the modelling approach

The methodology chosen includes four-node shell elements with homogeneous orthotropic linear elastic behavior, to simulate CLT properties of diaphragm panels, and linear elastic frame elements that represent GLT beams, rocking walls, steel plates and wing plates. The GLT members are in agreement with Douglas-fir properties from grades 24F-V4 and 24F-V8 ($E = 12.4$ GPa, $G = 0.780$ GPa). In turn, it is assumed that the CLT rocking walls are practically rigid by assigning a stiffness value that is a thousand times greater than the value assigned to the beams, since the relevant behavior refers to the diaphragm deformations relatively to the walls. The mechanical properties of the ASTM A36 steel ($E_s = 200.0$ GPa, $\nu = 0.26$) were assigned to

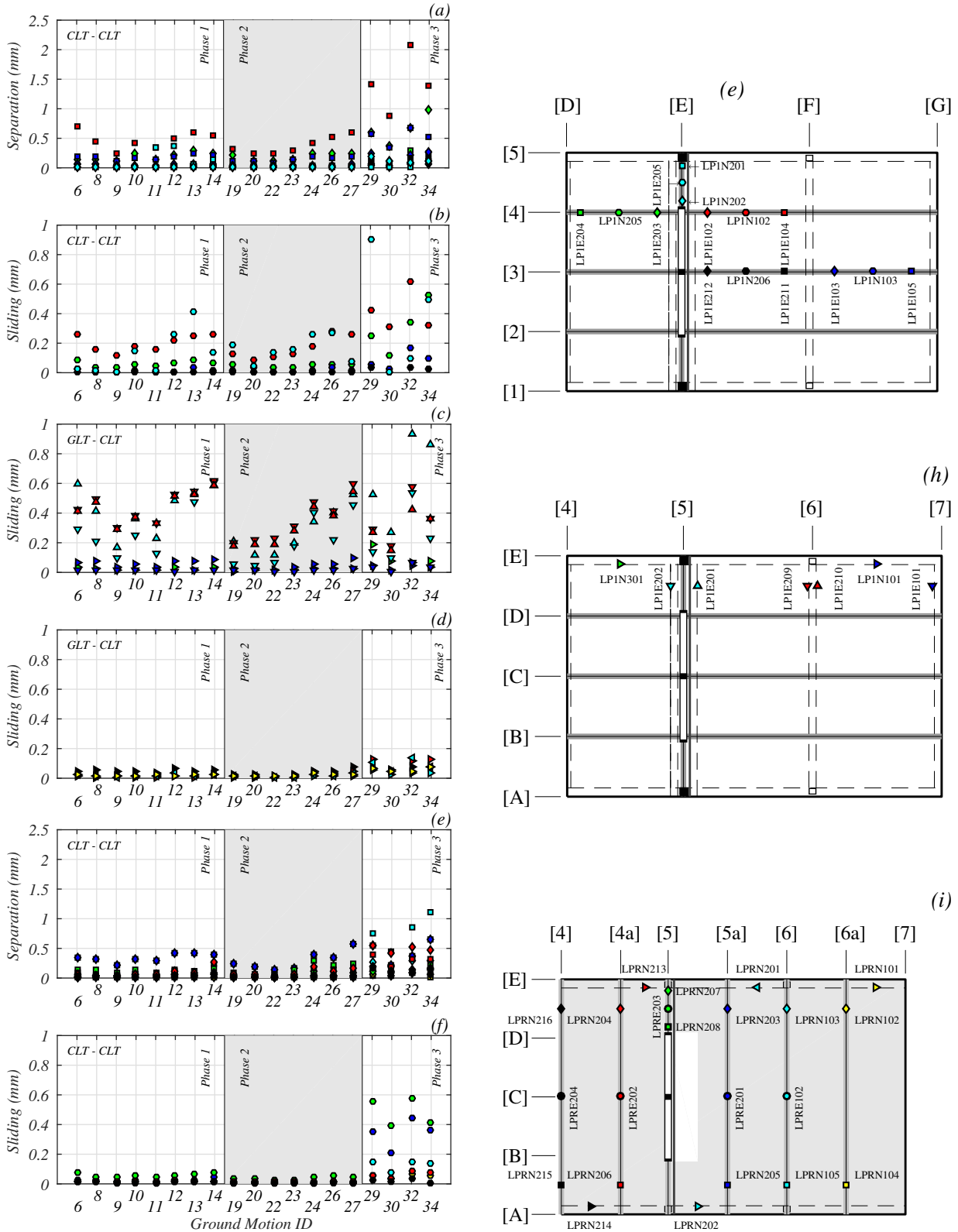


Figure 2.9: Relative displacements: (a) between CLT panels at 1st Floor; (b) between CLT and GLT beams at both Floors; (c) between CLT panels at 2nd Floor; (d) LP used at 1st Floor; (e) LP used for sliding between CLT and GLT at 1st Floor; (f) LP used at 2nd Floor

the steel plates used as chord splices and collectors. To simulate the rigid connection between the diaphragm and the wall panels, two rigid frames (the same used for walls) are connected through rigid links to the four-node shell elements, used to model the CLT panels of floors. The mesh used is shown in Figure 2.10a, where the nodes are equally spaced at 304.8 mm (1 foot). Border nodes of each individual panel shall be defined as special joints for further definition of zero-length elements (links), making use of SAP2000 interactive editing feature. Several special joints share the same coordinates, as suggested by Figure 2.10b, where two beams are connected, and by Figure 2.10c that shows a junction of four beams. It is assumed beam-to-beam connections as rigid given their high stiffness when compared to the panel-to-beam connections. As presented in Figure 2.10d, the nodes used to represent the walls are fully restrained. In Figure 2.10d, one can also see that complete joint penetration (CJP) welds are represented by rigid links. The collector frames were also divided according to the predefined mesh and linked to the CLT through zero-length elements that represent the connectors used to install the steel plates. It is worth noting that the links used to represent surface-splines must represent sliding, tension, and panels' closure. Consequently, a high stiffness is assigned for compression, which is modeled with a value that is a thousand times greater than the one assumed for tension, as recommended in Breneman et al. (2016).

2.4.2 In-plane stiffness of CLT panels

The V1 grade panels are manufactured using No.2 Douglas fir-Larch lumber in the major strength direction and No.3 Douglas fir-Larch lumber in the minor strength direction (APA, 2018). When a diaphragm is being analyzed for earthquake effects that represent full unreduced seismic loads it is preferable to use expected or average material properties (Breneman et al., 2016). Thus, the timber members are independently modeled with their mean properties. According to Bogensperger et al. (2010), the effective shear modulus is dependent on the shear modulus of the boards and on the local torsional moment at layer interface. A correction factor is also considered to account for the number of layers used. The in-plane effective shear modulus (G_{xy}) calculated is equal to 575.7 MPa. The longitudinal elastic modulus in the principal directions was computed using the composite theory presented in H. Blaß and Fellmoser (2004), where the elastic properties of the minor strength direction cross layers were considered. From the calculations performed, an elastic modulus of 7461.9 MPa and 3462.8

MPa, was obtained for the major and minor directions, respectively. Despite the present chapter focusing only on the in-plane behavior, SAP2000 requires values for E_z, G_{xz} and G_{yz} properties. The following ratios were taken from the study developed by Gsell et al. (2007): $E_x/G_{xz} = 15.43$ and $E_x/G_{yz} = 87.78$. Moreover the value assumed for E_z is equal to 500 MPa.

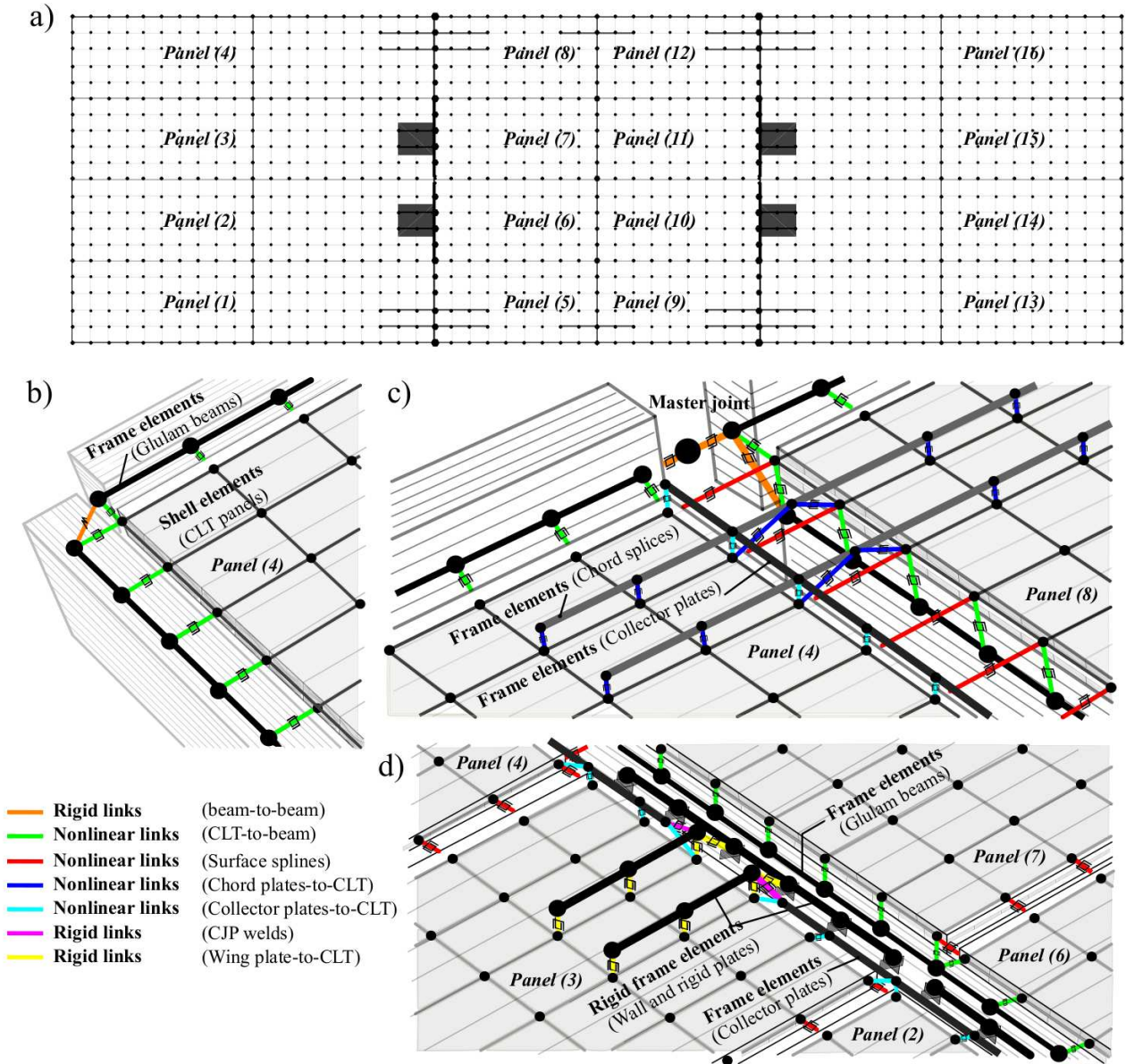


Figure 2.10: Two dimensional finite element model: (a) Mesh-refinement; (b) Beam-to-beam connection; (c) Chord splices; (d) Wall connection

2.4.3 Numerical model of diaphragm connections

The envelope curves used to model the connections assumed a rigid plateau associated to friction forces (F_{μ}) developed between members. These forces are dependent on the tributary weight

(W) and on the clamping forces (F_{cl}) applied when the screws were fastened, as suggested by Figure 2.11a. However, the values assumed for the clamping forces are uncertain given that the assemblage of the structure was performed without using any torque specification. In fact, the construction workers simply ensured that the joint or connector being fastened was tight to the surface and the fastener was fully installed. The friction force is computed as:

$$F_{\mu} = (W + F_{cl}) \cdot \mu \quad (2.1)$$

where W is the tributary weight transmitted associated to each node, F_{cl} is the clamping force, and μ is the friction coefficient. It is worth noting that surface-splines do not have any weight transmission associated. In the scope of the present work, two levels of Clamping Force (F_{cl}) were assumed, corresponding to 10 % and 20 % of the connections' yielding force (F_I). Additionally, three different levels of static friction coefficient were considered: 0.3, 0.4, and 0.5. When the applied force exceeds F_{μ} the model assumes the behavior of the connectors that are modeled with a multilinear constitutive law. Given the lack of experimental results for the connections used in the diaphragm studied, the values of stiffness and strength were based on the work performed by Closen (2017), where several shear connections were subjected to cyclic dynamic tests. The CLT panels used were produced with spruce-pine-fir (SPF) and the self tapping screws used were the MytiCon ASSY 3.0 ECOFAST Screw 16 - 80/50, with a smooth shank diameter equal to 5.8 mm ($d_s = 5.8$ mm). The results obtained experimentally were fitted by defining the points I to III, shown in Figure 2.11b. The correspondent force-deformation values used to define the envelope curve are presented in Table 2.2.

The determined force-deformation values had to be corrected, since the materials used in the diaphragm under study do not correspond to the exact materials used in the tests presented in Figure 2.11b. The differences found affect the slip modulus (strongly related with timber density) and yielding force of screws (strongly related to embedment strength of timber and screws yielding bending moment). In order to convert the force-deformation curve per screw obtained by Closen (2017) to an envelope curve able to represent the connections built in the diaphragm under study, two correction factors were established. The correction factor (λ_K) is used to adjust the stiffness as:

$$\lambda_K = \frac{K_{ser,con}}{K_{ser,dyn}} \quad (2.2)$$

where K_{ser} is the slip modulus prescribed in Eurocode 5 CEN (2005) for timber to wood based panels connections. Thus, $K_{ser,con}$ is the slip modulus obtained with the material properties used at the shake-table test, whereas $K_{ser,dyn}$ is the slip modulus computed with the properties of the material used in Closen (2017). The second correction factor (λ_F) is used to affect the strength properties obtained experimentally and it is given by the ratio:

$$\lambda_F = \frac{III_{s,con}}{III_{s,dyn}} \quad (2.3)$$

where III_s is the force associated to the failure mode that implies fastener yield in bending at one hinge and bearing-dominated yield of plywood fibers (side element) in contact with the fastener. This force was determined according to AWC (2015), with properties of the materials used at the shake-table test ($III_{s,con}$), and the properties of the materials used in Closen (2017) ($III_{s,dyn}$). The same approach was considered to compute the force-deformation response (per screw) associated to panel-to-beam connections and steel-to-CLT connections (chord splices and collector plates). The results obtained are shown in Table 2.2, where force-displacement values are presented for the notable nodes shown in Figure 2.11b.

Table 2.2: Constitutive law parameters for multi-linear plastic models (SAP 2000)

	F_I [N]	δ_I [mm]	K_I [N/mm]	F_{II} [N]	δ_{II} [mm]	K_{II} [N/mm]	F_{III} [N]	δ_{III} [mm]	K_{III} [N/mm]
Surface Splines ^a	963.8	1.4	700	3260.9	7.8	358.9	4458.6	27.2	61.7
Surface Splines ^b	1002.4	1.4	714	3391.3	7.9	366.1	4636.9	27.7	62.9
Chord Splices ^c	1831.2	1.3	1449.0	6195.7	7.1	742.9	8471.3	25.0	127.7
Panel over Beam ^d	2438.4	3.7	651.0	8250.1	21.2	333.8	11280.3	74.0	57.4

^a Experimental tests from Closen (2017)

^b Fastener: Simpson Strong - Tie 5.6 x 86 TRUSS/EWP PLY

^c Fastener: Simpson Strong - Tie 6.4 x 90 (SDS25312)

^d Fastener: Simpson Strong - Tie 5.6 x 200 (SDWS22800 LOG)

2.5 Nonlinear static analyses (pushover)

Load controlled nonlinear static analyses were performed, being the applied loads consistent with the accelerations measured experimentally and the tributary mass. All nodal loads were applied incrementally from zero to the full specified magnitude, which was equal to the inertial

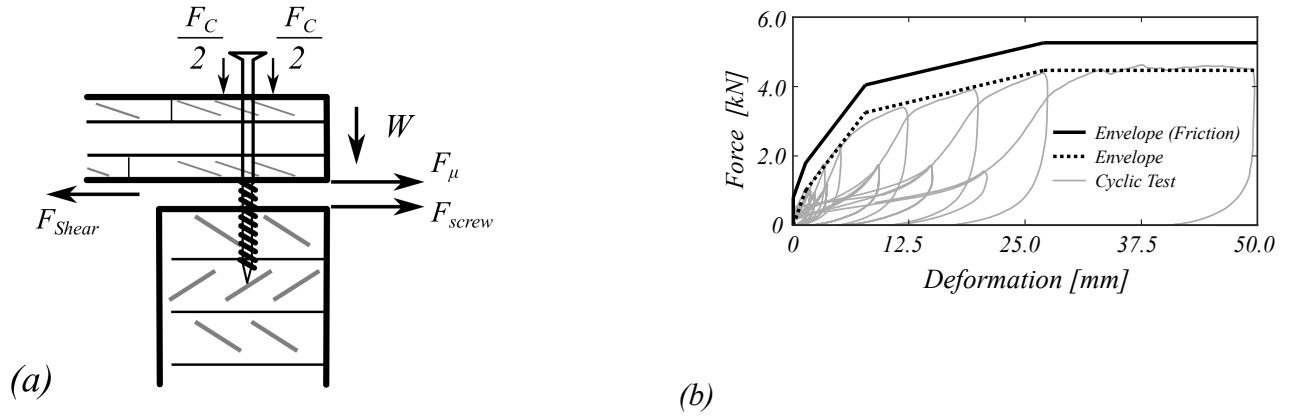


Figure 2.11: Numerical model features: (a) CLT-to-Beam friction scheme; (b) Envelope Curve for screws

load that results from the product of the tributary mass by the nodal acceleration obtained from the shake-table tests results.

Given the uncertainty associated to friction forces, the level of friction is deemed variable and object of a parametric study. On the other hand, the in-plane shear stiffness of the CLT panels was determined according to the theory proposed by Bogensperger et al. (2010) whereas the longitudinal stiffness was computed using the composite theory (H. Blaß & Fellmoser, 2004). Taking into account the uncertainty related to these variables, their impact on the diaphragm numerical results was studied by varying the Young modulus and the shear modulus of the Douglas-fir lumber used in the cross directions of the CLT panels.

A deformation diagram of the first level diaphragm is shown in Figure 2.12, where two different splines are indicated, namely SS1 and SS2. Those splines were the ones that demonstrated the highest demands on the pushover analysis. Thus, the experimental results of those connections are used to evaluate the effectiveness of the modeling approach in the following section.

2.5.1 Numerical Results

The numerical results presented refer to the two ground motion tests (6 and 19) scaled to the DBE hazard level and two ground motion tests scaled to the MCE (13 and 14) hazard level. The inertial forces were applied in agreement with the accelerations pattern shown in Figures 2.6b, 2.6c and 2.7b.

The evaluation of the numerical results focused first on the deformations of the different non-

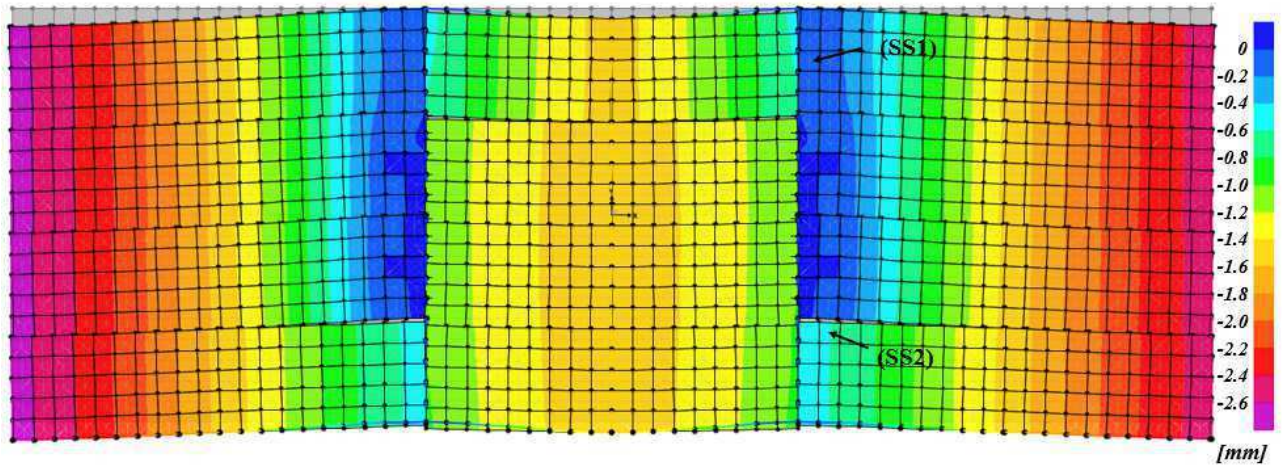


Figure 2.12: Deformation diagram at the first level diaphragm

linear links used to model surface splines and afterwards, on the stresses obtained for chord splices, by comparing them with the values measured experimentally and the ones assumed during the design phase.

The results obtained through a pushover analysis were compared with the deformations measured experimentally. The influence of friction is evaluated through a parametric study that considers two different variables: clamping force and friction coefficient. For clarification purposes, the henceforth nomenclature used is $C0XXFRYY$, where XX is the percentage of the force (F_I) used to model the clamping force ($C0$) and YY is related with the friction coefficient (FR) considered ($\mu=0.5$ corresponds to $YY = 05$).

In Figure 2.13, one can evaluate how the model captures the deformations experienced by the surface spline SS1 during the shake-table test. The model C020FR05 is able to capture the deformations that are perpendicular to the surface spline (Figure 2.13a and Figure 2.13b) and is the closest one in terms of sliding between panels (Figure 2.13b). It is important to refer that the forces presented are the ones sustained only by the connectors and consist on the resultant of both directions (parallel and perpendicular to the surface spline). Thus, the perpendicular force is considered only when the surface splines are in tension. In opposition, during the design phase, only the forces parallel to the spline that would be transferred from the center of the diaphragm to the walls were considered, as presented by the area highlighted in Figure 2.13. The design force presented in Figure 2.13c refers to the force per foot (304.8 mm), since the values presented for the numerical results are obtained according with link positions (every 304.8 mm). It is worth noting that the forces resisted exclusively by the fasteners decrease

considerably when the friction forces increase from model to model, as presented in Figures 2.13c and 2.13f. The maximum force obtained with the C020FR05 model, which approximates better the deformations measured, is 62 % lower than the one obtained with the model that neglects friction. The force obtained by the model without friction is 36.2 % lower than the design force considered for these tests (0.70 g). It is worth noting that the diaphragm was designed to resist an acceleration of 1.01 g for phase 3. Nevertheless, the results can be comparable since the earthquake-induced floor horizontal accelerations obtained experimentally were 0.90 g (test 13) and 0.84 g (test 14). Attending to the difference between numerical results and the load capacity, one can state that the design method produced a conservative solution for spline SS1.

Given the symmetry of the diaphragm, the numerical results obtained for SS2 can be compared with the experimental results measured on the the surface-spline positioned along the horizontal grid line [D] and comprehended between vertical grid lines [5] and [6] (Figure 2.9d). From the graphs presented in Figure 2.14, for the the horizontal surface spline (SS2), one can conclude that the model that better approximates the slip between panels differs from the model that captures their separation. This feature may indicate that different friction coefficients should be applied for perpendicular directions. The design force presented is equivalent to the shear flow resultant from the in-plane bending of the diaphragm. The acceleration used to compute the forces was 1.01 g (phase 3). Compared to the design value, the value obtained with the model without friction is 56.4 % lower in test (13). The model that best fits the experimental results (*C010FR03*) presents a reduction of 66.1% from the design value. The load capacity of the surface spline connection was 2.6 times higher than the one obtained numerically, as presented in Figure 2.14c and 2.14f.

In order to evaluate the efficiency of the method proposed, it is necessary to observe cases where the intensity of ground motion used is lower. Consequently, the pushover was applied considering the accelerations of test 6 (0.683 g) and 19 (0.620 g). Globally, the results presented in Figure 2.15, show a satisfactory compromise between numerical results and experimental data. It is worth noting that the measurements given by LP1N201 were not available during test 6. Thus, in Figure 2.15a it is not possible to compare the separation measured experimentally to the one obtained through the numerical model, at the end of surface spline SS1. This particular spline underwent a low value of sliding (0.02 mm) during test (6), being the numerical values 10 times higher. Nevertheless, the results obtained through the pushover analyses provide de-

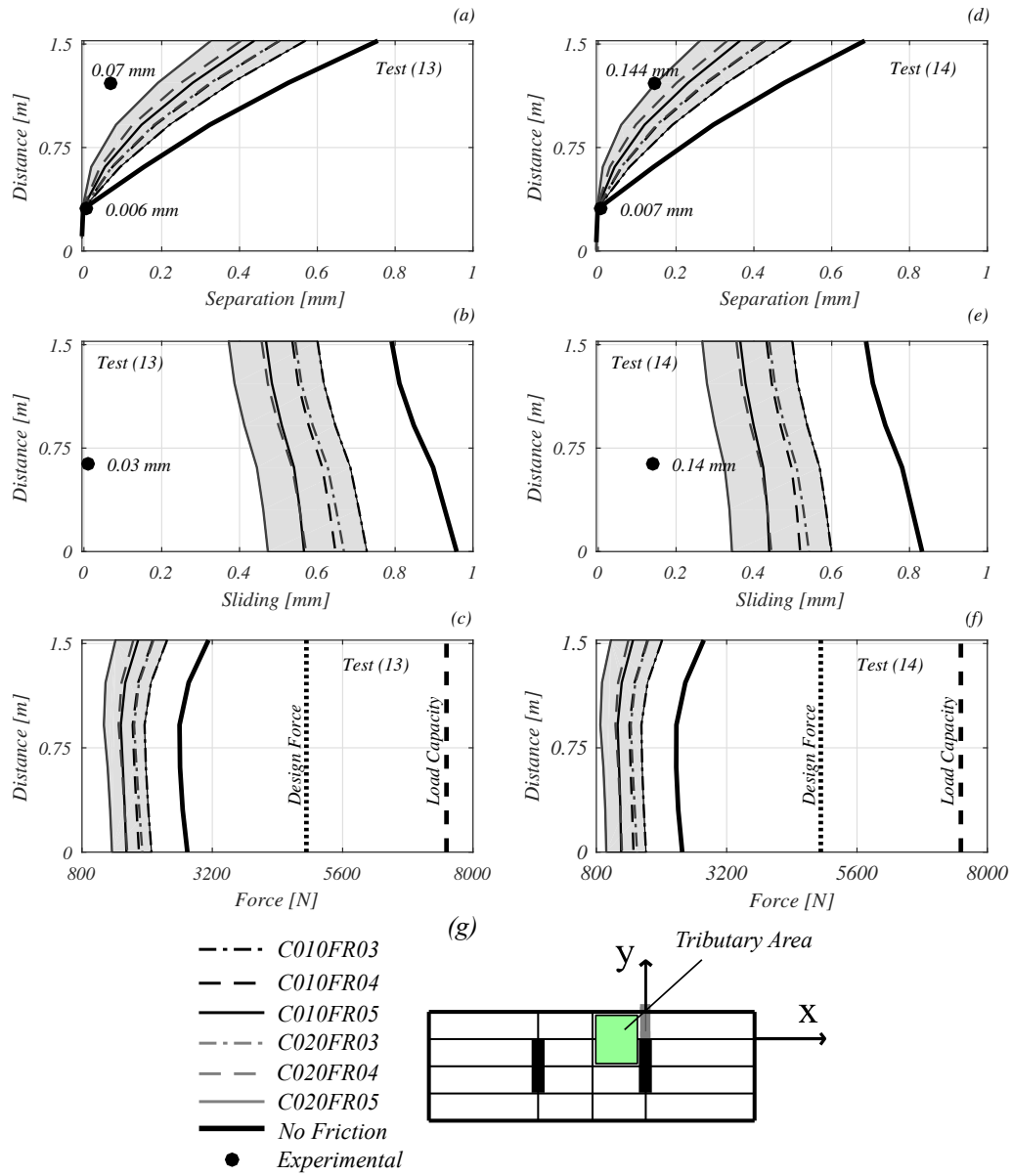


Figure 2.13: Numerical results for MCE hazard level earthquakes at surface spline SS1: (a) Separation - Test 13; (b) Sliding - Test 13; (c) Forces - Test 13; (d) Separation - Test 14; (e) Sliding - Test 14; (f) Forces - Test 14

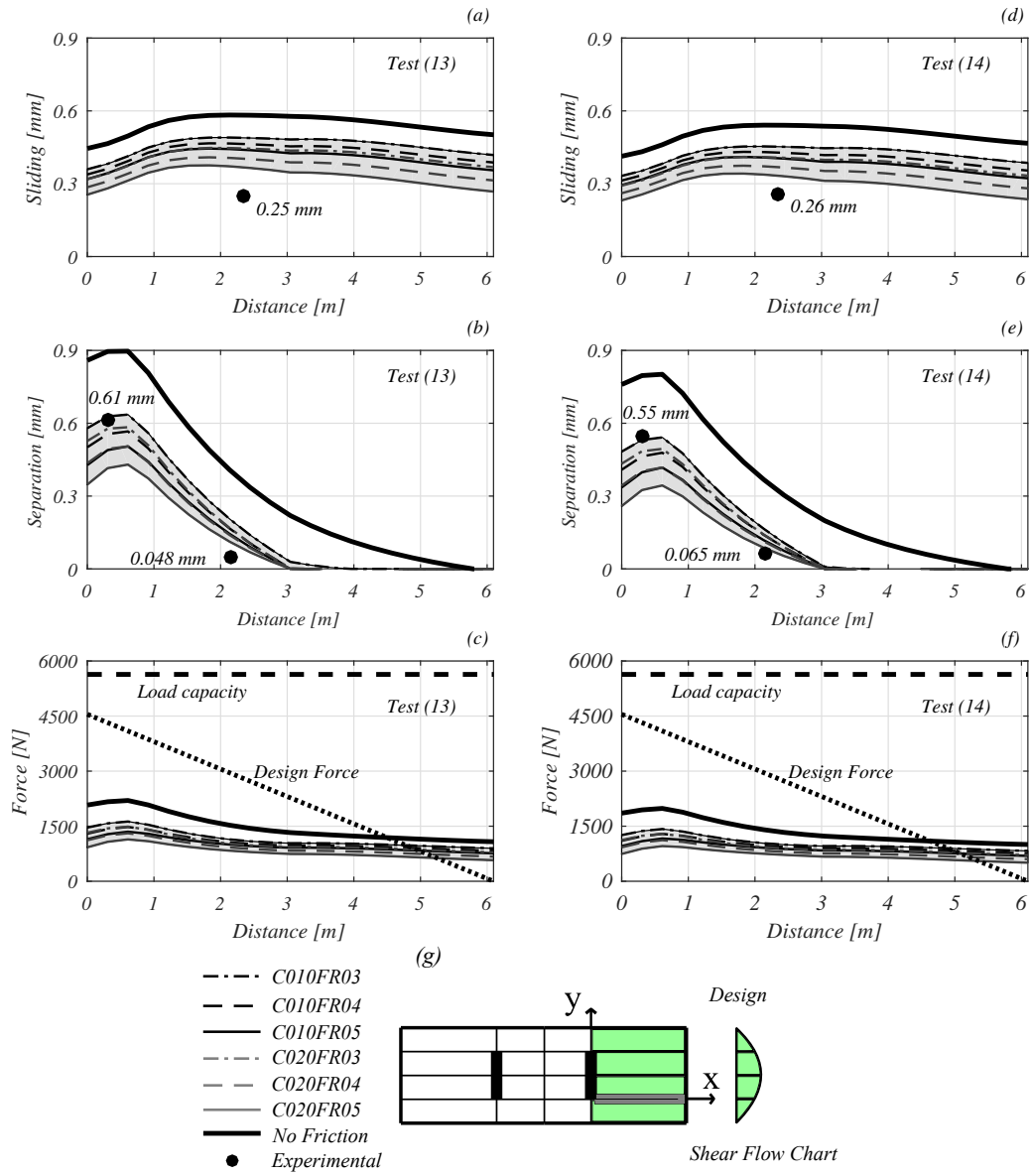


Figure 2.14: Numerical results for MCE hazard level earthquakes at surface spline SS2: (a) Sliding - Test 13; (b) Separation - Test 13; (c) Forces - Test 13; (d) Sliding - Test 14; (e) Separation - Test 14; (f) Forces - Test 14

formation values that are always higher than the ones observed during the tests. This indicates that the model provides always conservative results.

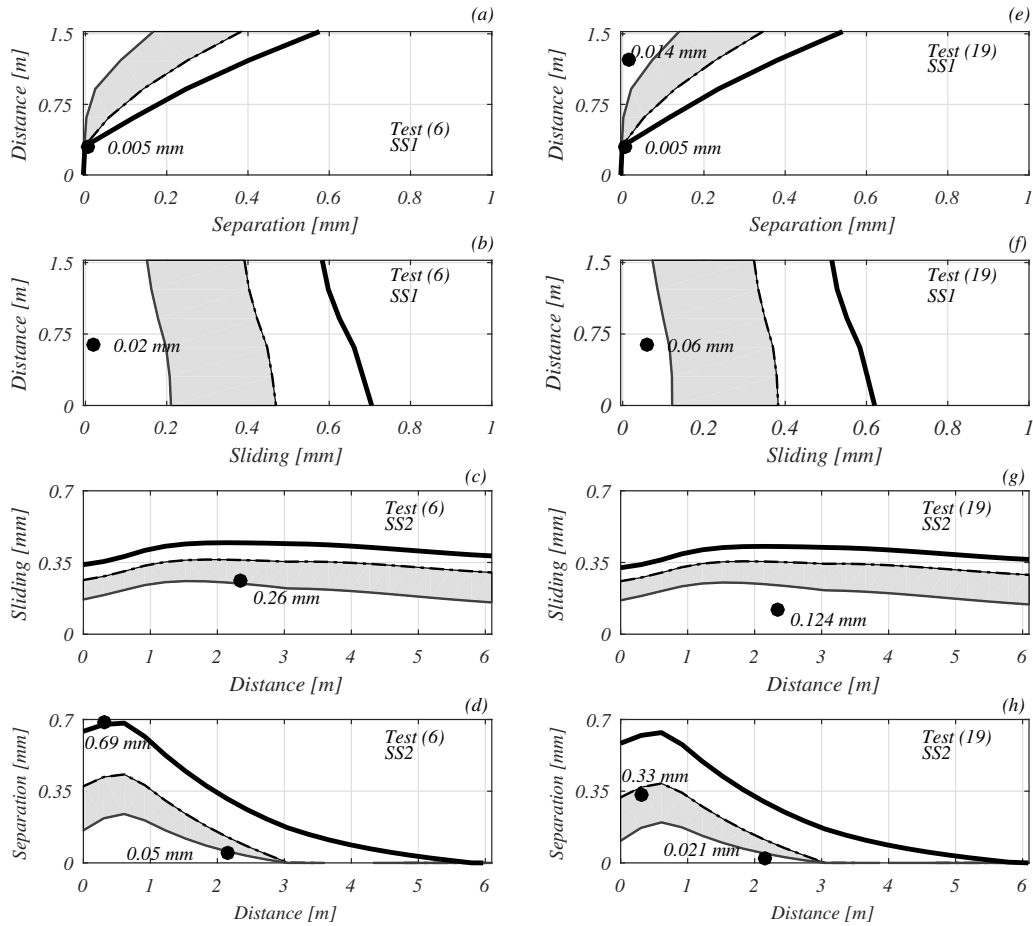


Figure 2.15: Numerical results for DBE hazard level earthquakes: (a) Separation at SS1 - Test 6; (b) Sliding at SS1 - Test 6; (c) Sliding at SS2 - Test 6; (d) Separation at SS2 - Test 6; (e) Separation at SS1 - Test 19; (f) Sliding at SS1 - Test 19; (g) Sliding at SS2 - Test 19; (h) Separation at SS2 - Test 19

The design of CLT diaphragms due to in-plane loading is influenced by their load-carrying capacity, rather than the analysis of their in-plane deformations. Consequently, the assessment of the forces applied on the surface splines are important. The consideration of variability, due to friction, resulted on a maximum coefficient of variation of 11% at surface-spline SS1. On the other hand, the coefficient of variation obtained for SS2 is equal to 7%.

2.5.2 Influence of in-plane stiffness values on surface splines

The method used here to compute the effective shear stiffness considers the superposition of shear deformations in the lamellae and in the crossing areas (Bogensperger et al., 2010). It

also includes coefficients calibrated through finite element analysis, to account for the number of boards used in CLT panels. The longitudinal elastic modulus for the shell elements was determined according to the composite theory provided in H. Blaß and Fellmoser (2004). Consequently, the elastic properties of shell elements may be a source of uncertainty on the global diaphragm behavior and also on the local response of connections. It is not evident that a panel with a high longitudinal elastic modulus has also a high shear stiffness, given its dependency on the cross layers interface slip modulus. Thus, a parametric study was performed to evaluate the influence of different combinations of stiffness properties on the numerical results of surface splines SS1 and SS2. The variability was imposed to the Douglas-fir elastic modulus, in both directions, and to the shear modulus of the wood lamellae. The values used refer to the mean values, as well as, the 5th and 95th percentiles. In order to compute these percentiles, a coefficient of variation (CoV) equal to 13 % was considered as recommended in Köhler et al. (2007) for Nordic Spruce species. Two numerical models were used as reference, namely *C010FR03* and *C020FR05*, in order to address the influence of combining variability in stiffness and in friction. The results regarding the stiffness properties parametric study are shown in Figure 2.16.

As presented in Figures 2.16b and 2.16e, the separation between adjacent panels was not affected by the variability in lumber properties. In turn, it is possible to see an influence on sliding (Figures 2.16a and 2.16d), which causes deviations in terms of forces carried by connectors. Regarding surface spline SS1, it is possible to conclude that higher values of shear modulus and elastic modulus conduct to higher values of forces. The opposite occurs at surface-spline SS2, where higher forces were obtained when the 5th percentile value was assigned to shear modulus and elastic modulus.

The variability assigned to the elastic properties of panels had a very low influence on the forces applied on the surface splines. The forces obtained at surface-spline SS2 had a maximum coefficient of variation of 2.35 %, while the value for surface-spline SS1 was equal to 4 %. Comparing to the results obtained when variability is applied to friction, in-plane stiffness variability has a low influence on the design of fasteners.

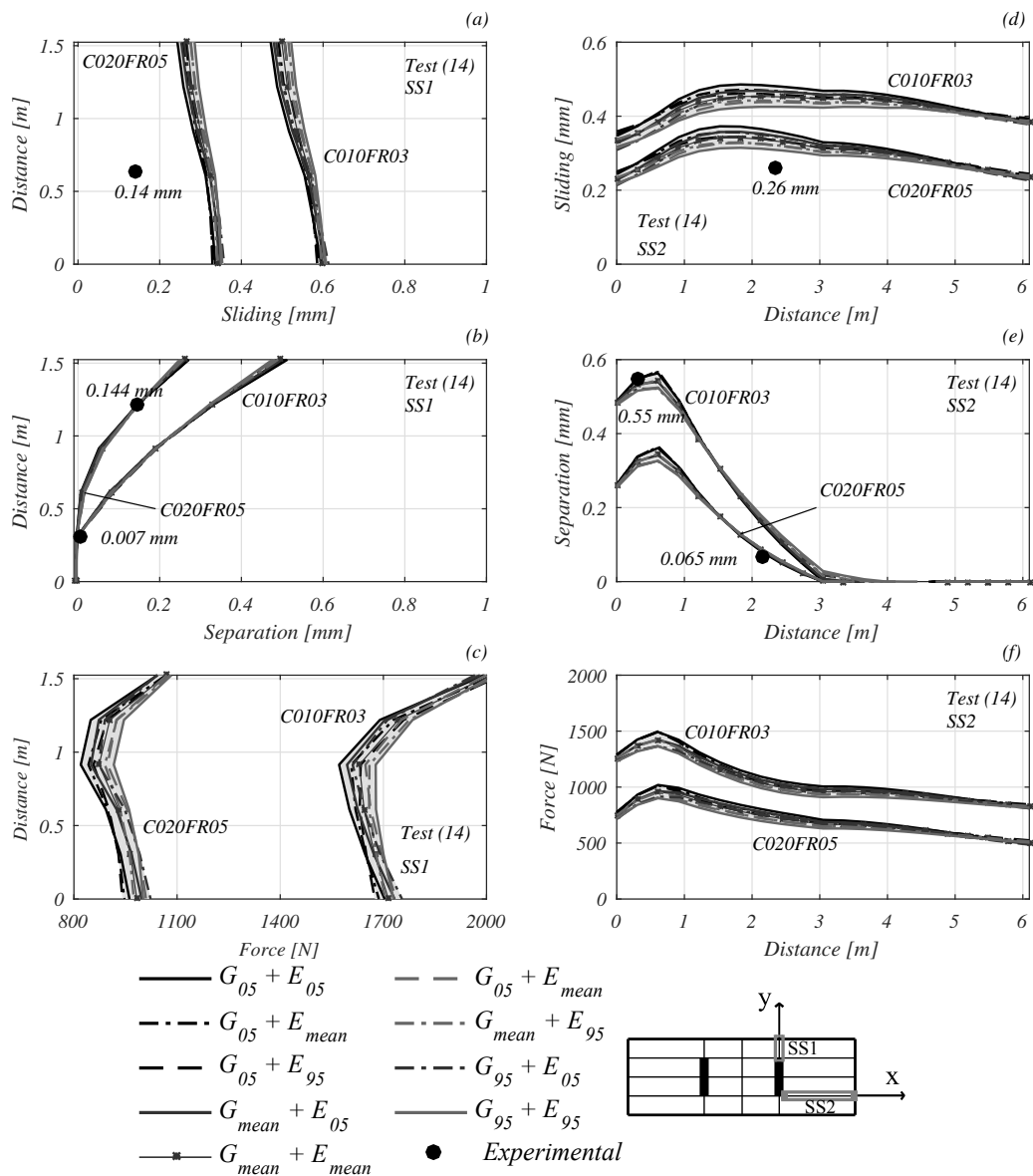


Figure 2.16: Impact of elastic modulus variability and shear modulus variability on numerical results of surface splines: (a) Sliding at SS1; (b) Separation at SS1; (c) Forces at SS1; (d) Sliding at SS2; (e) Separation at SS2; (f) Forces at SS2

2.5.3 Chord splices results

During the shake-table tests, it was possible to evaluate the response of different chord splices through strain gauges that were installed at the steel plates' top surfaces. In the scope of the present chapter, the chord splice studied is the one that connects panels 12 and 16, as presented in Figure 2.4a. Each steel plate had a strain gauge glued at the geometric center of the plate to measure the longitudinal strains. Through the application of Hooke's law, the stresses were calculated considering the elastic modulus of ASTM A36 steel (200 GPa). The peak stresses are presented in Table 2.3 for the DBE and MCE tests that were used to perform the numerical analysis. The occurrence of rocking at the walls led to uplift movements between panels 12 and 16, since the wall-to-diaphragm connection was made only on the cantilever side. Consequently, the strains measured can result from axial forces and bending moments. Unfortunately, the instrumentation used did not allow to decouple these effects.

In the 2D numerical model used in the analyses, the linear elastic frame elements representing the steel plates are also subjected to axial forces and bending moments but solely in-plane. The uplift movements could be captured if a 3D model was used to study the structural behavior. In addition, since the strain gauge was placed on the neutral axis of the plate, the experimental results presented in Table 2.3 can be compared only with the stresses related to axial forces. As previously mentioned, only two frames were used to model the three plates under analysis. Through the results presented in Table 2.3, it is also possible to compare the experimental values with the values that are obtained by the application of the design method, using the average peak accelerations given in Table 2.1.

The values computed through the pushover analysis present significant discrepancies in comparison to the experimental values. In particular, one can observe that the values obtained with the design method are the most conservative ones. During the design, the contribution of the surface splines, positioned below the steel plates, as presented in Figure 2.4, was neglected, which conducts to an overestimation of the chord forces.

Table 2.3: Longitudinal stresses of steel plates of a chord splice at 1st floor

^a Method used in the design was applied considering the average peak acceleration of 1st level diaphragm										
T - Top plate										
M - Middle plate										
B - Bottom plate										
Test (ID)	Experimental		Design Method ^a		Numerical (No Friction)		Numerical (C010FR03)		Numerical (C020FR05)	
	Plate	σ [MPa]	Plate	σ [MPa]	Plate	σ [MPa]	Plate	σ [MPa]	Plate	σ [MPa]
(6)	T	23.6	T	44.0	T	9.9	T	8.3	T	8.6
	M	19.9	M	44.0	-	-	-	-	-	-
	B	22.5	B	44.0	B	6.2	B	5.5	B	7.0
(13)	T	61.8	T	58.0	T	13.3	T	11.5	T	11.2
	M	42.1	M	58.0	-	-	-	-	-	-
	B	36.1	B	58.0	B	8.2	B	7.5	B	8.5
(14)	T	51.4	T	54.1	T	12.5	T	10.3	T	10.2
	M	35.5	M	54.1	-	-	-	-	-	-
	B	35.1	B	54.1	B	7.8	B	6.8	B	8.0
(19)	T	26.4	T	39.9	T	9.6	T	7.7	T	8.2
	M	22.2	M	39.9	-	-	-	-	-	-
	B	17.4	B	39.9	B	6.0	B	5.2	B	6.3

2.6 Final Remarks

A numerical modeling strategy was presented in this chapter for the design of CLT diaphragms to earthquake loads. The satisfactory results obtained in terms of displacements and the model's capability to capture the most important phenomena regarding connections' response prove its feasibility and accuracy. In this way, the model constitutes a good alternative to simplified methodologies applied during the design phase. Since a structural engineer must find a compromise between numerical efficiency and tight schedules, the time and effort associated with developing the numerical model also weighs on the choice of design method. Although an experienced user of finite element model software can handle most of the features proposed in this chapter, the definition of all the special joints and zero-length elements can be a time consuming task that might hinder the usage of this methodology in structural design projects.

Future studies must concentrate on keeping model reliability while decreasing the effort expended in including crucial behaviors such as panels' closure in surface spline connections. For instance, the solution proposed by Breneman et al. (2016), where the connection zones are modeled with 2D shell elements with distinct properties of the CLT panels, already constitutes a good step in this direction. Further investigations should be carried out in order to evaluate and validate such proposal with experimental results, keeping in mind that it as to provide different behavior for perpendicular directions.

Regarding the modeling strategy presented in this chapter, the application of the model without

friction is suggested as a less demanding option. This model ensures a good compromise between accuracy and development effort, providing values of design forces higher than the ones obtained from models with friction (more accurate models), and therefore more conservative, but lower than the values obtained from the simplified design methods.

2.7 Conclusions

The seismic performance of a CLT diaphragm and a CLT-concrete diaphragm was studied in this work through shake-table tests performed on a two-story full-scale mass-timber building at UCSD San Diego facilities in July 2017. Distinct lateral resisting systems were tested: (i) post-tensioned rocking walls; (ii) non-tensioned rocking walls; and (iii) stacked CLT walls connected with shear anchors and rod hold-downs.

The accelerations induced at each diaphragm level were evaluated for each structural system considering three hazard levels: (i) Service Level Earthquake (SLE); (ii) Design Basis Earthquake (DBE); and (iii) Maximum Considered Earthquake (MCE). From the results observed, the method proposed in ASCE 7-16 (Ghosh, 2016) provides an approximate distribution in height of the floor horizontal accelerations, when conventional stacked wall systems are in use (Phase 3). Nevertheless, it failed to predict the floor horizontal accelerations for the self-centering CLT rocking wall systems tested. During phase 1 and phase 2, the CLT wall panels started to experience rocking movements with the increase in ground motions intensity (DBE and MCE), causing a shift on the fundamental period and a reduction on the dynamic response at both story levels.

The experimental results confirmed that the composite CLT-concrete solution is able to guarantee a quasi uniform in-plane distribution of the accelerations, contrary to the response demonstrated by the solution built only with CLT panels. The majority of its responses were characterized by uniform accelerations at the central core of the diaphragm and higher acceleration at the cantilever extremes. Nevertheless, the relative displacements recorded during the ground motion tests revealed that the connections responded in the elastic range according to the objectives of the design.

The peak response of different earthquake tests were captured through nonlinear static analyses

that applied nodal loads incrementally from zero to the full specified magnitude. The loads were determined considering the material weights and the accelerations measured *in situ*. A phenomenological computational model approach was proposed and validated by comparing experimental and numerical peak deformations of the diaphragm built at the first floor level of the building, when it was connected to rocking wall systems. The modeling strategy made use of SAP 2000 interactive editing feature allowing to represent the different connections built on the diaphragm. The zero-length elements used to model the connections were calibrated according to recent test results. The influence of friction was also studied by assuming a rigid behavior of the connections until the static friction force was reached. A parametric study was performed, considering different clamping forces and distinct friction coefficients. The main observations from this part of the work were:

- The consideration of friction allows to capture accurately the surface splines peak deformations resultant from the ground shaking;
- A conservative design is reached when friction is neglected. The model with the highest friction coefficient as well as the highest clamping forces produces a maximum spline force that is 62 % lower than the one obtained with the model that neglects friction;
- The variability assumed for friction forces resulted on surface-spline forces with a coefficient of variation equal to 11 %.

The design values assumed for surface splines are considerably higher than the ones obtained through the several nonlinear static analyses performed. Although, model development might be time consuming, it produces reliable results and can be used for design purposes. Time and effort can be reduced if the engineer neglects to include friction in the model, since it provides conservative design forces.

Regarding the chord splices, the numerical outcomes present a major difference relatively to the experimental ones. These results can be influenced by the following aspects:

- The contribution of surface splines were not considered when designing the chord splices, which results on a overestimation of the forces;

- The occurrence of wall rocking at their base may cause uplift between adjacent panels at the diaphragm. These occurrence may originate normal stresses due to bending of the steel plates. This behavior is not captured through the two-dimensional model proposed in this work.

The influence of in-plane stiffness properties was addressed by combining independently the mean value, and the 5 % and the 95 % percentiles of the elastic modulus and shear modulus of the lumber. The results indicate that the responses in terms of surface-spline forces present low (4 %) coefficients of variation.

The modelling approach presented allows to reproduce with accuracy the experimental results obtained through the shake-table tests. Nevertheless, there is room for improvements by considering different behaviors for perpendicular directions, both in terms of strength and stiffness properties of the connections and also regarding the friction coefficients. Future research may include the definition of torque specifications for fasteners installation, as performed in steel structures, in order to improve the accuracy in terms of clamping forces. The finite element model construction can be cumbersome for inexperienced users. However, it allows to consider different mechanisms that are neglected by simplified design methodologies. The present model can be included in a 3D model that includes the wall panels and respective connections. This would improve the understating of the combined wall-diaphragm behavior through the performance of nonlinear dynamic analyses.

Chapter 3

Seismic assessment of a heavy-timber frame structure

3.1 Introduction

The performance of timber structures under intense earthquake ground shaking depends strongly on the type of failure modes, and in particular, their ductility (H. Blaß et al., 1994). The failure of timber elements is usually brittle, whereas the failure of connections between timber elements can be ductile. Design recommendations for timber structures focus mainly on the formation of inelastic deformations on connections by increasing the slenderness of connectors, guaranteeing that failure occurs after yielding of the connectors, and thus enhancing the capacity of joints to withstand large inelastic deformations without rupture. The common analyses methods for the design of multi-story timber buildings in seismic regions do not consider explicitly the inelastic behavior of joints. Since nonlinear dynamic analyses are time consuming and imply high computational efforts, it is common for practicing engineers to design timber framed structures through static analyses, simplified dynamic analyses (or equivalent static), and multi-modal response spectrum analyses (Foliente, 1997).

During the design of timber structures, according to Eurocode 8 (EC8) (CEN, 2013b), the capacity of a specific structure to dissipate energy is taken into account by considering a behavior factor q , which affects seismic loads by reducing the linear elastic seismic response spectrum. The q -factors considered in EC8 are prescribed considering three classes of ductility: low (DCL),

medium (DCM), and high (DCH). Such levels are dependent on the structural typologies and their local and global ductility. The q -factor is a function of the ductility of the structure, which depends on its redundancy and the ductility of elements and connections. Local ductility is associated with the capacity of joints to undergo large deformations without failure. Large displacements can be developed in connections when slender dowels are used and adequate detailing is provided to prevent brittle failure modes such as splitting. Global ductility is related to the ability of the structural system to remain stable, exploiting its redundancy, after yielding of the joints (Jorissen & Fragiaco, 2011). These principles can lead to a reserve in strength and ductility while preventing significant structural damage.

According to Fajfar (1996) the behavior factor q is dependent on the ductility factor, R_μ , which represents the dissipative capacity of a structure, and the so-called overstrength, R_Ω , defined as the ratio of the actual strength to the design strength. Miranda and Bertero (1994) provided a basic definition of the ductility factor R_μ while reporting the influence of specific elements on its value. In Vidic et al. (1994) and Miranda and Bertero (1994) it is suggested that the ductility factor depends on the principal elastic period of the structure and the type of soil. On the other hand, several authors, including Mitchell and Paultre (1994), Humar and Rahgozar (1996), and R. Park (1996), provided discussions regarding the inclusion of overstrength values in the design of structures. These contributions are the basis of the overstrength factors used to compute the behavior factor q prescribed in the present seismic design codes.

Contrary to what happens in the case of steel and reinforced concrete structures, the q -factor values suggested in EC8 for timber structures do not account for the overstrength factor and structural particularities (e.g connection types). On the other hand, only the more common timber building systems are mentioned in EC8, which means that there is an absence of values regarding innovative systems such as the ones consisting of heavy-timber frame structures built with cross-laminated timber (CLT) or moment resisting frames. Nevertheless, the contributions of several authors, including Andreolli et al. (2011), Ceccotti et al. (2013) and Gavric et al. (2015), have provided studies on ductility and overstrength properties of innovative structural systems that make use of CLT. For example, in Ceccotti et al. (2013), the behavior factor q of a seven-story full-scale CLT building was computed. The approach used to calculate the q -factor was proposed by Ceccotti and Sandhaas (2010), where the q -factor is given by the ratio of the peak-ground acceleration (PGA) observed in full-scale tests, for a previously defined near-

collapse state, and corresponding PGA used in the design. A mixed analytical-experimental procedure was presented in Pozza (2013), by exploiting the results of cyclic tests, which was applied to several building typologies. The procedure proposed in Pozza (2013) combines quasi-static pushover tests of representative walls and analytical models to establish capacity curves. In this study, the q -factor is given by the ratio between the peak-ground acceleration of the ultimate spectra and the yielding spectra (Fajfar, 1996).

Despite the remarkable results obtained so far, there is an absence of studies where material uncertainties are considered to compute the ductility properties of timber structures. Timber as a natural material presents a high variability in its mechanical properties (Faber et al., 2011), which contributes directly to an increase in the uncertainties associated with the expected strength and peak drift capacities of timber structures. Therefore, it is crucial to develop studies that account for material uncertainties as well as the uncertainties associated with the seismic loading (Foliente, 1997).

3.1.1 Numerical modeling of cyclic behavior of timber connections

The numerical models available in the literature for modeling steel connections in timber structures can be classified into three levels, ranging from micro-level to macro-level. In micro-scale models the hysteresis deformation of single connectors is modeled (Foschi, 2000). The meso-models simulate the behavior of entire connections built with several fasteners (Rinaldin et al., 2013). Macro-scale models can be used to represent the behavior of wood shear walls (Dean et al., 1986), diaphragms (Falk & Itani, 1989) or complete structures themselves (Foliente, 1995). To analyze moment-resisting timber frame structures under dynamic loads, meso-level models can be used to capture the behavior of connections and timber elements without disproportionate computational costs. These meso-level models include the use of nonlinear springs that capture the macro response of connections and linear beam-column elements for the structural members.

Laboratory test results are essential to calibrate numerical models and assess their adequacy to capture the degradation modes exhibited by moment-resisting joints. The experimental tests presented in the literature show that the cyclic response of such connections often present a pinched behavior with stiffness and strength degradation (e.g. Folz and Filiatrault (2004), Chui

and Li (2005), Polastri et al. (2013)). Consequently, the numerical model used to represent the joints must incorporate these features to reproduce the expected progressive weakening of timber structures due to strong ground motions. The degradation modes observed in timber moment-resisting joints, used in heavy timber structures, share many similarities with those observed in reinforced concrete and steel structures allowing the use of models originally developed for other materials, such as the ones in Foliente and Mohammad (1996); Ibarra, Medina, and Krawinkler (2005).

The main challenge in modeling the connection behavior consists in choosing a hysteretic model and in the calibration of the associated model parameters. The Open System for Earthquake Engineering Simulation (OpenSees) finite element platform (McKenna et al., 2009) includes several hysteretic models that have already been used to model the cyclic behavior of timber connections and structural systems. The Bouc-Wen-Baber Noori (BWBN) model was used by Foliente (1995) to generate a general hysteresis model for wood joints and structural systems, incorporating stiffness and strength degradation with pinching effect. A more general phenomenological model that captures the pinched cyclic strength and stiffness degradation of plywood panels was developed in Ibarra et al. (2005). Another model that can be used to represent the pinched hysteretic response of timber connections is a beam-column joint model proposed by Lowes et al. (2003), which was implemented in OpenSees as *Pinching4* force-deformation model. Although originally developed to simulate reinforced concrete beam-column joints, *Pinching4* was also used to perform a seismic reliability analysis of a Timber-Steel-Hybrid-System X. Zhang et al. (2015) due to its ability to represent a pinched load-deformation response and to enable three modes of cyclic degradation: unloading stiffness degradation, reloading stiffness degradation, and strength degradation.

Despite the lack of a database of experimental results for moment-resisting connections between timber elements, existing experimental results indicate that these connections are able to dissipate energy during cyclic tests without significant strength reduction. One of possible moment-resisting connections in timber frame structures is known as the ring-type doweled connection. Bouchair, Racher, and Bocquet (2007) studied the distribution of loads among fasteners of a ring-type doweled connection and compared theoretical results with experimental monotonic tests in terms of stiffness and strength properties. Ring-doweled joints were also the subject of an experimental campaign (Polastri et al., 2013) that comprised monotonic and

cyclic reversal tests to study the effectiveness of different joint patterns and their capacity to satisfy the criteria for DCH structures presented in EC8. One of the joint patterns studied in Polastri et al. (2013) is used to calibrate the analytical model presented in this chapter.

Using a bilinear model, Polastri (2010) characterized the q -factor for structures built with ring-doweled moment connections. However, the work in Polastri (2010) did not account for strength and stiffness degradation nor material uncertainties, which could be important to account for uncertainty in the capacity of connections.

3.1.2 Fragility curves for timber structures

A fragility curve is a conditional distribution of the probability of exceeding a specific threshold (e.g. drift, damage, or collapse) as a function of one or more hazard intensity measures (e.g. peak-ground acceleration, spectral acceleration at a fundamental period of the structure). In essence, a fragility curve F_R is defined as the conditional probability of the structural demand parameter (DMP) exceeding the structural capacity (SC) for a given level of intensity measure (IM) of the hazard :

$$F_R = P[DMP > SC|IM] \quad (3.1)$$

Fragility curves can be developed using four different approaches: expert judgment, empirical methods, analytical methods, or hybrid methods that combine in some form the first three approaches (Porter, 2015). Fragility curves are commonly assumed to follow a lognormal cumulative distribution function (e.g. Rosowsky and Ellingwood (2002), Porter et al. (2007), Baker (2015)). The parameters of analytical fragility functions can be determined through different methods. Monte-Carlo simulation is the most widely used method due to its simplicity and robustness. For this, samples of the random variables are generated from their joint probabilistic distributions. The limit state function considered is evaluated for each realization that is treated as a deterministic quantity (Rubinstein & Kroese, 2011). In order to achieve a robust fragility function, it is necessary to perform a considerable number of numerical simulations, which, when combined with nonlinear finite element models, may require very high computational efforts. Such drawbacks can be partially overcome by using efficient sampling methods

such as Latin Hypercube Sampling (Melchers, 1999) or other methods described in Baker (2015).

To assess the response of light-frame timber constructions, several seismic fragility analyses are available in the literature (e.g. Lee and Rosowsky (2006), van de Lindt and Dao (2009), Sutley and van de Lindt (2016)). Seismic fragility curves for shear wall systems, typically found in residential construction were developed by Li and Ellingwood (2007) for three performance levels, including Immediate Occupancy (IO), Life Safety (LS), and Collapse Prevention (CP). The authors considered both demand and capacity related uncertainties, accounting for record-to-record variability due to ground motion accelerogram amplitude and phasing and the effect of openings in the shear walls, known as SAWS. The variability of strength, stiffness, and various hysteretic parameters of a macro-model (Folz & Filiatrault, 2001) were considered in Yin and Li (2010). In Yin and Li (2010), the impact of aleatoric and epistemic uncertainties on the fragility functions was evaluated. However, the study only considered typical one-story residential buildings with reduced collapse risk.

Even though extensive work has been performed to develop fragility curves for light-frame constructions, limited research has focused on the development of fragility curves for heavy-timber structures, and especially for those designed with ring-doweled moment resisting connections (Rodrigues et al., 2018).

3.1.3 Objectives

The main objective of this chapter is to evaluate the performance of heavy-timber structures designed with ring-doweled moment resisting beam-column connections. The performance is evaluated based on characterization of the behavior factor q using a large number of nonlinear structural analyses, which account for uncertainty in mechanical properties of members and connections. This chapter involves the use of pushover analyses and multi-record incremental dynamic analyses (Vamvatsikos & Cornell, 2002), where nonlinear analytical models account for the post-yielding behavior of calibrated moment-rotation connections models. Secondary objectives of this chapter are the definition of interstory drift limit states, assessment of the distribution of q -factors, and the development of fragility curves for different damage state levels, including IO, LS, CP, and Global Collapse (GC) accounting for both material and

seismic loading uncertainties.

3.2 Methodology

A three-story timber moment-resisting frame designed with ring-doweled connections is used as a case study in this chapter. The structure had been designed in Callegari (2009) and was here re-checked using a modal response spectrum analysis, following Eurocode 8 (EC8) (CEN, 2013b) and Eurocode 5 (EC5) (CEN, 2005), for a site located in Lisbon, Portugal. The structure was designed to verify the requirements for a DCH structure according to EC8.

The assessment of the q -factor and the fragility curves involves the use of nonlinear static and nonlinear dynamic analyses. The analytical models were built in OpenSees (McKenna et al., 2009), using meso-level connections models that incorporate strength and stiffness degradation under cyclic loads.

In the nonlinear finite element model development, the first task included fitting a constitutive moment-rotation model to capture the fully reversal cyclic experimental results in Polastri et al. (2013). The constitutive model selected was the *Pinching4* model. Considering the designed structure, all numerical analyses account for uncertainties in the member mechanical properties and material parameters that influence the strength and stiffness behavior of the connections (yielding moment and elastic stiffness). Uncertainties in the post-yielding behavior of moment-resisting connections were also considered by varying the parameters used to define the envelope curve of the *Pinching4* model. It is worth noting that the variability of the member properties also affect the strength and stiffness parameters of the moment-rotation model used for the connections, thereby having a direct impact on the dynamic properties of the structure and consequently their response when subjected to ground shaking. The Latin Hypercube Sampling (LHS) was used in this study to generate a set of 1000 structural models, in which each structural model corresponds to a realization of the random variables used to define the structural model. Using the correlation matrix proposed in the Probabilistic Model Code (PMC) (Köhler et al., 2007), intra-element and inter-element correlation of the member properties was considered. Moreover, inter-element correlation was also assumed. More details are provided in section 3.

To address the impact of modeling uncertainties, two structural models considering median parameters and design parameters were subjected to the same analysis, for comparison purposes. Henceforth, these structural models will be denominated as "median structure" and "design structure", respectively. It is worth noting that there is no spatial variability of members and connections properties on both median structure and design structure. Moreover, it is important to stress that the post-yielding rotations of the design structure were computed considering the characteristic value of the parameters used to define the envelope curve of the *Pinching4* model.

Displacement controlled nonlinear static pushover analyses were performed in order to assess the impact of modeling uncertainties on the q -factor and on the seismic resistance of the timber moment-frame and to define damage state levels. The lateral load distribution, for each structural model, is based on the the first vibration mode configuration of that specific structural model realization. A vector of lateral loads $\{p_i\}$ were applied at floor level i , as:

$$\{p_i\} = \{M\} \{\phi_i\} \quad (3.2)$$

where $\{M\}$ is the lumped mass matrix, and $\{\phi_i\}$ is the normalized first mode nodal displacements. The lumped masses are assigned to the points coincident with the intersections between beams and columns, at each floor level. The control node is positioned at the roof and a displacement increment of 0.001 m is considered at each analysis step.

The seismic loading uncertainties were combined with the modeling uncertainties performing an IDA study for the set of analytical models generated with LHS method. Henceforth, this set of analytical models will be designated as "structural set". An IDA study is accelerogram and structural model specific (Vamvatsikos & Cornell, 2002). It consists in subjecting a structural model to an accelerogram of increasing intensity. Consequently, it is necessary to consider several accelerograms to account for ground motion record-to-record variability. The records used are selected in section 3.3. The intensity measure (IM) adopted was the "first mode" spectral acceleration ($S_a(T_1, 2\%)$) and the engineering demand parameter (DMP) chosen was the peak interstory drift ratio. The selection of $S_a(T_1)$ as an IM follows suggestions by Shome (1999) and Baker and Jayaram (2008). Other authors have also provided discussions on the topic, including Barbosa (2011), Faggella et al. (2013), Mollaioli et al. (2013), and Donaire-Ávila,

Mollaioli, Lucchini, and Benavent-Climent (2015) and have shown that $S_a(T_1)$ corresponds to a good predictor of the structural response, both for linear and nonlinear response.

During an IDA, the global collapse of a structural model is related with dynamic instability. In this thesis, it is assumed that an IDA curve reached dynamic instability when its slope is lower than 20% of the initial (elastic) curve (Vamvatsikos & Cornell, 2002).

The total number of IDA curves developed corresponds to the product of the number of models in the structural set ($N_{Sim} = 1000$) and the number of ground motion records considered ($N_{GMR} = 24$). Considering approximately 30 intensity levels, the total number of nonlinear dynamic analyses performed was approximately 720,000. To reduce computational time, a sequential version of OpenSees and a batch-queue system called HTCCondor (v7.8.0) was used Ribeiro et al. (2014). From the results obtained from multi-record IDA, the variability of structural responses due to both epistemic and aleatoric uncertainties was thus evaluated. The effect of considering modeling uncertainties was also assessed by comparing the results of the structural set with the results obtained for a structure in which the median parameters were assigned for mechanical properties of members and connections.

Damage state levels were defined using the peak interstory drift ratio as the limit state parameter, which is tied to the behavior of the moment-resisting connections or the building capacity curve, which is defined as the base-shear versus roof displacement. It is assumed that the IO damage state is reached when any connection exceeds the yielding point. In turn, the LS damage state is reached when any connection exceeds the deformation associated with the capping point. Finally, it is assumed that the CP damage state is reached when the descending branch of the building capacity curve passes below 80% of the peak building strength capacity. The GC damage state is exceeded when an IDA curve reaches dynamic instability.

Fragility functions were defined for different damage state levels, based on the multi-record incremental dynamic analysis. These fragility functions were obtained by fitting a lognormal distribution to the values of intensity measure (spectral acceleration) that caused the exceedance of a predefined demand threshold values associated with different damage state levels (IO, LS and CP) considered. In addition, the impact of modeling uncertainties on the GC damage state fragility curves is evaluated. Moreover, incremental dynamic analysis and fragility curves were analyzed for different q -factor levels. A disaggregation process, which consists in aggregating the structural models according to their values of measured q -factors, was followed by the

analysis of the common incremental dynamic analysis and fragility curves in each group.

3.3 Case study: A three-story heavy-timber frame building

3.3.1 Description of the structure

The structure under analysis is a residential three-story timber building designed using GL24h elements. The GL24h correspond to glued laminated timber with materials defined per EN14080 (CEN, 2013a), with characteristic bending strength equal to 24 MPa and a mean value of modulus of elasticity of 11.5 GPa. The plane frame structure has two 6-meter long bays in the X-direction and three 3-meter high storeys (Figure 3.1a). The columns consist of two elements each with a rectangular cross-section of 160 mm by 600 mm. The beams consist of a single rectangular glulam element with a cross-section of 120 mm by 600 mm. The connections between columns and beams are executed with a ring-doweled joints with two layers of connectors, as shown in Figure 3.1b. The first layer of connectors is composed by 10 dowels located 165 mm from the center, and the second layer by 16 dowels located at a radius of 240 mm. All dowels are M4.6 dowels with a diameter of 12 mm. At foundation level, columns are considered as hinged supports. Braced timber frames ensure lateral resistance in the perpendicular out-of-plane direction. To tie the structure together, these elements are fastened with screws to the main beams. Moreover, diagonal steel bars are connected to the columns at floor level, as presented in Figure 3.1d.

The floors consist of a low weight solution frequently used in residential buildings in Europe. The top layer is parquet that is placed over a leveling 20 mm thick layer of mortar, followed by 18 mm thick Oriented Strand Boards (OSB) fixed to the GL24h joists with a cross-section of 120 mm by 200 mm. The joists are covered by a wood cover and plasterboard on the underside, and connected with screws to the main beams as shown in Figure 3.1e. The model assumes that the floors respond as rigid diaphragms due to their large in-plane stiffness.

Considering the median density of the materials and their thicknesses, the weight of the floor is taken as 1.37 kN/m². The characteristic value of 2 kN/m² is considered for the floor live load,

according to Eurocode 1 (CEN, 2002b). The design considered serviceability limit states and ultimate limit states from EC5 and EC8. Nevertheless, the governing loading for the beam column connections used was the seismic loading.

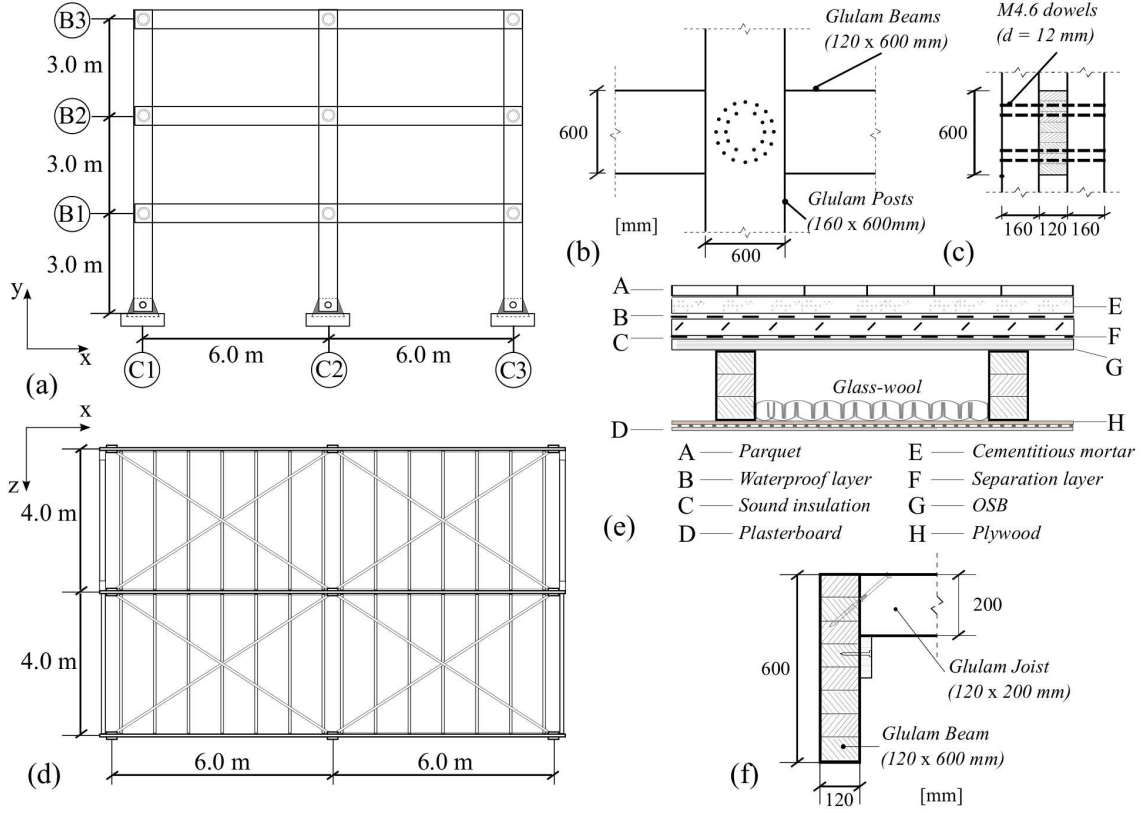


Figure 3.1: Moment-resisting frame structure:(a) elevation; (b) ring doweled joint - elevation; (c) ring doweled joint - cross section; (d) floor plan; (e) floor components; (f) joist connection

The floor loads will be assumed as deterministic, and inertial effects of these loads were considered on the seismic assessment as prescribed in EC8. The combination coefficient (ψ_{E_i}) was considered for variable loads to account for a reduced participation of their mass, which depends on the quasi-permanent coefficient (ψ_2) for variable loads, and is given by:

$$\psi_{E_i} = \varphi \cdot \psi_{2_i} \quad (3.3)$$

In equation (3.3), the parameter φ is related to the story occupancy. The value assumed is equal to 0.8, which is the value prescribed for stories with correlated occupancies. For residential buildings the quasi-permanent coefficient is equal to 0.3. Consequently, the mass related with variable loads is computed considering an uniformly distributed area load of 0.48 kN/m^2 . There is no reduction for permanent loads and consequently the area load considered to compute the

structural mass is 1.37 kN/m².

3.3.2 Finite element modeling and analysis

The beams and columns were modeled using linear elastic frame elements connected with zero-length springs (*Pinching4*), as shown in Figure 3.2a, to account for the rotational stiffness of moment-resisting joints. Geometric non-linearities are incorporated in the form of $P - \Delta$ effects. Rayleigh damping is assumed and a damping ratio $\xi = 0.02$ is assigned to the first and second modes of vibration. It is worth noting that the Rayleigh viscous damping ratio is assigned to the model to account for energy dissipation that cannot be directly captured in the analytical model (e.g. friction at steel connections and stressing of nonstructural elements). In addition, the energy dissipation due to the hysteretic response of the connections are explicitly accounted for in the *Pinching4* model when performing the nonlinear analyses.

The Newton-Raphson method is used to solve the nonlinear algebraic system of equations. The tolerance adopted is 10^{-8} on the inner product of the unbalanced load and displacement increments at each iteration (Chopra, 1995). Newmark integration was used considering $\gamma_{NM} = 0.5$ and $\beta_{NM} = 0.25$, which results in the average acceleration method (Newmark, 1959). The time step adopted for the transient analysis is 0.002 seconds.

A preliminary study comprised the evaluation of brittle failure occurrences. This assessment involved performing nonlinear dynamic analysis, where the structure was subjected to different time history records. After each analysis step, the occurrence of brittle failures was checked through a set of user implemented algorithms written in tcl/tk (Welch, 1995). The brittle failure modes considered are related with axial forces, shear forces and bending forces of timber members. The safety of timber elements in terms of shear stresses was verified through equation 6.13 of EC5 (CEN, 2005). The flexural resistance of beams was verified according to section 6.3.3 of EC5 (CEN, 2005), where the lateral torsional stability is also considered. The columns were verified for combined bending and axial tension and combined bending and axial compression, in agreement with the verifications included in sections 6.2.3, 6.2.4 and 6.3.2 of EC5 (CEN, 2005). The shear strength of dowels was checked by considering the embedment failure modes correspondent to equations 8.7g and 8.7h of EC5. Given the EC8 (CEN, 2013b) requirements for DCH structures in terms of size members, the verifications prescribed in EC5 for axial

forces, shear forces and bending forces were verified with high safety margins. Thus, in order to improve computational cost-efficiency these verification were avoided during the nonlinear dynamic analysis performed for the incremental dynamic analysis.

Analytical model for hysteretic behavior of joints

A Single-Degree-Of-Freedom (SDOF) model was used to calibrate the parameters of *Pinching4* model based on the results of fully reversal cyclic rotational tests from an experimental campaign performed at University of Trento (Polastrri et al., 2013). The *Pinching4* model was used to construct an uniaxial pinched load-deformation response with degradation under cyclic loading. The *Pinching4* model is defined by a response envelope, unload-reload rules, and three damage rule that control evolution of these paths. The calibration consists in the definition of four model states, the rules that control changes between states, and the rules that govern evolution of states. Each state is defined by moment-rotation ($M - \theta$) pairs which define the limits of each state. Given the test results, shown in Figure 3.2c, a symmetric behavior was assumed and consequently the same backbone-curve was considered for both directions. The response envelope obtained experimentally was fitted by defining the points *I* to *IV*, shown in Figure 3.2b. The calibrated moment-rotation values used to define the backbone curve are presented in Table 3.1.

Table 3.1: Points used to define the backbone curve

Point	M_i [kN.m]	θ_i [rad]
<i>I</i>	83.9	0.012
<i>II</i>	114.5	0.034
<i>III</i>	128.6	0.068
<i>IV</i>	16.8	0.129

The points where reloading begins, shown as points *VI* and *IX* in Figure 3.2b, depend on the ratio between the rotation at which reloading begins and the maximum historic rotation demand (r_{Disp}), and the ratio between the strength at which reloading begins and the maximum historic strength demand (r_{Force}). The moments corresponding to points *V* and *VIII* are dependent on the ratio of strength developed upon unloading from negative (positive) load to the maximum (minimum) strength (u_{Force}). The parameters r_{Disp} , r_{Force} , and u_{Force} were assumed equal for both directions given the symmetric response of the connection observed in the testing results. The calibration of these parameters account for the energy dissipated per cycle and also the

fitting of the position of points V to IX to match experimental results. Hysteretic damage is simulated through degradation of unloading stiffness, degradation in strength developed in the vicinity of the maximum and minimum rotation demands (strength degradation), and degradation in stiffness (reloading stiffness degradation). The form assumed for each damage rule is the same and represents a more general version of the damage index proposed in Y. Park and Ang (1985). Each damage index, δ_i defined in the *Pinching4* model is given by:

$$\delta_i = \left(\alpha_1 \cdot \left(\tilde{d}_{max} \right)^{\alpha_3} + \alpha_2 \cdot \left(\frac{E_i}{E_{monotonic}} \right)^{\alpha_4} \right) \quad (3.4)$$

where \tilde{d}_{max} is given by:

$$\tilde{d}_{max} = \max \left(\frac{d_{max,i}}{def_{max}}, \frac{d_{min,i}}{def_{min}} \right) \quad (3.5)$$

and where i refers to the current displacement increment, α_i are parameters used to fit the damage rules to the experimental data, E is the hysteretic energy and $E_{monotonic}$ is the energy required to achieve failure under monotonic loading. The values def_{max} and def_{min} are, respectively, the positive and negative deformations that define failure, and $d_{max,i}$ and $d_{min,i}$ are, respectively, the overall maximum and minimum deformation demands achieved until increment i . In Mazzoni et al. (2006) and Y. Park and Ang (1985), each parameter of *Pinching4* model is presented with more details.

To find the parameters that define pinching and degradation behavior, it was necessary to approximate the numerical model to the experimental results in terms of median strength degradation measured in three completed cycles at the same maximum rotation level. Based on the calibration performed, the parameters α_i used to model strength degradation, reloading stiffness and unloading stiffness degradation are presented in Table 3.2. Additional parameters obtained from the calibration are $r_{Disp} = 0.60$, $r_{Force} = 0.50$, and $u_{Force} = 0.05$. Figure 3.2c shows a good approximation of the *Pinching4* model adopted to the experimental results, both in terms of hysteretic response and strength degradation. Moreover, the approximation between experimental and analytical results can also be evaluated in terms of dissipated energy, as shown in Figure 3.2d, where the maximum relative error determined was 18%, although it can be seen that the difference is mainly due to the energy dissipated in the initial cycles which is not as

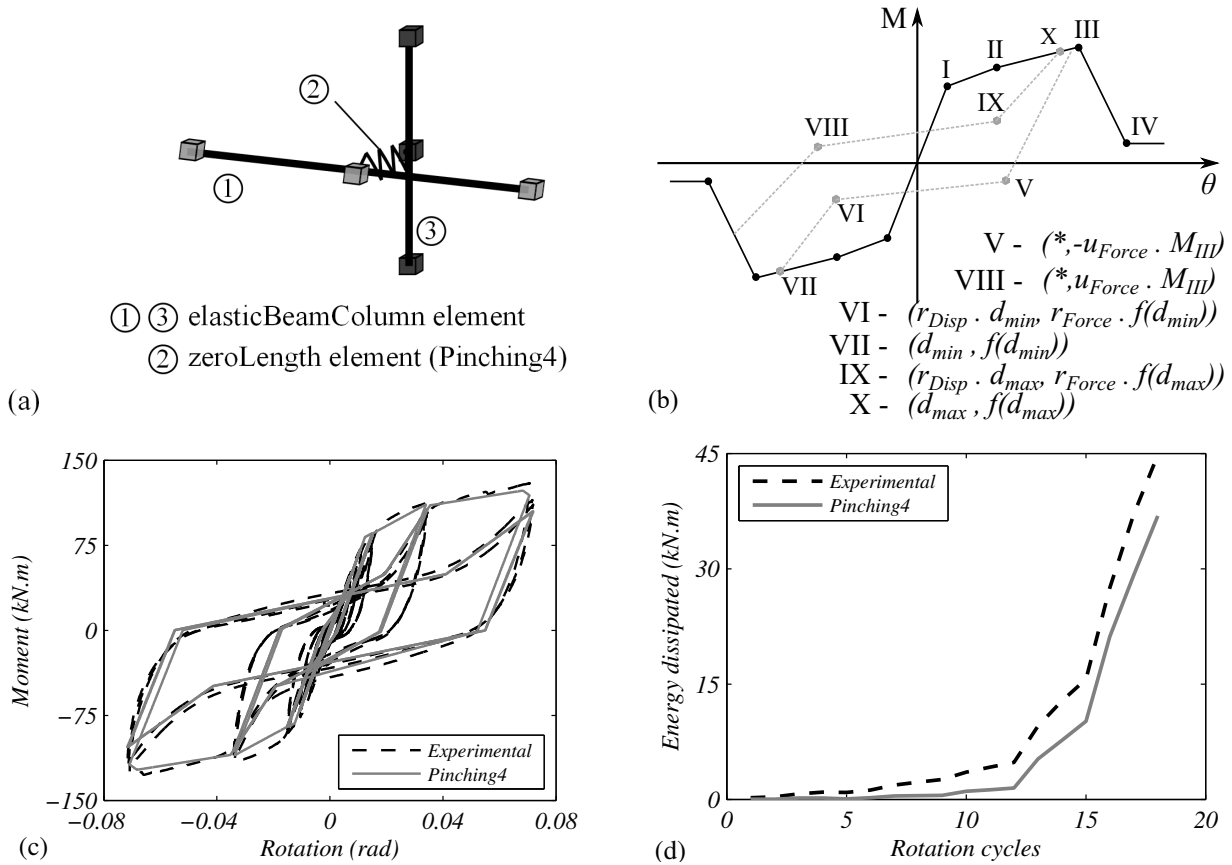


Figure 3.2: Numerical model of moment-resisting joints (a) OpenSees model for moment-resisting joint; (b) *Pinching4* parameters; (c) Experimental test and numerical results; (d) Energy dissipated: test vs numerical results

well captured by the model or could be associated with damping in the experimental setup.

Table 3.2: Parameters used to model the degradation

Parameter	δ_{d_i}	δ_{f_i}	δ_{k_i}
α_1	0.05	0.05	0.10
α_2	0.05	0.05	0.10
α_3	2.00	2.00	1.00
α_4	0.10	0.10	0.50

3.3.3 Basic random variables and assumed statistical correlations

Uncertainties in timber members

The inherent uncertainties of timber, as a material, are considered in this chapter by assigning different mechanical properties to each element. As presented in Table 3.3, seven random variables are considered for each timber element. The distribution parameters of the reference properties (bending strength, bending modulus of elasticity, and density) are computed based on characteristic values, defined in EN14080 (CEN, 2013a) for the homogeneous GL24h strength class, and on the coefficients of variation and probabilistic distributions proposed in Köhler et al. (2007). The expected values and the coefficients of variation of the remaining properties are computed according with the expressions proposed by Köhler et al. (2007), for Nordic softwood. Table 3.4 presents the intra-element correlation coefficients considered.

Table 3.3: Random variables for timber material properties

\mathbf{X}	Dist.	$E[X]$	CoV $[X]$	Description
R_m	LN	31	0.15	Bending strength // to the grain (N/mm^2)
E_m	LN	11500	0.13	Bending modulus of elasticity (N/mm^2)
ρ_{den}	N	420	0.1	Density (kg/m^3)
$R_{t,0}$	LN	18.6	0.18	Tension strength // to the grain (N/mm^2)
$R_{c,0}$	LN	23.4	0.12	Compression strength // to the grain (N/mm^2)
G_v	LN	718.8	0.13	Shear modulus (N/mm^2)
R_v	LN	3.12	0.15	Shear strength (N/mm^2)

It is considered that the properties of different elements are also correlated. A high inter-element correlation coefficient of 0.8, shown in Table 3.5, is assumed to simulate the assumption that laminations of different elements are assumed to origin from the same consignment of sawn wood.

Table 3.4: Intra-element correlation coefficient matrix (PMC)

	R_m	E_m	δ_{den}	$R_{t,0}$	$R_{c,0}$	G_v	R_v
R_m	1.0	0.8	0.6	0.8	0.8	0.4	0.4
E_m		1.0	0.6	0.6	0.6	0.6	0.4
ρ_{den}			1.0	0.4	0.8	0.6	0.6
$R_{t,0}$				1.0	0.5	0.4	0.6
$R_{c,0}$					1.0	0.4	0.4
G_v						1.0	0.6
R_v							1.0

Table 3.5: Inter-element correlation coefficient matrix

	B1	B2	B3	C1	C2	C3
B1 - 1 st floor beam	1.0	0.8	0.8	0.8	0.8	0.8
B2 - 2 nd floor beam		1.0	0.8	0.8	0.8	0.8
B3 - 3 rd floor beam			1.0	0.8	0.8	0.8
C1 - Left column				1.0	0.8	0.8
C2 - Center column					1.0	0.8
C3 - Right column						1.0

Uncertainties in ring-doweled connection properties

The probabilistic assessment performed in this study implies the computation of yielding moment and rotational stiffness for each moment-resisting joint. In the case of ring-doweled connections, these properties depend strongly on the embedment strength of the connected elements, which can be related to the density of wood. According to Bouchaïr et al. (2007) a constant stiffness per dowel for each of the dowels within a single connection can be assumed. This results in an equal distribution of load among all connectors, for each layer, and also to a geometrical center of the joint coincident with the center of rotation. A constant stiffness for all dowels within a single connection is assumed here, in order to compute stiffness and strength properties of the joints. Nevertheless, it is important to stress that small tolerances and wood variations likely lead to an un-equal stiffness and load distribution. According to EC5 and Porteous and Kermani (2013), the elastic rotational stiffness K_{el} can be estimated as:

$$K_{el,EC5} = n_{sp} \cdot k_{ser} \cdot \sum_{i=1}^n r_i^2 \quad (3.6)$$

where n_{sp} is the number of shear planes, r_i is the distance of each fastener from the center, and k_{ser} is the slip modulus per shear plane (CEN, 2005) given by:

$$k_{ser} = \frac{\rho_{con}^{1.5} \cdot d}{23} \quad (3.7)$$

where ρ_{con} is the wood density, in kg/m^3 , and d is the diameter of the dowels, in millimeters. It is worth noting that due to the variability of connected elements it is necessary to consider different densities for different members. Thus, ρ_{con} used in the equation (3.7) is the geometric mean of the density of adjacent members given by $\rho_{con} = \sqrt{\rho_{den,1} \cdot \rho_{den,2}}$, as proposed in EC5 for connections involving members with different densities. In this work, $\rho_{den,1}$ and $\rho_{den,2}$ are the densities of outer (columns) and inner (beams) elements respectively. The rotational stiffness of the beam column joint is then defined as:

$$K_{el} = \lambda K_{el} \cdot n_{sp} \cdot k_{ser} \cdot \sum_{i=1}^n r_i^2 \quad (3.8)$$

where $\lambda_{K_{el}}$ is a bias coefficient. As reported in Polastri et al. (2013), equation (3.6) overestimates the rotational stiffness. Considering the envelope experimental backbone curve, the value obtained through the experimental tests ($K_{el,test}$) is equal to 6936.6 kN.m/rad. Nevertheless, the rotational stiffness obtained through equation (3.8) is equal to 12572.0 kN.m/rad, with a measured wood density of 467 kg/m^3 . Thus, to consider this feature the rotational stiffness used to perform the nonlinear analysis is affected by a bias coefficient $\lambda_{K_{el}} = K_{el}^{test}/K_{el,EC5}^{test} = 0.55$.

According to Porteous and Kermani (2013), the yielding moment of a ring-doweled joint can be determined from equilibrium as

$$M_{y,EC5} = \sum_{i=1}^n F_{R,i} r_i \quad (3.9)$$

where $F_{R,i}$ is the yielding force of fastener i , which is given by:

$$F_{R,i} = 2 F_{V,R} \left(\frac{r_i}{r_{\max}} \right)^A \quad (3.10)$$

where parameter A is a constant that accounts for the nonlinear load-deformation response of isolated dowels and r_{\max} is the distance between the center and the farthest layer. For

the moment-resisting connection studied in this thesis, A is assumed equal to 0.5 (Polastri et al., 2013). The determination of dowel resistance force $F_{V,R}$ per shear plane is based on the Johansen's yielding theory (Johansen, 1949). Considering moment resisting connections used in the case study, the resistance force $F_{V,R}$ of a dowel per shear plane is computed as:

$$F_{V,R} = \min \begin{cases} F_{R,a} = f_{h,\alpha,1} \cdot t_1 \cdot d \\ F_{R,b} = 0.5 f_{h,\alpha,2} \cdot t_2 \cdot d \\ F_{R,c} = 1.05 \frac{f_{h,\alpha,1} \cdot t_1 \cdot d}{2 + \beta_h} \left[\sqrt{2\beta_h(1 + \beta_h) + \frac{4\beta_h(2 + \beta_h)M_{y,dowel}}{f_{h,\alpha,1} \cdot t_1^2 \cdot d}} - \beta_h \right] \\ F_{R,d} = 1.15 \sqrt{\frac{2\beta_h}{1 + \beta_h}} \sqrt{2M_{y,dowel} \cdot f_{h,\alpha,1} \cdot d} \end{cases} \quad (3.11)$$

where t_i is the thickness of the members, $f_{h,\alpha,i}$ is the embedment strength of the members in the direction of the load applied (α) on the fastener; β_h is the ratio between the embedment strength of the beam and the embedment strength of the column ($\beta = f_{h,\alpha,2}/f_{h,\alpha,1}$), and d is the diameter of dowels. Thus, $f_{h,\alpha,1}$ and $f_{h,\alpha,2}$ are determined considering the influence of the angle α relative to the grain ($\alpha = 0$ corresponds to the direction parallel to grain). The embedment strength $f_{h,\alpha}$ is computed through the following equation:

$$f_{h,\alpha} = \frac{f_{h,0}}{k_{90} \sin^2 \alpha + \cos^2 \alpha} \quad (3.12)$$

where $k_{90} = (1.35 + 0.015d)$ for softwood (CEN, 2005) and $f_{h,0}$ is the embedment strength in the parallel to grain direction given by:

$$f_{h,0} = 0.082(1 - 0.01d)\rho_{den} \quad (3.13)$$

Failure modes given in equation (3.11 a) and (3.11 b) refer to timber embedding failure. To guarantee the ductility of connections, it is recommended to design the connections to fail in the failure modes correspondent to equations (3.11 c) and (3.11 d), which are dependent on the yielding moment of each dowel $M_{y,dowel}$ that can be obtained through the following equation:

$$M_{y,dowel} = 0.3f_u d^{2.6} \quad (3.14)$$

where f_u is the ultimate yield capacity in tension. The ultimate capacity in tension of dowels f_u is also assumed as a random variable varying from connection to connection. This variable follows a lognormal distribution with a median value of 427.2 MPa and a coefficient of variation equal to 0.04 (PMC, 2011) corresponding to a characteristic value of 400 MPa. A bias coefficient λ_{M_y} has to be considered to affect the values of yielding moment obtained through equation (3.9). As in the case of rotational stiffness, the yielding moment is also over-estimated by the formulae proposed in EC5. Consequently, the coefficient λ_{M_y} is the ratio between the yielding moment of the experimental backbone curve ($M_I = 83.93$ kN.m) and the predicted yielding moment $M_{y,EC5}^{test}$ ($= 101.04$ kN.m) obtained through equation (3.9) using the mechanical properties of the experimental specimens ($f_u = 580$ MPa). Thus, the deterministic value of λ_{M_y} is considered in the Latin Hypercube samples is given by:

$$\lambda_{M_y} = \frac{M_I}{M_{y,EC5}^{test}} = 0.83 \quad (3.15)$$

Consequently, the yielding moment used for Latin Hypercube samples is defined by the following equation:

$$M_{I,LHS} = M_y = \lambda_{M_y} \sum_{i=1}^n F_{R,i} r_i \quad (3.16)$$

From the set of structural model samples generated using the parameters presented in Tables 3.3 to 3.5, the yielding moment (equation (3.9)) and elastic rotational stiffness (equation (3.8)) were computed for each joint, and each structure in 9000 size samples for each property with parameters shown in Table 3.6.

Table 3.6: Lognormal parameters for moment-resisting joints properties

X	$\mu_{\ln X}$	$\xi_{\ln X}$	$E[X]$	$CoV[X]$	KS ($p - value$)
$M_{y,LHS}$ [kNm]	4.103	0.051	60.6	0.05	0.144
$K_{el,LHS}$ [kNm/rad]	8.679	0.143	5937.6	0.143	0.130

Due to the current requirements of EC8 for high ductility class structure, it is worth noting that the capacity of the ductile failure mode shown in equation (3.11 d) was the one that governed the strength capacity of the dowels, even when variability on timber properties and dowels ultimate strength was assumed. This is a consequence of the high slenderness of dowels

($t \geq 10d$) and the mild steel quality assumed during design.

The parameters defining the post-yield behavior of the hysteretic models defined for the connections are also considered as random variables. The envelope curve of the cyclic test presented in Figure 3.2c was used in defining points I to IV of the backbone curve of *Pinching4*. The ratios between the yielding moment (M_I) and the values M_{II} and M_{III} were assumed to be deterministic and equal to those observed in the experimental tests. From the response envelope obtained, through the process defined in section 3.3.2, the parameters M_{II} and M_{III} are given by:

$$M_{II} = \frac{M_{II}^{test}}{M_I^{test}} M_I \approx 1.36 M_I \quad (3.17)$$

$$M_{III} = \frac{M_{III}^{test}}{M_I^{test}} M_I \approx 1.53 M_I \quad (3.18)$$

where $M_I^{test} = 83.9$ kN.m; $M_{II}^{test} = 114.45$ kN.m and $M_{III}^{test} = 128.6$ kN.m. The residual strength (M_{IV}) is defined as 20% of the yielding moment (M_I^{test}). The rotations necessary to define the backbone of moment-resisting joints are also assumed as random variables. Their values are defined considering the yielding rotation θ_y and the parameters X_{II} , X_{III} , and X_{IV} , as presented in the following equations:

$$\theta_y = \frac{M_y}{K_{el}} \quad (3.19)$$

$$\theta_{II} = \theta_y + X_{II} \cdot \theta_y \quad (3.20)$$

$$\theta_{III} = \theta_{II} + X_{III} \cdot \theta_y \quad (3.21)$$

$$\theta_{IV} = \theta_{III} + X_{IV} \cdot \theta_y \quad (3.22)$$

Lognormal distributions were assumed for X_{II} , X_{III} and X_{IV} , as these parameters must be positive. The mean values for the parameters are illustrated in Figure 3.3, which was obtained from calibration of the backbone curve of the experimental results shown in Figure 3.2c. Since there are no studies available in the literature regarding the variability of post-yielding rotations of ring-doweled connections, and, there are more factors (*e.g.* cracks on the vicinity of dowels) that

may induce deviations on the idealized backbone, a high coefficient of variation was assumed for the variables X_{II} , X_{III} and X_{IV} . The parameters used to represent post-yielding rotation properties are presented in Table 3.7 and illustrated in Figure 3.3. Additional parameters used to define the hysteretic behavior of connections are assumed to be deterministic.

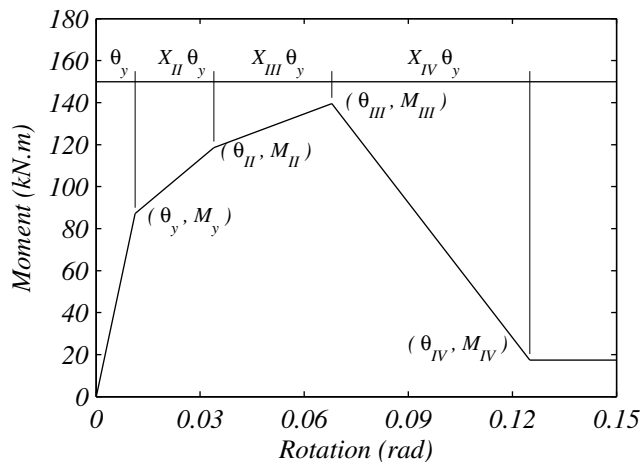


Figure 3.3: Backbone curve used for ring-doweled response

Table 3.7: Post-yielding rotations variability

X	$\mu_{\ln X}$	$\xi_{\ln X}$	$E[X]$	$\text{CoV}[X]$
X_{II}	0.514	0.385	1.80	0.4
X_{III}	0.970	0.385	2.84	0.4
X_{IV}	1.535	0.385	5.00	0.4

Distribution of the periods of vibration of the structural set

The random variables considered in this chapter affect mass and stiffness of the structure which in turn induce variability on periods of vibration of each generated structural model realization. It is worth noting that the fundamental period T_1 plays an important role on the development of multi-record IDA, since the time-history records considered are scaled to the same first mode spectral acceleration $S_a(T_1)$, and therefore its expected value needed to be determined in this section before performing the ground motion selection and before defining the reference intensity measure. The first natural period for the 1000 structural models generated through LHS has a median value equal to 0.97 s while the median of the second natural period is 0.14 s. All the realizations of the structural set have in common the fact that 95% modal mass is reached with only two lateral modes of vibration. The probability distribution of computed natural periods can be approximated by lognormal distributions (p -value equal to 0.83 and

0.99 respectively, for a significance level of 5%): ($T_1 \sim LN(\mu_{LN} = -0.032, \xi_{LN} = 0.057)$ and $T_2 \sim LN(\mu_{LN} = -1.991, \xi_{LN} = 0.052)$).

3.3.4 Ground motion selection

A set of 24 ground motion records was selected and scaled to the 2% damped linear elastic acceleration response spectra considered in EC8 for a site in Lisbon, Portugal. According to the national document of application of EC8, it is necessary to consider two types of seismic action for any site in Portugal, including the Type 1 far-field ground motions which correspond to magnitudes higher than 7.0, and Type 2 near-field ground motions characterized by magnitudes lower than 7.0. The set of ground motions were extracted from the Pacific Earthquake Engineering Next-generation Attenuation (PEER NGA) database (PEER, 2002). The main characteristics of the time-history records selected are presented in Table 3.8. The respective response spectra are shown in Figure 3.4 where the elastic response target spectra of EC8 is also presented. In this figure, it can be seen that the response spectra of the selected records match the target spectra in the period range of interest, taken as $0.2T_1$ to $3.0T_1$, where T_1 is the median fundamental period of vibration of the structural set. The values presented in Table 3.8 to characterize the time-history records used are the peak-ground acceleration (PGA), the median first-mode spectral acceleration ($S_a(T_1)$), and the scale factors (SF_i) used to scale the records to the target response spectra.

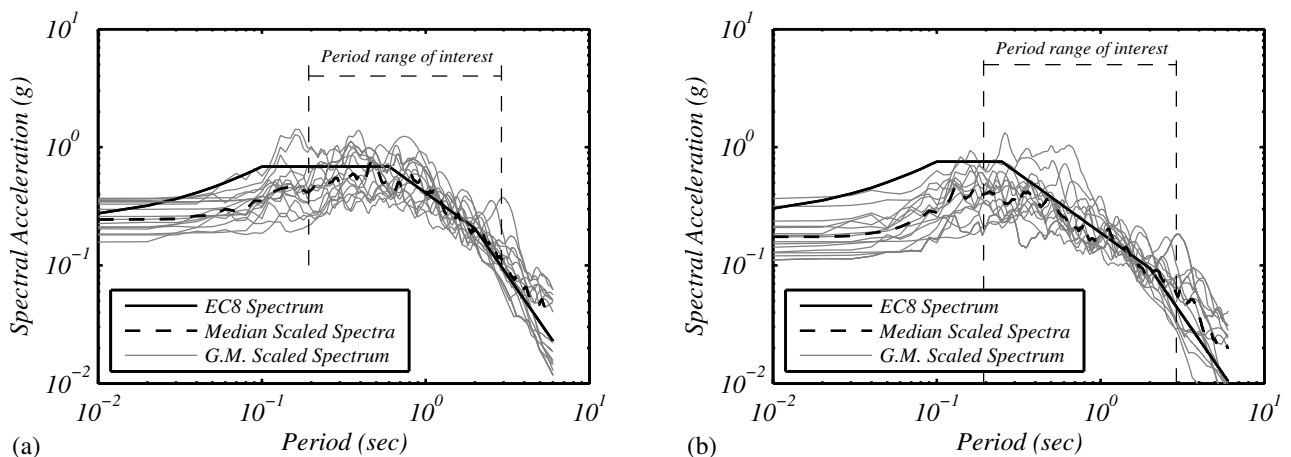


Figure 3.4: Response spectra used to perform multi-record IDA: (a) Type 1; (b) Type 2

Table 3.8: Set of ground motion records selected

Event	Station	PGA (g)	$S_a(T_1)$	SF ₁	SF ₂
Kobe, Japan, 1995	Fukushima #000	0.185	0.913	0.977	-
Kobe, Japan, 1995	Fukushima #090	0.215	0.558	0.978	-
Loma Prieta, 1989	Hollister Diff. Array #255	0.252	0.612	1.066	-
Loma Prieta, 1989	Sunnyvale Colton Ave #270	0.170	0.254	1.091	-
Kobe, Japan, 1995	Shin-Osaka #000	0.217	0.369	1.153	-
Superstition Hills, 1987	Wildlife Liquefaction Array # 360	0.185	0.456	0.759	-
Kobe, Japan, 1995	Amagasaki #000	0.233	0.883	0.740	-
Kobe, Japan, 1995	Kobe University #000	0.259	0.603	0.669	-
Kobe, Japan, 1995	Amagasaki #090	0.327	0.693	0.647	-
Kobe, Japan, 1995	KJMA #090	0.630	1.348	0.589	-
Loma Prieta, 1989	Agnews State Hospital #090	0.161	0.194	1.517	-
Kobe, Japan, 1995	KJMA #000	0.590	1.620	0.415	-
Friuli, Italy-01,1976	Tolmezzo #000	0.357	0.252	-	1.028
Friuli, Italy-01,1976	Tolmezzo #270	0.301	0.299	-	1.001
Kobe, Japan, 1995	Abena #000	0.149	0.351	-	1.078
Kobe, Japan, 1995	Abena #090	0.231	0.172	-	0.908
Northridge, 1994	LA, Baldwin Hills(985)	0.239	0.154	-	0.896
Imperial Valley, 1979	El Centro Array, #13 #140	0.145	0.175	-	0.892
Kobe, Japan, 1995	HIK #000	0.118	0.257	-	1.141
Loma Prieta, 1989	Coyote Lake Dam Downstream #285	0.180	0.178	-	0.848
San Fernando, 1971	LA, Hollywood Stor. Lot #090	0.225	0.250	-	0.829
Imperial Valley, 1979	El Centro Array, #12 # 140	0.118	0.144	-	1.208
Kobe, Japan, 1995	Kakogawa #090	0.324	0.305	-	0.540
Kobe, Japan, 1995	Kakogawa #000	0.240	0.233	-	0.746

3.4 Performance assessment

In this section, the seismic capacity of the structural set of 1000 structural models obtained with LHS method, is evaluated through nonlinear static analysis and incremental dynamic analysis.

3.4.1 Pushover analysis

Estimates of equivalent reference system parameters

From the results of the capacity curves shown in Figure 3.5a, the parameters shown in Figure 3.5b that define the equivalent bilinear inelastic were obtained, including the peak base shear F_{max}^* , the reference yield displacement d_y^* , and associated yield force F_y^* , and the ultimate displacement d_u^* . The initial stiffness is determined considering the secant stiffness to the point of the first yield of one of the moment resisting connections. The ultimate displacement d_u^* is defined as that corresponding to a decrease of 20% from F_{max}^* ("near - collapse" state). The yielding force F_y^* results from the application of the Energy Equivalent Elastic Plastic (EEEP) method (Foliente, 1996), which consists in balancing the total energies below the obtained capacity curve and the equivalent bilinear model. The distribution of the parameters are listed in Table 3.9. All the parameters fit a lognormal distribution according to the Kolmogorov-Smirnov (KS) test.

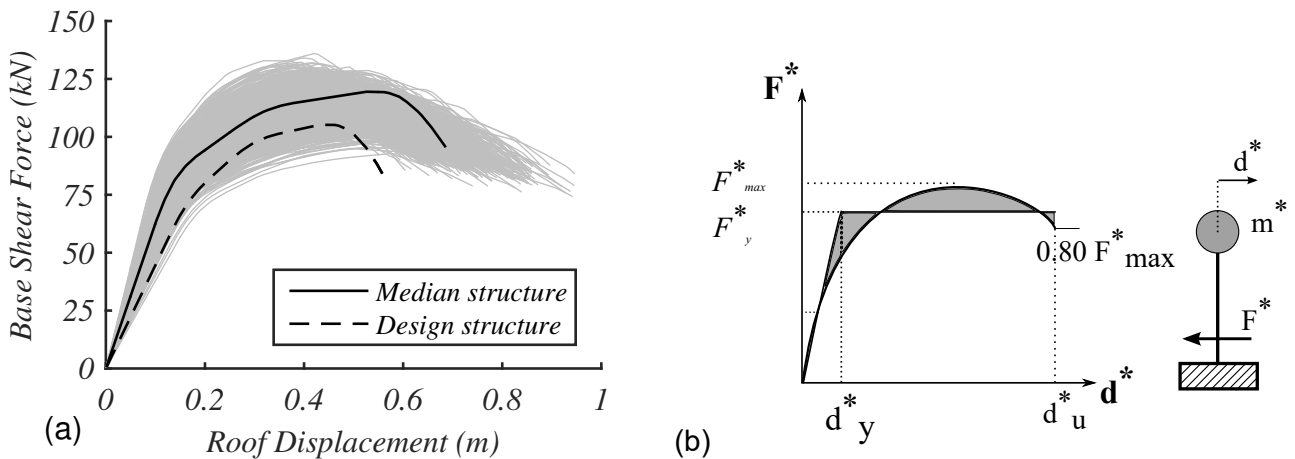


Figure 3.5: Nonlinear static analysis: (a) Capacity curves; (b) Equivalent bilinear inelastic model

Table 3.9: Lognormal parameters for q -factor estimates

X	$\mu_{\ln X}$	$\xi_{\ln X}$	$X_{0.50}$	$E[X]$	$\text{CoV}[X]$	KS (p -value)
$F_y^*[kN]$	4.670	0.059	106.7	106.9	0.048	0.58
$d_y^*[m]$	-1.765	0.076	0.171	0.172	0.076	0.99
$F_u^*[kN]$	4.531	0.061	92.9	93.0	0.061	0.66
$d_u^*[m]$	-0.383	0.111	0.681	0.686	0.112	0.84
R_μ	1.382	0.076	4.0	4.0	0.076	0.96
R_Ω	0.580	0.059	1.8	1.8	0.059	0.58
q -factor	1.959	0.084	7.1	7.2	0.084	0.90

Estimation of the q -factors

According to Fajfar (1999) the q -factor is given by:

$$q = R_\mu \cdot R_\Omega \quad (3.23)$$

where R_μ is the ductility factor and R_Ω is the overstrength factor. In this chapter, R_μ is computed with the formulae proposed by Vidic et al. (1994):

$$R_\mu = \begin{cases} (\mu - 1) T_1/T_C + 1 & , T < T_C \\ \mu & , T > T_C \end{cases} \quad (3.24)$$

where the coefficient μ is the ratio between ultimate and yielding displacements of the equivalent inelastic model (i.e. $\mu = d_u^*/d_y^*$), T_1 is the fundamental period of a structure, and T_C is the transition period that is equal to 0.8 s for the site considered in this study. All the fundamental periods computed, for the structural set, are higher than T_C , which means that $R_\mu = \mu$.

In turn, the overstrength factor R_Ω is considered equal to the ratio between the yielding force F_y^* , of each structural sample, and the base shear force $F_{1,d}^*$. This value was taken from the design structure capacity curve, presented in Figure 3.5a, when any connection reaches the yielding moment ($F_{1,d}^* = 59.8$ kN).

The quantities used to evaluate the q -factor can be computed using the parameters listed in Table 3.9. The table shows that the median value of the q -factor obtained from the pushover analysis with modeling uncertainties ($q_{0.50} = 7.1$) is significantly higher than the q -factor recommended in EC8 for structural design ($q_{EC8} = 4.0$), respectively. Moreover, it is worth noting

that the median value of the ductility factor R_μ obtained is 4.0, which is similar to the q -factor used in the design of this structure. On the other hand, a linear correlation coefficient of 0.46 and 0.74 are obtained between the q -factor and R_Ω and between the q -factor and R_μ , respectively. A lognormal probability density function was fitted to the values of q -factor obtained, as shown in Figure 3.6. The median value of the q -factor is approximately 7.1.

Results listed in Table 3.9 for the R_μ and q -factor indicate that the q -factor considered in EC8 and the detailing requirements defined in EC8 and EC5 are adequate for the design of this moment resisting frame structure, even though they also indicate that the detailing requirements may be optimized to achieve more cost-effective connections and members in future studies.

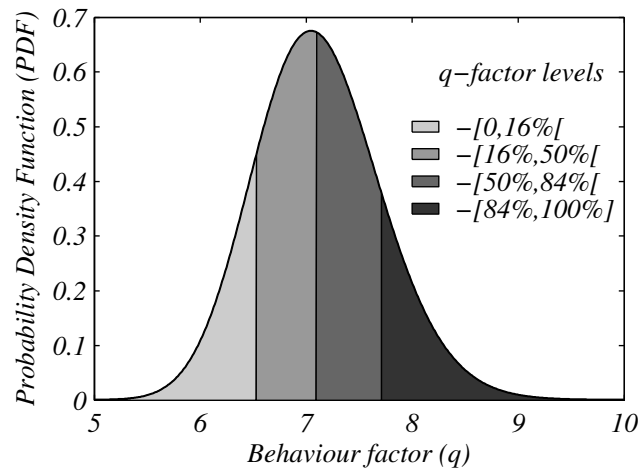


Figure 3.6: q -factor levels and fitted PDF

Estimation of interstory drift ratio limit states

The estimation of a relationship between the interstory drift ratios and the joint rotations is performed in this section. These values are obtained here from the capacity curves, where each damage state is associated with a certain structural damage. It is assumed that the Immediate Occupancy damage state (IO) is reached when an interstory drift ratio associated with the first yielding of any connection in the building. It is considered that Life Safety damage state (LS) is reached when any moment-resisting connection reaches its capping rotation θ_{III} , shown in Figure 3.3. For the Collapse Prevention (CP) damage state, the threshold is given from the highest interstory drift ratio obtained when the structure reaches the "near - collapse" state (20% decrease from maximum capacity).

Table 3.10 lists the lognormal parameters obtained for each limit state interstory drift ratio. The results in Table 3.10 show that the mean threshold values of interstory drift ratio are 1.2%, 4.9%, and 7.9% for the IO, LS, and CP damage states. The values of the coefficient of variation vary from 9% to 14.4%.

Table 3.10: Lognormal parameters for limit state interstory drift ratios

Damage state	$\mu_{\ln \theta_{\max}}$	$\xi_{\ln \theta_{\max}}$	$\theta_{\max,0.50}$	$E[X]$	$\text{CoV}[X]$	KS (p -value)
IO	-4.437	0.091	0.012	0.012	0.091	0.46
LS	-3.015	0.144	0.049	0.049	0.144	0.90
CP	-2.540	0.108	0.079	0.080	0.109	0.97

The Kolmogorov-Smirnov (KS) goodness-of-fit test confirms that the lognormal distribution is an acceptable distribution for the limit state thresholds considered with a confidence level of 95%. The goodness-of-fit of the distributions is also shown in the lognormal probability plots presented in Figure 3.7.

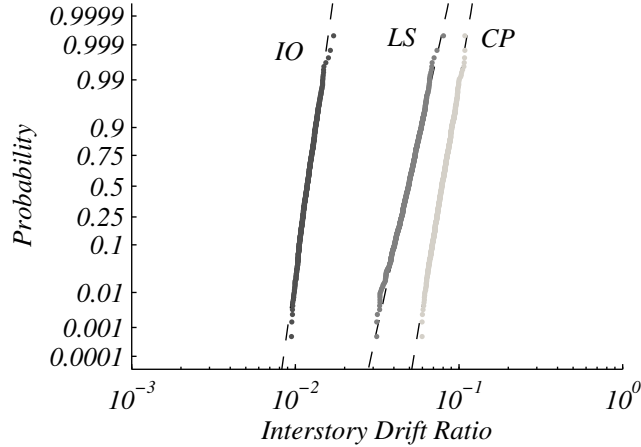


Figure 3.7: Lognormal probability plots for different limit state interstory drift ratio

3.4.2 Incremental Dynamic Analysis

In order to evaluate the effect of record-to-record variability, the single-record curves IDA for both design structure ($T_1 = 1.13\text{s}$) and median structure ($T_1 = 0.97\text{s}$) are shown in Figure 3.8a and 3.8b, respectively. The design structure shows a lower capacity both in terms of spectral acceleration and peak interstory drift ratio at global collapse. Despite the differences regarding strength and stiffness between the two structures, the ability of joints to deform in the nonlinear range contributes considerably to these results. The parameters X_{II} , X_{III} and X_{IV} , used to

compute the backbone curve, differ considerably since the 5th percentile value was used for the design structure, instead of the median value used for the median structure.

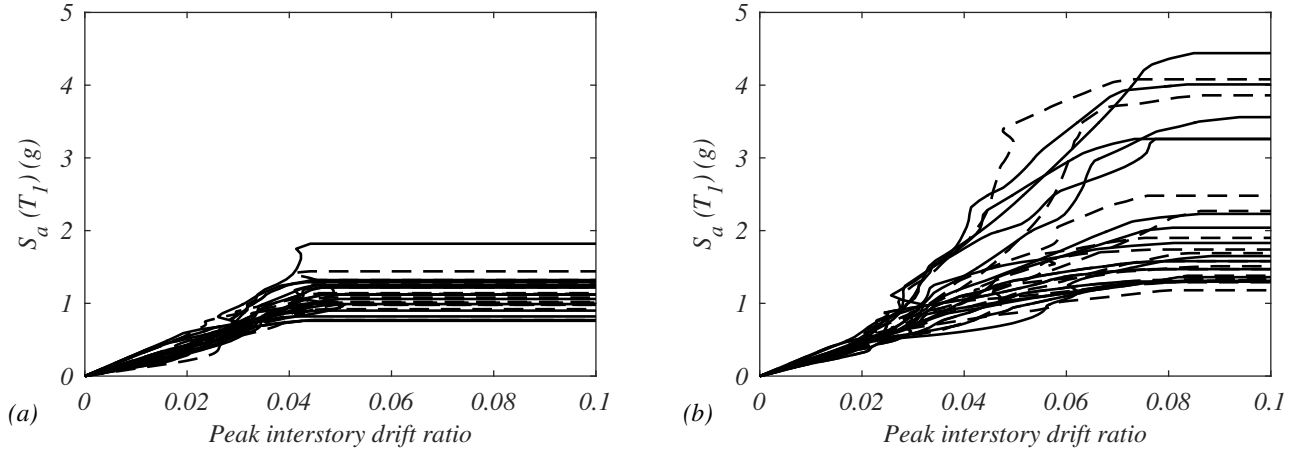


Figure 3.8: Single-record IDA Curves: (a) Design structure; (b) Median structure

In Figure 3.9a, the results for all multi-record IDA curves ($N_{IDA} = 24000$) are summarized by the mean and median IDA curves for the structural set. In addition, the mean and median IDA curves of the median structure ($N_{IDA} = 24$) are also shown in this figure. Figure 3.9b shows the coefficient of variation of the estimated capacity ($S_a(T_1)$) versus peak interstorey drift ratio.

From the results shown it possible to see that the structural set and median structure present similar mean and median curves for peak interstorey drift ratios lower than 5%. The coefficient of variation of spectral acceleration is higher for the structural set, for peak interstorey drift ratios lower than 5%, as shown in Figure 3.9b. These results were expected as a consequence of including structural uncertainties. For peak interstorey drift ratios greater than 5%, the median structure presents higher mean and median capacity, but similar coefficient of variation, when compared to the structural set. Similar observations have been reported in the literature for RC structures (Liel et al., 2009).

Disaggregation of the multi-record IDA results by the q -factor

The seismic capacity of heavy-timber frame structures depends strongly on the hysteretic energy dissipation of connections, which is related to the deformation capacity of the moment-resisting joints. In the following disaggregation of the results, the q -factor is subdivided into four intervals, as shown in Figure 3.6. The first interval comprises structures with q -factor lower than its 16th percentile ($q_{0.16} = 6.5$), while the second groups structures with q -factor between the

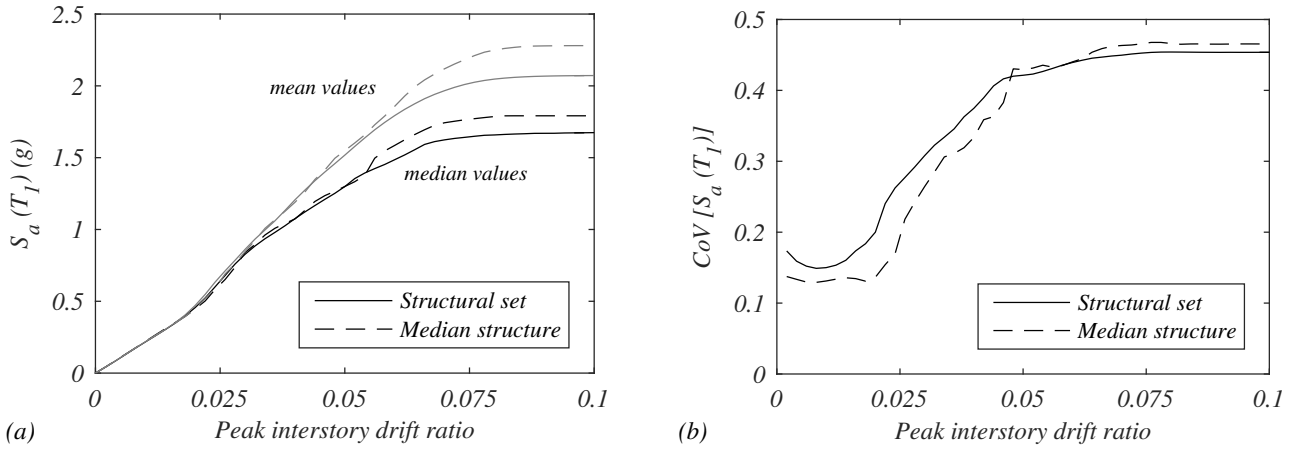


Figure 3.9: Multi-record IDA results: (a) mean and median IDA curves; (b) coefficient of variation of $S_a(T_1)$

16th percentile $q_{0.16}$ and the 50th percentile $q_{0.50}$, ($q \in [6.5, 7.1]$). The third interval is equal to $q \in [q_{0.50}, q_{0.84}[$ and the last one comprises structures with q -factor higher than its 84th percentile ($q_{0.84} = 7.7$).

For improved clarity only the median fractile multi-record IDA curves are presented in Figure 3.10a. It is evident that for drift ratio levels greater than 2.5%, the capacity of the structure increases as the q -factor increases for the same level of deformation. It can also be seen the higher the q -factor, the higher the structural capacity associated with the global collapse. In Figure 3.10b, the coefficients of variation of the spectral acceleration versus peak interstory drift ratios are shown, for different levels of the q -factor. There are no generalized differences in terms of coefficient of variation when different levels of q -factor are considered across all values of peak interstory drift ratios.

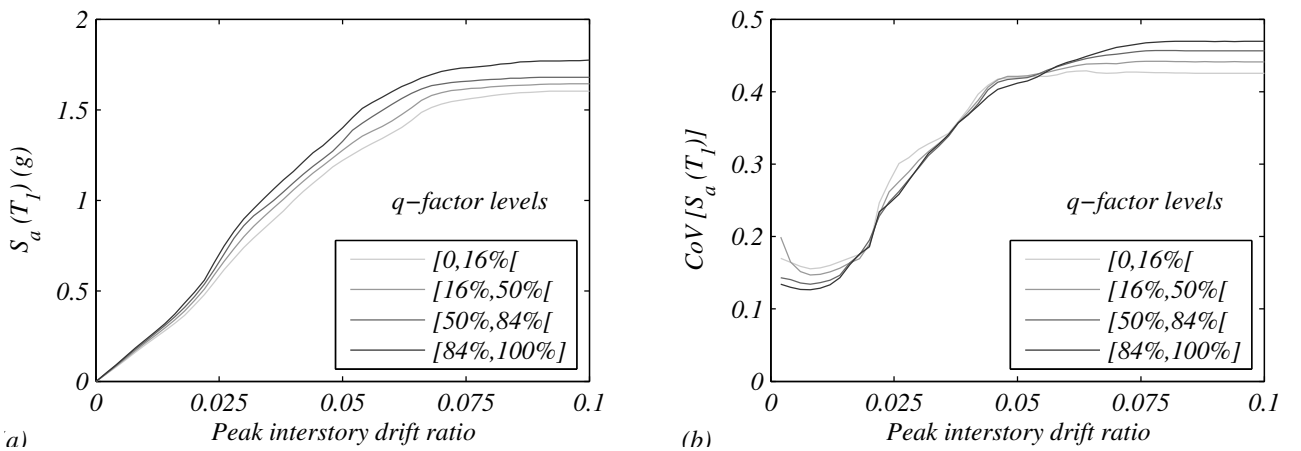


Figure 3.10: Multi-record IDA curves for different q -factor levels: (a) median fractile curves; (b) coefficient of variation of $S_a(T_1)$

3.5 Fragility Analysis

The fragility functions computed here result from fitting a lognormal distribution to the spectral accelerations extracted from the IDA curves for each limit state. In this section, the effect produced by modeling uncertainties and q -factor variability on the different fragility functions are presented. Table 3.11 summarizes the results for the fragility curves, determined for IO, LS, and CP damage states. For each damage state level, three different values were chosen to define exceedance of a certain capacity level, namely 16th, 50th and, 84th percentile of each limit state. The influence of limit state threshold on the fragility functions can therefore be assessed for the median structure and the structural set. It can be seen that the expected values are similar for both structural set and median structure when IO damage state is considered. Nevertheless, the coefficient of variation is higher for the structural set. For example, in Table 3.11, it can be seen that, when the median value of interstory drift ratio is considered as threshold ($\theta_{\max} = 0.0118$), the difference on expected values is negligible whereas the coefficient of variation of the structural set is 18% higher than the one obtained for the median structure. The expected values of the structural set are 2% to 4% higher when compared with the median structure for LS damage state. In terms of coefficient of variation, the values obtained for the structural set are higher, ranging from 11% to 13%. For the CP damage state, the differences between the structural set and the median structure are negligible in terms of coefficient of variation. Nevertheless, the expected value obtained for the median structure is 3% to 6% higher than the expected value of the structural set. From the IO and LS fragility curves, graphically represented in Figure 3.11a and Figure 3.11b, respectively, it is observed that the limit state interstory drift ratios admitted as thresholds influence both the expected value and the coefficient of variation. Consequently, these values may be considered as random variables in further studies.

Table 3.12 presents the fragility curve parameters for GC damage state. These parameters are similar to the ones obtained for the CP damage state. This observation can be justified by the peak interstory drift ratios used as thresholds for the CP damage state, since these values may exceed the peak interstory drifts ratios related to the dynamic instability observed in the IDA curves. As shown in Table 3.12, the expected value of GC damage state peak interstory drift ratio, for the structural set, is lower than the expected value used for CP limit state value. Consequently, a considerable number of structural models reached instability for the interstory

drift ratios considered for CP. Moreover, the coefficient of variation of global collapse peak interstory drift is 37% higher than the one obtained for CP damage state.

Table 3.11: Fragility curves parameters for IO, LS and CP

Limit state	θ_{max}	Structural set				Median structure			
		$\mu_{\ln D}$	$\xi_{\ln D}$	$E[X] (g)$	$CoV[X]$	$\mu_{\ln D}$	$\xi_{\ln D}$	$E[X] (g)$	$CoV[X]$
D > IO	0.0108	-1.457	0.136	0.235	0.137	-1.461	0.117	0.234	0.117
	0.0118	-1.370	0.137	0.257	0.138	-1.373	0.117	0.255	0.117
	0.0130	-1.275	0.140	0.282	0.141	-1.279	0.117	0.280	0.117
D > LS	0.0425	0.164	0.387	1.270	0.402	0.143	0.345	1.225	0.356
	0.0490	0.287	0.413	1.451	0.431	0.282	0.359	1.414	0.371
	0.0566	0.413	0.441	1.666	0.463	0.410	0.401	1.633	0.418
D > CP	0.0708	0.549	0.468	1.932	0.495	0.582	0.461	1.990	0.487
	0.0789	0.582	0.481	2.010	0.510	0.632	0.477	2.108	0.506
	0.0878	0.594	0.483	2.035	0.513	0.650	0.480	2.150	0.509

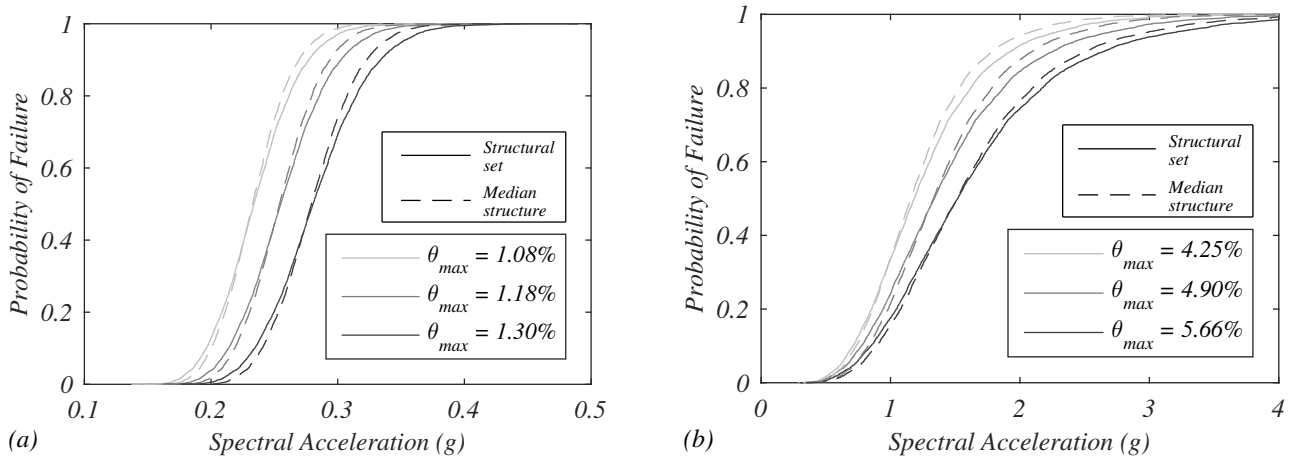


Figure 3.11: Fragility curves for different θ_{max} levels: (a) Immediate Occupancy; (b) Life Safety

The impact of considering modeling uncertainties, on a GC fragility curve, is reflected in the expected values presented in Table 3.12, for both structural set and median structure. As shown in Figure 3.12b, a similar dispersion is observed, but neglecting modeling uncertainties may lead to an overestimation of the collapse capacity. A higher variability is observed for the structural set whereas the median structure presents a greater expected value. The cumulative distribution functions of peak interstory drift ratios are presented for GC in Figure 3.12a.

The disaggregation of the multi-record IDA results by different levels of q -factor, allow to present fragility curves for different q -factor levels. Table 3.13 shows results for both LS and CP damage states, considering median values of interstory drift ratios as limit-state thresholds. The disaggregation of fragility curves in different q -factor levels shows that higher q -factors correspond to higher expected values and higher coefficients of variation of the structural capacity.

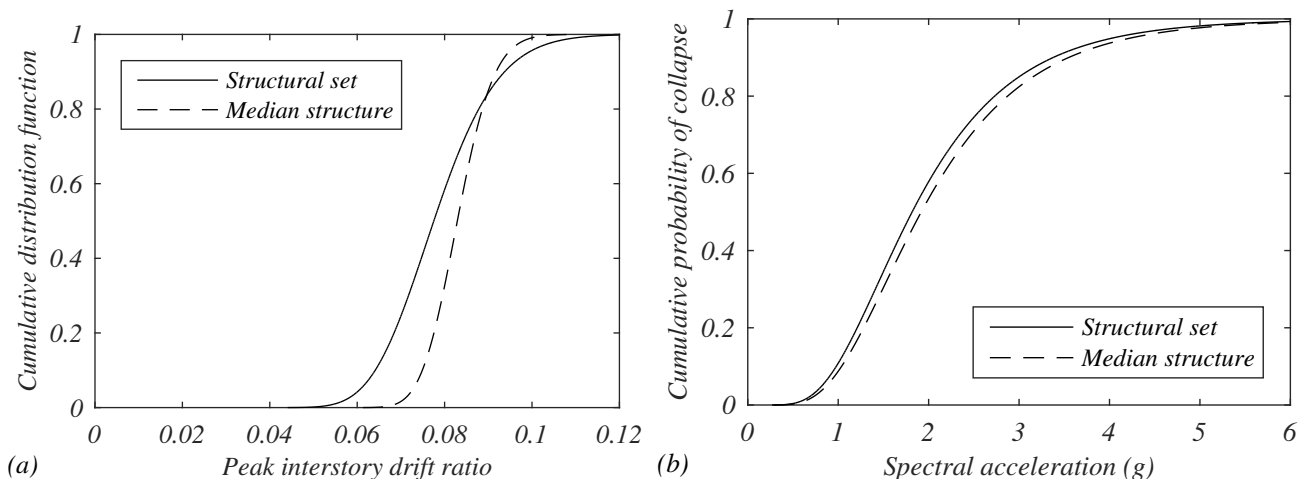


Figure 3.12: Global collapse fragility curves: (a) for different q -factor levels ; (b) median structure and structural set

Table 3.12: Lognormal parameters for peak interstory drift ratio and spectral acceleration at GC

	Spectral acceleration ($S_a(T_1)$)				Peak interstory drift ratio (θ_{\max})			
	μ_{\ln}	ξ_{\ln}	$E[X]$ (g)	$CoV[X]$	μ_{\ln}	ξ_{\ln}	$E[X]$	$CoV[X]$
Structural set	0.598	0.483	2.044	0.513	-2.557	0.148	0.078	0.149
Median structure	0.652	0.480	2.154	0.510	-2.490	0.079	0.083	0.079

These results are shown graphically in Figure 3.13. The capacity/demand ratio for timber members and the beam-column joints were checked for a sample of the ground motions with the 5% damped linear response spectral accelerations at the fundamental period of vibration of the structure ranging from 1.4g to 4.5g. It was observed that neither the members nor the beam-column joints reached their ultimate deformation capacity.

Table 3.13: LS and CP fragility curves parameters for different levels of q - factors

Fractile	LS - $\theta_{\max,0.50} = 0.0490$				CP - $\theta_{\max,0.50} = 0.0789$			
	$\mu_{\ln D}$	$\xi_{\ln D}$	$E[X]$	$CoV[X]$	$\mu_{\ln D}$	$\xi_{\ln D}$	$E[X]$	$CoV[X]$
[0, 16%[0.199	0.393	1.318	0.409	0.474	0.437	1.767	0.459
[16%, 50%[0.263	0.404	1.411	0.421	0.559	0.472	1.955	0.500
[50%, 84%[0.314	0.416	1.493	0.435	0.604	0.492	2.065	0.523
[84%, 100%]	0.361	0.432	1.575	0.453	0.656	0.499	2.183	0.532

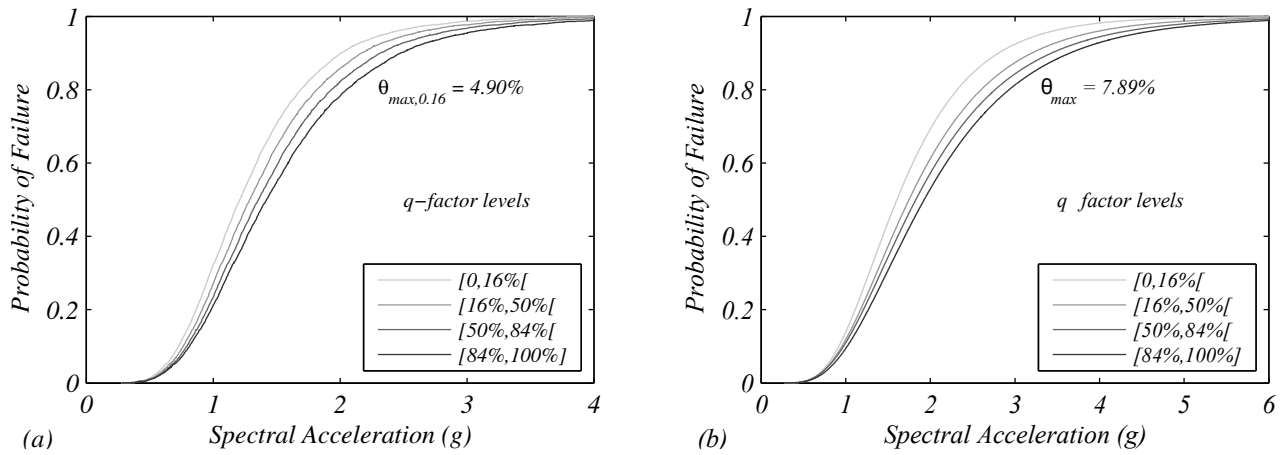


Figure 3.13: Fragility curves for different q -factor levels: (a) Life Safety; (b) Collapse Prevention

3.6 Conclusions

The performance of a heavy-timber structure designed with ring-doweled moment resisting connections was evaluated in this chapter. It is important to note that the results obtained here are specific to one direction of a three-story building. The ring-doweled joints used to connect beams and columns had already been experimentally studied under cyclic testing in Polastri et al. (2013). The results had shown that the connection could fulfill the requirements of EC8 for high ductility class structures. To evaluate the effectiveness of this connection on a prototype structure, a three-story building designed following EC5 and EC8 codes was subjected to a comprehensive seismic performance assessment which included numerical nonlinear static and nonlinear dynamic analysis. OpenSees was used for the numerical analysis, in which the *Pinching4* constitutive model was used to capture the moment-rotation behavior of ring-doweled moment resisting connections, which was calibrated based on testing data available in the literature. The inherent variability of the timber structural members was included in the analysis as modeling uncertainties, which influenced the structural capacity and the notable points used to characterize the hysteretic response of the connections. Using a set of 1000 structural models generated with the Latin Hypercube Sampling method, a probabilistic assessment was performed including spatial variability of strength and stiffness of timber elements and connections properties.

Nonlinear static analyses were first performed to evaluate the variability of limit-state interstory drift ratios and q -factors. The consideration of modeling uncertainties allowed the estimation of a probabilistic distribution of q -factors for the structural set. The main observations from

this part of the chapter were:

- Parameters for the peak value of interstory drift ratio θ_{max} associated with different damage states were obtained. Median values obtained were 1.2%, 4.9%, and 7.9% for the IO, LS, and CP damage states, respectively. In addition, the coefficient of variation of θ_{max} ranged from 9% to 15%, which are relatively low values, specially since modeling uncertainties were explicitly considered;
- The median value of the q -factor obtained from analyses was considerably higher ($q = 7.1$) than the value prescribed in EC8 ($q_{EC8} = 4.0$). Moreover, the median value of the ductility factor R_{μ} obtained was 4.0. These results indicate that the q -factor values considered in EC8 and the detailing requirements defined in EC8 and EC5 are adequate for design of this type of structure.

In a second part of the chapter, a multi-record incremental dynamic analysis (IDA) was performed assuming the first mode spectral acceleration as the intensity measure and peak interstory drift ratio as the damage measure. Main observations from the IDA curves were:

- The results showed that modeling uncertainties have a slight influence on the expected values of the IDA curves for peak interstory drifts ratios lower than 5%. Nonetheless, when modeling uncertainties are taken into account the coefficient of variation increases up to 43%;
- From the disaggregation of the IDA curves according to four different q -factor levels, it was observed that structural models with higher q -factors are more likely to resist ground shaking with higher intensities. These results can be partially explained due to the fact that a positive linear correlation of 0.46 was observed between the q -factor and R_{Ω} ;
- No brittle failures were observed in the dynamic analyses conducted to compute the IDA curves, indicating that the sizing requirements in EC8 are adequate, but potentially too conservative, thus leaving room for improvements of the slenderness of the members and dowels.

Several seismic fragility curves for different performance levels, including Immediate Occupancy, Life Safety, Collapse Prevention, and Global Collapse, were determined using multi-record incremental dynamic analysis. These were based on interstory drifts that were defined considering

the limit-states of the moment-resisting joints and the building capacity curves, specifically for the global collapse estimates. In this case, the main observations were:

- Modeling uncertainties did not affect the median values of the fragility curves associated with IO and LS. However, the coefficient of variations increased by 18% and 13% when the modeling uncertainties were considered for the IO and LS damage states, respectively;
- When modeling uncertainties are neglected an overestimation of the capacity is obtained, both in terms of spectral acceleration and peak interstory drift for the CP and GC damage states, by approximately 3% and 5%, respectively. However, the coefficient of variation did not change for the CP and GC damage states, when modeling uncertainties were considered.

As described above, there is room to perform further experimental tests to evaluate how a reduction in connected elements thicknesses and slenderness of dowels would impact the ductility and strength degradation of ring-doweled joints. Such tests, along with the methodology proposed in this thesis, could contribute to a proposal for new design values and detailing requirements to moment-resisting joints, in future works. Moreover, the variability on the responses observed during this study also indicates that more experimental tests need to be performed in the future to build a database of moment-resisting timber connections. This would also allow for characterization of the uncertainty of the expected model parameters used in design and their correlation with observed joint performance.

Chapter 4

Robustness Assessment of a heavy-timber frame structure

4.1 Introduction

Robustness is commonly associated with the ability of a structure to avoid progressive collapse due to local damage, resulting from an unpredictable event. The unpredictable event, can consist of an unprovoked gas explosion (e.g. Ronan Point apartment tower, in London), a blast from an explosive device (e.g. Murrah building, in Oklahoma, U.S.), undetected material deterioration and design or construction errors (e.g. Siemens Arena, near Copenhagen). Therefore, structural engineering can only truly address a building's vulnerability and robustness, when it comes to the probability of disproportional collapse.

The definition of the adopted terminology is quite important, especially when there is not consensus surrounding many of the common terms used in this field. In this work, failure and damage are terms used interchangeably when applied to structural components, and both mean that the performance criteria established were not fulfilled. For example, a connection is damaged when it failed due to excessive deformation, or a column is damaged due to shear failure. When addressing the whole structure, failure shares the definition established for structural components (not fulfilling performance criteria), while the term damage refers to a deviation from the design state that partially compromises functionality, due to failure of a structural component.

The definition of robustness itself is still up to debate among engineers, building owners, and remaining agents involved. According to the EN-1991-1-7 (CEN, 2006), robustness is the ability of a structure to withstand events like fire, explosions, impact or the consequences of human errors while not being damaged to an extent that is disproportionate to the original cause. ISO (2007) defines robustness as the ability of a structure to withstand abnormal events or consequences of human errors, while not being damaged to an extent disproportionate to the original cause. Another similar definition is given by SIA (2004) where robustness is mentioned as the ability of a structure and its members to keep the amount of deterioration or failure within reasonable limits in relation to the cause.

From these definitions, is possible to understand that the concept of robustness is intrinsically connected with the terms "progressive collapse" and "disproportionate collapse". One considers that a progressive collapse refers to a series of components' failures that resulted from an unrelated initial component failure. It means that an initial, contained collapse provoked a chain reaction of failures throughout the structure. On the other hand, a "disproportionate collapse" occurs when the subsequent structural collapse is exaggerated ("disproportionate") when compared to the initial failure. Therefore a progressive collapse can be disproportionate, but the reverse is not necessarily true (Starossek & Haberland, 2010; Huber et al., 2018). To sum up, the concept of robustness adopted refers to the ability of the structure to withstand a local failure, caused by an unforeseen event, without developing a disproportionate collapse.

To avoid ambiguities in the definition, Starossek and Haberland (2010) proposed the definition of robustness using a probabilistic model, where EX is an exposure or abnormal event acting on a structure, which may cause the local damage, D , which in turn might lead to the disproportional collapse, DC . The probability of disproportionate collapse, $P(DC)$ is determined as follows:

$$P(DC) = P(DC|D) \cdot P(D|EX) \cdot P(EX) \quad (4.1)$$

where $P(EX)$ is the probability of occurrence of a certain exposure, $P(D|EX)$ is the conditional probability of initial damage given the exposure, and $P(C|D)$ is the conditional probability of disproportionate collapse given the initial damage. These probabilities correspond in general terms to exposure, vulnerability, and robustness (Starossek & Haberland, 2010). The work

presented in this chapter focuses exclusively on robustness analysis, which corresponds to the quantification of the conditional probability of disproportionate collapse given the initial damage $P(DC|D)$.

4.1.1 Review of progressive collapses cases

Infamous cases of progressive collapses include the collapse of the Ronan Point apartment tower (1968), the Murrah Federal Building (1995), and the World Trade Centre twin towers (2001). The progressive collapse mechanisms of concrete and steel buildings, as the ones previously mentioned, have been widely researched, and such effort must also be directed at timber buildings, especially if one takes into consideration the brittle bending and tensile failure of timber elements. Next, a brief review of notable cases that shaped robustness research is presented, followed by a discussion of the two of the most well-known collapses of timber structures (Byfield et al., 2014).

Relevant concrete and steel structures

The progressive collapse of the Ronan Point Apartment Tower can be considered the starting point of studies related to robustness, since many relevant questions were raised regarding the adequacy of existing codes, design methods, and construction techniques. In May 16, 1968, a gas explosion took place in the 18th floor of the 22 story apartment, which completely sheared off the corner walls of the apartment. This led first to an upward progressive collapse and then downward collapse of the corner of the building closest to the explosion site (see Figure 4.1), which was clearly disproportionate to the initial wall collapse. From investigations conducted at the time and research performed throughout the years, it became clear that the main reason for the observed collapse sequence was related to the lack of structural redundancy. When designing the structure, no alternative load-paths were considered, in case unexpected events could interrupt the principal one. In this particular case, these events were related with inappropriate choice of structural system, poor workmanship, and inadequacy of existing building codes (Pearson & Delatte, 2005).

The Ronan Point Apartment Towers were built using the Larsen-Nielsen system, which relied on a structural system of load-bearing wall panels directly supporting floor panels, being all



Figure 4.1: Ronan Point progressive collapse

elements made out of precast concrete, including stairways. Walls and floors were bolted together and the connections were consolidated with dry-pack mortar. One of the obvious problems, was the application of this Danish method to a 22-story building, which completely disregarded the recommendation of its use to buildings of up to 6 stories and did not allow a proper structural design of the building. During demolition, a significant amount of construction errors were also documented, particularly on the connections between walls and floor panels. Another severe problem, concerned the inadequacy of building codes to this type of buildings, both in terms of demand quantification and design recommendations. Existing codes at the time underestimated the wind load, since they did not take into account the increased wind speed with the height of the building, and also did not quantify correctly the effects of fire. Both strong winds and uncontrolled fire could have started the progressive collapse observed due to the explosion, as it was later verified through surveys and testing. Additionally, codes at the time did not include any provisions regarding redundancy or robustness, which could provide structural fail-safes (Pearson & Delatte, 2005). The inability of the structure to withstand the consequences of all these factors pointed out the pressing need to perform significant changes to building codes from several countries and to change the mindset of practitioners, when it came to ensuring global structural integrity in the face of local damage.

The Murrah building, in Oklahoma, U.S., partial collapse in 1995, is relevant, because it clearly points out the importance of having alternative load paths as response to sudden loss of a single column. The building lost a column after a vehicle-borne improvised explosive device (VBIED) exploded nearby, and the two neighboring columns failed in shear, leading to a progressive collapse that propagated nearly to half of the building, as shown in Figure 4.2.



Figure 4.2: Murrah building: (a) intact structure; (b) partial collapse

The combination of specific features of the building are the cause of a disproportionate collapse that killed 168 people. The combination of an open-space architecture with a glazed facade (very low stiffness), in a non-seismic region, led to a lightly reinforced concrete frame structure, with no interior walls or facades that could provide load redistribution, in case of a local failure (Byfield & Paramasivam, 2011).

The biggest tragedy related to building collapse is without a doubt the collapse of the World Trade Center in 2001, but very little research has been done surrounding this case. In a simplified explanation, the structural system can be described as composed by a peripheral rigid frame connected, by a truss system incorporated between the 107th and 110th floors, to a load-bearing central core. There is some discussion surrounding the reason why the towers did not collapse immediately after the impact of the airplanes, which reportedly severed up to 36 perimeter columns in each tower. One explanation suggests that the structural system was able to redistribute the dead-loads from the damaged columns to the surrounding ones by Vierendeel frame action, and possibly due to the presence of the truss system that redirected

loads to the central core (Byfield et al., 2014).

Siemens Arena

A failure of a cycling arena in Ballerup, near Copenhagen, allowed a discussion about robustness design and assessment for large-span timber roofs. As shown in Figure 4.3a, the main structure was composed by 12 meters equally spaced fish belly beams with a free span of 72 m. For the secondary system, the designers opted for simply supported purlins. As shown in Figure 4.3b, two of the main beams collapsed without warning while subjected to normal wind and snow loads. This fact evidences that a human error was the cause of the collapse.



Figure 4.3: Siemens Arena Roof: (a) fish shape truss; (b) failure of two main beams (Munch-Andersen & Dietsch, 2009)

The corner joints of the beams were executed with concealed steel plates and embedded dowels and bolts. Further investigation showed that the cross section of the bottom arch was only 30% of that required. Design errors were the principal reason for the collapse. For instance, the strength of timber elements considered was higher due to mistakes on the consideration of the modification factor k_{mod} . The failure, shown in Figure 4.4a, is justified by the reduction of the effective timber cross section near the joint. It was proved that during structural calculations the presence of connectors and steel plates was not taken into account to evaluate the strength of timber frames. A connection between concrete columns and Glulam elements is shown in Figure 4.4b, where one can see that the rupture was caused by an extended rotation (Hansson & Larsen, 2005). The secondary system was not able to redistribute the loads to other main beams. Indeed, the purlins between the trusses were only moderately fastened resulting in connections with low strength and stiffness. Due to repetition of elements and analogical construction process of timber buildings, it is expected that the same mistakes were done along the structure. In this case the damaged area could increase and cause the whole structure

collapse if secondary system had more stiffness and strength. Considering that all main beams had a much lower strength than the required it might be fair to conclude that the extent of the collapse was not disproportionate to the cause (Munch-Andersen & Dietsch, 2009).



Figure 4.4: Failure of corner connections: (a) due to tension forces (b) due to increased rotation (Munch-Andersen & Dietsch, 2009)

Bad Reichenhall Ice-Arena

The Bad Reichenhall Ice-Arena, shown in Figure 4.5, was built between 1971 and 1972 and consisted of a timber roof structure with a span of, approximately, 75 m. The principal structure was composed by box-girders with glulam upper and lower members connected through lateral boards. The girders were made of 16 meters long sections with finger joints. In this structure, the secondary system was fixed with stiff connections, acting as purlins and lateral bracing. Thus, in case of main girders' failure the structure had the ability to redistribute the loads to adjacent girders.

The structure collapsed without warning on the 2nd of January of 2006, during a period of significant but not extreme snow load. Several reasons were pointed out for the failure, most of them associated with human errors. Indeed, the resistance of the glue to moisture was not appropriate. It was possible to conclude that the thermal radiation between the ice surface and the roof parts, facing the ice surface, led to cooling and thereby increased condensation occurrence. Proper maintenance actions would help to detect that glued-lines and finger joints were significantly damaged. The existence of leaks on roof coating and on drainage system allowed water penetration. Since these minor repairs were not made, the timber elements were being increasingly damaged.



Figure 4.5: Bad Reichenhall Ice-Arena (Munch-Andersen & Dietsch, 2009)

Just like the case of Siemens Arena, some errors in design can also justify the collapse of the Reichenhall Ice-Arena. There are no records including structural integrity examination during building maintenance inspections. For instance, the bending strength was considered for tensile and compression resistance of the glulam elements that compose the top and bottom flanges of the girders. After the structure collapse some investigations concluded that one part of the east side girder failed first. Since the cross bracing system was stiff and resistant the load was transmitted to adjacent girders. Therefore, the load increment on the damaged remaining girders also caused their failure resulting on a progressive collapse that is presented in Figure 4.6.



Figure 4.6: Collapse of the Bad-Reichenhall Ice-Arena (Munch-Andersen & Dietsch, 2009)

Discussion

The Division of Structural Engineering of Lund Institute of Technology wrote a report in 2007 (Fruehwald et al., 2007) about how to learn from structural failures in concrete, steel, and timber structures. The purpose of this study was to quantify sources of errors and to indicate their relative importance for timber structures collapses. Despite their description being succinct, it was possible to conclude that most failures have human errors as original cause. It is also important to point out that the buildings considered were mainly long-span roof structures supported by concrete structures or consisting in timber portal frames. Another important feature of the structures involved in this database is their location. Almost all buildings were placed in central and northern European countries. Thus, the exposures considered do not contemplate earthquakes. In addition, the timber buildings built in earthquake prone areas require an higher level of detailing for connections during the design phase and more attention in the construction phase. This feature can improve considerably the resistance of timber structures built in seismic regions in comparison with the ones built in other zones where earthquake are less likely to occur (Branco & Neves, 2011).

The cases of the Siemens Arena and the Bad Reichenhall Ice-Arena reinforce the idea proposed by Starossek (2006), that alternate load path approach may in certain circumstances not prevent but rather promote collapse progression. They also show that structural failures due to human errors may trigger a progressive collapse if the secondary system is able to redistribute loads. The reason is that timber structures (primary and secondary structural systems) are usually composed of repetitive elements connected by analogical construction principles. This proceeding implies that a mistake, made during design, planning or construction phase, will most likely repeat itself in all identical elements (Fruehwald et al., 2007). In Dietsch (2011) the author defends that for large-span timber roof structures, the primary structure should be more redundant and the secondary system designed to cause damage compartmentalization.

4.1.2 International projects on structural robustness and timber buildings

A research network had as main objective the development of a basic framework and for the efficient and sustainable use of timber as a structural and building material. The COST Action

E55, “Modeling of the Performance of Timber Structures”, was structured into three working groups; a) assessment of failures and malfunctions, b) vulnerability of timber structures and c) robustness of timber structures. Within the scope of the Working Group 3 (Kirkegaard et al., 2010) was the development of a guideline for assessment and design for robustness of timber structures.

Despite the analysis focusing mainly in portal frames and large-span timber roofs, it is possible to conclude, by consulting the guidelines, that compartmentalization is the most efficient strategy to avoid progressive collapse. Thus, the secondary elements that are included in the bracing system should be moderately fastened to the primary structure. Nevertheless, this strategy is not compatible with the seismic recommendations. Thus, it is relevant to study the effects of seismic design on the robustness of timber structures. Moreover, it is important to verify a range of ductility and redundancy level that can satisfy either seismic and robustness requirements. In Branco and Neves (2011), the influence of connections ductility is studied for a long-span timber roof indicating that seismic provisions ensure an improvement towards progressive collapse resistance of this type of structures. Within the scope of COST Action E55, a theoretical framework (Sørensen, 2011) for structural robustness was proposed. This framework is based on the risk and reliability robustness framework proposed by Baker et al. (2008). An example of application of the framework proposed in Sørensen (2011) refers to a sports hall studied in Čizmar et al. (2011). The total area of the sports centre is 5910 m² and consists of a plane frame truss equally spaced at 5 m each, as showed in Figure 4.7.



Figure 4.7: Sports hall in Samobor (Čizmar et al., 2011)

The structure was designed following EC5 (CEN, 2005), whereas the stochastic variables of

glulam members and loads were characterized based on Köhler et al. (2007) and JCSS (2001). In Čizmar et al. (2011), the robustness assessment was performed at a component level by studying only one damage scenario at a time. This methodology can provide a preliminary indication of whether the structure can be considered robust or not. On the other hand, robustness is considered to be related to the disproportionate spreading of structural failure. Consequently, a better indication of robustness requires models that represent the propagation of damage throughout the structure providing an assessment at a system level. Such type of analyses requires sophisticated models that consider both geometric and material nonlinearities.

In addition, it is crucial to use models that incorporate the behavior of connections when subjected to long deformations. This feature is even more important in mid-rise and high-rise timber buildings that are considered a key future development in timber construction. In order to fill this gap, a three-year project (2017-2020) has been recently funded by the Australian Research Council (ARC) Industrial Transformation Research Hub on tall timber buildings (Lyu et al., 2018). This project aims at experimentally and numerically investigate the progressive collapse of mass timber frame buildings with CLT floors. Preliminary experimental tests were already performed on a 2D double-span frame (Figure 4.8) to evaluate: (i) overall ductility, (ii) capacity to develop catenary actions, and (iii) the sole contribution frame systems in resisting progressive collapse.

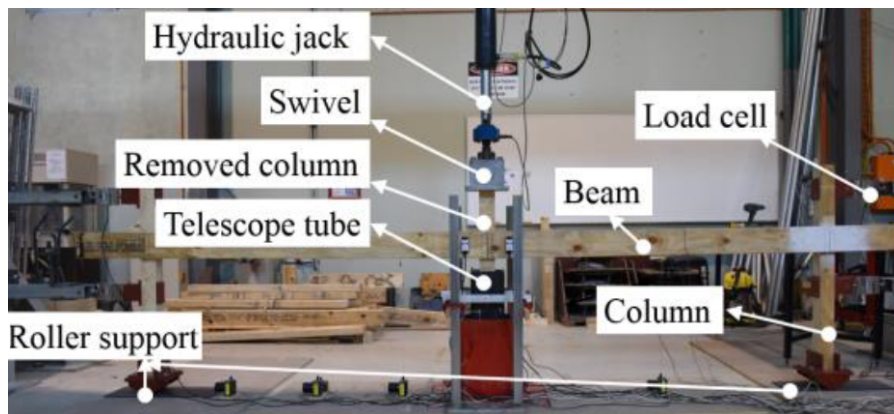


Figure 4.8: 2D Frame test setup (Lyu et al., 2018)

Two distinct connections were used and compared in Lyu et al. (2018). The first connection, shown in Figure 4.9b, consisted of a perforated T-aluminum bracket that has its flange connected to the columns, resulting on a steel-to-timber connection. On the second system, a double beam solution was used where each beam is connected directly to the columns (see Figure 4.9b). One row of seven bolts is used at each beam extreme in a timber-to-timber joint

with two shear planes.

The results indicate that the T-section connectors provided lower rotational capacity hindering the development of catenary action. In addition, the failure, shown in Figure 4.10, occurred when the aluminum web reached its shear capacity. The double beam connectors exhibited rotations that underwent 0.2 rad, which corresponds to the rotation necessary to be achieved in the Department of Defense (2016) for the beams to carry the tie forces Lyu et al. (2018).

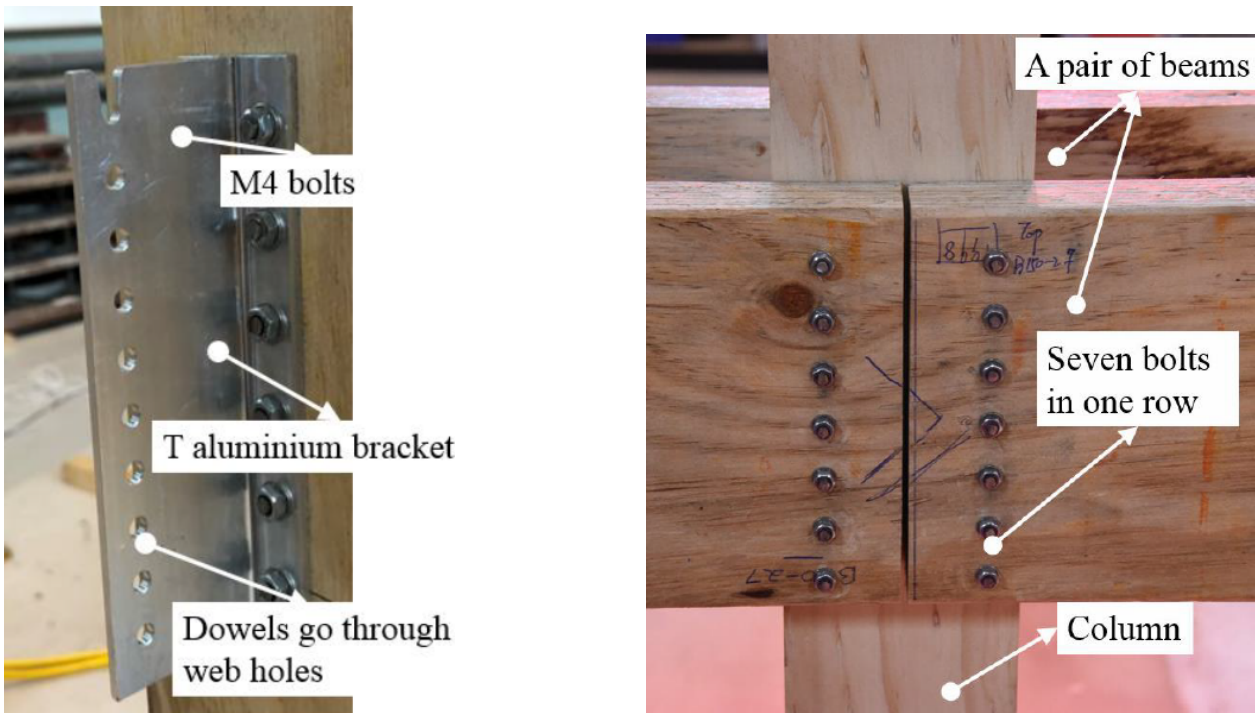


Figure 4.9: Beam to Column: (a) Aluminum alloy T-section perforated bracket (b) Double beam connected with bolts (Lyu et al., 2018)

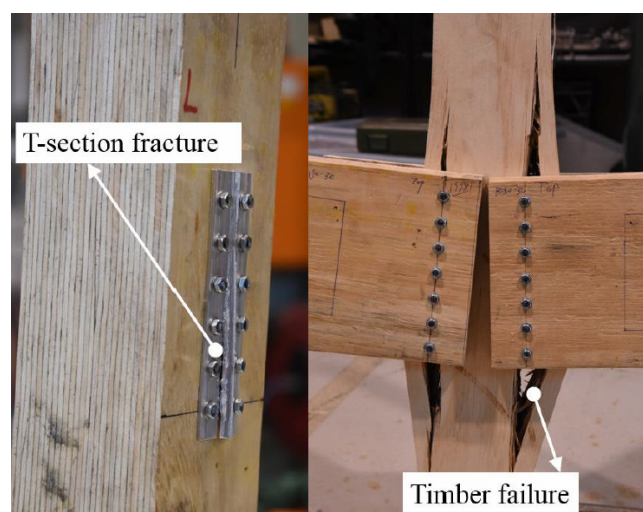


Figure 4.10: Distinct failures of connections in a 2D frame test (Lyu et al., 2018)

Recently, Mpidi Bita et al. (2017) confirmed that design against disproportionate collapse is a

major concern for multi-story CLT buildings. This work was based on dynamic analysis on the Stadthaus building that accounted for material and geometric nonlinearities. A sudden loss of the ground floor internal wall scenario was studied. The main conclusions of this work refers to the lack of rotation capacity of angle brackets and screws in order to develop catenary or membrane actions as resistance mechanisms to avoid disproportionate collapse. These studies focused on the progressive collapse modeling of multi-story timber buildings. Nevertheless, a robustness assessment requires the consideration of uncertainties related to material and loading.

Following a great interest on timber frame construction for medium rise buildings, in the U.K., a feasibility study was commissioned, in 1994, which indicated the need to perform component and large-scale tests, to properly define codes and regulations. As a result, the Timber Frame 2000 (TF2000) project was initiated. As shown in Figure 4.11, disproportionate collapse tests were conducted on a six-story timber frame building that was built in BRE Cardington.



Figure 4.11: Disproportionate collapse test (Mettem et al., 1998)

From the data obtained, several improvements were made to robustness design for platform frame buildings. Design guidelines for horizontal and vertical ties, alternative load-path analysis, and key element approach were performed. From the analysis done during TF2000 project, it was possible to propose minimum values for nails diameters and distributed tie forces on the spans. On the other hand, it was also possible to demonstrate which loads to consider for the design of rim beams, in order to withstand the effect of a notionally removed wall.

4.1.3 Robustness analyses

Although robustness analysis can be performed through three methods - risk analysis, reliability analysis, and deterministic analysis (Cavaco et al., 2010)- this chapter will focus on the deterministic methods. Risk analysis is based on the consideration of probabilities and consequences of structural failures. In this type of analysis, event trees are used to understand the relationship between exposures, damages, failures, and respective consequences. The path starts with the probability of occurring one of many types of exposures, followed by the quantification of the probability of damage. The final branches of the tree would concern the consequences associated with the different paths (see Figure 4.12). Reliability analysis involves the computation of the reliability indexes of damaged and intact structures, which are linked to the probability of failure, via the cumulative standard normal distribution function (Huber et al., 2018). Both methods are probabilistic approaches to the problem and further information can be consulted in Baker et al. (2008); Köhler et al. (2007); Sørensen (2011); Čizmar et al. (2011).

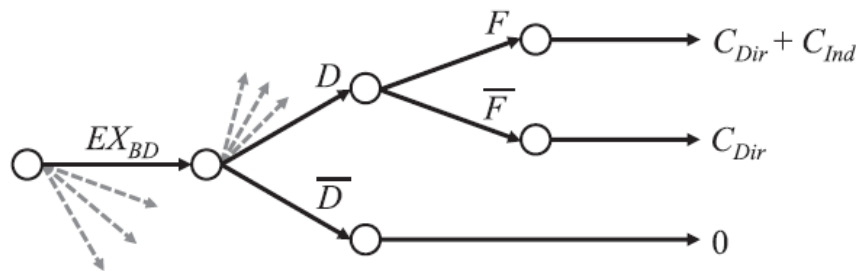


Figure 4.12: Decision tree for risk analysis (Baker et al., 2008)

The deterministic analysis is based on the response of the structure to an initial damage or specific event. The first is scenario-independent and relies on notional damage to assess how the structure reacts, while the second is scenario-dependent and analyzes specific types of exposures such as fire, explosions, etc. Focusing more on the scenario-independent approach, the notional damage is referred as "hypothetical damage to the structure", which in most cases corresponds to the removal of a primary load-bearing element of the structure such as a column (see Figure 4.13). This is implemented by performing an alternative load path analysis (ALPA). With this analysis, one can evaluate the capacity of the structure to promote alternative load paths, after notionally removing an element, and to estimate the extent of progressive collapse (Huber et al., 2018).

In terms of procedures used in ALPA, one has to choose the adequacy of the methods considering the suitability of the method, the complexity of the model and of the procedure itself, and the computational and time costs. There are five types of procedures (Byfield et al., 2014):

- Linear static analysis with dynamic load factors (DLFs);
- Nonlinear static analysis with DLFs;
- Nonlinear static pushover analysis (with simplified dynamic response);
- Linear dynamic analysis;
- Nonlinear dynamic analysis.

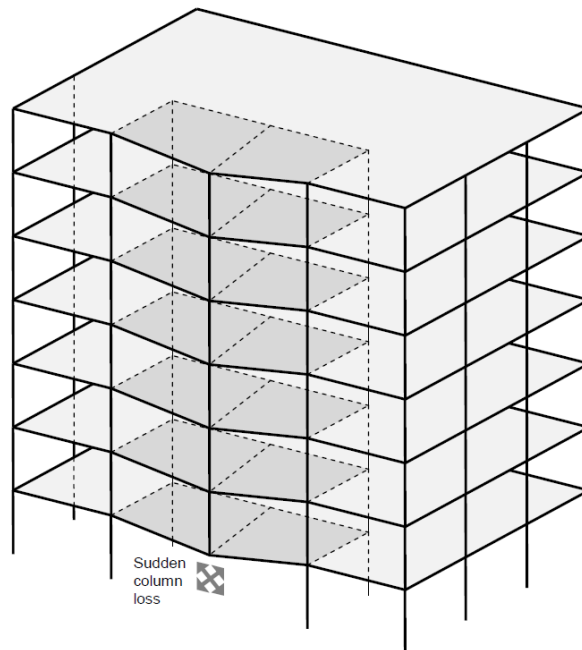


Figure 4.13: Removal of a load-bearing column (ARUP, 2011)

Since removal of an element is a sudden event, choosing a static analysis implies the use of dynamic load factors (DLFs) to take into account the effect of dynamic loads. The DLF affects the dead and live loads considered in the analysis and it can range from 1 to 2, corresponding respectively to fire scenarios and sudden column loss in a linear elastic model. The linear static analysis procedure with DLFs is the easiest to implement of the five procedures, providing very conservative results, since material properties remain linear elastic and does not include second-order ($P - \delta$) effects or instabilities. Therefore, it does not take advantage of beneficial distribution mechanisms (Byfield et al., 2014).

A nonlinear static analysis with DLFs considers material and geometric nonlinearities, which enables the formation of load distribution mechanisms such as catenary action, membrane action, arching action, Vierendeel action, and compression strut action. The first three are important in timber structures, while the two last mechanisms are more common in concrete and steel frames, and masonry walls, respectively. As shown in Figure 4.14a, the catenary or chain action is a tensile mechanism, meaning that it explores the tensile capacity of the beams or floor to distribute the loads, after the removal of an element below. For deep beams, shear strength might be the governing capacity in the catenary mechanism. Ductile connections are essential in the formation of this mechanism, since they have to accommodate some extent of rotation. Membrane or diaphragm action is similar to the catenary action but acts on a plane (see Figure 4.14b). The mechanism results from the development of compression ring forces and tensile membrane forces in the diaphragm, and from the capacity of the connections to accommodate large rotations. The Arching action shown in Figure 4.14c, as the name indicates, results from the formation of an arch between two beams or slabs, therefore is a compression mechanism. The removal of an element below causes rotation at the connections, and when the upper parts of the floors or beams get in contact, compression forces develop, while they crush into one another (Huber et al., 2018).

Although is generally accepted to also use the term pushover analysis to describe a nonlinear static analysis for vertical loads, Ellingwood et al. (2007), cited by Huber et al. (2018) suggests the term pushdown analysis. This term will be adopted in this thesis.

Izzuddin et al. (2008) developed a procedure based on a nonlinear static pushover, which accounts the dynamic load effects through a simplified dynamic assessment, also known as, energy balance assessment. The procedure consists of three steps: (i) performance of a nonlinear static analysis under gravity loading of the damaged structure; (ii) transformation of the nonlinear static response into the maximum dynamic response by energy balance of the system; and (iii) ductility assessment of connections (ARUP, 2011). The procedure proposed is less time consuming and has lower computational cost than a nonlinear dynamic analysis.

Dynamic analysis procedures include the structure's time history response, therefore accounting for the dynamic load effects. These analyses can be linear or nonlinear, sharing the same characteristics already described in the linear and nonlinear static analysis. The nonlinear dynamic analysis is the most complete procedure and gives the most accurate results, since it is

able to incorporate all the specificities in terms of material and geometric nonlinearities, as well as, dynamic inertial loads, damping, and strain rate material effects. In conclusion, simpler procedures lead to more conservative results, in general, which will promote overdesign of the structure. On the other hand, more complex procedures require more expertise and might have higher computational cost, but are more accurate, leading to a more efficient design. In addition, the choice of analysis procedure is also limited by the type of building, particularly by material, height, and regularity in plan and elevation.

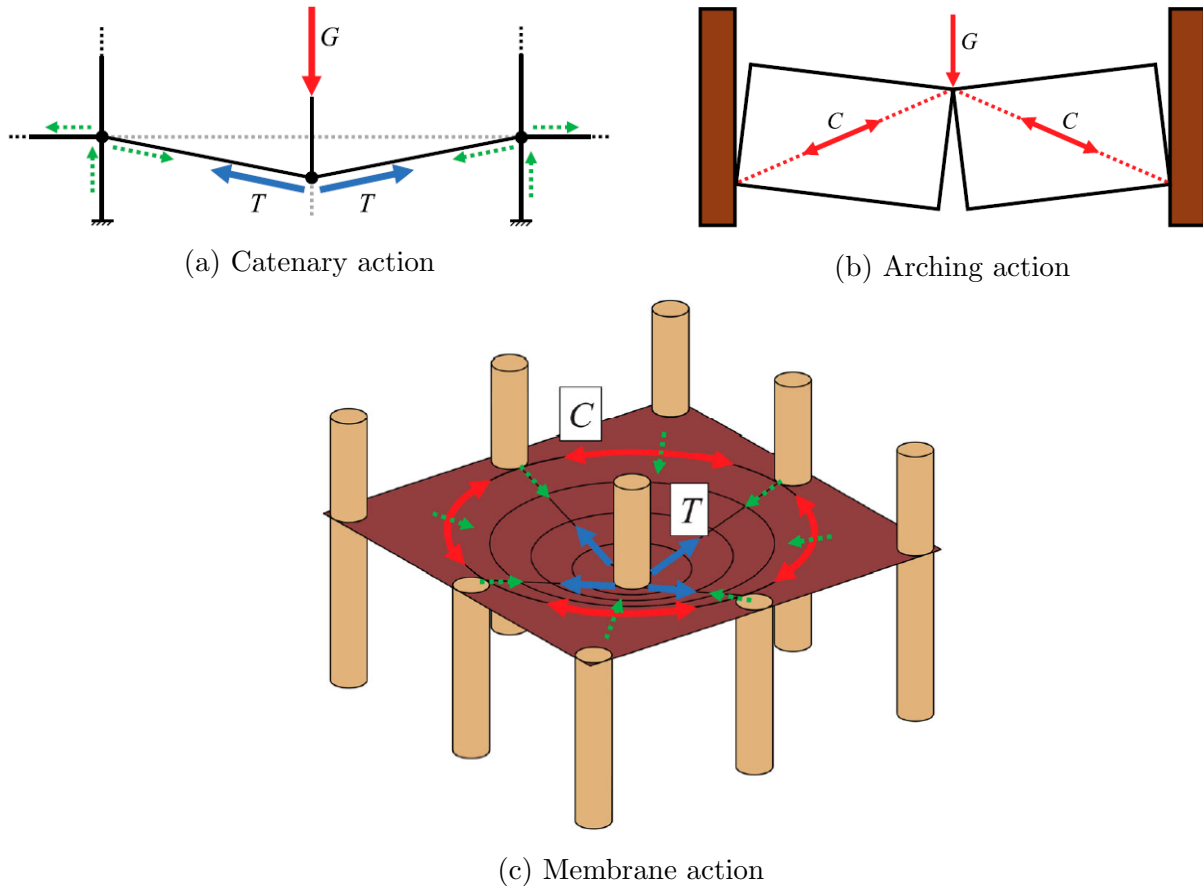


Figure 4.14: Load distribution mechanisms, from ARUP (2011); Huber et al. (2018)

4.1.4 Design procedures, codes and regulations for robustness

The design of redundant structures is one of the main recommendations given to avoid disproportionate collapse due to abnormal loads (Ellingwood & Dusenberry, 2005). In order to increase buildings' global tolerance to progressive collapse, and therefore improve their structural robustness, one must incorporate in the design characteristics such as redundancy, ties, ductility, adequate shear strength, and capacity for resisting load reversals (Ellingwood et al.,

2007). After the sudden loss of a load-bearing member, the structure undergoes large deformations and load redistribution, which require redundant paths for load transfer, continuity between vertical and horizontal members, and capacity to deform and rotate without premature instability. With adequate shear strength, brittle shear failures can be prevented and ductile failures promoted.

While the indirect method is prescriptive, incorporating in the design characteristics that will improve overall robustness, the direct method relies on structural analysis such as the ALPA method to obtain quantitative information regarding building performance (Huber et al., 2018; Ellingwood et al., 2007; Department of Defense, 2016).

The indirect methods are the first step towards design and are scenario independent. General design guidelines contemplate continuity, ductility, and structural redundancy as cornerstones of this approach. Redundancy design methods enable load redistribution and alternative load paths, preventing extensive damage due to local failures (Huber et al., 2018). These alternative load paths must be composed by elements and connections with adequate reserve of strength and ductility (Vogel, 2009), in order to avoid the opposite effect. For timber buildings, robustness is strongly dependent on the structures capacity to redistribute loads to undamaged parts, and thus on their ductility and redundancy. The most detailed and applied indirect method is the tie force (TF) method, indicated for low-risk structures. It ensures that the structural elements are mechanically tied together, providing continuous load-paths. Tying requirements contemplate which elements are to be tied and how, being detailing of the connections very important (ARUP, 2011).

According to Huber et al. (2018), the direct methods include: 1) the alternative path method (ALPA), which was already described in the analysis methods and requires the structure to be able to bridge over a missing load bearing element, while ensuring that the damage is localized, 2) the enhanced local resistance (ELR) method, also known as the specific local resistance (SLR) method or the key element method, which is based on the design of "key" elements to have sufficient strength to resist a specific load or threat, and 3) compartmentalization or segmentation, consists of dividing the structure in compartments that are independently robust.

The ALPA method was already described in section 4.1.3 and its application is proposed in all of the most relevant guidelines (CEN, 2006; Department of Defense, 2016; GSA, 2013). The particularities of which elements to remove depend on the buildings' risk category, being

recommended when more reliable analyses are required. As referred by Byfield et al. (2014), a limitation of the ALPA method is associated with the requirement of removing one element at a time, which does not always agree with reality. For example, in the cases of the Murrah building in 1995 and the WTC in 2001, presented in section 4.1.1, the initial local damage regarded the collapse of three columns, and the collapse of several walls and columns, respectively.

The enhanced local resistance method is a scenario-dependent approach, since certain load-bearing elements are designed to sustain specific loads or to prevent them from failing, making them "key" elements. This method is intended for cases when other design methods can not ensure that a disproportionate response will not take place, therefore used to design elements that failed the ALPA method acceptance criteria. A limitation of this method is related to the possibility of failure of a key element, which will most probably lead to a sudden decrease in performance of the structure, leading to disproportionate collapse (ARUP, 2011).

The compartmentalization or segmentation method is described by Ellingwood et al. (2007) and intends to avoid horizontal damage propagation, by isolating parts of the structure. This can be achieved by strengthening the compartment boundaries and decreasing continuity, reducing load transfer to other parts of the structure. Compartmentalized design is more effective in large and low-rise buildings, and for certain building components, such as long cantilever balconies. For tall buildings, the concept of compartmentalization is materialized in "strong floors" capable of sustaining the additional load caused by falling debris and add stability to the structure. This concept was used in the design of the Treet building, in Bergen, Norway (see chapter 1).

The existing codes and regulations for robustness recommend different design methods to distinct typologies of buildings, depending on their risk category (Department of Defense, 2016) or consequence class (CEN, 2006). The risk categories or consequence classes are defined according to the level of occupancy, size, and function or importance.

The US UFC 4-023-03 (Department of Defense, 2016) establishes four risk categories (RC) for robustness, from I to IV, dependent on other type of risk categories defined in the UFC 3-301-01 (Department of Defense, 2016), which divide buildings according to function, importance, and occupancy. Each category has different robustness design requirements, based on the following admissible design methods: tie force, ALPA, and ELR. Category I refers to low occupancy buildings such as agriculture facilities, which does not require specific robustness design. Category II includes high occupancy family housing and inhabited buildings with less

than 50 personnel. This category has two options of design. A first one that suggests providing vertical and horizontal ties to the entire structure and enhance local resistance of the corner and closest columns or walls to the corner at the first story, and a second option regarding the implementation of ALPA where columns or walls are removed one at a time at specific locations. Buildings in category III represent a substantial hazard to human life or represent significant economic loss in the event of failure (e.g. elementary schools, secondary schools, or daycare facilities with an occupant load greater than 250). Consequently, they require the fulfillment of the acceptance criteria for the ALPA and ELR methods. The latter should be applied to all first story perimeter columns and walls. In category IV, the included structures are considered as essential facilities as power-generating stations, hospitals, fire, rescue, and police stations, and emergency vehicle garages. Besides the requirements of category III (ALPA plus ELR), ties should also be provided. Buildings included in category V, independently of the number of floors, shall be designed with the ALPA method. The US UFC 4-023-03 (Department of Defense, 2016) determines that structural members are acceptable as ties, if they can carry longitudinal, transverse or peripheral tie forces while being capable of rotating 0.20 rad (11.3 degrees). The design for tie forces follows the Load and Resistance Factor Design (LRFD) approach together with requirements and material specific over-strength factors found in ASCE/SEI 41-13 (ASCE, 2014). Requirements for wood can be found in chapter 12 of the latter code. Vertical ties should be straight from top to bottom, but are not required to extend to the foundations. For implementation of the ALPA method, different column or wall removal locations are considered depending on the risk category. In regard to external walls and columns, for RC II-option 1, the vertical elements that can not carry tie forces, should be removed one at a time, while for RC II-option 2, III, and IV, the minimum requirement includes removal of external columns and walls near the middle of the short side, near the middle of the long side, and at the corner of the building. For RC II-option 2, III, and IV, or internal columns and walls near the "middle of the short side, near the middle of the long side and at the corner of the uncontrolled space" should be removed. Additional locations are recommended and there is also room for engineering reasoning in choosing the elements to remove. Recommendations for modeling, acceptance criteria, loading, and other parameters are defined for the three accepted analysis procedures: linear static, nonlinear static, and nonlinear dynamic. All three types of analyses should rely on three dimensional models, clearly expressing that two dimensional models are incapable of characterizing the damage structure. Design also

follows a LFRD approach adapted from ASCE (2010), with the analysis procedures being adapted from the ASCE/SEI 41-13 (ASCE, 2014). Structural elements should be classified as primary or secondary, being the inclusion of secondary elements not necessary for the linear static analysis, and optional for the other two procedures. All component actions have to be classified as force-controlled or deformation-controlled, which will dictate how the acceptance criteria are defined among other parameters. For the ELR method, the clear design objective defined by the US UFC 4-023-03 (Department of Defense, 2016) is that the column or wall must not fail by shear before reaching the maximum flexural strength, promoting a ductile failure mode of the key element. For the design, the LFRD approach is used, where the required shear strength of the column or wall has to be equal or higher than the required nominal flexural strength affected by strength reduction factors (in this case 1).

The European Eurocode 1-7 (CEN, 2006) proposes three consequence classes (CC) according to building categories. These categories are effectively four (1, 2a, 2b, and 3) and to each one of them corresponds a different design approach (DA), from 1 to 4. These approaches depend on the identification of the hazard event type, if it is specified or not. Buildings for single occupancy up to 4-stories, for agricultural purposes and where risk to human life is small or negligible fit into CC1. If they were designed in agreement with EN 1990 to EN 1999, these structures do not need specific robustness design considerations regarding unspecified or specified events (only if the complete collapse of the structure may be acceptable), as prescribed by design approach DA-1.

CC2a concerns buildings with more intensive use and height as single occupancy buildings up to 5-stories, hotels, residential, and offices' buildings up to 4-stories, being considered a lower risk group. For this class, DA-2 approach is recommended, which requires the verification of the design condition for CC1 and the use of structural effective horizontal ties or effective anchorage of suspended floors to walls for framed and load-bearing wall construction.

For CC2b buildings, which comprehends most buildings with a significant occupancy between three or four stories to fifteen storeys, horizontal ties must be provided for framed and load-bearing wall buildings. Furthermore, all supporting columns and walls should have vertical ties ensuring stability. Alternatively to the ties, the DA-3 design approach also states that the stability of the buildings can be checked for a load case that consists on the notional removal of each supporting column and beam supporting a column, or any nominal section of

load-bearing walls (ALPA method). When a specific element removal results in damage greater than a certain acceptable limit, such an element should be designed as a key element. The limit of admissible local failure may be different for each type of building. The recommended value is 15% of damaged area, or 100 m², whichever is smaller, in each of two adjacent stories. Figure 4.15 represents the admissible damaged area. The key element should be capable of sustaining an accidental design load of 34 kN/m² in horizontal and vertical directions (in one direction at a time). This value was obtained from the estimation of the over-pressure resulting from the Ronan Point gas explosion, previously described in section 4.1.4. The safety of these members and any attached components must be evaluated with regard to the ultimate strength capacity. Nevertheless, this load value (34 kN/m²) proposed by CEN (2006) is extremely onerous for timber structures. The Timber Research and Development Association (TRADA) and the UK Timber Frame Association (TFA) suggest that multi-story timber buildings should be designed to avoid disproportionate collapse through the application of adequate ties to resist a notional horizontal force of 7.5 kN/m applied on the notionally removed wall (Harris, 2007).

At last, for buildings belonging to CC3 (all buildings that do not fit any of the previous categories) a systematic risk assessment should be undertaken taking into account both foreseeable and unforeseeable hazards (DA-4 approach), which consists of three steps: (i) assessment of the probability of occurrence of different types of hazards and respective intensities; (ii) assessment of the probability of different damage states to the structure and corresponding consequences from different hazards; and (iii) assessment of the probability of deficient responses of the damaged structure with their respective consequences.

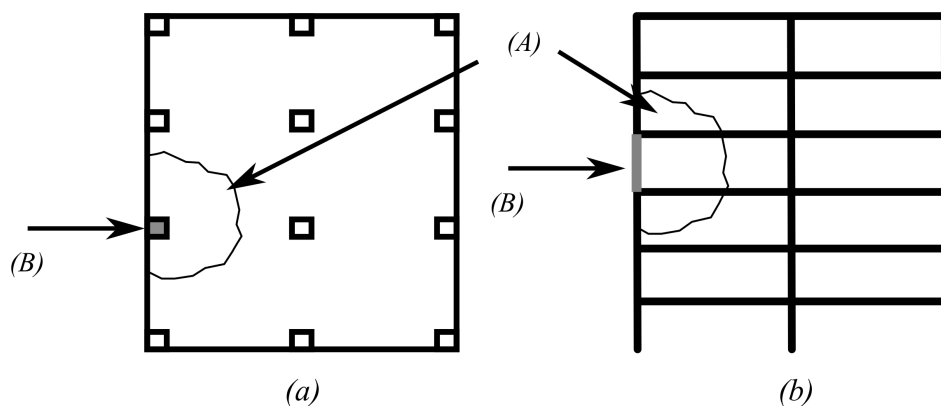


Figure 4.15: Recommended limit of admissible damage: (a) Plan View; (b) Elevation;

The design requirements to resist progressive collapse are covered in other international specifications with different degrees of details. In Australia, the National Construction Code (ABCB, 2015) only states that the structure should remain stable, being able to survive the removal of one isolated load bearing element and that the collapse should not extend further from the original local failure. Another guidance could be found in AS1170.0 (AS/NZS 1170.0, 2002) which provides the general requirements for structural robustness. All parts of the structure should be tied in both horizontal and vertical directions, which allows the structure to withstand an abnormal event without collapsing. Requirements for the tie forces are given in the standard.

4.2 Objectives

The main objective of the present chapter is to evaluate the progressive collapse of heavy-timber structures by considering material and loading variability. The evaluation involves the application of alternative load path method that has been widely applied to steel (Khandelwal et al., 2009; Khandelwal & El-Tawil, 2011) and concrete structures (Helmy et al., 2012). Distinct damage scenarios are considered and the structural responses due to elements loss are evaluated through a large number of nonlinear static analyses (nonlinear uniform pushdown analysis). Consequently, the finite element models account for the post-yielding behavior of connections. Moreover, the nonlinear models account for elements separation due to brittle failure in timber members and connections. Fragility curves are constructed to address the robustness of timber structures built with different diaphragms.

4.3 Methodology

The two three-story buildings used as case studies have the same lateral resisting systems, which are composed by moment-resisting timber frames, previously analyzed in Chapter 3 with 2D models, and braced timber frames. The difference between those structures relies on the diaphragm typologies used in each building. The floors of the first structure were built with a light weight solution with OSB panels fastened to GLT joists. A floor composed by CLT panels was applied on the second structure, being the shear transfer between panels

guaranteed by half-lap joints. Both structures were designed using a modal response spectrum analysis, following EC8 (CEN, 2013b) and EC5 (CEN, 2005), for a site location in Lisbon. Members and connection sizes were determined to verify the requirements for a DCH structure according to EC8. The seismic design provisions followed may lead to an enhanced redundancy, which is deemed adequate to limit the extend of damage due to a localized failure. The robustness assessment presented in this chapter aims to verify if the buildings are able to avoid disproportionate collapse after the notional removal of distinct supporting elements.

The 3D finite element model was built in the Opensees platform, where the first task involved fitting constitutive models to experimental results available in literature. Distinct models were used depending on each connection type. The *Pinching4* constitutive model was used for moment-resisting joints representation, as well as, for joints executed with concealed steel plates. Alternatively, simple linear models were used for shear and withdrawal of connections executed with self-tapping screws.

The progressive collapse assessment is based on the application of the ALPA method, which is a design approach that shall be conducted for buildings comprised in consequence class 2b (CC2b) of European Eurocode 1-7 (CEN, 2006). The nonlinear static analyses are displacement controlled (pushdown analyses), using meso-level connection models. This type of numerical analysis was already applied for robustness assessment of steel structures (J. Park & Kim, 2010). Each analysis starts with the notional removal of a column and consecutive displacement increments of 0.001 m are applied, according with the gravitational loads applied at each story level. The control node is positioned at the beam's end, adjacent to the removed column. It is worth nothing that between two consecutive pushdown steps, a stability analysis is performed at local and global levels. The local assessment is related with failure of timber members and connections, while global assessment refers to the equilibrium of the structure. When a connection fails due to excessive force, the respective zero-length element is removed. On the other hand, a connection that has experienced an excessive applied moment is substituted by a linear elastic zero-length element with zero stiffness (hinged connection). Finally, if a timber member fails due to axial force, shear or bending, a new node is created and the correspondent member is segmented in that particular location.

Although the structure was designed according to the Eurocodes, for the application of the ALPA method the U.S. standard US UFC 4-023-03 was used. This choice was based on the

fact that the latter code (Department of Defense, 2016) is more comprehensive and detailed than Eurocode 1-7 (CEN, 2006), which is currently under revision. The US code recommends 20 percent higher load factor than the European Eurocode 1-7 (1.2 instead of 1.0) for the dead load contribution, making its results more conservative. Hence, the load combination assumed for the alternative path method is given in the format:

$$G = \Omega [1.2DL + 0.5LL] \quad (4.2)$$

where DL is the dead load, LL is the live load and Ω is a dynamic amplification factor. In this work, the nominal gravitational loads are calculated assuming $\Omega = 1$. From the pushdown analysis, an overload factor OF is calculated by the ratio between the load that a damaged structure is able to sustain G_R and the nominal gravity loads G_n .

$$OverloadFactor(OF) = \frac{G_R}{G_n} \quad (4.3)$$

The overload factor can be compared with the dynamic load factor proposed for wood constructions, which is equal to 2.0 (ARUP, 2011). Consequently, for structural models with an overload factor greater than 2.0, one can assume that seismic design provisions allow to fulfill the requirements for the robustness design according to the alternative load path method.

Considering the designed structure, all numerical analyses account for uncertainties in the member mechanical properties and material parameters that influence the strength and stiffness of the connections (e.g. yielding forces and elastic stiffness). It is worth noting that in this chapter the spatial variability is included exclusively to the connections' properties, given their preponderance over the remaining variables. In case of an unpredictable local damage, the rotational capacity of connections between floors and the main beams is crucial to allow large deformations without rupture. However, there is a lack of unified models for rotational response of the connections executed with self-taping screws used in the structure under study. The rotational models proposed are based on basic mechanical principles and may represent a source of uncertainty, which is taken into account by introducing variability to elastic rotational stiffness and ultimate joint rotation.

The Latin Hypercube Sampling (LHS) was used in this study to generate a set of 1000 structural models, for both buildings, in which each model corresponds to a realization of the random variables assumed. The total number of pushdown analyses developed corresponds to the product of the number of models ($N_{Sim} = 1000$) in each structural set ($N_{Set} = 2$) and the number of element loss scenarios considered ($N_{Ele} = 4$). Consequently, the progressive collapse assessment presented in this work implies the performance of 8000 nonlinear static pushdown analysis.

Fragility functions were defined for different damage state levels by fitting a lognormal distribution to the values of the overload factor that caused the exceeding of predefined demand threshold values. These damage state levels were based on the rotational capacity of floor-to-beams connections and on the extent of the damaged area. The first failure state (FF) is reached when any floor-to-beam connection exceeds their moment capacity. In turn, collapse prevention (CP) limit state is exceeded when the damage is extended to an adjacent bay. This is evaluated by verifying the safety of moment-resisting connections and glulam members.

4.4 Case study: a three-story heavy-timber frame building

The structure under analysis is a residential three-story building with three 3-m high stories. The design considered serviceability limit states and ultimate limit states from EC5 (CEN, 2005) and EC8 (CEN, 2013b). The governing loading for the connections design was the seismic action. On the other hand, members sizing was determined to guarantee an appropriate stiffness that ensure the fulfillment of the serviceability limit states in terms of long-term deformations and floor vibrations.

4.4.1 Lateral resisting systems

The frame elements used in the lateral resisting systems are made of GL24h that correspond to glued laminated timber defined per EN14080: 2013 (CEN, 2013a), with characteristic bending strength equal to 24 MPa and a mean value of modulus of elasticity of 11.5 GPa. The major

length of the building is aligned with the X-direction and consists of a moment-resisting frame as presented in Figure 4.16a. The moment-resisting frame structure has continuous 13.2 m long beams with a cross-section of 160 by 600 mm. The columns consist of two posts each with a rectangular cross-section of 160 by 600 mm. The connections between columns and beams are executed with ring-doweled joints with two layers of connectors. As presented in Figure 4.17a, the first layer of connectors is composed by 10 dowels located 165 mm from the center, and the second layer by 16 dowels located at a radius of 240 mm. All dowels are from strength class 4.6 with a diameter of 12 mm. At the foundation level, the column shoes consist on pinned connections executed with welded steel plates and $\phi 50$ stainless steel dowels. The column shoe presented in Figures 4.17a and 4.17b, consist of a hinged connection with a low rotational stiffness.

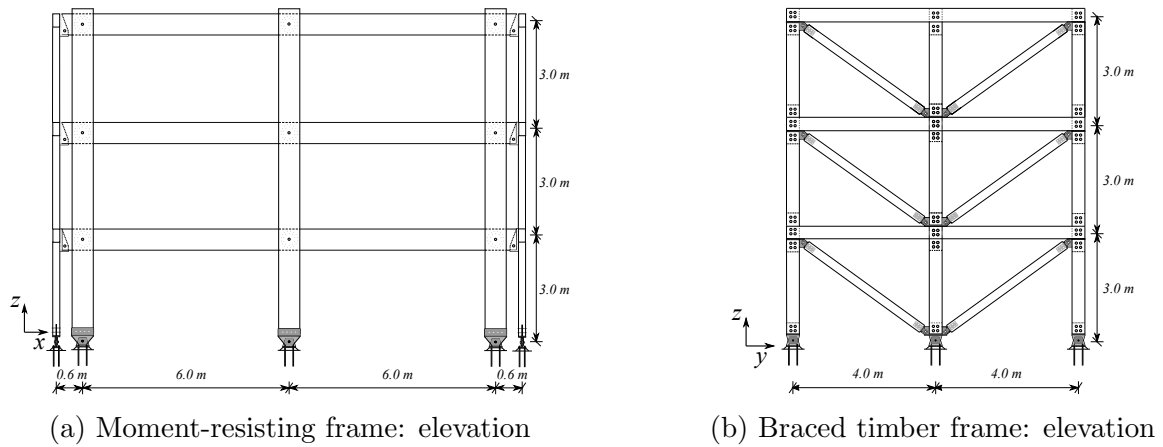


Figure 4.16: Lateral resisting systems

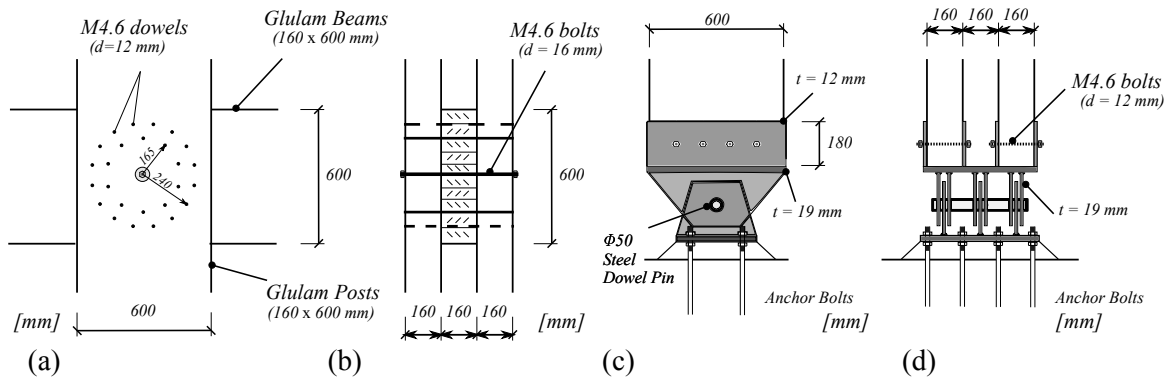


Figure 4.17: Moment-Resisting Frame: (a) ring doweled joint-elevation; (b) ring doweled joint-section; (c) shoe for columns-elevation; (d) shoe for MRF columns - elevation

On the perpendicular direction, the lateral resisting system makes use of GLT members interconnected through concealed steel plates and bolts. As presented in Figure 4.16b, continuous beams with a cross-section of 200 by 360 mm span over two 4-m long bays. The columns have

the same cross sections as the beams and their base shoes are built with slotted in steel plates that are welded to a pinned support as shown in Figure 4.18. The diagonals have a cross-section of 140 by 240 mm. Their end connections are executed with lateral steel plates and 4.6 steel grade bolts with diameter equal to 12mm. These plates are welded to a support that is connected to the concealed plates through a $\phi 40$ stainless steel dowel. These connections details are presented in Figure 4.19. In order to guarantee a connection between the two different lateral systems, a bearing plate is connected to the beams and columns of the braced-frame system, as presented in Figure 4.20. A single M12 bolt is used to connect the beams oriented perpendicularly to the concealed steel plate. This connection allows rotation in the plan of the moment-resisting frame.

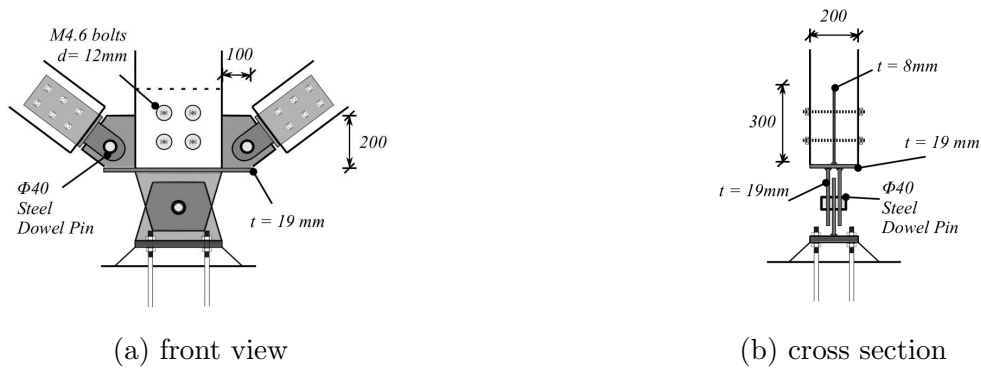


Figure 4.18: Column shoe from braced frame system

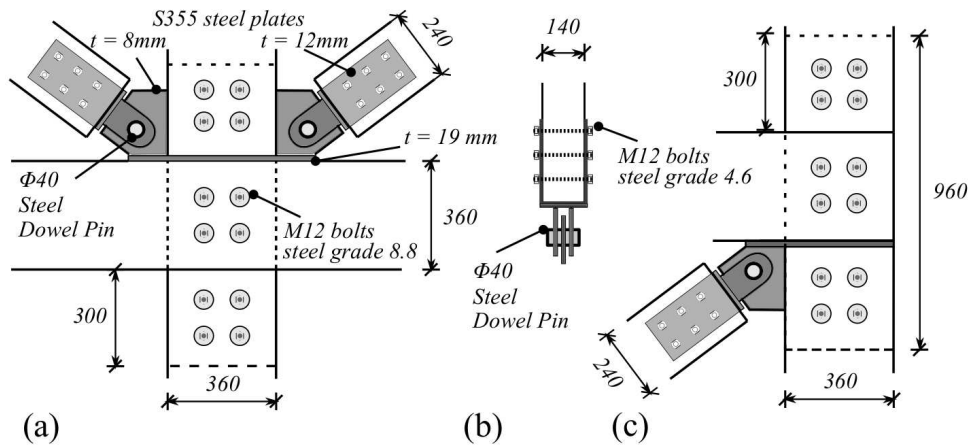


Figure 4.19: Braced timber frame: (a) connections between diagonals and other frames; (b) diagonal cross-section; (c) connections between diagonals and other frames

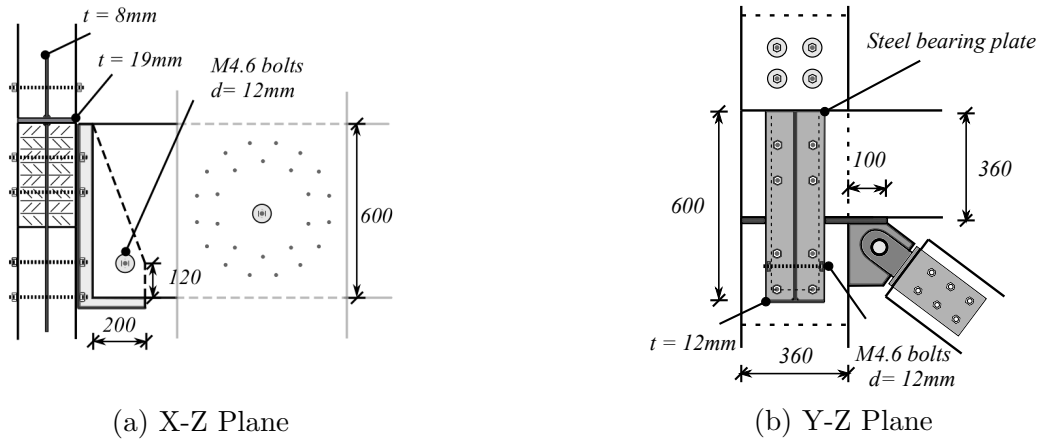


Figure 4.20: Connections between moment-resisting frames and braced frame system

4.4.2 CLT floor diaphragm

The CLT solution used for the floor is built with 5-ply panels (nominally 140.0 mm thick) with the major strength along the Y-direction of the building. The panels are manufactured with lumber from strength class C24 according to EN 338: 2016 (CEN, 2016). Due to construction constraints, related with the continuity of columns, the panels adjacent to the braced frames span over only one bay, having a 4 m free span, while the others are continuous over two spans as showed in the plan view presented in Figure 4.21.

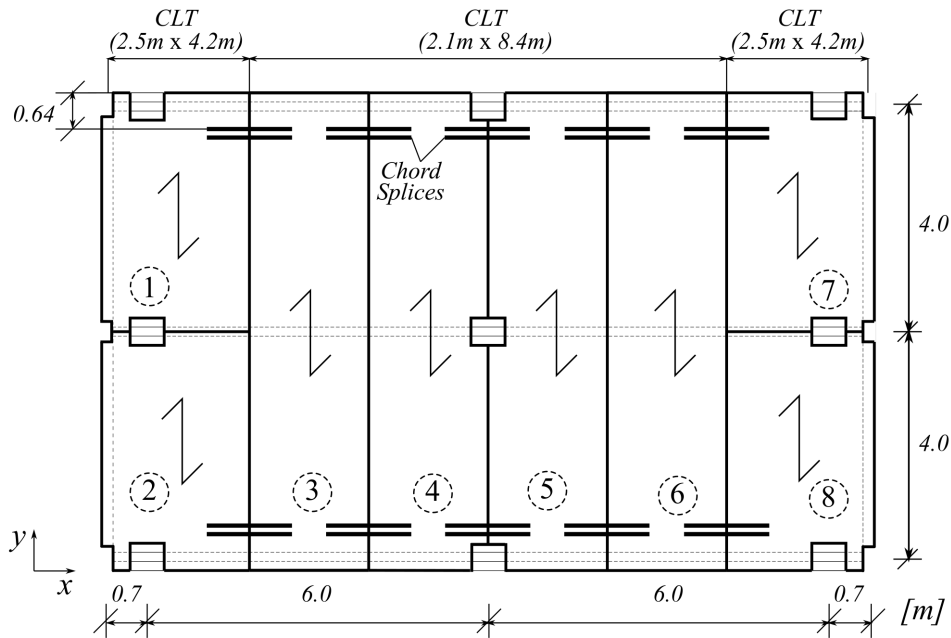


Figure 4.21: CLT diaphragm - plan view

The connection between CLT panels and beams is executed with ASSY plus VG 8 x 260 mm

that are fully threaded self-taping screws with a head diameter (d_h) of 22 mm. Figure 4.22a presents a construction detail from a beam edge, next to a column. Given the interruption of the connection between CLT and beams, caused by the columns position, the ASSY plus VG screw used to fix the panels placed at the corners of the diaphragm are spaced 150 mm on center. The remaining panels are fixed with screws spaced 200 mm on center. These fasteners were designed to allow the transfer of inertial loads from the diaphragm to the seismic lateral resisting systems. A support block made of solid wood was used to guarantee a sufficient bearing length for interrupted CLT panels placed at diaphragms edges, as presented in Figure 4.22c.

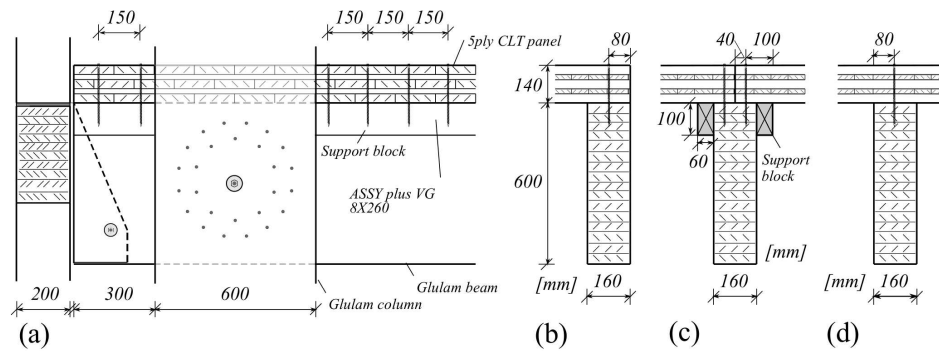


Figure 4.22: Construction details for overlap connections between CLT and glulam beams

The shear transfer between adjacent CLT panels is guaranteed through half-lap joints with 100 mm wide laps. The connection is executed with ASSY 3.0 ecofast 8x120 mm spaced 100 mm on center, as presented in Figure 4.22b. The diaphragm moments are resisted by tension chords that consist of S235 structural steel plates (6.35 mm x 50.8 mm x 1500 mm), that meet the requirements of standard EN 10025: 2004 (CEN, 2004a). These plates are fastened to the CLT panels with Simpson Strong Tie 6.4 x 90 HEAVY-DUTY connectors spaced 60 mm on center, as shown in Figure 4.23.

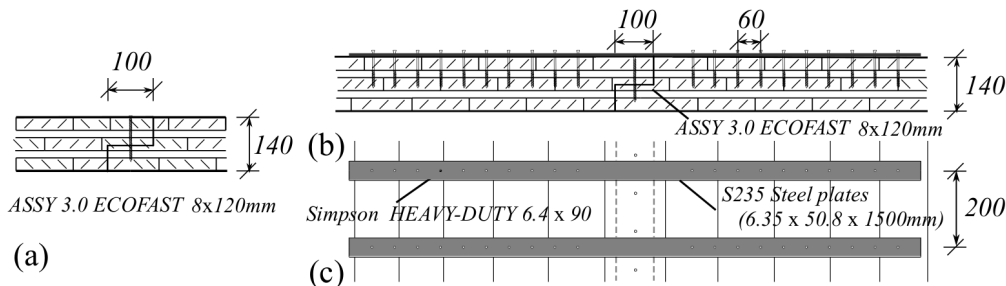


Figure 4.23: CLT diaphragm - chord splices

4.4.3 Light-weight diaphragm

The diaphragm studied in this work consists of a low weight solution composed by GLT joists and OSB panels, as shown in the plan view presented in Figure 4.24. The top layer of the floor is parquet that is placed over a leveling 20 mm thick layer of mortar, followed by 18 mm thick OSB panels fixed to the GL24h joists with a cross-section of 120 by 200 mm. The fasteners used to fix the panels to the GLT members are the S10SND5E (2.8 x 60) stainless steel ring shank nails produced by Simpson Strong-Tie. The nails are spaced 100 mm on center at the panels edges, and spaced 250 mm for inner connections over joist. In order to transfer shear loads from the diaphragm to GLT members of the lateral resisting system, the nails are also spaced 100mm on center at those connection, as shown in Figure 4.25a.

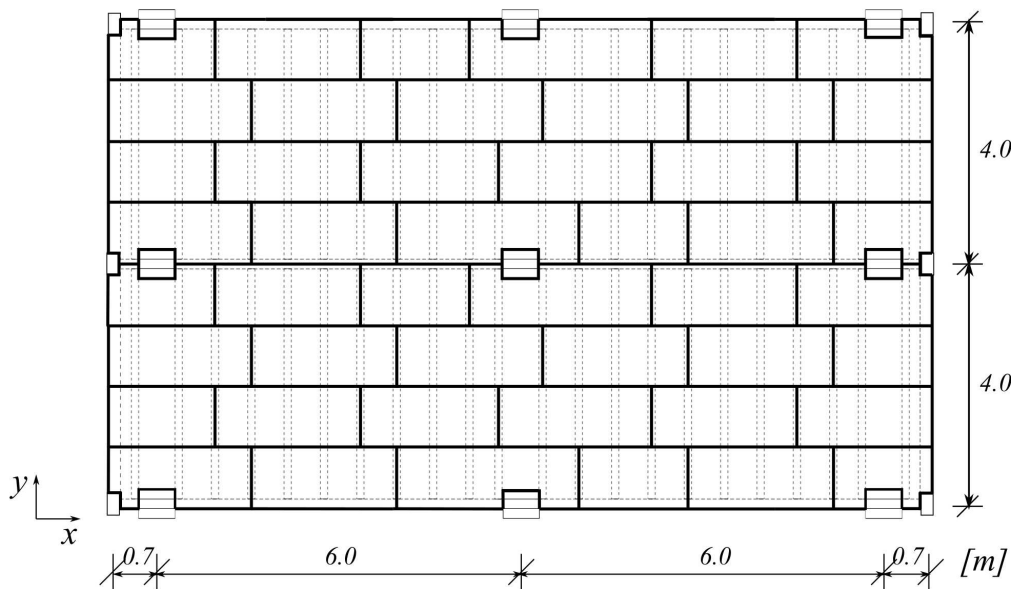


Figure 4.24: OSB diaphragm - plan view

In order to ensure an adequate shear strength for the connections between joists and beams, those joints are made with two WT-T-8,2x190 carbon steel screws fastened at 45 degrees, which results on a concealed connection presented in Figures 4.25b-4.25e. A solid timber block is fastened to the GLT beams, in order to restrain out-of-plan rotation and torsional rotations of joists ends.

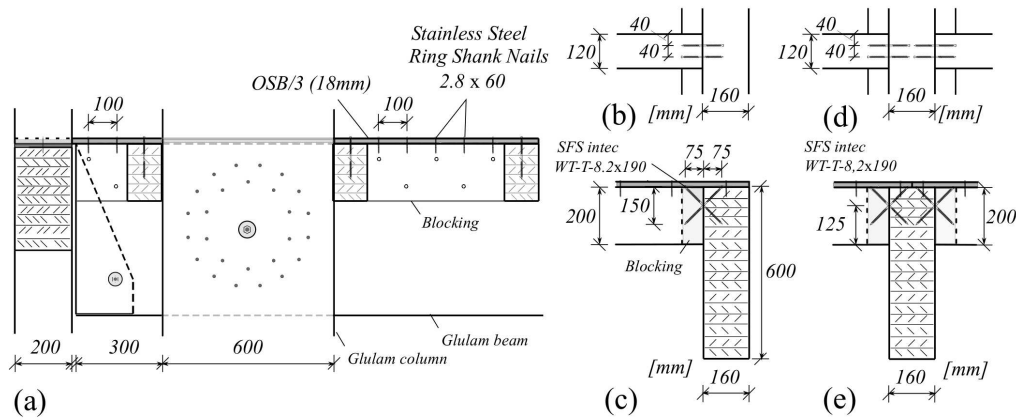


Figure 4.25: Connections between OSB diaphragm and the lateral resisting systems

4.5 Finite element modeling and analysis

The beams and columns were modeled using linear elastic frame elements, while the CLT and OSB panels were modeled with elastic orthotropic ShellMITC4 four node elements (Dvorkin & Bathe, 1984). Geometric nonlinearities were incorporated in the form of $P - \Delta$ effects for columns and corotational transformation for beams. The connections were represented by zero-length elements that account for their nonlinear behavior. Force-deformation relationships were incorporated considering experimental results available in the literature. The modeling strategy adopted for the diaphragm is based on the work presented in Chapter 2, while the representation of ring-doweled connections is based on the method presented in Chapter 3. Figure 4.26 presents an overview of the numerical model developed in Openses framework.

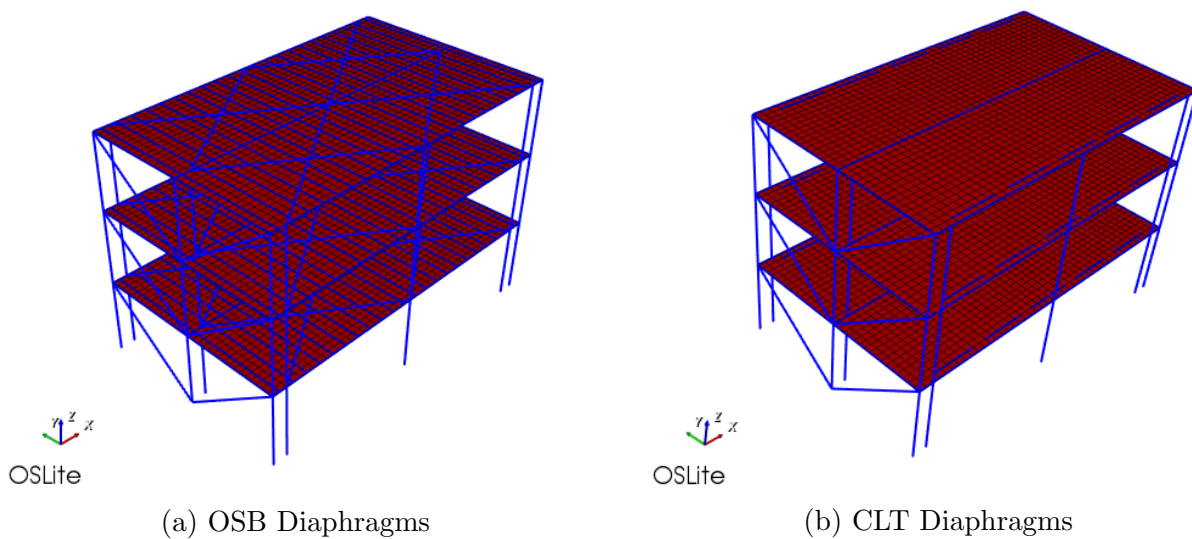


Figure 4.26: Finite element model

The Newton–Raphson method is used to solve the nonlinear algebraic system of equations. The tolerance adopted is 10^{-8} on the inner product of the unbalanced load and displacement increments at each iteration. In addition, the Umfpack package was used to construct a sparse system of equations given the number of degrees of freedom considered in the numerical model.

4.5.1 Numerical modeling of members and connections

Progressive collapse assessment of timber structures requires sophisticated finite element models that are able to predict large displacements. In order to achieve reliable results with the application of the alternative load path method, it is important to incorporate constitutive force-deformation models for connections based on experimental results that give special emphasis on the post-yielding response. This task involves a literature review to collect experimental data from monotonic and cyclic tests developed for connections that are similar to those executed in the prototype building under study. Despite using nonlinear static pushdown analysis to perform ALPA, the envelope curves used to represent the connections are preferably based on fully reversal cyclic tests. When a bearing element is suddenly removed, a nonlinear dynamic response is triggered. Consequently, it is preferable to seek for cyclic tests rather than monotonic that may also provide nonconservative values for properties as yielding strength, initial stiffness, and ductility. The calibration procedures made use of a single-degree-of-freedom model that was implemented in Opensees. The parameters of the *Pinching4* model, already described in chapter 3, were determined in order to reach an accurate approximation between experimental and numerical results in terms of strength degradation and dissipated energy. However, there are connections schemes that were only tested through monotonic tests, in these cases attention is paid only to fit the parameters of an envelope curve (see Figure 4.27) to the experimental results. In addition, some joint configurations have specificities that can be modeled either by other numerical formulations with different uniaxial materials (Mazzoni et al., 2006) or by properly assuming constraints between distinct nodes through the EqualDOF command available in Opensees framework.

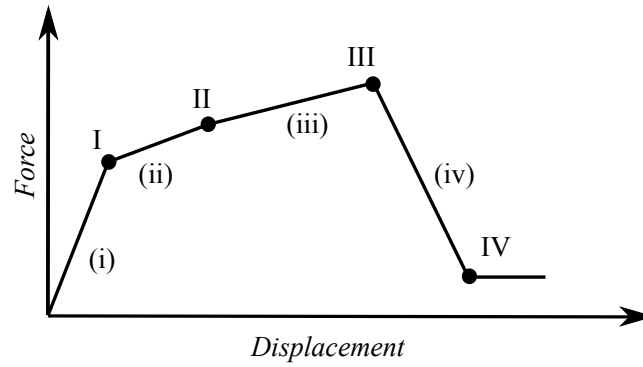


Figure 4.27: Envelope Curve for *Pinching4* model

Dowel-type connections with concealed plates

The connection between columns and beams from the braced frame system make use of slotted-in 8 mm thick steel plates fastened to glulam elements through M12 threaded bolts from 8.8 steel grade, as shown in Figure 4.19. Despite the absence of cyclic tests developed in this particular connection, several monotonic tests have been carried out in order to assess the adequacy of EC5 (CEN, 2005) design values for strength and stiffness properties. In addition, these studies provided good references to validate numerical simulations for steel-to-timber connections executed with concealed steel plates or side steel plates (Quenneville & Mohammad, 2000; Dorn et al., 2013; Zarnani & Quenneville, 2014; Y. Zhang et al., 2016). From the tests performed in Dorn et al. (2013) it is possible to verify a standardized response of single dowel-type connection to uniaxial tension tests. This type of response is characterized by distinct loading phases that can be identified in Figure 4.28a. In addition, the length of each load phase is related to timber and dowels geometric and mechanical properties (Dorn et al., 2013; Y. Zhang et al., 2016). In the scope of this thesis, the experimental results used to adjust envelope curves for *Pinching4* numerical model were performed in Dorn et al. (2013) and resulted from uniaxial tension tests on single dowel steel-to-timber connections loaded parallel to the grain direction, as showed in Figure 4.28b.

The calibration of an envelope curve is commonly done by fitting the numerical response to the first loading phase, decrease of stiffness phase and loading plateau. First loading phase (*i*) is used to define the elastic stiffness through a linear fitting to the results. A decrease of stiffness (*ii*) occurs gradually by reaching the compression strength in part of the wood matrix and the growth of plastic deformation of dowels. The loading plateau (*iii*) is more evident for specimens with lower density. This three phases can be identified in Figure 4.29 where the experimental

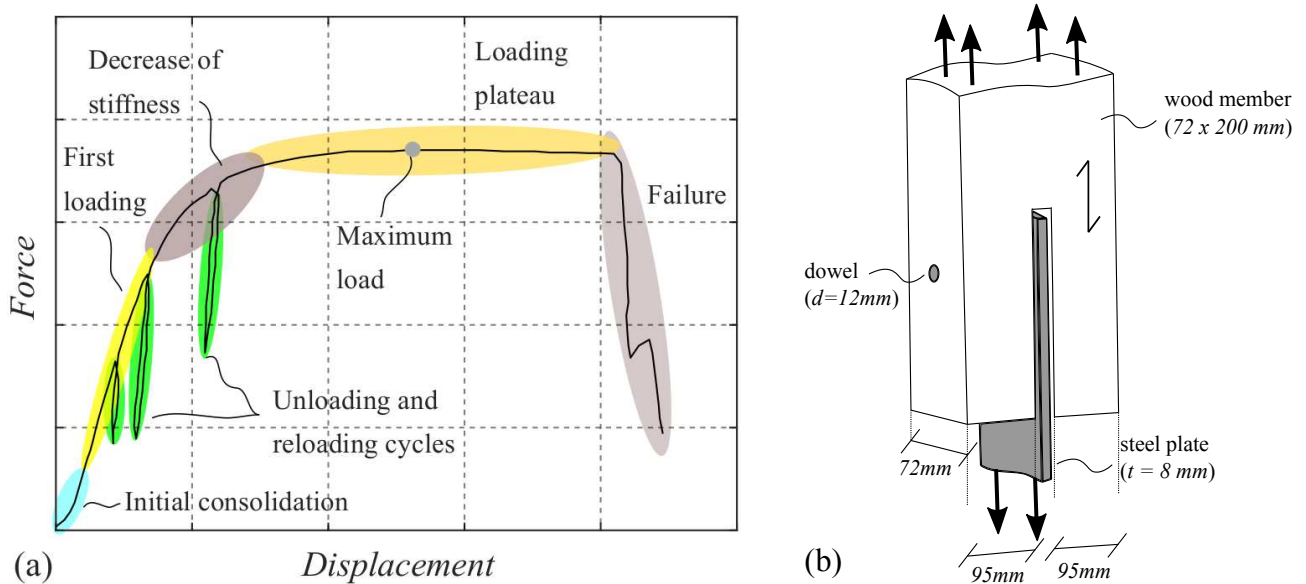


Figure 4.28: Steel-to-timber joints with center plate (Dorn et al., 2013): (a) typical single-dowel response; (b) connection scheme

results are presented. The wood specimens used in these tests were made of Norway spruce having a cross-section of 72 x 200 mm² with a 10 mm slot at the center where a 8 mm thick S 355 steel plate was inserted. The 12 mm diameter dowels used were sanded to increase their roughness. In addition, tensile tests performed on dowels revealed a mean ultimate strength equal to 708 N/mm².

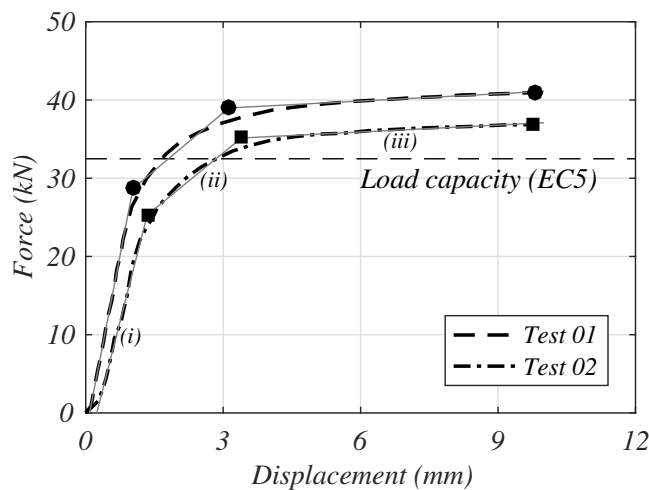


Figure 4.29: Experimental results for steel-to-timber joints with center plate (Dorn et al., 2013)

Linear branches with distinct slopes were adjusted and allowed to define different points for the response envelope, as presented in Figure 4.28b. The load-carrying capacity, highlighted in Figure 4.29, was calculated according to EC5 (CEN, 2005) formulae for symmetric dowel connections

$$F_{v,Rk} = \min \begin{cases} f_{h,1,k} \cdot t_1 \cdot d & (f) \\ f_{h,1,k} \cdot t_1 \cdot d \left[\sqrt{2 + \frac{4 \cdot M_{y,Rk}}{f_{h,1,k} \cdot t_1^2 \cdot d}} - 1 \right] & (g) \\ 2.3 \sqrt{M_{y,Rk} \cdot f_{h,1,k} \cdot d} & (h) \end{cases} \quad (4.4)$$

where $F_{v,Rk}$ is the characteristic load-carrying capacity per shear plane (in N).

Three distinct failure modes are considered for this connection scheme. The mode (f) occurs frequently in connections with low slenderness and consist in splitting failure due to embedment of timber and low dowel's deformation. Failure mode (g) is associated to a central plastic hinge in the dowel combined with plastic deformations in wood (intermediate slenderness). The third failure mode (h) is characterized by a central plastic hinge and secondary plastic hinges inside wood layers. In equation (4.4), the characteristic embedment strength along the grain direction $f_{h,1,k} = 0.082(1 - 0.01 d)\rho_k$ is given in N/mm² with d in mm and ρ_k in kg/m³, the characteristic plastic moment of the dowel $M_{y,Rk} = 0.3 f_{u,k} d^{2.6}$ is given in Nmm with dowel's ultimate tensile strength given in N/mm². For the mechanical properties of the materials used in the tests, presented in Figure 4.29, the failure mode (g) was the one predicted by equation (4.4) with a load value of 32.5 kN. It is worth noting that EC5 (CEN, 2005) does not provide any restriction on the maximum allowable displacements. A yield displacement prediction can only be done by determining the connection's stiffness through the slip modulus (per shear plane) $k_{ser} = \rho_m^{1.5} d/23$. A initial stiffness equal to 18.2 kN/mm was determined considering a measured density of 424 kg/m³. It is worth noting that the connection studied has two shear planes and EC5 (CEN, 2005) suggests that the slip modulus of steel-to-timber connections shall be multiplied by 2.0. However, this prediction does not consider member's thickness nor the roughness of dowel, which can influence the response in terms of strength and stiffness as demonstrated in Dorn et al. (2013) and Y. Zhang et al. (2016).

As presented in the previous chapters, the mechanical properties calculated by code formulae present important deviations from the values observed through testing. Figure 4.29 presents the difference between the load-carrying capacity calculated using EC5 (CEN, 2005) and the results obtained. These differences can be evaluated in Table 4.1, where the elastic stiffness obtained in both tests are also compared with the value provided by the code.

The *Pinching4* envelope curve that can be used to represent the test results is determined with the mean values of forces (*I-III*) and stiffness (*i-iii*). However, the connections used at the

Table 4.1: Strength and stiffness comparison between monotonic tests (Dorn et al., 2013) and EC5 calculations for steel-to-timber connections with a single dowel

Test 01				Test 02			
	F_i [kN]		K_i [kN/mm]		F_i [kN]		K_i [kN/mm]
<i>I</i>	28.7 (-11.7%)	<i>i</i>	30.24 (66.2%)	<i>I</i>	25.3 (-22.2%)	<i>i</i>	23.0 (26.4%)
<i>II</i>	39.0 (20.0%)	<i>ii</i>	4.92	<i>II</i>	35.1 (8.1%)	<i>ii</i>	4.80
<i>III</i>	41.0 (26.2%)	<i>iii</i>	0.31	<i>III</i>	36.9 (13.4%)	<i>iii</i>	0.30
$K_{EC5} = 18.2$ kN/mm							
$F_{v,R,EC5} = 32.5$ kN							

three story building under study make use of multiple bolts. According to EC5 (CEN, 2005), the effective number of fasteners in a row is dependent on the type of fastener and the direction of loading relative to the grain. The reduction in row capacity parallel to the grain for bolts is given by:

$$n_{ef} = \min \left\{ n, n^{0.9} \sqrt[4]{\frac{a_1}{13d}} \right\} \quad (4.5)$$

where n_{ef} is the effective number of bolts or dowels in a row parallel to the grain, a_1 is the bolt spacing in the grain direction, d is the diameter of the bolt, and n is the number of bolts in the row.

Considering a 100 mm spacing between fasteners at the same row, as shown in Figure 4.30a, the effectiveness of bolts is 83.4%. For loading perpendicular to the grain there is no reduction on the load-carrying capacity. When bolts are loaded due to moments the force makes a 45 degree angle to the grain direction. Given the connection's configuration, it is possible to consider that for moment-resistance the bolts are aligned in a row. However, the embedment strength is reduced for directions that differ from the grain direction, as presented in equation (3.12), which has direct impact on the load-carrying capacity of the connection. In this work, the forces per fasteners are multiplied by the factor $c = F_{v,Rk,0}/F_{v,Rk,\alpha}$, where $F_{v,Rk,0}$ is the load-carrying capacity for the grain direction and $F_{v,Rk,\alpha}$ is the load-carrying capacity for a direction at an angle α . Considering this feature, the load-carrying capacity perpendicular to the grain is 70% of the one determined in the mean values of the test, while the capacity in a direction at 45° is 81.5%. The envelope curves per bolt are shown in Figure 4.30b.

The translational behavior of the connection can be modeled by just multiplying the envelope

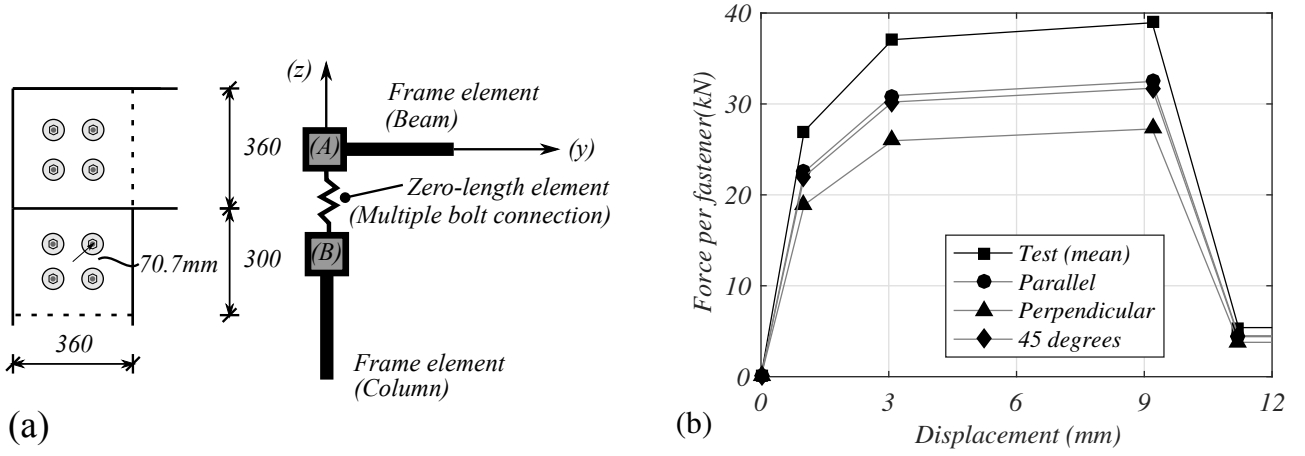


Figure 4.30: Multiple bolts connection at braced frame system: (a) OpenSees model for joint; (b) *Pinching4* envelope curves for single bolts with center plate

forces by the number of fasteners ($n=4$), as presented in Figure 4.31a. In order to determine the envelope curve for moment-rotation relationship, one can consider that for a small angle of rotation, the fastener slip can be expressed by

$$s = r \tan(\theta) \cong r\theta \quad (4.6)$$

where r is the distance of the fastener to the rotation center of the group of fasteners and is assumed to be unchanged during rotation. In turn, s is the slip of the fastener and θ is the rotation angle. On the other hand, the moment of a multiple-bolted joint can be determined from equilibrium as given by equation (3.9) for ring-doweled connections. Thus, the moment-rotation ($M - \theta$) pairs which define the envelope curve are presented in Figure 4.31b. The values used to define the envelope curves for *Pinching4* model are presented in Table 4.2.

Table 4.2: Envelope curve parameters to define the response of multiple bolted connections

Direction Y Envelope curve			Direction Z Envelope curve			Direction X Envelope curve		
Point	F_i [kN]	d_i [mm]	Point	F_i [kN]	d_i [mm]	Point	M_i [kN.m]	θ_i [rad]
<i>I</i>	75.6	1.01	<i>I</i>	90.1	1.01	<i>I</i>	6.22	0.014
<i>II</i>	103.8	3.09	<i>II</i>	123.7	3.09	<i>II</i>	8.54	0.044
<i>III</i>	109.0	9.18	<i>III</i>	129.9	9.18	<i>III</i>	8.97	0.130
<i>IV</i>	15.1	11.21	<i>IV</i>	18.1	11.21	<i>IV</i>	1.25	0.159

The nodes (*A*) and (*B*), presented in Figure 4.30a, were forced to have the same displacements in X-direction as well as the same rotations along Y and Z directions. These conditions are enforced by using the *equalDOF* command included in Opensees.

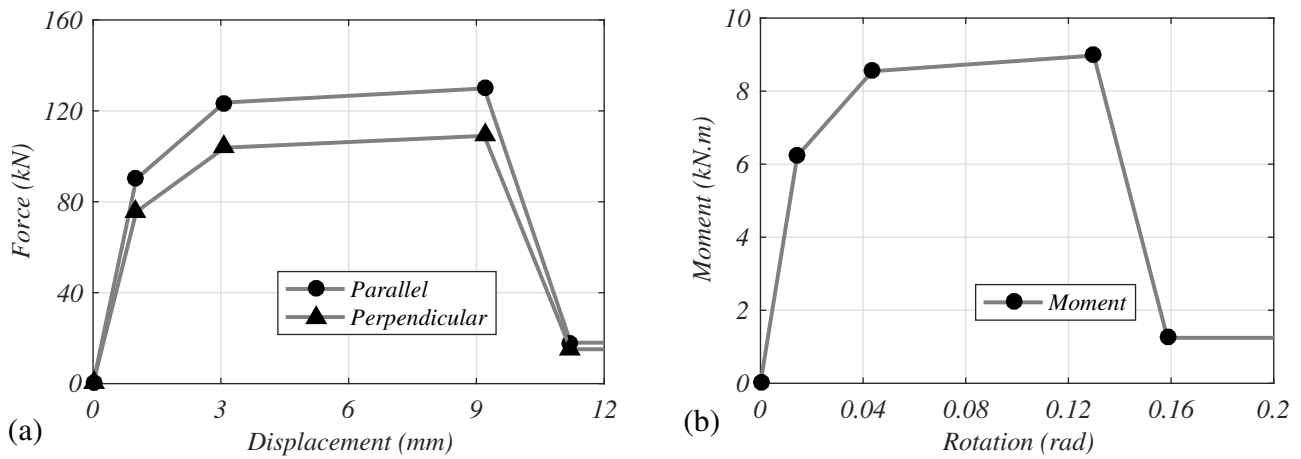


Figure 4.31: *Pinching4* envelope curves for multiple bolted connection: (a) Force-displacement; (b) Moment-rotation

Steel-to-timber joints with side steel plates

The braced frame connections used in the present work were executed using 12 mm thick side steel plates. The glulam members are 140 mm thick while the fasteners used are M12 bolts from 4.6 steel grade. Regarding experimental tests that involved monotonic and cyclic tests of this type of connections, the most extensive and relevant work found was developed in Popovski (2000). The results obtained from fully reversal cyclic tests on riveted and bolted connections are also presented in Popovski et al. (2002). The experimental results used to calibrate *Pinching4* model refer to a connection executed with six 12.7 mm diameter bolts that showed an average ultimate tension stress of 497 MPa. The glulam members used to study the connections had a cross section of 130 by 304 mm² and a average wood density of 403.8 kg/m³. The same calibration approach described for joist-to-beam connections was used to fit a numerical model for steel-to-timber connections (see Figure 4.32).

Despite some discrepancies between the materials used in this thesis and the ones used in Popovski (2000), the parameters obtained from the calibration process can be directly applied to the median envelope curve that is used in the pushdown analyzes of the ALPA proposed. The *Pinching4* parameters that resulted from fitting the numerical model to the experimental results can be consulted in Table 4.3. The parameters used to account for pinching are $r_{Disp} = 0.60$, $r_{Force} = 0.25$, and $u_{Force} = 0.05$.

To properly model the connections between diagonals and columns it was necessary to consider them as pinned. This is guaranteed by assigning a very low stiffness (0.001 kN.m/rad) to the

zero-length element rotational stiffness along X-direction. On the other hand, all the joints from *A* to *E* (see Figure 4.33) are constrained to have the same rotations along Y and Z directions as well as the translations along X direction. The zero-length element that represents the side-plates connections are oriented along the longitudinal axis of the diagonal members. The properties of the zero-length element along its longitudinal direction are presented in Table 4.3. Despite being considered a truss member, it is necessary to include the transversal behavior for the zero-length elements. Thus, the approach followed for bolted connections is also applied here by multiplying the envelope forces by 0.70 to account for the lower embedment strength capacity at the perpendicular direction to the grain.

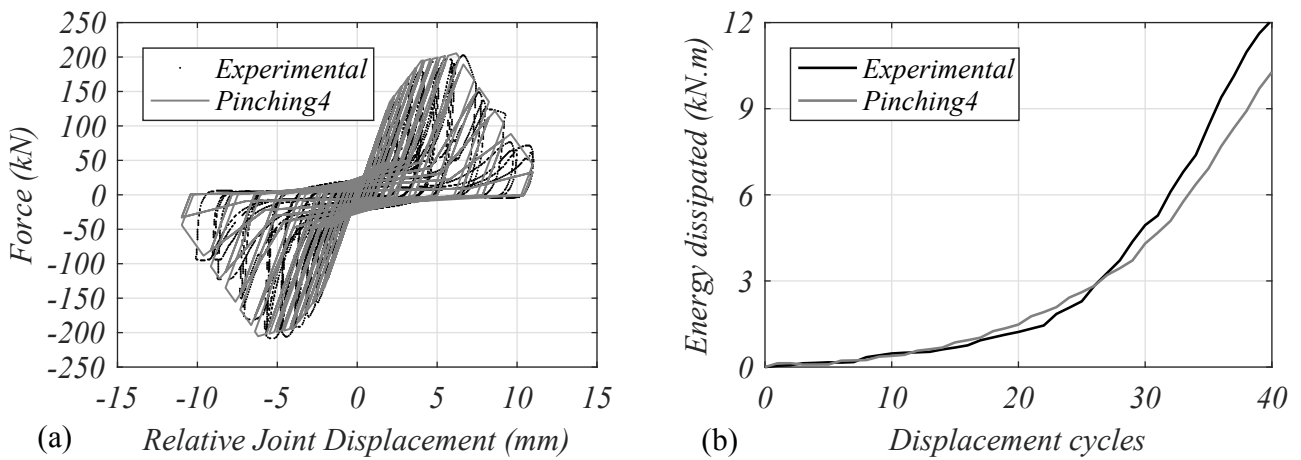


Figure 4.32: Steel-to-timber joints with side plates: (a) experimental tests and numerical results; (b) energy dissipated: test versus numerical results

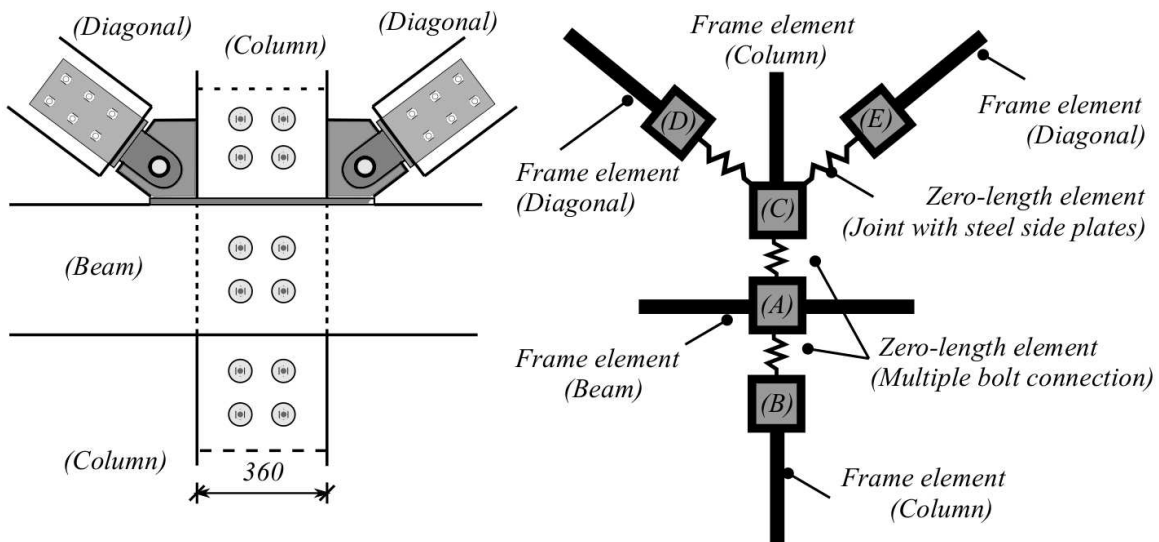


Figure 4.33: Numerical modeling of connections within the braced framed system

Table 4.3: Parameters used to define *Pinching₄* model to represent steel-to-timber joints

Cyclic backbone curve			Cyclic degradation			
Point	F_i [kN]	d_i [mm]	Parameter	δ_{d_i}	δ_{f_i}	δ_{k_i}
<i>I</i>	141.6	2.0	α_1	0.05	0.05	0.05
<i>II</i>	212.4	4.0	α_2	0.01	0.1	0.1
<i>III</i>	229.4	6.2	α_3	1.0	1.0	1.0
<i>IV</i>	28.3	11.2	α_4	0.1	0.1	0.1

Half-lap joints with screws at 90 degrees connections

The shear transfer between adjacent CLT panels is guaranteed through half-lap joints made with the stainless steel ASSY 3.0 ECOFAST 8x120 screws placed at 90 degrees every 100 mm. A similar half-lap joint, presented in Figure 4.34, was subjected to cyclic tests in Closen (2017). The main differences between the half-lap joint used in the structure and the ones tested relies on the screws length and on the spacing between them. The fasteners used in Closen (2017) are the ASSY 3.0 ECOFAST 8x90 spaced 64 mm on center. These difference can be considered by adjusting the results according to the effective number of fasteners in a row, given by equation (4.5) and by evaluating the influence of members thickness on the governing failure mode.

The experimental results are presented in Figure 4.35(a), as well as, the ones obtained with a calibrated numerical model. These results correspond to the force-displacement response of a singular screw. Table 4.4 presents the values used to define the envelope curve and the parameters referent to cyclic degradation. In addition, the parameters used to account for pinching are $r_{Disp} = 0.50$, $r_{Force} = 0.05$, and $u_{Force} = 0.05$.

Table 4.4: Parameters used to define *Pinching₄* model to half-lap joints experimental tests (Closen, 2017)

Cyclic backbone curve			Cyclic degradation			
Point	F_i [kN]	d_i [mm]	Parameter	δ_{d_i}	δ_{f_i}	δ_{k_i}
<i>I</i>	1.80	1.0	α_1	0.1	0.1	0.1
<i>II</i>	4.32	9.0	α_2	0.1	0.1	0.1
<i>III</i>	6.12	27.5	α_3	2.0	2.0	1.0
<i>IV</i>	0.36	41.5	α_4	0.1	0.1	0.5

The envelope curve presented in Table 4.4 can be adjusted in order to consider the effective number of fasteners of the half-lap joints included in the structural models used for the push-

down analyses performed in this work. In Cloosen (2017), eight screws were used for a 450 mm length connection corresponding to 5.76 (71.9%) effective fasteners. If one considers the same connection with a screw spacing of 100 mm on center, the number of screws is reduced to 4.5. However, the effective number of screws is equal to 3.83, which represents a higher percentage of fasteners (85.1%).

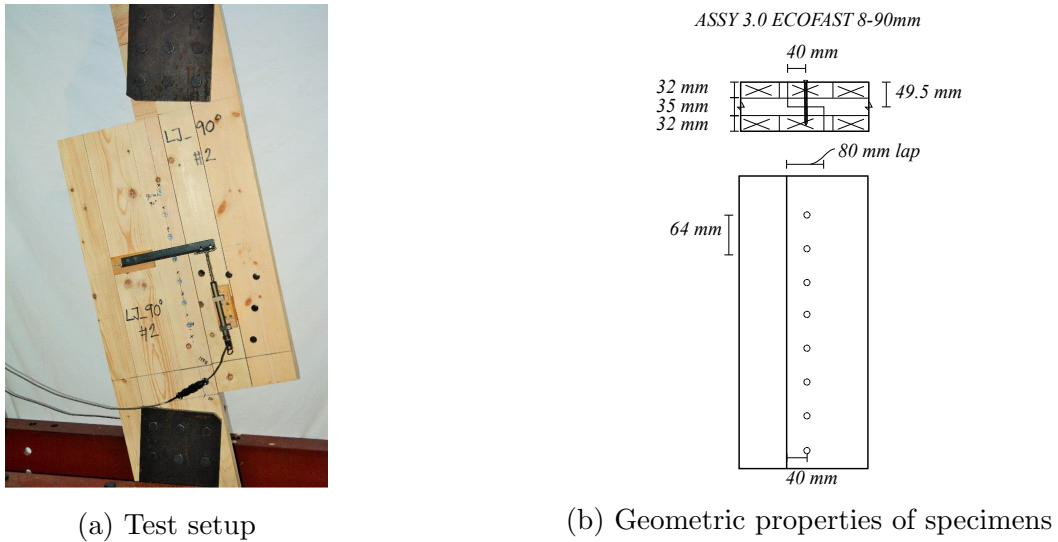


Figure 4.34: Cyclic test layout half-lap joints with screws at 90 degrees

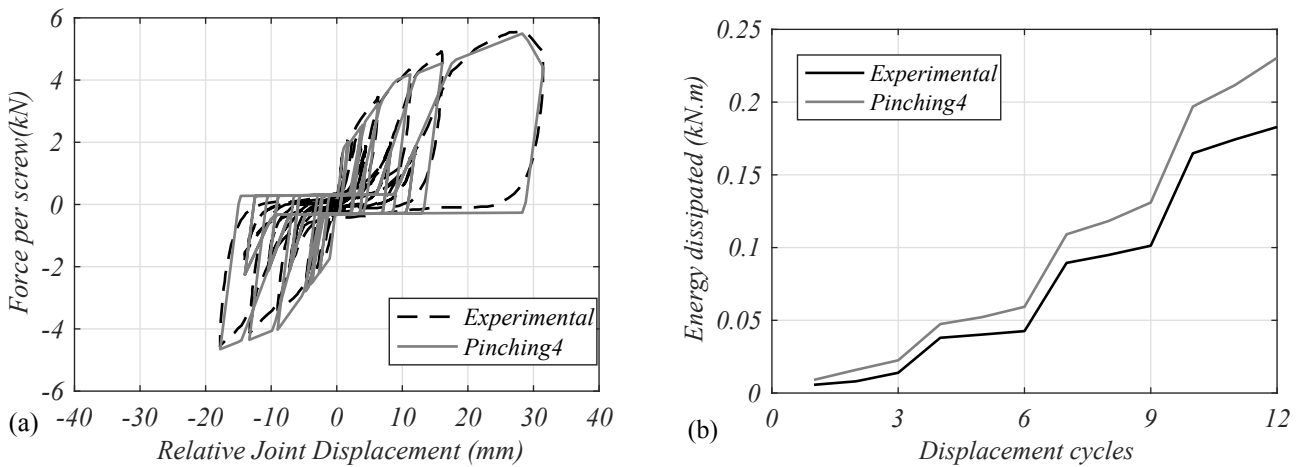


Figure 4.35: Overlap connections between CLT and glulam beams: (a) experimental tests and numerical results; (b) energy dissipated: test versus numerical results

As mentioned above, the thickness of members can play a crucial role on the load-carrying capacity of timber-to-timber joints. Consequently, the values presented for the envelope curve in Table 4.4 shall be adjusted to consider the impact of members' thickness. In this work, it is assumed that the force values shall be multiplied by a coefficient that is given by the ratio $F_{v,l,test}/F_{v,l,built}$, where $F_{v,l,test}$ is the load-carrying capacity per fastener per shear plane

according to EC5 (CEN, 2005) using the geometrical and mechanical properties of the test specimens, while $F_{v,l,built}$ is the equivalent load-carrying capacity per fastener per shear plane but using the properties assigned for the structure studied in this chapter. According to EC5 (CEN, 2005) the load-carrying capacity of a timber-to-timber connection is given by

$$F_{v,l} = \min \left\{ \begin{array}{ll} f_{h,1} \cdot t_1 \cdot d & \text{(a)} \\ f_{h,2} \cdot t_2 \cdot d & \text{(b)} \\ \frac{f_{h,1} \cdot t_1 \cdot d}{1+\beta} \left[\sqrt{\beta + 2\beta^2 \left[1 + \frac{t_2}{t_1} + \left(\frac{t_2}{t_1} \right)^2 \right]} \beta^3 \left(\frac{t_2}{t_1} \right)^2 - \beta \left(1 + \frac{t_2}{t_1} \right) \right] + \frac{F_{ax,R}}{4} & \text{(c)} \\ 1.05 \frac{f_{h,1} \cdot t_1 \cdot d}{2+\beta} \left[\sqrt{2\beta(1+\beta) + \frac{4\beta(2+\beta)M_{y,R}}{f_{h,1} \cdot t_1^2 \cdot d}} - \beta \right] + \frac{F_{ax,R}}{4} & \text{(d)} \\ 1.05 \frac{f_{h,1} \cdot t_2 \cdot d}{1+2\beta} \left[\sqrt{2\beta^2(1+\beta) + \frac{4\beta(1+2\beta)M_{y,R}}{f_{h,1} \cdot t_2^2 \cdot d}} - \beta \right] + \frac{F_{ax,R}}{4} & \text{(e)} \\ 1.15 \sqrt{\frac{2\beta}{1+\beta}} \sqrt{2M_{y,R} \cdot f_{h,1} \cdot d} + \frac{F_{ax,R}}{4} & \text{(f)} \end{array} \right. \quad (4.7)$$

where $f_{h,1}$ and $f_{h,2}$ are the embedment strengths of timber members that are given by $f_{h,i} = 0.082(1 - 0.01d)\rho_i$ for loads parallel to grain direction; t_1 and t_2 are the thicknesses of timber members; d is the outer thread diameter of the screw; β is given by the ratio $f_{h,2}/f_{h,1}$; $M_{y,R}$ is the dowel's yielding moment given by $0.3f_u d^{2.6}$ and $F_{ax,R}$ is the fasteners withdrawal capacity. For screws used on timber-to-timber connections there are three possible failure modes according to EC5 (CEN, 2005): withdrawal of the threaded part of the screw; failure by the screw head pulling through the timber, and screw failure in tension. The following equation is used to determine the withdrawal capacity per fastener:

$$F_{ax,R} = \min \left\{ \begin{array}{ll} \frac{f_{ax,d} \cdot d \cdot l_{ef,1}}{1.2 \cos^2 \alpha + \sin^2 \alpha} \cdot \left(\frac{\rho_1}{350} \right)^{0.8} & (1) \\ \frac{f_{ax,d} \cdot d \cdot l_{ef,2}}{1.2 \cos^2 \alpha + \sin^2 \alpha} \cdot \left(\frac{\rho_2}{350} \right)^{0.8} & (2) \\ f_{head} \cdot d_h^2 \cdot \left(\frac{\rho_2}{350} \right)^{0.8} & (3) \\ f_{tens} & (4) \end{array} \right. \quad (4.8)$$

where $f_{ax,d}$ is the axial withdrawal capacity of the threaded part of the screw (N/mm²), d is the outer thread diameter of the screw (mm), α is the angle between the load and the grain direction of wood, $l_{ef,i}$ is the penetration length (mm) of the threaded part of the screw in a timber member i , ρ_i is the density (kg/m³) of member i , f_{head} is the screw's head pull-

through capacity (N/mm^2), d_h is the head diameter of screw and f_{tens} is the tensile capacity of the screw (N). The screws used in the half-lap joints tests (Figure 4.34a) have a threaded length of 50 mm. The properties used to compute the theoretical load-carrying capacity and the withdrawal capacity per fastener are summarized in Table 4.5.

Table 4.5: Parameters used to compute withdrawal capacity per fastener of half-lap joints tested in Cloßen (2017)

Geometrical and mechanical properties			Withdrawal capacity			load-carrying capacity		
Property	Value	Unit	Mode	Value	Unit	Mode	Value	Unit
$\rho_1 = \rho_2$	420.0	(kg/m^3)	$F_{ax,R(1)}$	1.0	(kN)	$F_{v,l(a)}$	12.6	(kN)
t_1	49.5	(mm)	$F_{ax,R(2)}$	3.9	(kN)	$F_{v,l(b)}$	10.3	(kN)
t_2	40.5	(mm)	$F_{ax,R(3)}$	3.4	(kN)	$F_{v,l(c)}$	5.0	(kN)
d	8.0	(mm)	$F_{ax,R(4)}$	12.0	(kN)	$F_{v,l(d)}$	4.9	(kN)
$M_{y,R}$	11000	(Nmm)				$F_{v,l(e)}$	4.1	(kN)
f_{ax}	11.0	(N/mm^2)				$F_{v,l(f)}$	3.0	(kN)
$l_{ef,1}$	9.5	(mm)						
$l_{ef,2}$	40.5	(mm)						
f_{head}	13.0	(N/mm^2)						
d_{head}	14.8	(mm)						
f_{tens}	12.0	(kN)						

The half-lap joints built within the CLT diaphragms of the three story building under study are executed with stainless steel ASSY 3.0 ECOFAST 8x120 screws that have a threaded length of 80 mm, which implies an increment of withdrawal resistance. This fact can be confirmed by the values presented in Table 4.6. The governing failure mode, according to EC5 CEN (2005) corresponds to mode (f) of equation (4.7), which is a ductile mode, associated to the formation of two plastic hinges in the screw, one within each timber member. From the results presented in Tables 4.5 and 4.6 it is possible to state that the threaded penetration length has influence on the lateral load-carrying capacity for connections with screws.

Finally, the final envelope curve is obtained by multiplying the forces of the experimental envelope curve by two distinct factors that consider the differences between the connection tested experimentally and the one built in the structure. The first coefficient refers to the effective number of screws and is given by $\lambda_{eff} = n_{eff,str}/n_{eff,test}$, where $n_{eff,str}$ is the effective number of fasteners for the connection built within the structure under analysis and $n_{eff,test}$ is the effective number of fasteners for the connection tested. The λ_{eff} coefficient is equal to 1.18. On the other hand, as presented above, the lateral load-carrying capacity of the half-lap joint built in the structure, calculated according to EC5 (CEN, 2005), is higher than the

Table 4.6: Parameters used to compute withdrawal capacity per fastener of half-lap joints used in the structure

Geometrical and mechanical properties			Withdrawal capacity			load-carrying capacity		
Property	Value	Unit	Mode	Value	Unit	Mode	Value	Unit
$\rho_1 = \rho_2$	420.0	(kg/m ³)	$F_{ax,R(1)}$	3.1	(kN)	$F_{v,l(a)}$	17.7	(kN)
t_1	70.0	(mm)	$F_{ax,R(2)}$	4.8	(kN)	$F_{v,l(b)}$	12.7	(kN)
t_2	50.0	(mm)	$F_{ax,R(3)}$	3.4	(kN)	$F_{v,l(c)}$	7.2	(kN)
d	8.0	(mm)	$F_{ax,R(4)}$	12.0	(kN)	$F_{v,l(d)}$	7.1	(kN)
$M_{y,R}$	11000	(Nmm)				$F_{v,l(e)}$	5.4	(kN)
f_{ax}	11.0	(N/mm ²)				$F_{v,l(f)}$	3.5	(kN)
$l_{ef,1}$	30.0	(mm)						
$l_{ef,2}$	50.0	(mm)						
f_{head}	13.0	(N/mm ²)						
d_{head}	14.8	(mm)						
f_{tens}	12.0	(kN)						

one obtained for the half-lap joint tested. The factor that considers this effect is given by $\lambda_{F_v} = F_{v,l,str}/F_{v,l,test}$. For the present connection that value is equal to 1.17.

Table 4.7: Parameters used to define *Pinching4* model to represent overlap connections between CLT and glulam beams

Cyclic backbone curve			Cyclic degradation			
Point	F_i [kN]	d_i [mm]	Parameter	δ_{d_i}	δ_{f_i}	δ_{k_i}
<i>I</i>	2.50	1.0	α_1	0.1	0.1	0.1
<i>II</i>	5.95	9.0	α_2	0.1	0.1	0.1
<i>III</i>	8.43	27.5	α_3	2.0	2.0	1.0
<i>IV</i>	0.50	41.5	α_4	0.1	0.1	0.5

The behavior of half-lap joints is included in the model through zero-length elements that link adjacent nodes of distinct panels. As presented in Figure 4.36, the nodes (*A*) and nodes (*B*) share the same coordinates but are part of different shell elements. The *Pinching4* model with the parameters presented in Table 4.7 represents the connections response for forces aligned with X and Y directions. However, the negative stiffness along X direction (compression) is assumed to be 1000 times higher than the positive initial stiffness. Additionally, recent studies (Macpherson et al., 2018) refer that rotational stiffness modeling has impact on the vertical displacements predictions of CLT floors that use half-lap connections, therefore it should be considered. Based on the results presented in Macpherson et al. (2018) for 140 mm height CLT panels with 100 mm width half-lap joints, an uniaxial material with a constant stiffness equal

to 50 kNm/rad is used to model the rotational stiffness about Y axis. It is necessary to assume some node constraints to guarantee numerical stability. Thus, adjacent nodes from different panels have equal degrees of freedom for vertical displacements and rotations along the vertical axis (Z-Z) and the axis perpendicular to the connection (X-X).

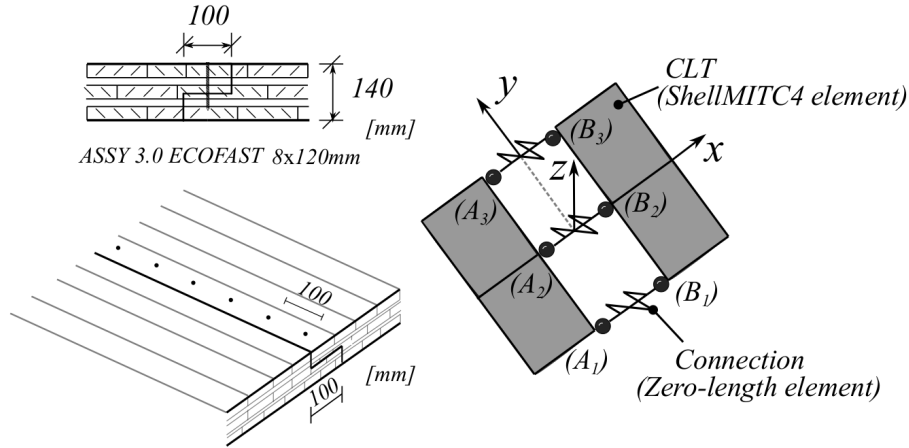


Figure 4.36: Numerical modeling of half-lap connections

Overlap connections between CLT and glulam beams

The overlap connections between CLT panels and beams are executed with ASSY plus VG 8x260 screws placed at 90 degrees. The numerical model used to represent these connections has to incorporate their in-plane behavior and their rotational response. The load-carrying capacity of the overlap connections between CLT and glulam beams can be compared with the response of half-lap joints with screw placed at 90 degrees. In fact, the governing failure mode is the same, which is given by equation (4.7f) as presented in Table 4.8.

The lateral load capacity increased when compared to half-lap joints, due to the larger threaded length of the screw used in these connections. The withdrawal capacity of the connection is now governed by the head pull-through capacity. The final parameters considered to represent the envelope curve of overlap connections between CLT and glulam beams are given in Table 4.9. It is worth noting that these values were calculated considering also the number of effective fasteners per row, as well as, the increase of load-carrying capacity in comparison to the half-lap joint tested in Cloßen (2017).

In terms of rotational response, one should distinguish the behavior of connections located at

the central bay and the ones located at extreme bays. As presented in Figures 4.37 and 4.38 it is assumed that the moments are resisted through a binary of forces for both cases. The force (F_c) is related to wood working in compression, while the traction force (F_t) is associated to the withdrawal capacity of the screw. However, it is important to stress that the rotational stiffness of the connections presented in Figure 4.37 must differ for negative and positive rotations/moments. Given the presence of adjacent panels the negative rotations are almost restrained and as a consequence, the stiffness must be very large when compared to the one assumed for positive rotations. The rotations used to establish the zero-lengths response are computed according to equation (4.6). It is assumed that the displacement s is given by the ratio between the withdrawal capacity, given in Table 4.8, and the axial slip modulus for threaded screws, which is given in DIBT (2013)

$$K_{ax,ser} = 780 \cdot d^{0.2} \cdot l_{ef}^{0.4} \quad (4.9)$$

where the d is the outer thread diameter of the screw (in mm) and l_{ef} is the minor penetration length of the screw in the wood-based member (in mm).

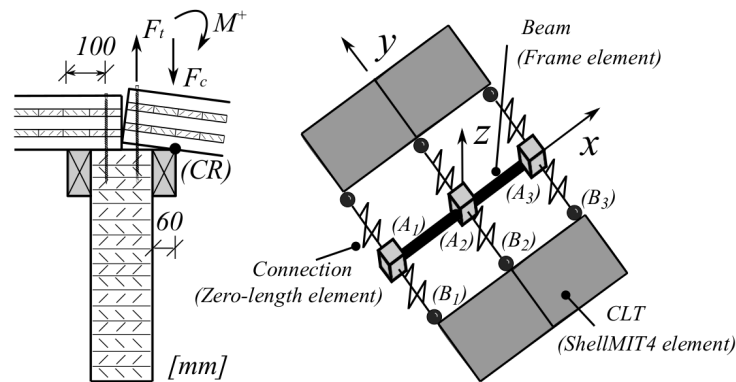


Figure 4.37: Numerical modeling of interrupted overlap connections between CLT and glulam beams

Since the withdrawal failure is brittle, the response can be represented by an elastic link that can be removed after reaching a certain level of deformation. The rotational properties of the zero-length elements, presented in Table 4.10, were computed considering that the maximum axial slip for one screw is equal to 0.70 mm.

It is worth noting that nodes from shells and nodes from frames, which share the same coordinates had to be constrained to have the same displacements along vertical axis (Z) and the

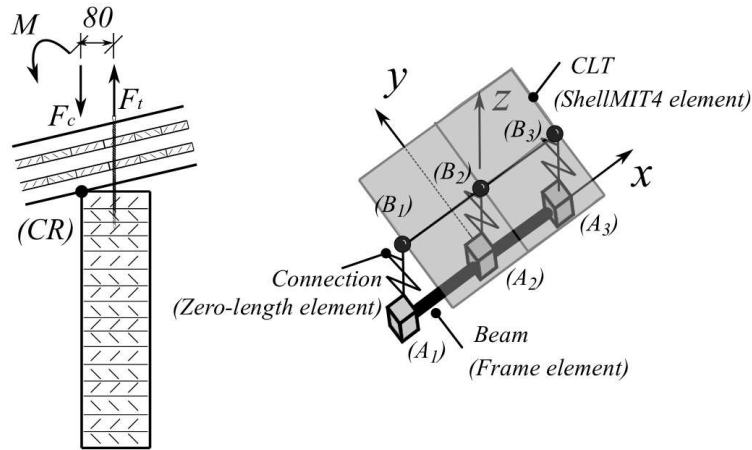


Figure 4.38: Numerical modeling for continuous overlap connections between CLT and glulam beams

same rotations along Y and Z directions. This constraints were enforced by using the equalDOF command available in Opensees.

Table 4.8: Parameters used to compute withdrawal capacity per fastener of overlap connections between CLT and glulam beams used in the structure

Geometrical and mechanical properties			Withdrawal capacity			load-carrying capacity		
Property	Value	Unit	Mode	Value	Unit	Mode	Value	Unit
$\rho_1 = \rho_2$	420.0	(kg/m ³)	$F_{ax,R(1)}$	14.25	(kN)	$F_{v,l(a)}$	35.5	(kN)
t_1	140.0	(mm)	$F_{ax,R(2)}$	11.5	(kN)	$F_{v,l(b)}$	30.4	(kN)
t_2	120.0	(mm)	$F_{ax,R(3)}$	5.6	(kN)	$F_{v,l(c)}$	15.1	(kN)
d	8	(mm)	$F_{ax,R(4)}$	17.0	(kN)	$F_{v,l(d)}$	14.0	(kN)
$M_{y,R}$	20000	(Nmm)				$F_{v,l(e)}$	12.2	(kN)
f_{ax}	11	(N/mm ²)				$F_{v,l(f)}$	5.1	(kN)
$l_{ef,1}$	140	(mm)						
$l_{ef,2}$	120	(mm)						
f_{head}	10	(N/mm ²)						
d_{head}	22	(mm)						
f_{tens}	12	(kN)						

Timber-to-timber joints connected with inclined screws

As presented in Figure 4.39b, the concealed connection between joists and main beams are executed with two self-tapping double-threaded screws WT-T-8,2x190 (steel grade 10.9) crossed at 45 degrees. Given the lack of experimental studies to characterize this connection, two sets of results available in the literature were used to define the parameters of the *Pinching4* model.

Table 4.9: Parameters used to define *Pinching4* model to represent overlap connections between CLT and glulam beams

Cyclic backbone curve			Cyclic degradation			
Point	F_i [kN]	d_i [mm]	Parameter	δ_{d_i}	δ_{f_i}	δ_{k_i}
<i>I</i>	4.25	1.0	α_1	0.1	0.1	0.1
<i>II</i>	10.2	9.0	α_2	0.1	0.1	0.1
<i>III</i>	14.5	27.5	α_3	2.0	2.0	1.0
<i>IV</i>	0.85	41.5	α_4	0.1	0.1	0.5

Table 4.10: Strength and stiffness properties for rotational response of overlap connections between CLT and glulam beams per screw

Interrupted CLT panel			Continuous CLT panel		
Property	Value	Unit	Property	Value	Unit
K_{rot}	80.239	(kNm/rad)	K_{rot}	51.353	(kNm/rad)
M_{max}	0.56	(kNm)	M_{max}	0.45	(kNm)
θ_{max}	0.007	(rad)	θ_{max}	0.0087	(rad)

A timber-to-timber connection, presented in Figure 4.39a, was studied in Tomasi et al. (2010) through the performance of monotonic push-out tests using WT-T-8,2x220 screws and glued laminated timber members of strength class GL24h.

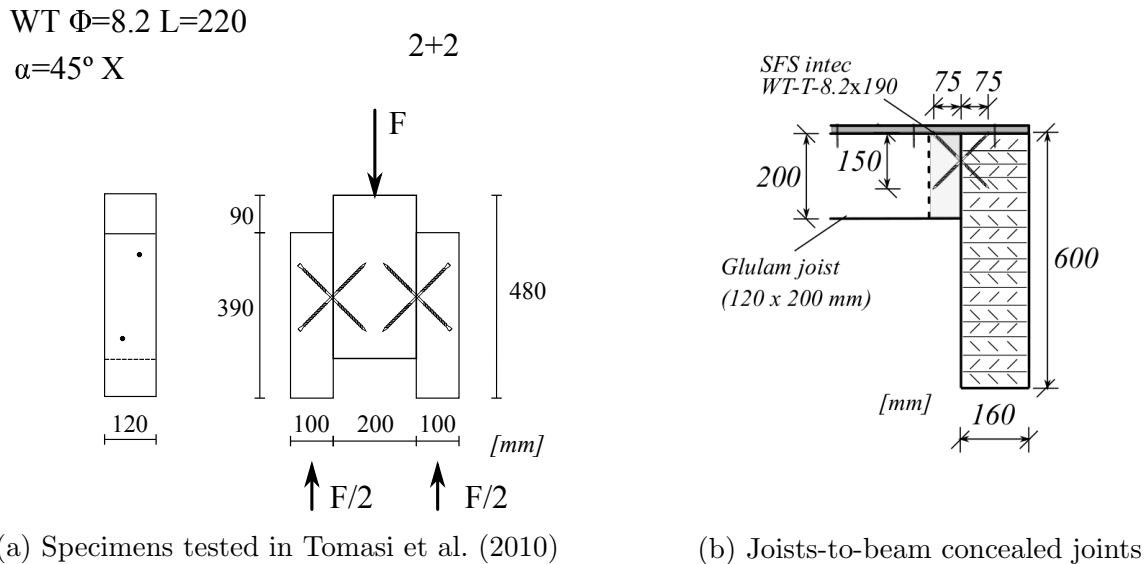
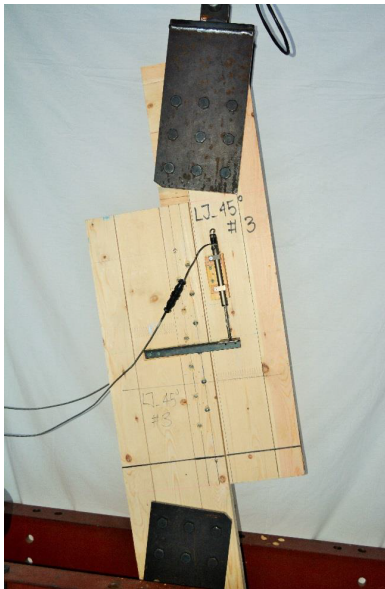
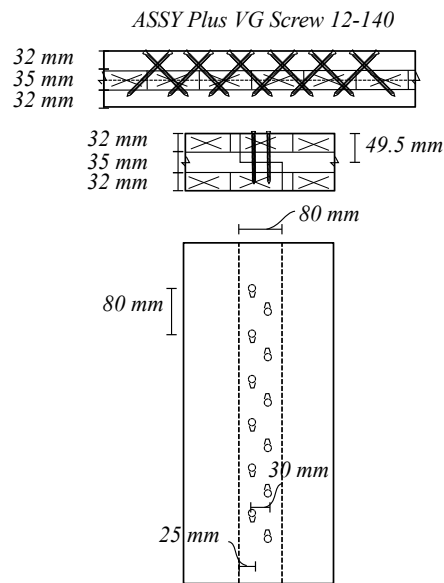


Figure 4.39: Connections with screws installed at 45 degrees

Tomasi et al. (2010) concluded that the load-carrying capacity increases when screws are crossed at 45 degrees (45° X) developing their withdrawal action. In this configuration, the pair works simultaneously since one screw develops shear-tension stresses while the other works under



(a) Test apparatus



(b) Geometric properties of specimens

Figure 4.40: Cyclic test layout half-lap joints with screws at 45 degrees

shear-compression stresses. In addition, the results obtained in Tomasi et al. (2010) for this layout (45° X) revealed a considerable increment in terms of initial stiffness when compared to solutions with screws crossed with different angles. However, the ductility is considerably reduced when screws develop their withdrawal action.

There are just a few cyclic tests available related to connections where pairs of screws develop shear-tension and shear-compression stresses simultaneously. Recently, cyclic tests were performed for half-lap joints and butt-joints suitable to be used in CLT diaphragms (Hossain et al., 2018; Closen, 2017; Loss et al., 2018). From these results, it was possible to find a connection scheme that can be compared to the joist-to-beam connection in terms of cyclic response. The experimental results used to fit a *Pinching4* model are available in Closen (2017) and refer to the half-lap connection presented in Figure 4.40, which was executed with screws placed at 45 degrees. The CLT panels used were manufactured by Structurlam Products Ltd. meeting the requirements of ANSI/APA PRG-320 (APA, 2017), while the fasteners were the ASSY 3.0 ECOFAST 12x140 with an ultimate tensile strength of 1015 MPa, which can be also included in the steel grade 10.9. These self-tapping screws were installed on the same panel face but with two different orientations at each shear plane, in a way that half of the screws were under shear-tension stresses and half under shear-compression stresses, for each direction of the shear loading. It is worth noting that Tomasi et al. (2010) and Closen (2017) used materials with similar mechanical properties in terms of lumber species used and fasteners' steel grade.

From the numerical results presented in Figure 4.41 for force-deformation curve and dissipated energy, it is possible to conclude that *Pinching4* model allows to satisfactorily represent the cyclic response of the connection. The principal difference relies on the dissipated energy, which can be justified by the asymmetric response observed at larger displacement cycles, where some screws had their head pushed-out or pulled-in.

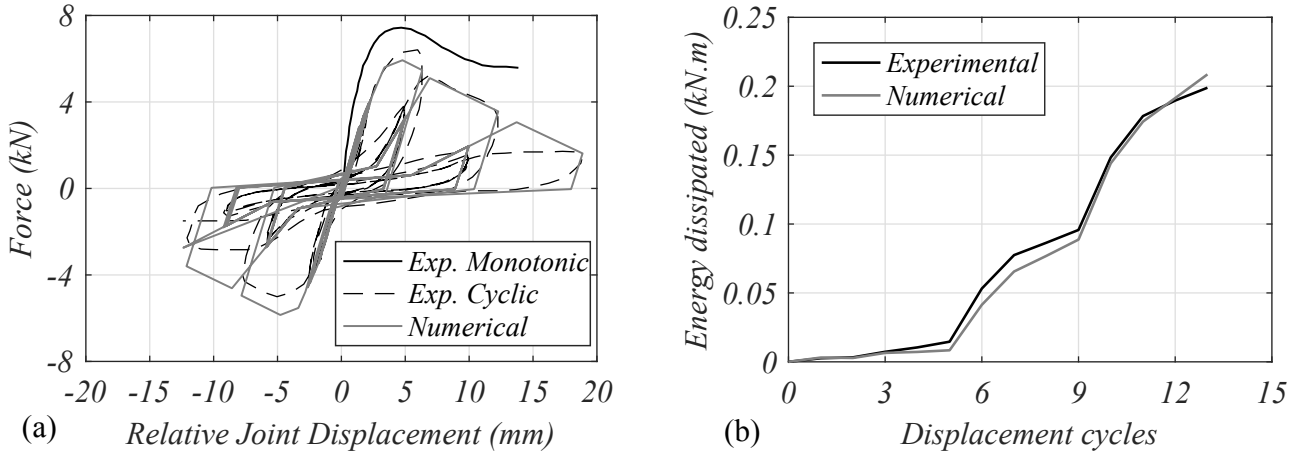


Figure 4.41: Half-lap joints with screws at 45°: (a) experimental tests and numerical results; (b) energy dissipated: test versus numerical results

As presented in Figure 4.41, monotonic results differ considerably in terms of strength and stiffness when compared to the cyclic envelope. This emphasizes the need of performing cyclic tests and consider them in the design and assessment of connections. The calibration procedure began by finding the force-displacement values of the backbone that better fits the envelope of the cyclic test. The second step consists in finding the pinching parameters that provide a good compromise in terms of dissipated energy per completed cycles. The parameters obtained from the calibration are $r_{Disp} = 0.40$, $r_{Force} = 0.20$, and $u_{Force} = 0.05$. Finally the last step is related to the definition of the parameters that are connected to strength and stiffness degradation. The aim consists of guaranteeing a low error in terms of maximum forces and dissipated energy per cycle. The final parameters obtained for the *Pinching4* model are presented in Table 4.11.

Table 4.11: Parameters used to define *Pinching4* model to represent half-lap joints

Monotonic backbone curve			Cyclic backbone curve			Cyclic degradation			
Point	F_i [kN]	d_i [mm]	Point	F_i [kN]	d_i [mm]	Parameter	δ_{d_i}	δ_{f_i}	δ_{k_i}
<i>I</i>	4.43	0.97	<i>I</i>	3.5	1.7	α_1	0.1	0.1	0.1
<i>II</i>	7.04	2.72	<i>II</i>	6.0	3.4	α_2	0.1	0.1	0.1
<i>III</i>	7.52	4.83	<i>III</i>	6.3	4.8	α_3	2.0	2.0	1.0
<i>IV</i>	2.75	20.0	<i>IV</i>	0.7	22.5	α_4	0.1	0.1	0.5

Given the lack of cyclic tests performed for the connections studied in Tomasi et al. (2010), it was necessary to assume simple relationships between parameters that enabled the determination of the cyclic envelope curve from the monotonic envelope curve. From the monotonic test performed by Cloesen (2017) it was possible to establish these relationships through the parameters of the *Pinching4* model. This was done by assuming that the yield displacement and the maximum load are the most important parameters extracted from the monotonic test. Consequently, the correspondent values used in monotonic and cyclic envelope curves for half-lap joints (Table 4.11) were compared through four different ratios (λ_i) and used afterwards to define envelope curves for cyclic response of the connection studied in Tomasi et al. (2010). These ratios are presented in Table 4.12. The remaining parameters that were used to define the envelope curve are presented in Table 4.13 and were obtained by keeping the slopes related to post-yielding branches equal to the ones obtained through the monotonic tests. The cyclic response, presented in Figure 4.42, was predicted with a SDOF model implemented in Opensees, where the imposed displacements were computed according to the European Standard EN 12512 (CEN, 2002a) assuming a joint yield slip equal to 0.50 mm.

Table 4.12: Ratios between *Pinching4* parameters for cyclic and monotonic tests

Parameter	$\lambda_i = X_{cyc}/X_{mon}$
d_I	1.76
F_I	0.79
d_{III}	0.98
F_{III}	0.83

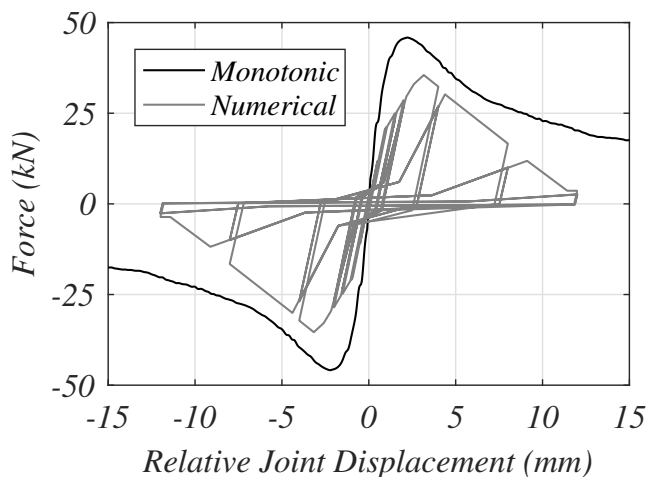


Figure 4.42: Monotonic test and cyclic response of concealed connection

Considering that the connection tested in Tomasi et al. (2010) makes use of the same materials as the ones used in the three story building under study, the envelope curve obtained is

considered as a mean envelope curve to be used in the pushdown analysis performed for the alternative load path analysis method proposed. The forces used on the envelope curve must represent only one shear plane (see Figure 4.39b).

Table 4.13: Envelope curve parameters for monotonic and cyclic tests

Monotonic backbone curve			Cyclic backbone curve		
Point	F_i [kN]	δ_i [mm]	Point	F_i [kN]	δ_i [mm]
<i>I</i>	26.6	0.51	<i>I</i>	21.0	0.89
<i>II</i>	44.3	1.39	<i>II</i>	35.7	1.71
<i>III</i>	46.1	2.31	<i>III</i>	38.4	2.28
<i>IV</i>	14.3	10.0	<i>IV</i>	4.20	10.55

According to Tomasi et al. (2010), the yield strength obtained through monotonic tests was 1.90 times higher than the value obtained by using the formulae presented in EC5. Moreover, the initial stiffness observed during the tests has values that are disproportionate when compared with the value computed through the codes. From this observations, one can conclude that it is important to represent the behavior of this connections based on experimental tests rather than values provided by codes.

The zero-length element used to represent the joist-to-beam connections has three degrees of freedom that are related to translation along Y and Z directions, as well as, rotations long X direction (see Figure 4.43).

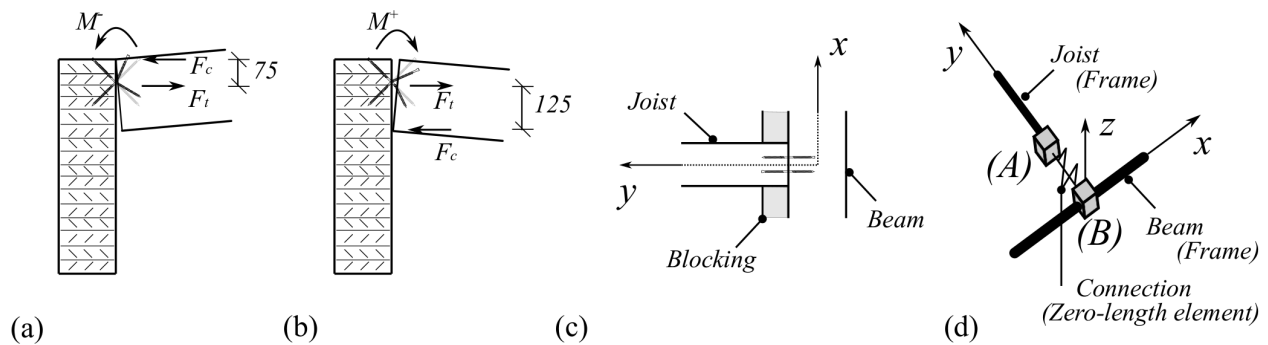


Figure 4.43: Joist-to-beam connections: (a) negative moment; (b) positive moment;(c) plan view; (d) numerical model

The load-deformation envelopes given in Table 4.13 for ALPA backbone curves are used for direction Z. Regarding forces along (Y-Y), it is necessary to consider different behaviors for tension and compression. Assuming that these deformations are reduced in comparison to the ones related to vertical forces and moments along X-X, the zero-length element is thus

modeled with an elastic *uniaxialMaterial* that has a positive stiffness equal to the one used for Z direction, and a negative stiffness with an absolute value that is 1000 times than the positive one. Two simplified free body diagrams are presented in Figure 4.43a and 4.43b for the joist-to-beam response against applied moments along X direction. The traction force F_t has the behavior assumed for the positive envelope curve used for Z direction. Thus, a similar approach of the one used for the multiple bolted connection presented in Figure 4.30 is followed for joist-to-beam moment capacity. The rotations used for the envelope curves are calculated through equation (4.6) and the respective moments through the equation (3.9), considering a single shear plane ($n_{sp} = 1$).

Table 4.14: *Pinching4* parameters for concealed joints with screws at 45 degrees

Direction (X-X) ^a (-) backbone curve			Direction (X-X) ^a (+) backbone curve			Direction (Z-Z) ^b backbone curve		
Point	M_i [kN.m]	θ_i [rad]	Point	M_i [kN.m]	θ_i [rad]	Point	F_i [kN]	δ_i [mm]
<i>I</i>	0.79	0.012	<i>I</i>	1.31	0.007	<i>I</i>	10.5	0.89
<i>II</i>	1.34	0.023	<i>II</i>	2.24	0.014	<i>II</i>	17.9	1.71
<i>III</i>	1.44	0.030	<i>III</i>	2.4	0.018	<i>III</i>	19.2	2.28
<i>IV</i>	0.16	0.130	<i>IV</i>	0.26	0.084	<i>IV</i>	2.10	10.55

^a rotational

^b translational

As presented in Figure 4.43c, the blocking members are used to prevent rotations along joists' longitudinal axis (Y-Y) and along vertical axis (Z-Z), as well as translations in X-direction. These assumptions are enforced by using the equalDOF command, where the nodes (*A*) and (*B*) presented in Figure 4.43d are constrained to have the same displacements/rotations in these directions.

OSB-to-joist connections in light-weight wood diaphragms

These connections are used to fix OSB panels on glulam joists. The representation of their behavior is based on OSB-to-framing connections studied in Sartori and Tomasi (2013). The authors performed fully reversal cyclic tests that are presented in Figure 4.45a. A SDOF model was used again to find the parameters (Table 4.15) of *Pinching4* model that allow to find a good balance in terms of strength degradation, stiffness degradation, and dissipated energy per cycle (see Figure 4.45b). The respective modeling scheme is presented in Figure 4.44.

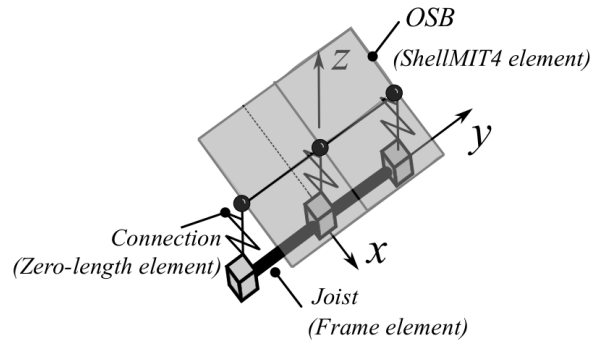


Figure 4.44: OSB-to-joists model in Opensees

The translations in plane were represented through the *Pinching4* model with properties presented in Table 4.15, while rotational stiffness of the zero-length elements along the vertical axis was assumed to be negligible. The nodes that share the same coordinates are constrained for the degrees of freedom correspondent to vertical displacements and rotations about X and Y axis.

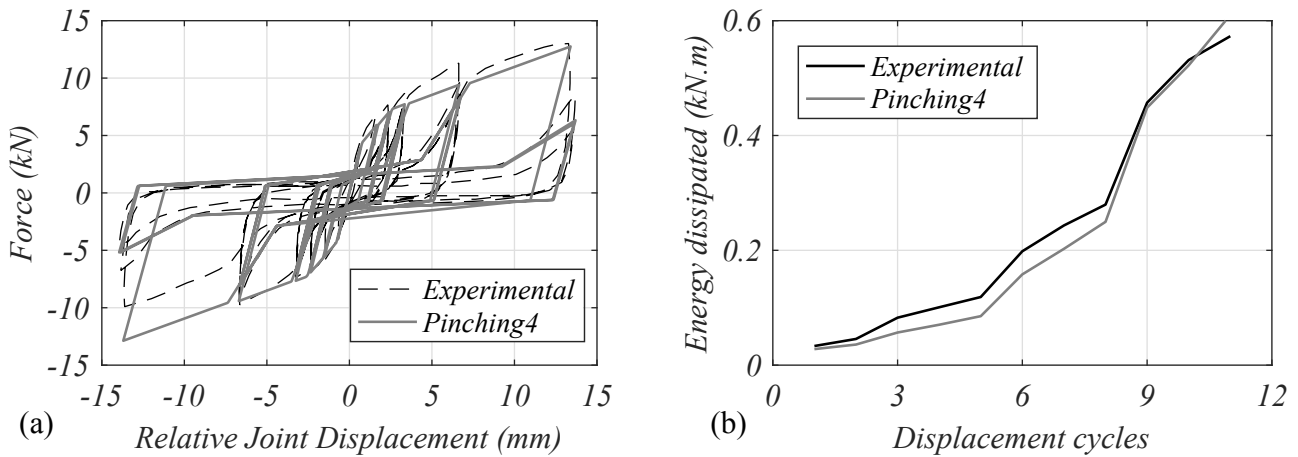


Figure 4.45: OSB-to-joists: (a) experimental tests and numerical results; (b) energy dissipated: test versus numerical results

4.5.2 Basic random variables and assumed statistical correlations

The probabilistic framework considers a total of 129 random variables. The majority of the variables are related to the properties used to define the behavior of the moment-resisting joints presented in chapter 3. The values used to create each backbone curve can be consulted

Table 4.15: Parameters used to define *Pinching4* model to represent OSB-to-joists

Cyclic backbone curve			Cyclic degradation			
Point	F_i [kN]	d_i [mm]	Parameter	δ_{d_i}	δ_{f_i}	δ_{k_i}
<i>I</i>	4.50	0.75	α_1	0.1	0.1	0.1
<i>II</i>	7.90	1.88	α_2	0.1	0.1	0.1
<i>III</i>	14.40	13.13	α_3	2.0	2.0	1.0
<i>IV</i>	0.90	16.88	α_4	0.1	0.1	0.5

in Tables 3.6 and 3.7. The properties of glulam members were assumed as presented in Table 3.3 with the intra-element correlation matrix shown in Table 3.4. Moreover, variability is also assumed for multiple bolts joints (Figure 4.30), steel-to-timber connections (Figure 4.28), overlap connections between CLT and glulam beams (Figure 4.38) and timber-to-timber joints connected with inclined screws at 45 degrees. The yielding force and the initial stiffness of each connection is modeled with lognormal distributions. Given the lack of experimental tests, a coefficient of variance of 15% is assumed for both properties being in the same range in terms of initial stiffness (see Table 3.6). However, the coefficient of variation assumed is higher than the one obtained for ring-doweled joints. This can be justified by the uncertainties related to the mechanical models used that shall be confirmed through testing in future studies. The remaining values used to establish the backbone curve are calculated by assuming the same ratios between each key points and the yielding point in terms of displacements and forces.

The permanent loads (dead loads) resultant from self-weights of materials do not vary significantly through the life of the structure. According to (Melchers, 1999), dead loads are assumed as Normal distributed, typically with a mean equal to the nominal load, and a coefficient of variation of 0.05–0.10. The variability of dead load is mainly associated to non-structural cladding, services and permanent installations rather than to the variability of the load-bearing materials themselves. As suggested by Pham (1985), the lognormal distribution is appropriate to model dead loads for a wide range of materials. In addition, the coefficient of variation proposed in JCSS (2001) is equal to 10% for wood materials. In this chapter, the dead loads are modeled with a lognormal probability distribution in order to avoid negative values, their mean values are assumed to be equal to the nominal value while the coefficient of variation is equal to 0.10.

The live load (*LL*) is produced by the gravity of people and equipment used in their actions and vary in time and space in a random manner. According to JCSS (2001), the variation in

time is represent by dividing the total live loads in two portions: sustained load (e.g weight of furniture) and intermittent load (e.g. crowded rooms during special events). These loads are usually represented through extreme value distributions (e.g Gumbel). However, Corotis and Doshi (1977) consulted the structural floor load data from five major live-load surveys and made goodness-of-fit tests in order to determine the accuracy of fitted normal, lognormal, and gamma distributions. Sentler (1976) fitted the gamma distribution and the lognormal distribution to his survey of floor loads. Although the gamma distribution appeared to best fit the data, he concluded that both distributions provided a good fit to residential load survey data. The loaded area admitted for the present robustness assessment is inserted in the category C1 of Table 6.2 presented in European Eurocode 1-1 (CEN, 2002b) that refers to areas where people may congregate (e.g. areas in schools). Given the lack of surveys regarding educational buildings, the lognormal distribution was assumed with a mean value of 2.0 kN/m² coefficient of variation of 0.30 (Sentler, 1976). Figure 4.46 provides the probability density functions obtained by fitting a lognormal distribution to the samples of gravity loads ($\Omega = 1.0$) generated through the LHS method.

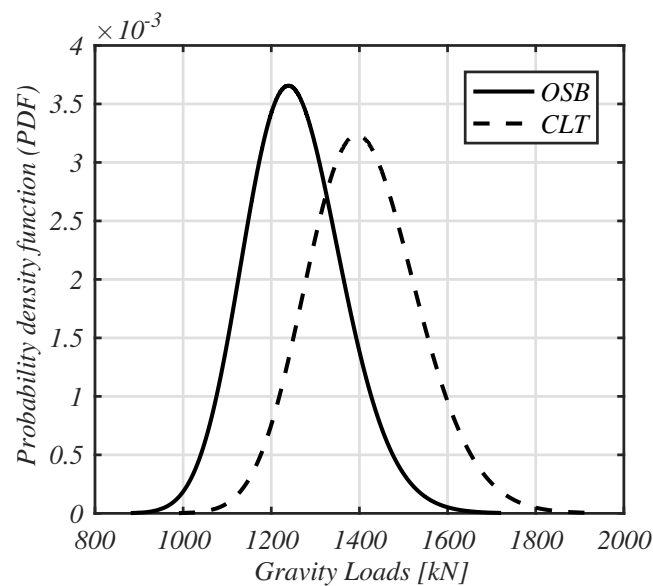


Figure 4.46: Probability density function of the gravity loads applied

4.5.3 Other variables assumed

The properties used for OSB panels were based on the experimental work developed in Zhu et al. (2005). The failure of OSB members is not considered as crucial for the progressive

collapse of the structure studied. Thus, the respective mechanical properties were assumed as deterministic and defined with their mean values. presented in Table 4.16, which were obtained through tension tests. Similar considerations were done for the CLT diaphragms, where the local failure of connections prevails over bending and shear failure of CLT panels. Their properties were introduced in an orthotropic material model with the values presented in Table 4.17 for lumber from strength class C24 according to EN 338 (CEN, 2016). The properties were obtained through methods introduced in Chapter 2 based on the works developed in H. Blaß and Fellmoser (2004) and Gsell et al. (2007).

Table 4.16: Mean properties used to model OSB orthotropic material

Property	Value [N/mm ²]	Property	Value [N/mm ²]	Property	Value [-]
E_{xx}	3770.0	G_{xy}	235.6	ν_{xy}	0.184
E_{yy}	2563.0	G_{yz}	50.0	ν_{yz}	0.312
E_{zz}	130.0	G_{zx}	50.0	ν_{zx}	0.013

Table 4.17: Mean properties used to model CLT orthotropic material

Property	Value [N/mm ²]	Property	Value [N/mm ²]	Property	Value [-]
E_{xx}	3526.7	G_{xy}	525.9	ν_{xy}	0.01
E_{yy}	8843.3	G_{yz}	228.6	ν_{yz}	0.01
E_{zz}	500.0	G_{zx}	40.2	ν_{zx}	0.01

The withdrawal stiffness of screws used to fix CLT panels to beams was calculated according to the values provided in the respective European Technical Approval (DIBT, 2013) as presented in equation (4.9). The withdrawal capacities of screws and shank nails used in the connections of both diaphragms are governed by their pull-through strengths, which are dependent on the density of the wood members, see equation (4.8).

4.5.4 Removal procedures in Opensees

Opensees framework allows elements, nodes, and loads removal through the remove command. This feature can be used to simulate the loss of capacity of timber members and connections. In addition, the removal can be performed between two consecutive steps through user defined routines in tcl.

In this work the removal of linear elastic elements (columns and beams) is simulated by disconnecting two consecutive frames. Thus, a new node is generated having the same coordinates

as the node associated to the local stresses that exceeded the respective cross-section strength capacity. The combination of shear and torsion of glulam elements was considered as it is proposed in STEP 1 (H. J. Blaß et al., 1995) and taken from equation (4.37) of (Porteous & Kermani, 2013). The flexural resistance of beams was verified according to section (6.3.3) of EC5 (CEN, 2005), where the lateral torsional stability is also considered. The columns were verified for combined bending and axial tension and combined bending and axial compression, in agreement with the verifications included in sections (6.2.3), (6.2.4) and (6.3.2) of EC5 (CEN, 2005). The failure of CLT panels due to shear, axial loading, and bending is verified according to the formulae available in NDS.

The failure of connections is evaluated in different ways depending on the typology of the joint. The failure of moment-resisting joints executed with dowels (4.17a) and bolts (4.30a) is given by the following equation:

$$\left(\frac{F_X}{F_{X,\max}}\right)^2 + \left(\frac{F_Z}{F_{Z,\max}}\right)^2 + \left(\frac{M_Y}{M_{Y,\max}}\right)^2 \leq 1.0 \quad (4.10)$$

where F_X , F_Z , and M_Y are the applied forces that are given by the numerical model results. In this work, the maximum capacities $F_{X,\max}$, $F_{Z,\max}$, and $M_{Y,\max}$ considered are the maximum values (*III*) of the respective envelope curves, see Tables 3.1 and 4.2. The connection between joists and glulam beams is evaluated considering vertical and horizontal loads. However, the horizontal loads are related to the moment applied through the following equation:

$$\left(\frac{F_Y + M_Z/h}{F_{Y,\max}}\right)^2 + \left(\frac{F_Z}{F_{Z,\max}}\right)^2 \leq 1.0 \quad (4.11)$$

where F_Y , F_Z , and M_Z are the applied forces that are given by the numerical model results (see Figure 4.43). The length h is the lever arm of the moment applied, which varies depending if the moment is positive ($h=75$ mm) or negative ($h=125$ mm).

A similar approach is applied for the verification of the moment capacity of overlap connections between CLT and glulam beams, as presented by the following equation:

$$\left(\frac{F_Z + M_X/b}{F_{ax,\max}}\right) \leq 1.0 \quad (4.12)$$

where F_Z and M_X are the applied forces (see Figures 4.37 and 4.38 and b is the correspondent lever arm. Regarding the forces applied perpendicular to the screws the verification is given by

$$\left(\frac{F_X}{F_{X,\max}}\right)^2 + \left(\frac{F_Y}{F_{Y,\max}}\right)^2 \leq 1.0 \quad (4.13)$$

where $F_{X,\max}$ and $F_{Y,\max}$ are the maximum values of the respective envelope curves presented in Table 4.9.

The pushdown procedure shown in Figure 4.47 starts with the notional removal of one or more elements to simulate an initial damage due to an unpredictable event. After each displacement increment step and respective structural analysis, a global failure assessment is conducted in order to evaluate if the damage was propagated to the adjacent bays. It is worth nothing that a disproportionate collapse is assumed when main beams, columns and connections reach their capacity. When the procedure confirms that all main elements of adjacent bays remain intact, there is a structural update that comprise the removal of zero-length elements, the disconnection of frame elements or a stiffness update of moment-resisting connections' properties (e.g. joist-to-beam joints presented in Figure 4.43).

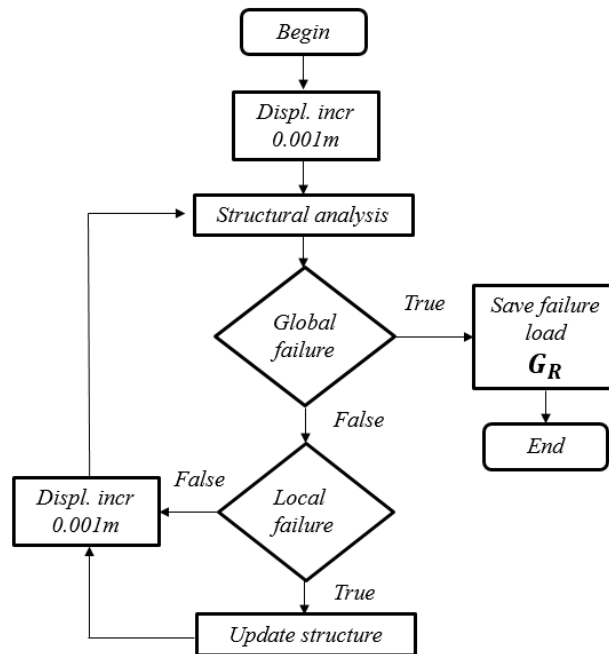


Figure 4.47: Pushdown procedure for progressive collapse assessment

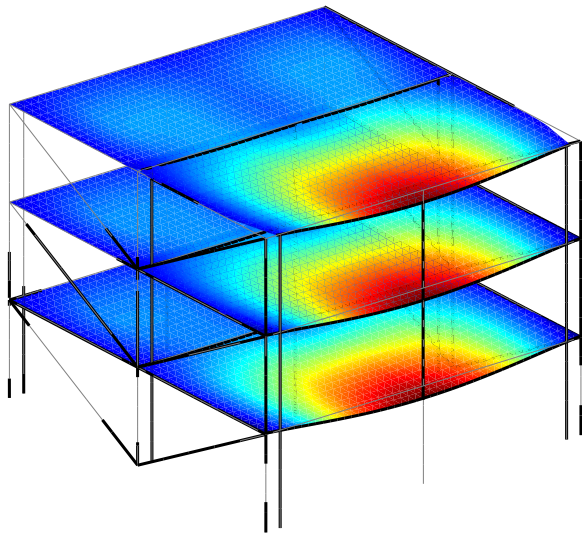
4.6 Alternative path method implementation

The pushdown analysis performed included four distinct initial damage (D) scenarios. Namely, the loss of a single column at the external bay (D_1 in Figure 4.48a), the simultaneous loss of two columns located at the corner of the structure at the external bay (D_2 in Figure 4.48b), the simultaneous loss of two columns and two diagonals located at the central bay (D_3 in Figure 4.49a), and the loss of the central column of the interior bay (D_4 in Figure 4.49b). These four initial damage scenarios were considered and their respective failure progression evaluated in each pushdown analysis. The LHS method was used to define a sample with 1000 structural realizations, which were sequentially assessed for each scenario and model structure corresponding to a total of 8000 pushdown analyses. The overload factor was calculated for two different load phases. The first one is related with the first failure of a floor-to-beam connection and the second is referent to the loss of capacity of a main load bearing element (beams, columns and moment-resisting joints). The developed models have some limitations that shall be considered when evaluating the results. These limitations pertain to the column shoes capacity, which were considered to be considerably stronger than the remaining elements. In addition, the effect of debris impact loads after fractures that lead to member separation was neglected. From the results obtained it was possible to define fragility curves that allow to compute the probability of failure given that a certain initial damage occurred ($P(\text{Failure}|D_i)$).

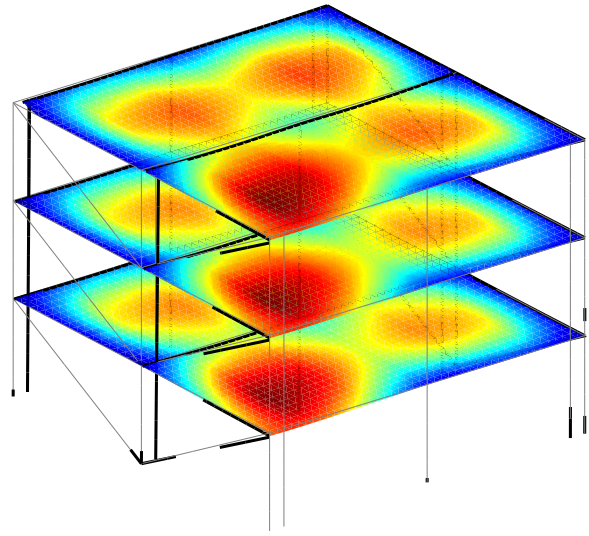
4.6.1 Pushdown analysis results

Similar collapse failure modes were observed for both types of diaphragms in each damage scenario. The configuration of the structural response is presented for each initial damage scenario through the vertical displacement diagrams showed in Figures 4.48 and 4.49.

The deformations were considerably higher for the damage scenarios related to the loss of single columns located in the central part of the structure (D_1 and D_4), as shown by the respective probability density functions of Figure 4.50. The capacity to deform without rupture of ring-doweled joints was exploited, while several connections where transformed in hinged joints. The collapse was reached after the failure of one ring-doweled connection. In other word, when the verification given though the equation (4.10) was not satisfied. Several analysis returned the failure of one main beam due to excessive bending stresses. From the numerical results obtained,

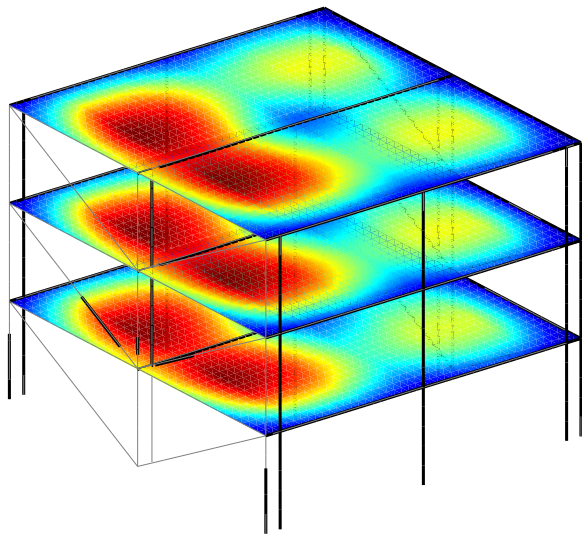


(a) Scenario D_1

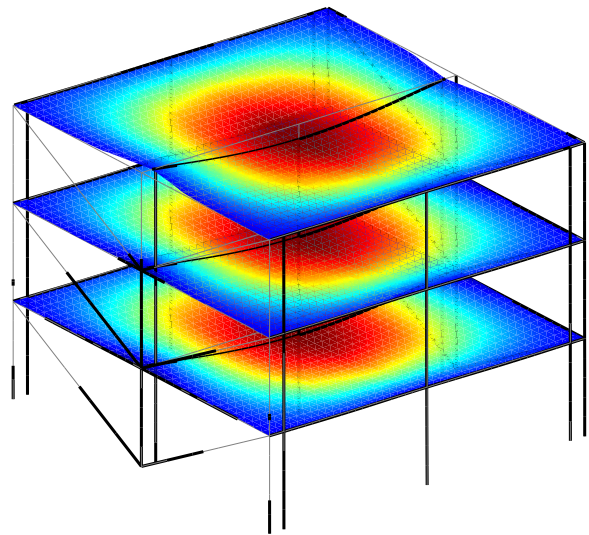


(b) Scenario D_2

Figure 4.48: Loss of elements at external bay



(a) Scenario D_3



(b) Scenario D_4

Figure 4.49: Loss of elements at internal bay

it is possible to state that the initial damage scenarios (D_2) and (D_3) conducted to collapses that did not exploit the ability of joints to deform. In these cases, the beams located just above the damaged elements sustained the loads and failed due to excessive bending stresses.

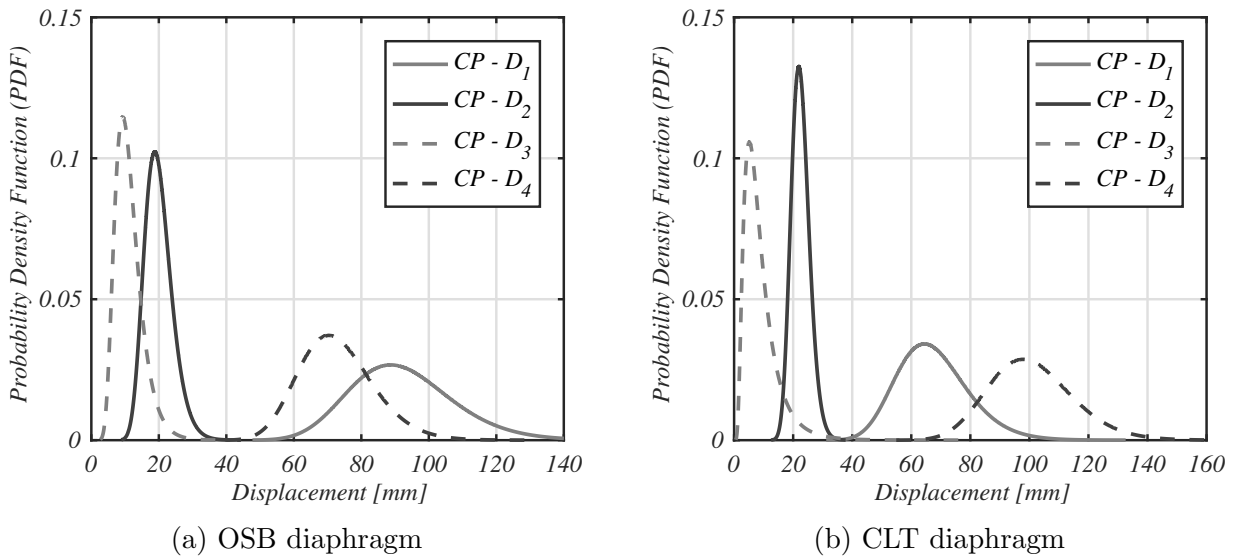


Figure 4.50: Probability density functions for maximum vertical displacements of the model structure for distinct elements loss scenarios

The distinct initial damage scenarios can also be compared in terms of the deformation capacity of the floor-to-beam connection by consulting the probability density functions of the the maximum rotations measured at the joists ends that are shown in Figure 4.51a. In general, the joist-to-beam connections used in the light weight solution rotated more than the connections of CLT-to-beams. However, it is worth noting that the scenario D_4 (interior column loss) conducted to larger rotations due to the continuity of the CLT panels used at the central part of the structure. The parameters used to fit the a lognormal distribution of maximum rotations and vertical displacements can be consulted in Tables 4.18 and 4.19, respectively. Another evidence depicted from the results refers to the absence of catenary actions or membrane behavior of floors. This is justified by the low level of displacements of glulam beams and small magnitude of the rotations measured at floor connections and moment-resisting joints. The main mechanism used to sustain the loads due to local failures was the beam action of the main glulam beams.

The pushdown curves presented in Figure 4.52 were computed using the median properties for all connections and members properties. The results shown in Figure 4.52a demonstrate that the initial damage scenarios associated to element losses at the central bay conducted to lower overload factors for structures built with light-weight diaphragms. It is worth noting

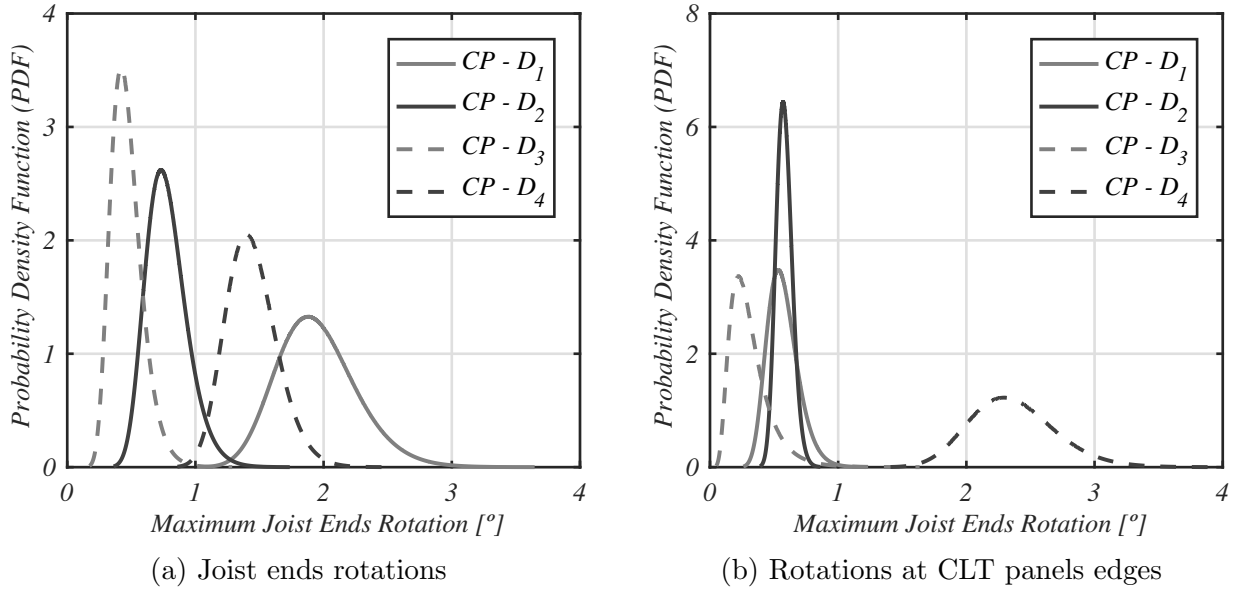


Figure 4.51: Probability density functions for joist ends rotations and CLT panels connections of the model structure for distinct elements loss scenarios

Table 4.18: Lognormal parameters used to represent the variability of maximum vertical displacements measured at the control node

Damage Scenario	Failure state	OSB diaphragms				CLT diaphragms			
		μ_{\ln}	ξ_{\ln}	$E[X]$ (mm)	$CoV[X]$	$\mu_{\ln D}$	ξ_{\ln}	$E[X]$ (mm)	$CoV[X]$
D_1	CP	4.513	0.166	92.5	0.167	4.198	0.179	67.6	0.180
D_2	CP	2.975	0.203	20.0	0.205	3.106	0.136	22.5	0.137
D_3	CP	2.354	0.352	11.2	0.363	2.010	0.608	9.0	0.67
D_4	CP	4.277	0.150	72.8	0.151	4.603	0.141	100.8	0.142

Table 4.19: Lognormal parameters for maximum relative rotations between floor elements (Glulam joists and CLT) and main glulam beams

Damage Scenario	Failure state	OSB diaphragms				CLT diaphragms			
		μ_{\ln}	ξ_{\ln}	$E[X]$	$CoV[X]$	$\mu_{\ln D}$	ξ_{\ln}	$E[X]$	$CoV[X]$
D_1	CP	0.656	0.158	1.951	0.159	-0.584	2.106	0.570	0.213
D_2	CP	-0.271	0.204	0.779	0.206	-0.550	0.108	0.580	0.108
D_3	CP	-0.796	0.260	0.466	0.264	-1.280	0.477	0.312	0.506
D_4	CP	0.354	0.138	1.439	0.139	0.850	0.140	2.363	0.141

that the central bay has a higher level of forces applied and the floor demonstrates a low capacity to transmit loads for adjacent bays. In opposition, the model structures built with CLT diaphragms showed better results (see Figure 4.52b) in terms of overload factors at the collapse limit state, specially for scenarios D_2 and D_4 where the overload increased around 37.5% and 60% in comparison to the light-weight solution. This is associated to the continuity of panels over bays in the central part, that allowed loads redistribution to undamaged parts. However, the initial damage scenario D_3 showed lower overload values since the CLT panels, right above the removed elements, were not continuous resulting on redistribution of loads that are dependent on the rotational capacity of floor-to-beam connections. As presented, in Table 4.10 the connections commonly used to connect CLT panels to glulam beams present a very low rotational stiffness.

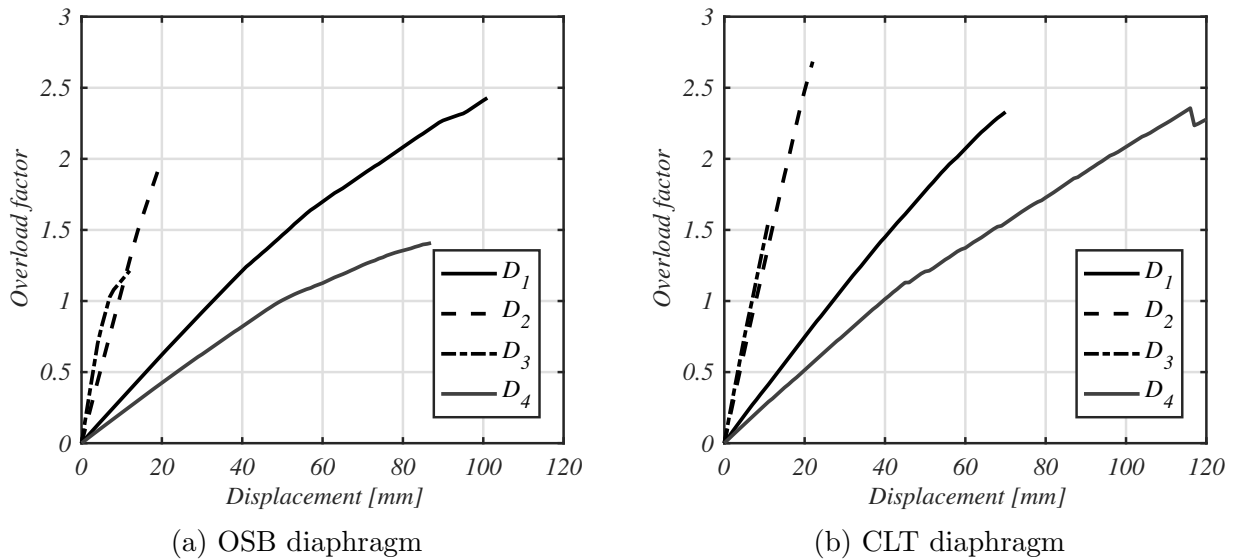


Figure 4.52: Pushdown curves for distinct damage scenarios

4.6.2 Fragility analysis

The fragility functions computed here result from fitting a lognormal distribution to the overload factor extracted from each pushdown analyses performed for the different damage scenarios admitted. From the fragility curves presented for structures built with light-frame diaphragms, it is possible to verify that the collapse fragility curves $P(CP|D_i)$ present mean values of overload factors that are considerably higher than the overload factors obtained at the first failure of a floor connection ($P(FF|D_i)$). This fact indicates the capacity of the structure to sustain a local damage without rupture, specially for initial scenarios D_1 and D_4 . Another

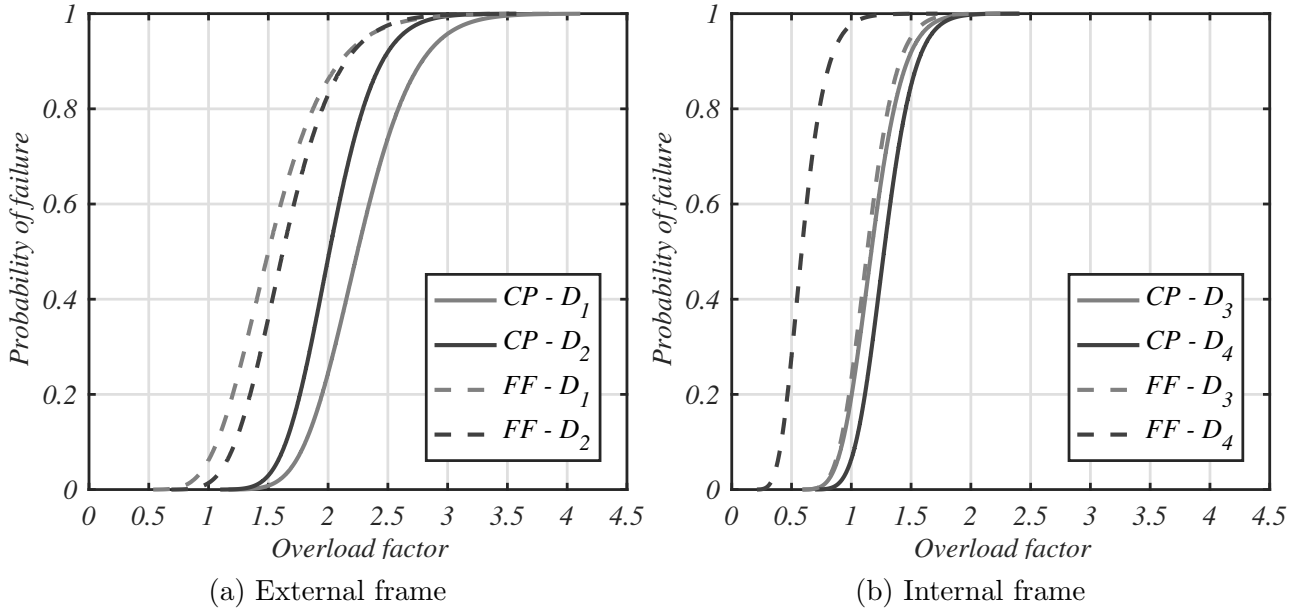


Figure 4.53: Fragility curves for distinct column loss scenarios for model structures with light frame diaphragms

important finding is related to the change from light-frame diaphragms to CLT floors that caused an increment in terms of the mean value of the overload factor related to all the collapse fragility curves built, except for the initial damage scenario D_3 . As stated above, according to the numerical results that is associated to the discontinuity of CLT panels at the diaphragm edges.

Table 4.20: Fragility curves parameters for overload factors related to distinct damage scenarios

Damage Scenario	Failure state	OSB diaphragms				CLT diaphragms			
		μ_{\ln}	ξ_{\ln}	$E[X]$	$CoV[X]$	$\mu_{\ln D}$	ξ_{\ln}	$E[X]$	$CoV[X]$
D_1	$P(FF D_i)$	0.406	0.264	1.554	0.269	0.815	0.144	2.283	0.145
	$P(CP D_i)$	0.809	0.168	2.278	0.169	0.842	0.135	2.342	0.136
D_2	$P(FF D_i)$	0.484	0.220	1.662	0.223	-0.053	0.108	0.954	0.108
	$P(CP D_i)$	0.700	0.155	2.038	0.156	0.995	0.106	2.720	0.106
D_3	$P(FF D_i)$	0.125	0.170	1.150	0.171	-0.351	0.210	0.720	0.212
	$P(CP D_i)$	0.155	0.180	1.187	0.182	-0.019	0.346	1.042	0.357
D_4	$P(FF D_i)$	-0.537	0.269	0.606	0.274	-0.008	0.140	1.002	0.141
	$P(CP D_i)$	0.242	0.159	1.290	0.160	0.720	0.175	2.086	0.177

According to ARUP (2011) the gravitational loads used to perform the ALPA method shall be multiplied by a dynamic amplification factor, that for timber structures is equal to 2.0. In order to address if the seismic design provisions, which were used to design structure system under study, also guarantee structural robustness against progressive collapse, the probability of failure associated to overload factor of 2.0 is evaluated for each damage scenario in Table

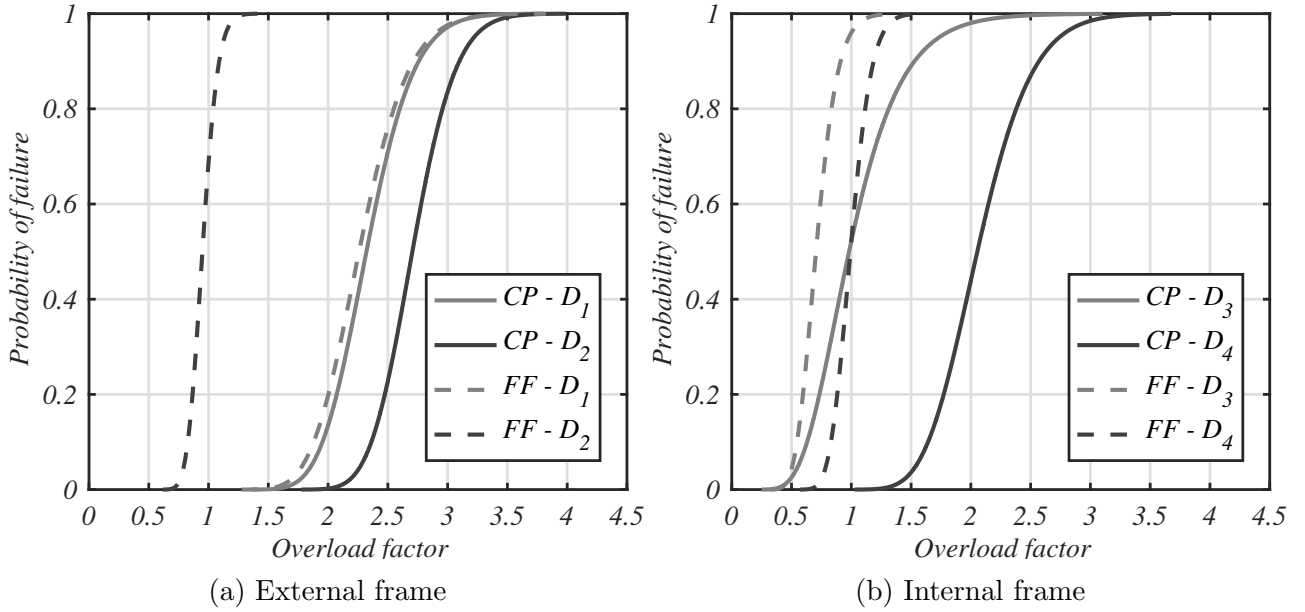


Figure 4.54: Fragility curves for distinct column loss scenarios for model structures with CLT diaphragms

4.21.

The reliability index, β , is another structural performance indicator used to assess robustness and is calculated in this thesis according to the following equation:

$$\beta = \Phi^{-1}(1 - p_f) \quad (4.14)$$

where β is the structural reliability index, p_f is the probability of failure that is determined from the fragility curves, and Φ^{-1} is the inverse cumulative distribution function of the standard normal distribution. The values obtained for respective reliability indexes are presented in Table 4.21 when the overload factor assumed is equal to 2.0. Attending to the results presented it is possible to conclude that structures built with CLT diaphragms present better performance against progressive collapse than light-frame diaphragms. The highest difference, favorable to CLT diaphragms, refer to the damage scenario D_2 where the probability of failure was reduced from 48.2 % to 0.2%. However, the results obtained for scenario D_3 reveal the importance of the panels being continuous over two bays.

There is a lack of research efforts to address the adequate dynamic amplification for distinct timber structures typologies. Such gap can be filled by the development of experimental tests on building prototypes that can be also compared to numerical results. These models shall

Table 4.21: Probability of failure and respective reliability indexes for overload factor of 2.0

Damage Scenario	Failure State	OSB diaphragms		CLT diaphragms	
		p_f	β	p_f	β
D_1	$P(CP D_1)$	0.245	0.690	0.135	1.103
D_2	$P(CP D_2)$	0.482	0.044	0.002	2.821
D_3	$P(CP D_3)$	0.999	-2.990	0.980	-2.052
D_4	$P(CP D_4)$	0.998	-2.837	0.439	0.153

improve the methodologies used to address structural robustness of timber structures.

Given that the dynamic amplification factor (Ω) of equation 4.2 can vary from 1.0 to 2.0, Figure 4.55 allows to compare the reliability indexes obtained for the distinct damage scenarios considering overload factors ranging from 1.0 to 2.0.

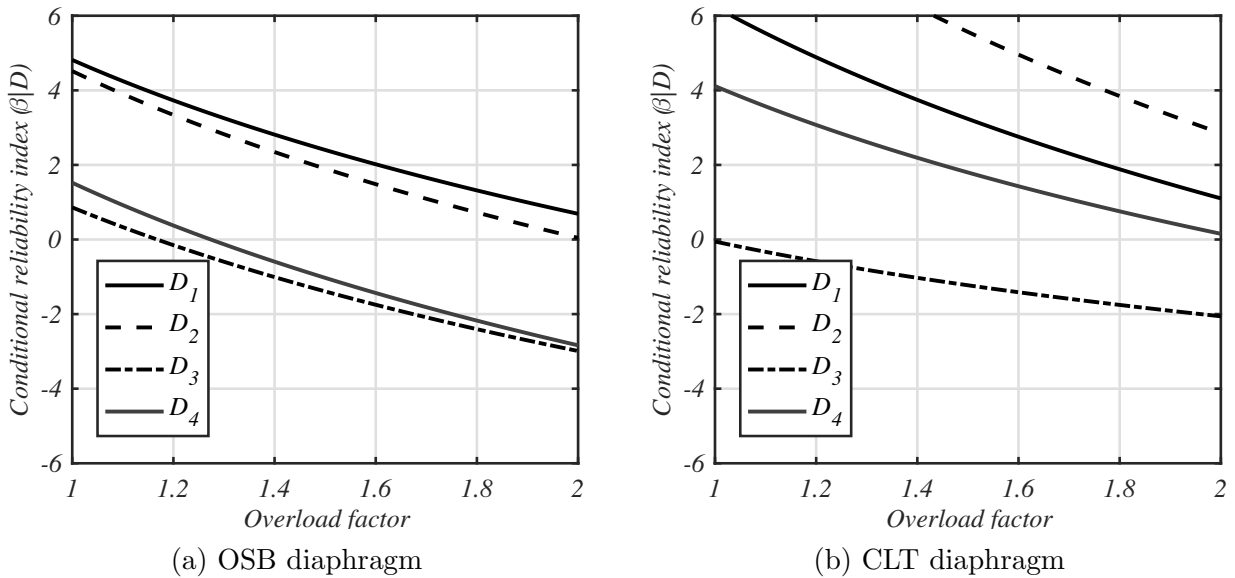


Figure 4.55: Conditional reliability indexes for overload factors between 1.0 and 2.0

The results reinforce that the structures with CLT diaphragms present higher conditional reliability indexes than the structures built with light-weight diaphragms. However, this statement is adequate only for damage scenarios D_1 , D_2 , and D_4 .

Since the collapse is associated with failure beams and ring-doweled connections, which is directly influenced by the length of beams spans, the reduction of the spans can constitute an adequate measure. This measure could also increase the structural capacity against seismic loads. Another hypothesis to improve robustness is associated to the increase of beams cross-section. On the other hand, the response of the light-frame diaphragm can be improved by building a similar system but with continuous beams spanning over two bays. This measure

would provide capacity to redistribute partially the loads from damaged bays to adjacent ones.

4.7 Conclusions

For multi-story timber buildings, robustness is strongly dependent on the structures capacity to redistribute loads to undamaged parts, and thus, on its ductility and redundancy. To contribute to the robustness assessment methodologies of timber structures, the propensity to progressive collapse of a three-story building is analyzed in this thesis. The lateral resisting systems consist of glued-laminated timber (GLT) braced frames and moment-resisting frames with doweled joints. Connections and members were designed to fulfill the seismic detailing requirements presented in Eurocode 5 and Eurocode 8 for high ductility class structures. Given the importance of diaphragms to guarantee alternative load paths, two diaphragm typologies were evaluated. The first one consists of a low weight solution with 18mm oriented strand boards fastened to the GLT joists, while the second solution makes use of CLT panels connected with half-lap joints.

The progressive collapse assessment of the structure was evaluated through a probabilistic approach, which accounts for uncertainties in mechanical properties of glulam members and connections. The Latin Hypercube Sampling method was used to generate a set of structural samples. For each realization, an alternative load path analysis (ALPA) was conducted through nonlinear static analyses that considered four distinct elements loss scenarios. The finite element model was built in Opensees framework given its ability to remove structural elements between consecutive analyses steps. This feature allowed to consider the effect of brittle failures in connections and timber members, while proceeding with the analysis. Fragility curves were developed for four distinct initial damage scenarios based on the overload factors obtained from each ALPA conducted. The 3D models used incorporated constitutive models for connections based on previous experimental results. Nevertheless, the tests available in the literature were not oriented directly for the connections used in the building under study. In addition, the experimental campaigns performed so far focused essentially on the shear capacity of joints, rather than their rotational capacity, which is deemed crucial to develop mechanisms for redistribution of loads after a local failure. Thus, experimental tests must be performed to reduce the uncertainties related with the constitutive models used in the present work. On the other

hand, a sudden loss of elements, due to impacts or explosions, triggers a dynamic response of the damaged structure. Thus, nonlinear dynamic analyses shall be performed in the future to assess the reliability of the fragility curves proposed in this chapter. Despite, the inherent limitations, the progressive collapse assessment performed here applied advanced methodologies, which were proposed by the most recent code provisions. The major findings achieved in this chapter were:

- The seismic design provisions do not dismiss a progressive collapse assessment during the design phase. This fact is justified by the fragility curves obtained in terms of overload factors for all the initial damage scenarios considered. Given that the dynamic amplification factor proposed for timber structures, in the literature, is equal to 2.0, the correspondent probabilities of failure are, in some cases very high;
- The pushdown analysis performed shown that structures with CLT diaphragms have higher progressive collapse resistance than the structures built with light-weight diaphragms. This results are associated with the use of continuous CLT panels over two adjacent bays. In opposition, the rotational capacity of the connections between joists and beams was very low, which compromised the load redistribution from damaged bays to the intact ones. In this case, the consideration of continuous joists over two bays could guarantee an improvement in the structural robustness;
- The principal failure modes observed were related to bending stresses of glulam beams, followed by the loss of capacity of moment-resisting joints to transfer loads from glulam beams to columns. Thus, the increase of strength of this properties would increase also the resistance of the structure to avoid a progressive collapse due to local failures.

The methodologies presented can be included in a risk based robustness assessment that consider also the probabilities of occurrence of different exposures, such as impacts and explosions, while considering the direct and indirect consequences of failures. Thus, following research efforts can focus on the quantification of those costs, while working on the reduction of the inherent model uncertainties

Chapter 5

Conclusions and Future work

5.1 Summary of the research work

The main objective of this thesis was to propose analyses approaches to assist in the design and assessment of heavy-timber structures due to seismic actions and robustness. These analyses account for uncertainties associated with connections behavior and timber mechanical properties, as well as the variability in failure modes of the different structural elements and connections.

Diaphragms are crucial to guarantee clear paths for inertial loads during earthquake ground motions. In order to improve the understanding of the behavior of CLT diaphragms, experimental data was collected during a shake-table testing of a two-story mass-timber prototype building (Pei et al., 2018a). A computational modeling approach was described as well as the the fundamental engineering concepts and principles of mechanics used to design the diaphragms under study. The experimental data was used to validate numerical results obtained from nonlinear static analysis performed in SAP2000 finite element analysis software. The peak response of different earthquake tests were captured through nonlinear static analyses performed on 2D models, where the nodal loads were applied incrementally from zero to the full specified magnitude. These loads were determined considering the material weights and the accelerations measured *in situ*. The modelling strategy made use of SAP 2000 interactive editing feature allowing to represent the different connections built on the diaphragm. The zero-length elements used to model the connections were calibrated according to cyclic tests performed on plywood surface-splines (Closen, 2017). The influence of friction was also studied by assuming a rigid

behavior for the connections until the static friction force was reached. A parametric study was performed, considering different clamping forces and distinct friction coefficients. The influence of in-plane stiffness properties was addressed by combining independently the mean value, and the 5 % and the 95 % percentiles of the elastic modulus and shear modulus of the lumber to compute the stiffness properties of the CLT panels added to the orthotropic shell elements used to model them.

The seismic performance of a heavy-timber structure designed with ring-doweled moment resisting connections was evaluated. The ring-doweled joints used to connect beams and columns had already been experimentally studied under cyclic testing in (Polastri et al., 2013). The results had shown that the connection could fulfill the requirements of EC8 for high ductility class structures. A comprehensive seismic performance assessment which included numerical nonlinear static and nonlinear dynamic analysis. OpenSees was used for the numerical analysis, in which the *Pinching4* constitutive model was used to capture the moment-rotation behavior of ring-doweled moment resisting connections, which was calibrated based on testing data available in the literature. The inherent variability of the timber structural members was included in the analysis as modeling uncertainties, which influenced the structural capacity and the notable points used to characterize the hysteretic response of the connections. Using a set of 1000 structural models generated with the Latin Hypercube Sampling method, a probabilistic assessment was performed including spatial variability of strength and stiffness of timber elements and connections properties. Nonlinear static analyses were first performed to evaluate the variability of limit-state interstory drift ratios and q -factors. In addition, multi-record incremental dynamic analysis (IDA) was performed assuming the first mode spectral acceleration as the intensity measure and peak interstory drift ratio as the damage measure. Several seismic fragility curves for different performance levels, including Immediate Occupancy, Life Safety, Collapse Prevention, and Global Collapse, were determined using the results from multi-record incremental dynamic analysis.

For multi-storey timber buildings, robustness is strongly dependent on the structures capacity to redistribute loads to undamaged parts, and thus, on its ductility and redundancy. To contribute to the robustness assessment methodologies of timber structures, the propensity to progressive collapse of a three-story building was analyzed in this thesis. The lateral resisting systems consist of glued-laminated timber (GLT) braced frames and moment-resisting frames

with doweled joints. Connections and members were designed to fulfil the seismic detailing requirements present in Eurocode 5 and Eurocode 8 for high ductility class structures. Given the importance of diaphragms to guarantee alternative load paths, two diaphragm typologies were evaluated. The first one makes use of CLT panels connected with plywood surface-splines, while the second solution consists of a low weight solution with 18 mm oriented strand boards fastened to the GLT joists. The progressive collapse assessment of the structure is evaluated through a probabilistic approach, which accounts for uncertainties in mechanical properties of members and connections. The Latin Hypercube Sampling method was used to generate a set of structural samples. For each realization, an alternative load path analysis (ALPA) was conducted through nonlinear static analyses that considered distinct column loss scenarios. The finite element model was built in Opensees framework given its ability to remove structural elements between consecutive analyses steps. This feature allowed to consider the effect of brittle failures in connections and timber members, while proceeding with the analysis. Fragility curves were developed based on the overload factors obtained on each ALPA conducted.

5.2 Summary of major findings

From the investigations carried out on CLT diaphragms tests and numerical modeling included in Chapter 2, the main observations were:

- The consideration of friction allows to capture accurately the surface splines peak deformations resultant from the ground shaking;
- A conservative design is reached when friction is neglected. The model with the highest friction coefficient as well as the highest clamping forces produces a maximum spline force that is 62 % lower than the one obtained with the model that neglects friction;
- The variability assumed for friction forces resulted on surface-spline forces with a coefficient of variation equal to 11 %;
- The contribution of surface splines were not considered when designing the chord splices, which results on a overestimation of the forces;

- The occurrence of wall rocking at their base may cause uplift between adjacent panels at the diaphragm. These occurrence may originate normal stresses due to bending of the steel plates. This behavior is not captured through the two-dimensional model proposed.

A numerical modeling strategy was presented for the design and assessment of CLT diaphragms subjected to earthquake loads. The satisfactory results obtained in terms of displacements and the model's capability to capture the most important phenomena regarding connections' response prove its feasibility and accuracy. In this way, the model constitutes a good alternative to simplified methodologies applied during the design phase. Since a structural engineer must find a compromise between numerical efficiency and tight schedules, the time and effort associated with developing the numerical model also weighs on the choice of design method. Although, an experienced user of finite element model software can handle most of the features proposed in this thesis, the definition of all the special joints and zero-length elements can be a time consuming task that might hinder the usage of this methodology in structural design projects. The application of the model without friction is suggested as a less demanding option. This model ensures a good compromise between accuracy and development effort, providing values of design forces higher than the ones obtained from models with friction (more accurate models), and therefore more conservative, but lower than the values obtained from simplified and conservative design methods.

From the seismic assessment performed on a heavy-timber structure designed with ring-doweled moment resisting connections, presented in Chapter 3, the major findings were:

- Parameters for the peak value of interstory drift ratio θ_{max} associated with different damage states were obtained. Median values obtained were 1.2%, 4.9%, and 7.9% for the IO, LS, and CP damage states, respectively. In addition, the coefficient of variation of θ_{max} ranged from 9% to 15%, which are relatively low values, specially since modeling uncertainties were explicitly considered;
- The median value of the q -factor obtained from the pushover analyses was considerably higher ($q = 7.1$) than the value prescribed in EC8 ($q_{EC8} = 4.0$). Moreover, the median value of the ductility factor R_{μ} obtained was 4.0. These results indicate that the q -factor values considered in EC8 and the detailing requirements defined in EC8 and EC5 are adequate for design of this type of structure;

- The multi-record IDA results showed that modeling uncertainties have a slight influence on the expected values of the IDA curves for peak interstory drifts ratios lower than 5%. Nonetheless, when modeling uncertainties are taken into account the coefficient of variation increases up to 43%;
- From the disaggregation of the IDA curves according to four different q -factor levels, it was observed that structural models with higher q -factors are more likely to resist ground shaking with higher intensities. These results can be partially explained due to the fact that a positive linear correlation of 0.46 was observed between the q -factor and R_{Ω} ;
- No brittle failures were observed in the dynamic analyses conducted to compute the IDA curves, indicating that the sizing requirements in EC8 are adequate, but potentially too conservative, thus leaving room for improvements of the slenderness of the members and dowels;
- Modeling uncertainties did not affect the median values of the fragility curves associated with IO and LS. However, the coefficient-of-variations increased by 18% and 13% when the modeling uncertainties were considered for the IO and LS damage states, respectively;
- When modeling uncertainties are neglected an overestimation of the capacity is obtained, both in terms of spectral acceleration and peak interstory drift for the CP and GC damage states, by approximately 3% and 5%, respectively. However, the coefficient-of-variation did not change for the CP and GC damage states, when modeling uncertainties were considered.

From the robustness assessment performed on a heavy-timber structure, presented in Chapter 4, the major findings were:

- The overload factors computed through the pushdown analysis performed for structures with CLT diaphragms are higher than the values obtained for structures built with the light weight solution. This results can be partially associated to the use of continuous CLT panels over two adjacent bays;
- The seismic design provisions used to define elements sizing and connections geometrical configurations do not dismiss a progressive collapse assessment during the design phase.

This finding is justified by the fragility curves obtained from the alternative load path analysis that simulate a sudden removal of first-story elements. The consideration of a dynamic amplification factor equal to 2.0 conducts to lower reliability indexes, which mean that the structural system is not robust against progressive collapse;

- The principal failure modes observed are related to bending stresses observed in GLT beams and the loss of capacity of moment-resisting joints to transfer loads from GLT beams to columns.

5.3 Limitations of the research work

The experimental results presented for CLT diaphragms were extracted from a full-scale shake-table test. Despite, the accuracy of the numerical results obtained through a 2D finite element model, some important phenomena as uplift can only be captured with a 3D model, including the remaining vertical elements and their connections. In addition, nonlinear dynamic analysis shall be performed and compared to the results presented. A parametric study was performed in order to assess the influence of friction on the diaphragm response. However, the values assumed for the clamping forces are uncertain given that the assemblage of the structure was performed without using any torque specification. In fact, the construction workers simply ensured that the joint or connector being fastened is tight to the surface and the fastener is fully installed. This limitation was opposed by considering different values of clamping force.

In Chapter 3, the seismic assessment involved nonlinear dynamic analysis on a 2D model of a moment-resisting frame structure, which is the lateral resisting system of single direction of a three-storey building. However, the influence of ground motion direction and duration was not considered. This variables can only be accounted with a 3D model that includes the representation of the perpendicular lateral resisting system as well as the diaphragms.

The alternative path analysis performed in Chapter 4 used 3D models that incorporate constitutive models for connections that were based on previous experimental results available in the literature. Nevertheless, the tests available in the literature were not oriented directly for the connections used in the building under study. In addition, the experimental campaigns performed so far focused essentially on the shear capacity of joints, instead of studying their

rotational capacity, which is deemed crucial to develop mechanisms for redistribution of loads after a local failure. Thus, experimental tests shall be performed to reduce the uncertainties related with the constitutive models used in the present thesis. On the other hand, a sudden loss of elements, due to impacts or explosions, triggers a dynamic response of the damaged structure. Thus, nonlinear dynamic analyses shall be performed in the future to assess the reliability of the fragility curves proposed in this thesis.

5.4 Applications

The research work presented throughout this thesis aims to provide guidelines for the design and assessment of multi-storey timber buildings. In this way, the model proposed for CLT diaphragms constitutes a good alternative to simplified methodologies applied during the design phase. Risk assessments are crucial for decision making and involve the computation of failure probabilities for distinct exposures as earthquakes, impacts and explosions. The values assumed are commonly obtained from qualitative measures based on past occurrences and experts opinions. This thesis presents quantitative methodologies that can be used in opposition, having the advantage of being directly related with the cases under study.

5.5 Future Work

In regard of CLT diaphragm modeling, future studies will concentrate on keeping model reliability while decreasing the effort expended in including crucial behaviors such as panels' closure in surface spline connections. For instance, the solution proposed by Breneman et al. (2016), where the connection zones are modeled with 2D shell elements with distinct properties of the CLT panels, already constitutes a good step in this direction. Further investigations should be carried out in order to evaluate and validate such proposal with experimental results, keeping in mind that it as to provide different behavior for perpendicular directions.

The seismic assessment performed on a moment-resisting frame structure with ring-doweled showed that there is room to perform further experimental tests in order to evaluate how a reduction in connected elements thicknesses and slenderness of dowels would impact the ductility

and strength degradation of ring-doweled joints. Such tests, along with the methodology proposed in this work, could contribute to propose new design values and detailing requirements to moment-resisting joints, in future works. Further investigations will also incorporate multi-record incremental analysis in three-dimensional models. The effect of ground motion direction and time duration will be studied also in a probabilistic approach. In addition, the variability on the responses observed during this study also indicates that more experimental campaigns need to be performed in the future to build a database of moment-resisting timber connections. This would also allow for characterization of the uncertainty of the expected model parameters used in design and their correlation with observed joint performance.

The rotational capacity of the diaphragm connections to the main lateral resisting systems is crucial to develop mechanisms that allow the redistribution of loads after a local failure. Thus, experimental tests shall be performed to reduce the uncertainties related with the constitutive models used of their representation. The methodologies presented to generate fragility curves can be included on a risk based robustness assessment that consider also the probabilities of occurrence of different exposures, such as impacts and explosions, while considering the direct and indirect consequences of failures. Thus, following research efforts can focus on the quantification of those costs, while working on a reduction of the inherent model uncertainties.

References

- ABCB, A. B. C. B. (2015). *National construction code*. Australian Building Codes Board.
- Abrahamsen, R. B., & Malo, K. A. (2014). Structural design and assembly of "Treet"—A 14-storey timber residential building in Norway. In *13th World Conference on Timber Engineering* (p. 8).
- American Wood Council. (2003). *Heavy Timber Construction* (Tech. Rep.). Washington, DC: American Forest & Paper Association, Inc.
- Amini, M. O., van de Lindt, J. W., Rammer, D., Pei, S., Line, P., & Popovski, M. (2018). Systematic experimental investigation to support the development of seismic performance factors for cross laminated timber shear wall systems. *Engineering Structures*, *172*, 392 - 404. Retrieved from <http://www.sciencedirect.com/science/article/pii/S0141029617317297> doi: <https://doi.org/10.1016/j.engstruct.2018.06.021>
- Andreolli, M., Piazza, M., Tomasi, R., & Zandonini, R. (2011). Ductile moment-resistant steel-timber connections. *Proceedings of the Institution of Civil Engineers-Structures and Buildings*, *164*(2), 65–78.
- APA. (2017). *ANSI/APA PRG-320 - Standard for Performance-Rated Cross-Laminated Timber*.
- APA. (2018). *APA PR-L320 DRJ Cross-Laminated Timber*.
- ARUP. (2011). *Review of International Research on Structural Robustness and Disproportionate Collapse* (Tech. Rep.). London.
- ASCE. (2010). *7-10 minimum design loads for buildings and other structures*. American Society of Civil Engineers, Reston, VA. U.S.A..
- ASCE. (2014). *ASCE/SEI 41-13. Seismic Evaluation and Retrofit of Existing Buildings*.
- ASCE. (2016). *Minimum design loads for buildings and other structures* (Vol. 7). American Society of Civil Engineers.
- Ashtari, S., Haukaas, T., & Lam, F. (2014). In-Plane Stiffness of Cross-Laminated Timber Floors. In *13th WCTE World Conference on Timber Engineering*. Quebec, Canada.
- AS/NZS 1170.0. (2002). *Structural design actions, part 0: General principles*. Standards Australia Sydney.
- ASTM. (2016). *E455-16, Standard Test Method for Static Load Testing of Framed Floor or*

- Roof Diaphragm Constructions for Buildings*. ASTM International, West Conshohocken, PA. (www.astm.org)
- AWC. (2015). *National Design Specification for Wood Construction*. Leesburg, Virginia: American Wood Council.
- Baker, J. W. (2015). Efficient analytical fragility function fitting using dynamic structural analysis. *Earthquake Spectra*, *31*(1), 579–599.
- Baker, J. W., & Jayaram, N. (2008). Correlation of spectral acceleration values from NGA ground motion models. *Earthquake Spectra*, *24*(1), 299–317.
- Baker, J. W., Schubert, M., & Faber, M. H. (2008). On the assessment of robustness. *Structural Safety*, *30*(3), 253–267.
- Barbosa, A. (2011). *Simplified vector-valued probabilistic seismic hazard analysis and probabilistic seismic demand analysis : application to the 13-story NEHRP reinforced concrete frame-wall building design example* (Unpublished doctoral dissertation). University of California, San Diego, CA.
- Bitá, H. M., & Tannert, T. (2017). Robustness of Multi-Storey Timber Buildings Robustness of Multi - Storey Timber Buildings. In *39th IABSE Symposium - Engineering the Future*. Vancouver, Canada.
- Blaß, H., Ceccotti, A., Dyrbye, C., Gnuschke, M., Hansen, K., Nielsen, J., ... Stieda, C. (1994). Timber structures in seismic regions RILEM state-of-the-art report. *Materials and Structures*, *27*(3), 157–184.
- Blaß, H., & Fellmoser, P. (2004). Design of solid wood panels with cross layers. In *8th WCTE World Conference on Timber Engineering*. Lahti, Finland.
- Blaß, H. J., Aune, P., Choo, B., Grolacher, R., Griffiths, R., Hilson, B., ... Steck, G. (1995). *Timber engineering. step 1: basis of design, material properties, structural components and joints*.
- Blomgren, H.-E., Pei, S., Zhibin Jin, J. P., Dolan, J., van de Lindt, J. W., Barbosa, A., & Huang, D. (2018). Full-scale Shake Table Testing of Cross-Laminated Timber Rocking Shear Walls with Replaceable Components. *ASCE Journal of Structural Engineering*. (Submitted Summer 2018 - Under Review)
- Bogensperger, T., Moosbrugger, T., & Silly, G. (2010). Verification of CLT-Plates under loads in plane. In *11th WCTE World Conference on Timber Engineering*.
- Bouchair, A., Racher, P., & Bocquet, J. (2007). Analysis of dowelled timber to timber moment-

- resisting joints. *Materials and Structures*, 40(10), 1127–1141.
- Branco, J. M., & Neves, L. A. (2011). Robustness of timber structures in seismic areas. *Engineering Structures*, 33(11), 3099–3105.
- Brandner, R., Dietsch, P., Dröscher, J., Schulte-Wrede, M., Kreuzinger, H., & Sieder, M. (2017). Cross Laminated Timber (CLT) Diaphragms Under Shear: Test configuration, Properties and Design. *Construction and Building Materials*, 147, 312–327.
- Brandner, R., Flatscher, G., Ringhofer, A., Schickhofer, G., & Thiel, A. (2016). Cross Laminated Timber (CLT): Overview and Development. *European Journal of Wood and Wood Products*, 74(3), 331–351. doi: 10.1007/s00107-015-0999-5
- Breneman, S., McDonnell, E., & Zimmerman, R. (2016). An approach to CLT Diaphragm Modeling for Seismic Design with Application to a U.S. High-Rise Project. In *14th WCTE World Conference on Timber Engineering*. Vienna, Austria.
- Butler, T. (2016). International House Sydney. In *22. Internationales Holzbau-Forum IHF* (pp. 1–11). Garmisch-Partenkirchen, Germany.
- Byfield, M., Mudalige, W., Morison, C., & Stoddart, E. (2014). A review of progressive collapse research and regulations. *Proceedings of the Institution of Civil Engineers - Structures and Buildings*, 167(8), 447–456. Retrieved from <http://www.icevirtuallibrary.com/doi/10.1680/stbu.12.00023> doi: 10.1680/stbu.12.00023
- Byfield, M., & Paramasivam, S. (2011). Murrah building collapse: Reassessment of the transfer girder. *Journal of Performance of Constructed Facilities*, 26(4), 371–376.
- Callegari, E. (2009). *Caratterizzazione del comportamento di telai sismoresistenti in legno lamellare* (M.S. thesis). Università degli Studi di Trento, Trento, Italia. ((in Italian))
- Cavaco, E. S., Casas, J. R., Neves, L. A., & Huespe, A. H. (2010). A framework for robustness assessment in the context of corroded rc structures. In *Bridge Maintenance, Safety, Management and Life-Cycle Optimization: Proceedings of the Fifth International IABMAS Conference, Philadelphia, USA, 11-15 July 2010* (p. 421).
- Ceccotti, A., Lauriola, M., Pinna, M., & Sandhaas, C. (2006). SOFIE project—cyclic tests on cross-laminated wooden panels. In *9th WCTE World Conference on Timber Engineering*. Portland, Oregon, USA.
- Ceccotti, A., & Sandhaas, C. (2010). A proposal for a standard procedure to establish the seismic behaviour factor q of timber buildings. In *11th World Conference on Timber*

Engineering.

- Ceccotti, A., Sandhaas, C., Okabe, M., Yasumura, M., Minowa, C., & Kawai, N. (2013). SOFIE project – 3D shaking table test on a seven-storey full-scale cross-laminated timber building. *Earthquake Engineering & Structural Dynamics*, 42(13), 2003–2021.
- CEN. (2002a). *EN 12512: 2001. Timber Structures - Test Methods - Cyclic Testing of Joints Made with Mechanical Fasteners.*
- CEN. (2002b). *EN 1991-1-1: Eurocode 1: Actions on structures – Part 1-1: General actions - Densities, self-weight, imposed loads for buildings.* European Committee for Standardisation.
- CEN. (2004a). *EN 10025 : 2004. Hot rolled products of structural steels.*
- CEN. (2004b). *EN 1995-2 (2004) (English): Eurocode 5: Design of timber structures - Part 2: Bridges.* European Committee for Standardisation.
- CEN. (2005). *EN 1995-1-1:2005, Design of timber structures. P. 1-1: General - Common rules and rules for buildings.* European Committee for Standardisation.
- CEN. (2006). *EN 1991-1-7 (2006) Actions on structures. Part 1-7: General actions - Accidental actions.* European Committee for Standardisation.
- CEN. (2013a). *EN 14080:2013. Timber structures — Glued laminated timber — Requirements.*
- CEN. (2013b). *En 1998-1: Eurocode 8: Design of structures for earthquake resistance – part 1: General rules, seismic actions and rules for buildings.* European Committee for Standardisation.
- CEN. (2016). *EN 338:2016. Structural timber. Strength classes.*
- Chopra, A. K. (1995). *Dynamics of structures* (Vol. 3). Prentice Hall New Jersey.
- Chui, Y. H., & Li, Y. (2005). Modeling timber moment connection under reversed cyclic loading. *ASCE Journal of Structural Engineering*, 131(11), 1757–1763.
- Čizmar, D., Kirkegaard, P. H., Sørensen, J. D., & Rajčić, V. (2011). Reliability-based robustness analysis for a croatian sports hall. *Engineering structures*, 33(11), 3118–3124.
- Closen, M. (2017). *Performance of CLT connections under dynamic loading.* (<http://www.my-ti-con.com/resources/slides-clt-connections-dyn-loading-usa>)
- CLT handbook: Cross-Laminated Timber. Canadian Edition.* (n.d.).
- Corotis, R. B., & Doshi, V. A. (1977). Probability models for live-load survey results. *Journal of the Structural Division*, 103(6), 1257–1274.
- CSI. (2017). *Sap2000 user's manual – version 19.* Berkeley, California.

- Dean, J., Stewart, W., & Carr, A. (1986). The seismic behaviour of plywood sheathed shear-walls. *Bulletin of the New Zealand National Society for Earthquake Engineering*, 19(1), 48–63.
- Department of Defense. (2016). *UFC 4-023-0.3. Design of buildings to resist progressive collapse*.
- DIBT. (2013). *ETA-11/0190. Self-tapping screws for use in timber constructions*.
- Dietsch, P. (2011). Robustness of large-span timber roof structures—structural aspects. *Engineering Structures*, 33(11), 3106–3112.
- Donaire-Ávila, J., Mollaioli, F., Lucchini, A., & Benavent-Climent, A. (2015). Intensity measures for the seismic response prediction of mid-rise buildings with hysteretic dampers. *Engineering Structures*, 102, 278–295.
- Dorn, M., de Borst, K., & Eberhardsteiner, J. (2013). Experiments on dowel-type timber connections. *Engineering structures*, 47, 67–80.
- Dröscher, J. (2014). *Prüftechnische Ermittlung der Schubkenngrößen von BSPScheibenelementen und Studie ausgewählter Parameter (in German)* (Unpublished master’s thesis). Graz University of Technology, Graz, Austria.
- Dujic, B., Strus, K., Zarnic, R., & Ceccotti, A. (2010). Prediction of Dynamic Response of a 7-Storey Massive XLam Wooden Building Tested on a Shaking Table. In *11th WCTE World Conference on Timber Engineering*. Riva del Garda, Italy.
- Dvorkin, E. N., & Bathe, K.-J. (1984). A continuum mechanics based four-node shell element for general non-linear analysis. *Engineering computations*, 1(1), 77–88.
- Ellingwood, B. R., & Dusenberry, D. O. (2005). Building design for abnormal loads and progressive collapse. *Computer-Aided Civil and Infrastructure Engineering*, 20(3), 194–205.
- Ellingwood, B. R., Smilowitz, R., Dusenberry, D. O., Duthinh, D., Lew, H. S., & Carino, N. J. (2007). *Best practices for reducing the potential for progressive collapse in buildings (NISTIR 7396)*.
- Faber, M., Köhler, J., & Nishijima, K. (2011). *Applications of statistics and probability in civil engineering*. CRC Press.
- Faggella, M., Barbosa, A. R., Conte, J. P., Spacone, E., & Restrepo, J. I. (2013). Probabilistic seismic response analysis of a 3-D reinforced concrete building. *Structural Safety*, 44, 11–27.

- Fajfar, P. (1996). Design spectra for the new generation of codes. In *11 th world conference on earthquake engineering*.
- Fajfar, P. (1999). Capacity spectrum method based on inelastic demand spectra. *Earthquake engineering and structural dynamics*, 28(9), 979–994.
- Falk, R. H., & Itani, R. Y. (1989). Finite element modeling of wood diaphragms. *Journal of Structural Engineering*, 115(3), 543–559.
- Flaig, M., & Blaß, H. (2013). Shear strength and shear stiffness of CLT-beams loaded in plane. In *Proceedings. CIB-W18 Meeting 46*.
- Foliente, G. C. (1995). Hysteresis modeling of wood joints and structural systems. *Journal of Structural Engineering*, 121(6), 1013–1022.
- Foliente, G. C. (1996). Issues in seismic performance testing and evaluation of timber structural systems. In *Proceedings of the International Wood Engineering Conference, New Orleans, La* (pp. 28–31).
- Foliente, G. C. (1997). Modeling and analysis of timber structures under seismic loads: State-of-the-art. *Earthquake performance and safety of timber structures*, 55–73.
- Foliente, G. C., & Mohammad, N. N. (1996). Equivalent linearization of generally pinching hysteretic, degrading systems. *Earthquake Engineering and Structural Dynamics*, 25, 611–629.
- Folz, B., & Filiatrault, A. (2001). Cyclic analysis of wood shear walls. *Journal of Structural Engineering*, 127(4), 433–441.
- Folz, B., & Filiatrault, A. (2004). Seismic analysis of woodframe structures. II: Model implementation and verification. *Journal of Structural Engineering*, 130(9), 1361–1370.
- Foschi, R. O. (2000). Modeling the hysteretic response of mechanical connections for wood structures. In *6th World Conference of Timber Engineering, Whistler, BC, Canada*.
- Fruehwald, E., Serrano, E., Toratti, T., Emilsson, A., & Thelandersson, S. (2007). *Design of safe timber structures-how can we learn from structural failures in concrete, steel and timber?* (Tech. Rep.). Lund, Sweden: Lund Institute of Technology.
- Ganey, R., Berman, J., Akbas, T., Loftus, S., Dolan, J. D., Sause, R., ... Blomgren, H.-E. (2017). Experimental Investigation of Self-Centering Cross-Laminated Timber Walls. *Journal of Structural Engineering*, 143(10), 04017135.
- Gavric, I., Fragiacomio, M., & Ceccotti, A. (2015). Cyclic behaviour of typical metal connectors for cross-laminated (clt) structures. *Materials and structures*, 48(6), 1841–1857.

- Ghosh, S. (2016). Alternative Diaphragm Seismic Design Force Level of asce 7-16. *Structure Magazine*.
- GSA, G. S. A. (2013). *Alternate path analysis & design guidelines for progressive collapse resistance*. GSA Washington, DC.
- Gsell, D., Feltrin, G., Schubert, S., Steiger, R., & Motavalli, M. (2007). Cross-Laminated Timber Plates: Evaluation and Verification of Homogenized Elastic Properties. *Journal of Structural Engineering*, 133(1), 132–138. Retrieved from [http://ascelibrary.org/doi/10.1061/\(ASCE\)0733-9445\(2007\)133:1\(132\)](http://ascelibrary.org/doi/10.1061/(ASCE)0733-9445(2007)133:1(132)) doi: 10.1061/(ASCE)0733-9445(2007)133:1(132)
- Hall, J. F., Holmes, W. T., & Somers, P. (1996). *Northridge earthquake of January 17, 1994: reconnaissance report* (Vol. 1). Earthquake Engineering Research Institute.
- Hansson, M., & Larsen, H. J. (2005). Recent failures in glulam structures and their causes. *Engineering Failure Analysis*, 12(5), 808–818.
- Harris, R. (2007). *Manual for the design of timber building structures to eurocode 5, london: The institution of structural engineers*. UK.
- Harris, R., Ringhofer, A., & Schickhofer, G. (2013). *Focus Solid Timber Solutions - European Conference on Cross Laminated Timber (CLT)*. University of Bath.
- Harte, A. M. (2017). Mass timber – the emergence of a modern construction material. *Journal of Structural Integrity and Maintenance*, 2(3), 121–132. Retrieved from <https://doi.org/10.1080/24705314.2017.1354156> doi: 10.1080/24705314.2017.1354156
- Helmy, H., Salem, H., & Mourad, S. (2012). Progressive collapse assessment of framed reinforced concrete structures according to ufc guidelines for alternative path method. *Engineering Structures*, 42, 127–141.
- Higgins, C., Barbosa, A., & Blank, C. (2017). *Structural Tests of Concrete Composite-Cross-Laminated Timber Floors* (Tech. Rep. No. 17-01). Oregon State University, Corvallis: Structural Engineering.
- Hirai, T., Meng, Q., Sawata, K., Koizumi, A., Sasaki, Y., & Uematsu, T. (2008). Some Aspects of Frictional Resistance in Timber Construction. In *10th WCTE World Conference on Timber Engineering*.
- Hossain, A., Lakshman, R., & Tannert, T. (2015). Shear Connections with Self-Tapping Screws for Cross-Laminated Timber Panels. *Structures Congress 2015*, 2251–2259.

Retrieved from <http://ascelibrary.org/doi/10.1061/9780784479117.195> doi:
10.1061/9780784479117.195

- Hossain, A., Popovski, M., & Tannert, T. (2018). Cross-laminated timber connections assembled with a combination of screws in withdrawal and screws in shear. *Engineering Structures*, *168*, 1–11.
- Huber, J. A. J., Ekevad, M., Girhammar, U. A., & Berg, S. (2018). Structural robustness and timber buildings – a review. *Wood Material Science & Engineering*, *0*(0), 1–22. Retrieved from <https://www.tandfonline.com/doi/full/10.1080/17480272.2018.1446052> doi: 10.1080/17480272.2018.1446052
- Humar, J., & Rahgozar, M. (1996). Concept of overstrength in seismic design. In *11 th world conference on earthquake engineering*.
- Ibarra, L. F., Medina, R. A., & Krawinkler, H. (2005). Hysteretic models that incorporate strength and stiffness deterioration. *Earthquake Engineering and Structural Dynamics*, *34*(12), 1489–1511.
- ICC. (2015). *International Building Code*. International Code Council.
- Iqbal, A., Pampanin, S., Palermo, A., & Buchanan, A. H. (2015). Performance and Design of LVL Walls Coupled with UFP Dissipaters. *Journal of Earthquake Engineering*, *19*(3), 383-409.
- ISO. (2007). *ISO 22111:2007(en), Bases for design of structures - General requirements*. International Organization for Standardization.
- Izzuddin, B., Vlassis, A., Elghazouli, A., & Nethercot, D. (2008). Progressive collapse of multi-storey buildings due to sudden column loss—part i: Simplified assessment framework. *Engineering structures*, *30*(5), 1308–1318.
- JCSS. (2001). *Probabilistic model code*. The Joint Committee on Structural Safety.
- Johansen, K. (1949). Theory of timber connections. In *International Association for Bridge and Structural Engineering* (Vol. 9, pp. 249–262).
- Jorissen, A., & Fragiacommo, M. (2011). General notes on ductility in timber structures. *Engineering structures*, *33*(11), 2987–2997.
- Karacabeyli, E., & Douglas, B. (2013). *CLT handbook: Cross-Laminated Timber. US Edition*. FPIInnovations.
- Khandelwal, K., & El-Tawil, S. (2011). Pushdown resistance as a measure of robustness in progressive collapse analysis. *Engineering Structures*, *33*(9), 2653–2661.

- Khandelwal, K., El-Tawil, S., & Sadek, F. (2009). Progressive collapse analysis of seismically designed steel braced frames. *Journal of Constructional Steel Research*, *65*(3), 699–708.
- Kirkegaard, P. H., Sørensen, J. D., Čizmar, D., & Dietsch, P. (2010). Robustness evaluation of timber structures-results from EU COST action E55: WG3. *Structures & Architecture: ICSA*, 129–131.
- Kode, A. (2018). *Testing of a Full-Scale Mass Timber Diaphragm* (Unpublished master's thesis). Colorado State University, Fort Collins, Colorado.
- Kohler, J., Fink, G., & Brandner, P. (2016). Basis of design principles – application to CLT. In *Cross Laminated Timber – a competitive wood product for visionary and fire safe buildings: Joint Conference of COST Actions FP1402 and FP1404*. Stockholm, Sweden.
- Köhler, J., Sørensen, J. D., & Faber, M. H. (2007). Probabilistic modeling of timber structures. *Structural Safety*, *29*(4), 255–267.
- Lee, K. H., & Rosowsky, D. V. (2006). Fragility analysis of woodframe buildings considering combined snow and earthquake loading. *Structural Safety*, *28*(3), 289–303.
- Li, Y., & Ellingwood, B. R. (2007). Reliability of woodframe residential construction subjected to earthquakes. *Structural Safety*, *29*(4), 294–307.
- Liel, A. B., Haselton, C. B., Deierlein, G. G., & Baker, J. W. (2009). Incorporating modeling uncertainties in the assessment of seismic collapse risk of buildings. *Structural Safety*, *31*(2), 197–211.
- Loss, C., Hossain, A., & Tannert, T. (2018). Simple cross-laminated timber shear connections with spatially arranged screws. *Engineering Structures*, *173*, 340–356.
- Lowes, L. N., Mitra, N., & Altoontash, A. (2003). *A beam-column joint model for simulating the earthquake response of reinforced concrete frames*. Pacific Earthquake Engineering Research Center, College of Engineering, University of California.
- Lyu, C., Gilbert, B. P., Gunalan, S., Karampour, H., Underhill, I. D., Masaeli, M., & Guan, H. (2018). Progressive Collapse (Robustness) Behaviour of Mid-Rise Mass Timber Frame Buildings. In *15th WCTE World Conference on Timber Engineering*. Seoul, Rep. of Korea.
- Macpherson, E., Papastavrou, P., Wallwork, T., Smith, S., & McRobie, A. (2018). The rotational stiffness of cross-laminated timber half-lap joints. In *15th WCTE World Conference on Timber Engineering*. Seoul, Rep. of Korea.
- Mazzoni, S., McKenna, F., Scott, M., & Fenves, G. (2006). *Opensees command language*

manual. Pacific Earthquake Engineering Research Center.

- McKenna, F., Scott, M. H., & Fenves, G. L. (2009). Nonlinear finite-element analysis software architecture using object composition. *Journal of Computing in Civil Engineering*, *24*(1), 95–107.
- Melchers, R. E. (1999). *Structural reliability analysis and prediction*. John Wiley & Son Ltd.
- Mettem, C. J., Bainbridge, R. J., Pitts, G. C., & Enjily, V. (1998). Timber frame construction for medium-rise buildings. *Progress in Structural Engineering and Materials*, *1*(3), 253-262. Retrieved from <https://onlinelibrary.wiley.com/doi/abs/10.1002/pse.2260010306> doi: 10.1002/pse.2260010306
- Miranda, E., & Bertero, V. V. (1994). Evaluation of strength reduction factors for earthquake-resistant design. *Earthquake spectra*, *10*(2), 357–379.
- Mitchell, D., & Paultre, P. (1994). Ductility and overstrength in seismic design of reinforced concrete structures. *Canadian Journal of Civil Engineering*, *21*(6), 1049–1060.
- Mollaioli, F., Lucchini, A., Cheng, Y., & Monti, G. (2013). Intensity measures for the seismic response prediction of base-isolated buildings. *Bulletin of Earthquake Engineering*, *11*(5), 1841–1866.
- Mpidi Bitu, H., Currie, N., & Tannert, T. (2017). Reliability analysis and disproportionate collapse for multi storey cross-laminated timber building. In *16th World Conference on Earthquake Engineering*. Santiago, Chile.
- Mugabo, I., Barbosa, A. R., & Riggio, M. (2018). Modal Identification Study of a Four-story Mass-timber Building. In *15th World Conference on Timber Engineering*. Seoul, Republic of Korea.
- Munch-Andersen, J., & Dietsch, P. (2009). Robustness considerations from failures in two large-span timber roof structures. In *Joint Workshop of COST Actions TU0601 and E55*.
- Newmark, N. M. (1959). A method of computation for structural dynamics. In *Proc. ASCE* (Vol. 85, pp. 67–94).
- Nordic Structures. (2017). *Nordic Structures. Publications*. Retrieved 24-10-2018, from <https://www.nordic.ca/en/documentation/publications/origine>
- Oberholzer, M. (2016). Building complex Arbora (434 residential units) in Montreal and Origine (13 storeys) in Quebec City. In *22. Internationales Holzbau-Forum IHF*. Garmisch-

Partenkirchen, Germany.

- Outes, J., Gay, R., Cañá, A., Díez Barra, M., & Fernández, M. (2011). Desarrollo de metodología para la determinación de los coeficientes de fricción estático y dinámico de diferentes especies de madera. In *1^o Congresso Ibero-Latino Americano da Madeira na Construção*. Coimbra, Portugal.
- Park, J., & Kim, J. (2010). Fragility analysis of steel moment frames with various seismic connections subjected to sudden loss of a column. *Engineering Structures*, *32*(6), 1547–1555.
- Park, R. (1996). Explicit incorporation of element and structure overstrength in the design process. In *11th World Conference on Earthquake Engineering*.
- Park, Y., & Ang, A. (1985). Mechanistic seismic damage model for reinforced concrete. *ASCE Journal of Structural Engineering*, *111*(4), 722–739.
- Patsy, B. (2017). Albina Yard - North Portland CLT Office Building. *Structure Magazine*.
- Pearson, C., & Delatte, N. (2005). Ronan Point Apartment Tower Collapse and its Effect on Building Codes. *Journal of Performance of Constructed Facilities*, *19*(2), 172–177. doi: 10.1061/(ASCE)0887-3828(2005)19:2(172)
- PEER. (2002). *Pacific Earthquake Engineering Research (PEER) NGA Database*. <http://www.peer.berkeley.edu/nga>.
- Pei, S., Rammer, D., Popovski, M., Williamson, T., Line, P., & van de Lindt, J. W. (2016). An Overview of CLT Research and Implementation in North America. In *14th WCTE World Conference on Timber Engineering*. Vienna, Austria.
- Pei, S., Van De Lindt, J., Popovski, M., Berman, J., Dolan, J., Ricles, J., ... Rammer, D. (2014). Cross-laminated timber for seismic regions: Progress and challenges for research and implementation. *Journal of Structural Engineering*, *142*(4), E2514001.
- Pei, S., van de Lindt, J. W., Barbosa, A., Berman, J., McDonnell, E., Dolan, J., ... Ryan, K. (2018b). Full-scale shake table test of mass-timber building with resilient post-tensioned rocking walls. In *15th WCTE World Conference on Timber Engineering*. Seoul, Rep. of Korea.
- Pei, S., van de Lindt, J. W., Barbosa, A., Berman, J., McDonnell, E., Dolan, J. D., ... Wichman, S. (2018a). Experimental seismic response of a resilient two-story mass timber building with post-tensioned rocking walls. *ASCE Journal of Structural Engineering*. (Under Review. Submitted Spring 2018)

- Pham, L. (1985). Load combinations and probabilistic load models for limit state codes. *Institution of Engineers (Australia) Civ Eng Trans*(1).
- PMC. (2011). *Probabilistic Model Code. Part 3, Resistance Models, Static Properties of Structural Steel (Rolled Sections)*. Zurich, Switzerland: JCSS. (Available from Internet: <http://www.jcss.ethz.ch>)
- Polastri, A. (2010). *Caratterizzazione del comportamento di giunti semirigidi per strutture lignee in zona sismica* (Unpublished doctoral dissertation). Università degli Studi di Trento, Trento, Italia. ((in Italian))
- Polastri, A., Tomasi, R., Piazza, M., & Smith, I. (2013). Moment resisting dowelled joints in timber structures: mechanical behaviour under cyclic tests. *INGEGNERIA SISMICA*, 30(4), 72–81.
- Popovski, M. (2000). *Seismic performance of braced timber frames* (Doctoral dissertation). doi: <http://dx.doi.org/10.14288/1.0064074>
- Popovski, M., Prion, H. G., & Karacabeyli, E. (2002). Seismic performance of connections in heavy timber construction. *Canadian Journal of Civil Engineering*, 29(3), 389–399.
- Popovski, M., Schneider, J., & Schweinsteiger, M. (2010). Lateral load resistance of cross-laminated wood panels. *11th WCTE World Conference on Timber Engineering*, 4, 3394–3403.
- Porteous, J., & Kermani, A. (2013). *Structural timber design to eurocode 5*. Chichester, United Kingdom: Blackwell Publishing Ltd.
- Porter, K. (2015). Beginner’s guide to fragility, vulnerability, and risk. *Encyclopedia of Earthquake Engineering*, 235–260.
- Porter, K., Kennedy, R., & Bachman, R. (2007). Creating fragility functions for performance-based earthquake engineering. *Earthquake Spectra*, 23(2), 471–489. Retrieved from <http://dx.doi.org/10.1193/1.2720892> doi: 10.1193/1.2720892
- Pozza, L. (2013). *Ductility and behaviour factor of wood structural systems* (PhD thesis). Università di Padova, Padova, Italy.
- Pryor, S. (2017). *Shear Strength of Self-tapping screws* (Tech. Rep.). Holly Street Riverside, CA: Simpson Strong-Tie, USA. (Personal Communication)
- Quenneville, J. H., & Mohammad, M. (2000). On the failure modes and strength of steel-wood-steel bolted timber connections loaded parallel-to-grain. *Canadian journal of civil engineering*, 27(4), 761–773.

- Ribeiro, F., Barbosa, A., & Neves, L. (2014). Application of reliability-based robustness assessment of steel moment resisting frame structures under post-mainshock cascading events. *ASCE Journal of Structural Engineering*, -(140, SPECIAL ISSUE: Computational Simulation in Structural Engineering, A4014008).
- Rinaldin, G., Amadio, C., & Fragiacommo, M. (2013). A component approach for the hysteretic behaviour of connections in cross-laminated wooden structures. *Earthquake engineering & structural dynamics*, 42(13), 2023–2042.
- Rodrigues, L. G., Branco, J. M., Neves, L. A., & Barbosa, A. R. (2018). Seismic assessment of a heavy-timber frame structure with ring-doweled moment-resisting connections. *Bulletin of Earthquake Engineering*, 16(3), 1341–1371.
- Rodriguez, M. E., Restrepo, J. I., & Carr, A. J. (2002). Earthquake-induced floor horizontal accelerations in buildings. *Earthquake Engineering & Structural Dynamics*, 31(3), 693–718. Retrieved from <https://onlinelibrary.wiley.com/doi/abs/10.1002/eqe.149>
doi: 10.1002/eqe.149
- Rosowsky, D. V., & Ellingwood, B. R. (2002). Performance-based engineering of wood frame housing: Fragility analysis methodology. *ASCE Journal of Structural Engineering*, 128(1), 32–38.
- Rubinstein, R. Y., & Kroese, D. P. (2011). *Simulation and the monte carlo method* (Vol. 707). John Wiley & Sons.
- Sadeghi, M., & Smith, I. (2014). Edge Connections for CLT Plates : In-Plane Shear Tests on Half-Lapped and Single-Spline Joints. In *13th WCTE World Conference on Timber Engineering*. Quebec, Canada.
- Sartori, T., & Tomasi, R. (2013). Experimental investigation on sheathing-to-framing connections in wood shear walls. *Engineering Structures*, 56, 2197–2205.
- Sentler, L. (1976). *Live load surveys: a review with discussions*. Division of Building Technology, Lund Institute of Technology.
- Shome, N. (1999). *Probabilistic seismic demand analysis of nonlinear structures*. Stanford University.
- SIA. (2004). *Standard SIA 260 - Basis of Structural Design*. Swiss Society of Engineers and Architects.
- Sørensen, J. D. (2011). Framework for robustness assessment of timber structures. *Engineering Structures*, 33(11), 3087–3092.

- Spickler, K., Cloßen, M., Line, P., & Pohll, M. (2015). *Cross laminated timber horizontal diaphragm design example* (Tech. Rep.). Granite Bay, CA: CLT White paper. (<http://structurlam.com/wp-content/uploads/2015/10/CrossLam-Horizontal-Diaphragm-Design-Example-Rv10.pdf>)
- Starossek, U. (2006). Progressive collapse of structures: Nomenclature and procedures. *Structural engineering international*, 16(2), 113–117.
- Starossek, U., & Haberland, M. (2010). Disproportionate Collapse: Terminology and Procedures. *Journal of Performance of Constructed Facilities*, 24(6), 519–528. Retrieved from <http://ascelibrary.org/doi/10.1061/%28ASCE%29CF.1943-5509.0000138> doi: 10.1061/(ASCE)CF.1943-5509.0000138
- Steiger, R., Fink, G., Nerbano, S., Hack, E., & Beyer, K. (2018). Experimental investigation of friction stresses between adjacent panels made of Oriented Strand Board (OSB) and between OSB panels and glued laminated timber (GLT) frame members. *Materials and Structures/Materiaux et Constructions*, 51(1), 1–14. Retrieved from <https://doi.org/10.1617/s11527-017-1124-5> doi: 10.1617/s11527-017-1124-5
- Sullivan, K. (2017). *Behavior of Cross-Laminated Timber Diaphragm Panel-to-Panel Connections with Self-Tapping Screws* (Unpublished master's thesis). Oregon State University, United States.
- Sustersic, I., Fragiaco, M., & Dujic, B. (2016). Seismic Analysis of Cross-Laminated Multistory Timber Buildings Using Code-Prescribed Methods: Influence of Panel Size, Connection Ductility, and Schematization. *Journal of Structural Engineering*, 142(4), E4015012. Retrieved from <http://ascelibrary.org/doi/10.1061/%28ASCE%29ST.1943-541X.0001344> doi: 10.1061/(ASCE)ST.1943-541X.0001344
- Sutley, E. J., & van de Lindt, J. W. (2016). Evolution of predicted seismic performance for wood-frame buildings. *Journal of Architectural Engineering*, B4016004.
- Thiel, A., & Brandner, R. (2016). Design of CLT Elements—Basics and some Special Topics. In *Cross laminated timber – a competitive wood product for visionary and fire safe buildings: Joint conference of cost actions fp1402 and fp1404*. Stockholm, Sweden.
- Tomasi, R., Crosatti, A., & Piazza, M. (2010). Theoretical and experimental analysis of timber-to-timber joints connected with inclined screws. *Construction and building materials*, 24(9), 1560–1571.

- Vamvatsikos, D., & Cornell, C. (2002). Incremental dynamic analysis. *Earthquake Engineering and Structural Dynamics*, 31(3), 491-514.
- van de Lindt, J. W., Bahmani, P., Mochizuki, G., Pryor, S. E., Gershfeld, M., Tian, J., ... Rammer, D. (2016). Experimental Seismic Behavior of a Full-Scale Four-Story Soft-Story Wood-Frame Building with Retrofits. II: Shake Table Test Results. *Journal of Structural Engineering*, 142(4), E4014004.
- van de Lindt, J. W., & Dao, T. N. (2009). Performance-based wind engineering for wood-frame buildings. *ASCE Journal of Structural Engineering*, 135(2), 169–177.
- van de Lindt, J. W., Furley, J., Amini, M. O., Pei, S., Tamagnone, G., Barbosa, A. R., ... Popovski, M. (2018). Experimental Seismic Behavior of a Two-Story CLT Platform Building. *ASCE Journal of Structural Engineering*. (Submitted Summer 2018 - Under Review)
- van de Lindt, J. W., Pei, S., Pryor, S. E., Shimizu, H., & Isoda, H. (2010). Experimental Seismic Response of a Full-Scale Six-Story Light-Frame Wood Building. *Journal of Structural Engineering*, 136(10), 1262-1272. doi: 10.1061/(ASCE)ST.1943-541X.0000222
- Vidic, T., Fajfar, P., & Fischinger, M. (1994). Consistent inelastic design spectra: strength and displacement. *Earthquake Engineering & Structural Dynamics*, 23(5), 507–521.
- Vogel, T. (2009). *Design for robustness* (Vol. 11). IABSE.
- Welch, B. (1995). *Practical programming in Tcl and Tk* (Vol. 3). Prentice Hall Upper Saddle River.
- WoodWorks. (2017). *Inspiration through Innovation* (Tech. Rep.). WoodWorks - Wood Products Council. Retrieved from <http://www.woodworks.org/project/john-w-olver-design-building-umass-amherst/>
- Yates, M., Linegar, M., & Dujic, B. (2008). Design of an 8-storey Residential Tower from KLH Cross Laminated Solid Timber Panels. In *10th WCTE World Conference on Timber Engineering*. Miyazaki, Japan.
- Yin, Y.-J., & Li, Y. (2010). Seismic collapse risk of light-frame wood construction considering aleatoric and epistemic uncertainties. *Structural Safety*, 32(4), 250–261.
- Zarnani, P., & Quenneville, P. (2014). Strength of timber connections under potential failure modes: An improved design procedure. *Construction and Building Materials*, 60, 81–90.
- Zhang, X., Fairhurst, M., & Tannert, T. (2015). Seismic reliability analyses of timber-steel-

hybrid system. In *12th International Conference on Applications of Statistics and Probability in Civil Engineering (ICASP12)*. Vancouver, Canada.

Zhang, Y., Raftery, G., & Quenneville, P. (2016). Predicting the load-deformation of bolted timber connections up to failure. In *International Network on Timber Engineering Research - Meeting 49*. Graz, Austria.

Zhu, E., Guan, Z., Rodd, P., & Pope, D. (2005). A constitutive model for OSB and its application in finite element analysis. *Holz als roh-und werkstoff*, 63(2), 87–93.